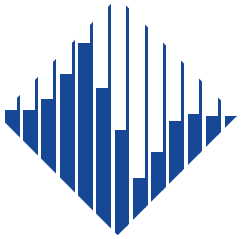

PACIFIC EARTHQUAKE ENGINEERING RESEARCH CENTER

NGA-East Ground-Motion Models for the U.S. Geological Survey National Seismic Hazard Maps

Christine A. Goulet
Yousef Bozorgnia
Nicolas Kuehn
Pacific Earthquake Engineering Research Center
University of California, Berkeley

Linda Al Atik
Linda Alatik Consulting

Robert R. Youngs
AMEC Foster Wheeler

Robert W. Graves
U.S. Geological Survey

Gail M. Atkinson
Western University

PEER Report No. 2017/03
Pacific Earthquake Engineering Research Center
Headquarters at the University of California, Berkeley

March 2017

PEER 2017/03
March 2017

Disclaimer

The opinions, findings, and conclusions or recommendations expressed in this publication are those of the author(s) and do not necessarily reflect the views of the study sponsor(s) or the Pacific Earthquake Engineering Research Center.

NGA-East Ground-Motion Models for the U.S. Geological Survey National Seismic Hazard Maps

Christine A. Goulet

Yousef Bozorgnia

Nicolas Kuehn

Pacific Earthquake Engineering Research Center
University of California, Berkeley

Linda Al Atik

Linda Alatik Consulting

Robert R. Youngs

AMEC Foster Wheeler

Robert W. Graves

U.S. Geological Survey

Gail M. Atkinson

Western University

PEER Report No. 2017/03
Pacific Earthquake Engineering Research Center
Headquarters at the University of California, Berkeley

March 2017

ABSTRACT

The purpose of this report is to provide a set of ground motion models (GMMs) to be considered by the U.S. Geological Survey (USGS) for their National Seismic Hazard Maps (NSHMs) for the Central and Eastern U.S. (CEUS). These interim GMMs are adjusted and modified from a set of preliminary models developed as part of the Next Generation Attenuation for Central and Eastern North-America (CENA) project (NGA-East). The NGA-East objective was to develop a new ground-motion characterization (GMC) model for the CENA region. The GMC model consists of a set of GMMs for median and standard deviation of ground motions and their associated weights in the logic-tree for use in probabilistic seismic hazard analysis (PSHA).

NGA-East is a large multidisciplinary project coordinated by the Pacific Earthquake Engineering Research Center (PEER), at the University of California, Berkeley. The project has two components: (1) a set of scientific research tasks, and (2) a model-building component following the framework of the "Seismic Senior Hazard Analysis Committee (SSHAC) Level 3" [Budnitz et al. 1997; NRC 2012]. Component (2) is built on the scientific results of component (1) of the NGA-East Project. This report does not document the final NGA-East model under (2), but instead presents interim GMMs for use in the U.S. Geological Survey (USGS) National Seismic Hazard Maps.

Under component (1) of NGA-East, several scientific issues were addressed, including: (a) development of a new database of empirical data recorded in CENA; (b) development of a regionalized ground-motion map for CENA, (c) definition of the reference site condition; (d) simulations of ground motions based on different methodologies, (e) development of numerous GMMs for CENA, and (f) the development of the current report. The scientific tasks of NGA-East were all documented as a series of PEER reports.

This report documents the GMMs recommended by the authors for consideration by the USGS for their NSHM. The report documents the key elements involved in the development of the proposed GMMs and summarizes the median and aleatory models for ground motions along with their recommended weights. The models presented here build on the work from the authors and aim to globally represent the epistemic uncertainty in ground motions for CENA.

The NGA-East models for the USGS NSHMs includes a set of 13 GMMs defined for 25 ground-motion intensity measures, applicable to CENA in the moment magnitude range of 4.0 to 8.2 and covering distances up to 1500 km. Standard deviation models are also provided for general PSHA applications (ergodic standard deviation). Adjustment factors are provided for hazard computations involving the Gulf Coast region.

ACKNOWLEDGMENTS

This study was sponsored by the Pacific Earthquake Engineering Research Center (PEER) as part of the NGA-East research project and was partially supported by the U.S. Nuclear Regulatory Commission (NRC), the U.S. Department of Energy (DOE), and the Electric Power Research Institute (EPRI), with the participation of the U.S. Geological Survey (USGS). Any opinions, findings and conclusions, or recommendations expressed in this material are those of the authors and do not necessarily reflect those of the sponsoring agencies.

In the tradition of all NGA projects, NGA-East benefited from very fruitful interactions among tens of participants. We gratefully acknowledge all NGA-East participants for their dedication and teamwork. We extend a very special thank you to Norm Abrahamson for his leadership and advisory role throughout the Project and to David Boore for his timely response to requests for the development of this report.

LIST OF ACRONYMS

1CCSP	Single Corner Constant Stress Parameter (DASG GMM)
1CVSP	Single Corner Variable Stress Parameter (DASG GMM)
2CCSP	Double Corner Constant Stress Parameter (DASG GMM)
2CVSP	Double Corner Variable Stress Parameter (DASG GMM)
ACP	Atlantic Coastal Plain
ACR	Active Continental Region
AEF(s)	Annual Exceedance Frequency(ies)
ANC	Al Nomand and Cramer GMM
ANSS	Advanced National Seismic System
APP	Appalachian Mountains
ATC	Active Tectonic Region
B_a04	Boore GMM based on Atkinson [2004]
B_ab14	Boore GMM based on Atkinson and Boore [2014]
B_ab95	Boore GMM based on Atkinson and Boore [1995]
B_bca10d	Boore GMM based on Boore et al. [2010]
B_bs11	Boore GMM based on Boatwright and Seekins [2011]
B_sgd02	Boore GMM based on Silva et al. [2002]
BCHydro	British Columbia Hydro
CAV	Cumulative Absolute Velocity
CBR	Center, body, and range
CDF	Cumulative Density Function
CENA	Central and Eastern North America
CERI	Center for Earthquake Research and Information
CEUS	Central and Eastern United States
CEUS SSC	Central and Eastern U.S. Seismic Source Characterization for Nuclear Facilities Project
CNS	Columbia Networking Station
CNA	Central North America
CI	Continental Interior
CV	Coefficient of Variation
DASG	Darragh, Abrahamson, Silva and Gregor GMM(s)
DCPP	Diablo Canyon Power Plant
DOE	United States Department of Energy
EAS	Effective Amplitude Spectrum
ENA	Eastern North America
EQUID	Earthquake identifier number
EPRI	Electric Power Research Institute
FAS	Fourier Amplitude Spectra
FFT	Fast Fourier Transform
GC	Gulf Coast
GCD	Global Crustal Database
GOF	Goodness-of-Fit
GMC	Ground-Motion Characterization
GMIM	Ground Motion Intensity Measure (PSA, PGA, PGV)

GMM	Ground Motion Model is used preferably in the report, GMMs includes GMPEs and other model formats
GMPE	Ground Motion Prediction Equation is used for GMMs that have been parameterized into equations
GSC	Geologic Survey of Canada
GP	Gaussian Processes
GWG	Geotechnical Working Group
HA15	Hassani and Atkinson GMM
Hanford Project	The Hanford Probabilistic Seismic Hazard Analysis Project
HQ	Hydro Québec
LDCO	Lamont-Doherty Cooperative Network
M	Generic symbol for magnitude (without specification of magnitude type)
M	Moment magnitude
MECE	Mutually Exclusive, Completely Exhaustive
MEM	Mississippi Embayment/Gulf Coast Region
MESE	Mesozoic and younger extension
MIA	Model Interface Advisor
MSE	Mean Square Error
NGA	Next Generation Attenuation
NGA-East	Next Generation Attenuation Relationship for the Central and Eastern North American Region
NGA-West	Next Generation Attenuation Relationship for shallow crustal earthquakes in active tectonic regions (original project)
NGA-West2	Next Generation Attenuation Relationship for shallow crustal earthquakes in active tectonic regions (phase 2 of NGA-West project)
NMESE	Regions with older or no extension
NNP	Nuclear power plant
NRC	United States Nuclear Regulatory Commission
NRCan	Natural Resources Canada
NSHMP	National Seismic Hazard Mapping Program
PCA	Principal Component Analysis
PDF	Probability Density Function
PEER	Pacific Earthquake Engineering Research Center
PEER_EX	PEER GMM based on EXSIM simulations [Atkinson and Assatourians 2015]
PEER_GP	PEER GMM based on Graves and Pitarka [2015] simulations
PGA	Peak Ground Acceleration
PGV	Peak Ground Velocity
PIE	Potentially-Induced Event
PCA	Principal Component Analysis
PS	Point-Source
PPRP	Participatory Peer Review Panel
PSA	Pseudo-Spectral Acceleration (5% damping in this report)
PSHA	Probabilistic Seismic Hazard Analysis
PRP	PEGASOS Refinement Project
PVNGS	Palo Verde Nuclear Generating Station sites

PZCT_M1SS	Pezeshk, Zandieh, Campbell and Tavakoli GMM, simulations-based magnitude scaling
PZCT_M2ES	Pezeshk, Zandieh, Campbell and Tavakoli GMM, empirical magnitude scaling
Q	Quality factor
R	Generic symbol for distance (without specification of distance type)
R_{HYP}	Hypocentral distance (km)
R_{JB}	Joyner-Boore distance: closest distance to the horizontal projection of the earthquake rupture plane (km)
R_X	The horizontal distance from the surface projection of the top edge of the earthquake rupture to the site, measured perpendicular to the strike of the earthquake rupture (km). RX is negative on the footwall side of the rupture and positive on the hanging-wall side
R_{RUP}	Rupture distance: closest distance to the earthquake rupture plane (km)
$RotD_{50}$	Median value of resultants of two horizontal components of ground motions as computed over each angle of rotation from 1 to 180°
RLME	Repeatable large-magnitude earthquake
RSN	Record sequence number
SCEC BBP	Southern California Earthquake Center Broadband Platform
SDOF	Single-degree-of-freedom
SCR	Stable Continental Region
SE	Squared Exponential
SLU	St. Louis University
SOMs	Self-Organizing Maps
SSC	Seismic-Source Characterization
SSHAC	Senior Seismic Hazard Analysis Committee
SGPM	SSHAC Guidelines Process Manager
StDB	Station Database
SWUS	Southwestern United States Ground Motion Characterization SSHAC Level 3 Project
USGS	United States Geological Survey
$\Delta\sigma$	Stress Parameter
T	Spectral period (in seconds)
TA	Transportable Array
TDI	Technically Defensible Interpretations
TI	Technical Integrator
TIP	Trial Implementation Project
TNSP	Thyspunt Nuclear Siting Project
UHS	Uniform Hazard Spectrum
U.S.	United States
USGS	United States Geological Survey
V_S	Shear-wave velocity
V_{S30}	Time-averaged shear-wave velocity in top 30 meters of geomaterial
WNA	Western North America
WUS	Western United States
YA15	Yenier and Atkinson GMM
YM	Yucca Mountain

Z_{hyp}, H_{hypo}	Depth to hypocenter (km)
Z_{tor}	Depth to top of rupture (km)

CONTENTS

LIST OF TABLES

LIST OF FIGURES

1 Introduction

1.1 BACKGROUND

The purpose of this report is to provide a set of ground motion models (GMMs) to be considered by the U.S. Geological Survey (USGS) for their National Seismic Hazard Maps (NSHMs) for the Central and Eastern U.S. (CEUS). These GMMs are adjusted and modified from a set of preliminary models developed as part of the Next Generation Attenuation for Central and Eastern North-America (CENA) project (NGA-East). *It should be emphasized that the GMMs reported in this document are not the final NGA-East GMMs, and their possible use is solely for the USGS NSHMs and not for any site-specific applications such as for nuclear facilities or for critical structures and systems.* The final NGA-East GMMs will be published in a separate comprehensive report. Since the root of the GMMs reported in this document is from the NGA-East, a short summary of scope of the NGA-East Project is provided below.

The goal of NGA-East has been to develop a new ground-motion characterization (GMC) model for the CENA region. The GMC model consists of a set of new GMMs—also known as ground-motion prediction equations (GMPEs) —for median and standard deviation of ground motions and their associated weights in the logic-trees for use in probabilistic seismic hazard analysis (PSHA).

The NGA-East Project is a multidisciplinary project coordinated by the Pacific Earthquake Engineering Research Center (PEER), at the University of California. The project was originally developed as a "science-based" research project [Bozorgnia 2008[. In 2010, the sponsors of the project recommended that the final results and models of NGA-East be coordinated under the Seismic Senior Hazard Analysis Committee (SSHAC) [Budnitz et al. 1997; NRC 2012] Level 3 framework. Thus, the project has two components: (1) a set of scientific research tasks, and (2) a model-building component following the SSHAC Level 3 process. Component (2) of the NGA-East Project was developed using the products of various scientific research tasks completed under Component (1) of NGA-East.

The recommendations in the current report come from the authors heretofore referred to as the "Project Team" in the rest of the text for simplicity (and to avoid the SSHAC notation of TI Team, which may be confusing).

1.2 PROJECT SCOPE AND LIMITATIONS

1.2.1 Project Scope

The scope of the NGA-East Project as well as the GMMs for the USGS NSHMs is as follows: to provide the best estimate of the distribution (median and standard deviation) of "average" horizontal ground motions for the peak ground acceleration (PGA), peak ground velocity (PGV), and 5%-damped pseudo-acceleration response spectra (PSA) for oscillator periods ranging from 0.01 to 10 sec on "hard-rock" sites located up to 1500 km from future earthquakes in CEUS with moment magnitudes (**M**) in the 4.0–8.2 range, and to provide the epistemic uncertainty associated with this estimate.

1.2.2 Study Region

The study region for the USGS NSHMs is the CEUS area of the CENA as shown in Figure 1.1 [Dreiling et al. 2014]. A summary of regionalization characteristics is presented in Chapter 4.

Figure 1.1 NGA-East CENA study region [Dreiling, et al. 2014].

1.2.3 Reference Site Conditions

The reference site conditions have been defined by the NGA-East Geotechnical Working Group as corresponding to shear-wave velocity V_S = 3000 m/sec and a kappa (κ) of 0.006 sec [Hashash et al. 2014; Campbell et al. 2014]. The models included in the current report should be used in conjunction with site effects models such as those developed by Stewart et al. [2017] for the assessment of ground motions on other site conditions.

1.2.4 Magnitude and Distance Ranges for Model Applicability

Models developed in the NGA-East Project are applicable to **M** in the 4.0–8.2 range, and for sites up to 1500 km from earthquakes source using rupture distance as a distance metric.

1.2.5 Ground-Motion Intensity Measures (GMIMs)

The minimum requested GMIMs are PGA, PGV, and 5%-damped elastic pseudo-spectral acceleration (PSA) for oscillator periods listed in Table 1.1. The GMIM of interest is $RotD_{50}$ [Boore 2014]: median value of resultants of two horizontal components of ground motions as computed over each angle of rotation from 1 to 180°. $RotD_{50}$ is computed independently for each spectral period/frequency.

Table 1.1 Minimum 5%-damped PSA periods, T, (and frequencies, F) for NGA-East GMM development, in addition to PGA and PGV.

T (sec)	F (Hz)
0.01	100
0.02	50
0.025	40
0.03	33.33
0.04	25
0.05	20
0.075	13.33
0.1	10
0.15	6.67
0.2	5
0.25	4
0.3	3.33
0.4	2.5
0.5	2
0.75	1.33
1	1
1.5	0.67
2	0.5
3	0.33
4	0.25
5	0.2
7.5	0.13
10	0.1

1.2.6 Categories of Median Ground-Motion Models

In the process of developing median GMMs, the Project Team developed the following nomenclature to differentiate the status of GMMs in the model development phase:

1. "**Candidate GMMs**": These include existing GMMs and a suite of 20 new GMMs, developed as part of NGA-East through interactions in the GMM Working Group. The candidate GMMs were evaluated by the Technical Integration (TI) team for inclusion as seed GMMs, from which the final GMMs were to be developed. The candidate GMMs are published in PEER Report 2015/04 [PEER 2015a].
2. "**Seed GMMs**": Following the evaluation of the candidate GMMs, the Project Team selected 19 GMMs for further investigation. Most of the selected GMMs required adjustments, mostly to cover the desired 1500-km distance range. The NGA-East Project Team extrapolated the candidate GMMs as needed. A certain level of smoothing of the extrapolated GMMs was also carried out. This set of 19 selected, extrapolated and smoothed GMMs are denoted as "seed GMMs." This GMM set was used to generate a continuous distribution of GMMs for each GMIM.
3. "**Sampled GMMs**": A set of 10,000 GMMs was sampled from the continuous GMM distributions developed in the project. These GMMs are referred to as sampled GMMs. At this stage, Sammon's maps were used to visualize the ground-motion space spanned by the seed and sampled GMMs.
4. "**Final GMMs for USGS NSHMs**": The 10,000 "sampled GMMs" were "grouped' into 13 cells in the Sammon's map. For each of these 13 cells, a process to define a representative model in each cell was defined. The 13 resulting GMMs are documented for consideration by the USGS in their development of CEUS portion of the NHSMs. These 13 GMMs were assigned weights for logic tree and PSHA applications.

1.2.7 Limitations

Due to lack of relevant data, the GMMs categorized in the previous section do not explicitly include attributes such as style of faulting and effects of source depth or directivity of ground motions. It is suggested to treat the effects hanging-wall conditions separately. This is also the case of "adjustments" for the Gulf Coast region, for which a recommended approach is summarized in Chapter 4.

1.3 NGA-EAST SCIENCE COMPONENT PRODUCTS

Since the GMMs reported in this document are partly based on a collection of scientific developments of the NGA-East Project, a brief summary of the NGA-East science products is provided below.

1.3.1 PEER NGA-East Database Report

PEER Report 2014-07 [Goulet et al. 2014] serves as a documentation of the empirical ground-motion database development for the NGA-East Project. The ground-motion database includes the two- and three-component ground-motion recordings from numerous selected events (**M** > 2.5, distances up to 1500 km) recorded in the CENA region since 1988. The database contains over 29,000 records from 81 earthquake events and 1379 recording stations. The time series and metadata collected went through numerous rounds of quality assurance and review. The NGA-East database constitutes the largest database of processed recorded ground motions in stable continental regions (SRCs). The motivation behind the development of the empirical database is the same as for other NGA projects (NGA-West1 and NGA-West2), which is to be used, along with other information and data, for the development of GMMs. The NGA-East ground-motion database, similar to those from the NGA-West projects, includes PSA for the 5%-damped elastic oscillators with periods ranging from 0.01 to 10 sec. Additionally, the NGA-East database includes Fourier amplitude spectra (FAS) of the processed ground motions.

1.3.2 PEER NGA-East Reference Rock Report: Part 1: Velocity

PEER Report 2014/11 [Hashash et al. 2014] deals with the definition of the reference *P*- and *S*-wave velocities. The significance of the reference rock definition is that it represents the site condition for which ground motions will be predicted using semi-empirical ground motion prediction equations. Moreover, it represents the site condition to which site amplification factors are referenced (i.e., site amplification is unity for reference rock). There are significant differences in the reference-rock site conditions between active tectonic regions, such as Western North America (WNA), and mid-plate regions, such as CENA. Using velocity measurements reported in the license applications at nuclear power plants, as well as published data, a set of criteria was developed to assess the presence of the reference-rock site condition that is based on the seismic velocities and their gradient with respect to depth. The criteria were applied to the available profiles from which the following seismic velocities for reference rock in CENA were defined:

1. $V_{s,\text{ref}}$ = 3000 m/sec or 9800 ft/sec (2700 to 3300 m/sec or 8900 to 10,800 ft/sec)
2. $V_{p,\text{ref}}$ = 5500 m/sec or 1,000 ft/sec (5000 to 6,100 m/sec or 16,400 to 20,000 ft/sec)

The range given for seismic velocities is based on a ±5% change in amplification using quarter wavelength theory. The study did not find evidence for regional dependence of the reference velocities, which were derived principally from three general geographic regions: (1) the Atlantic coast, (2) the continental interior, and (3) the Appalachian Mountains. The data do not provide reference velocities for the Gulf Coast region. In this region the depth to the CENA reference-rock condition is expected to be much greater than other CENA regions due to several kilometers of overlying sediments. The study did not provide a reference-rock condition for the Gulf Coast. The recommendation is to adopt a consistent reference-rock condition for the entire CENA region, as given above, and then estimate transfer functions to a softer reference condition (such as 760 m/sec) for application of the NGA-East ground-motion models.

1.3.3 PEER NGA-East Reference Rock Report: Part 2: Kappa

PEER Report 2014/12 [Campbell et al. 2014] presents the results of a comprehensive literature search and limited additional studies that support the recommendation of a probability distribution for the shear-wave site attenuation parameter κ_0, or site kappa, associated with a reference-rock site condition in CENA. This study was conducted as part of the Geotechnical Working Group (GWG) activities of the NGA-East. The recommended reference-rock site condition, which is documented in PEER Report 2014/11 [Hashash et al. 2014] is defined as a hard-rock site with a shear-wave velocity of 3000 ± 300 m/sec. The recommended distribution of the reference-rock site kappa κ_{0ref} for this reference-rock site condition is lognormal, with a media value of 0.006 sec, an aleatory standard deviation of 0.43, and epistemic standard deviations of 0.12, when uncertainty in source, path, and site-amplification effects are included in simulations used to develop GMPEs, and 0.20 when they are not. This distribution is intended to represent the center, body, and range of the technically defensible interpretations of the wider scientific community as defined in the SSHAC guidelines The reference-rock site conditions defined in this study and in Hashash et al. [2014] represent a reference for determining site amplification for other types of site conditions in CENA.

1.3.4 PEER NGA-East Regionalization Report

In this study, documented in PEER Report No. 2014/15 [Dreiling et al. 2014], the CENA is subdivided into four regions based on the geologic and tectonic setting. The regions are the Central North America (CNA), the Appalachian Province (APP), the Atlantic Coastal Plain (ACP), and the Mississippi Embayment/Gulf Coast region (MEM). Each region is described by a statistically representative crustal seismic velocity-depth structure and *Q*-factor model. The crustal structural models are for very hard rock conditions and do not include any sediments. The four regions are shown in Figure 1.1. The largest region is CNA and the others are, following a clockwise order in the figure, the APP, the ACP, and the MEM region.

The purpose of this study was to evaluate similarities and differences in attenuation for these regions and to assess whether regions needed to remain separate or if they could be grouped based on their attenuation properties. This was achieved through a series of ground-motion simulations. Seismic-wave propagation was simulated for earthquakes at focal depths of 5, 10, 20, and 30 km, using two different ground motion simulation codes. Synthetic time series and the 5% damped PSA provide insight into the attenuation of ground motions that are typical for each region. The calculated PSA covers a hypocentral distance range of 7.5–500 km and oscillator frequencies ranging from 0.5 to 20 Hz. Spectral accelerations were compared both within and between regions. The CNA is the biggest region geographically and offers the largest variety of crustal seismic velocity-depth structures associated with the unique geologic evolution of its sub-regions.

The CNA is defined as the base region; it is used for both comparisons and to estimate a reference range of within-region variability. After generalizing the 417 profiles available for CNA into one representative profile (CNA_{Rep}), ground motions were calculated for the four aforementioned focal depths. The within-region variability was also assessed using ground-motion simulations for a selected set of 18 alternative velocity models developed for the region (CNA_{Alt}). The PSA values calculated for CNA_{Rep} were compared to the PSA values for the 18

alternative crustal structures, CNA_{Alt}. To determine which of the four regions should be assigned to a common attenuation group, we compared the ACP, APP, and MEM regions to the CNA base region. Statistical distributions (histograms) of the PSAs for specific distance and frequency bands were used to show if there were significant differences between the regions. Additional analysis tools, such as moving window average of PSA versus distance for specific frequency bands, were also used in these comparisons. This analysis demonstrates that there are two distinct attenuation groups:

1. Mid-continent (GROUP 1): Central North America, Appalachians, and the Atlantic Coastal Plain
2. Gulf Coast (GROUP 2): Mississippi Embayment/Gulf Coast

The MEM region was found to clearly belong to a separate attenuation group. This result is in agreement with previous analyses that have found that the MEM region has unique attenuation characteristics.

1.3.5 PEER NGA-East Magnitude-Area Report

PEER Report 2014/14 [Somerville 2014] describes the development of scaling relations between seismic moment and rupture area of earthquakes in stable continental regions (SCRs). The report reviews existing relations, develops new relations, and compares the new relations with the existing relations. It also compares the scaling relations of SCR earthquakes with those in tectonically active continental regions (ACR). Three different methods of estimating rupture area—based on aftershocks, slip models, and duration—were used to analyze the relation between seismic moment and rupture area, using earthquake source parameters compiled from published literature. For each category of data, the relations obtained were not significantly different from those obtained by constraining them to be self-similar. Accordingly, these self-similar relations were adopted in this study. The stress drops corresponding to these scaling relations ranges from 51 to 86 bars, with an average of 65 bars. This value is comparable to the value of 58 bars obtained by Leonard [2010]. Because Leonard [2010] did not document his data and used an undifferentiated mixture of different ways of measuring fault area, the relation that he developed is less soundly based than that developed in this study. However, the two relations are not significantly different, and the Leonard [2010] relations have the advantage of having been derived in a self-consistent manner for a wide range of earthquake categories, including crustal earthquakes in tectonically active regions. Consequently, it is recommended that the Leonard [2010] scaling relations for SCR earthquakes be used for the NGA-East Project. To a first approximation, the results of this study indicate that the rupture areas of SCR earthquakes are about half those of ACR earthquakes, and their stress drops are about 2.8 times higher. Allmann and Shearer [2009] find less of a difference, presumably because their intraplate category includes some earthquakes that the NGA-East Project would assign to ACR instead of SCR. Their study indicates that the rupture areas of intraplate earthquakes are about two-thirds those of ACR earthquakes, and their stress drops are about two times higher.

1.3.6 PEER NGA-East Median GMM Report

PEER Report 2015/04 [PEER 2015a] documents the development of new median candidate GMMs. Models for standard deviations of ground motions are developed through a separate set

of tasks within NGA-East and were published separately. The GMMs have been developed using various tasks previously completed in NGA-East, notably the path regionalization, finite-fault simulations, and database development tasks. This report consists of eleven chapters. Each chapter has its own GMM developer team and may include multiple new GMMs. A total of 20 GMMs are described in this report, covering a range of alternative approaches for modeling ground motions, building on empirical relations for CENA and WNA, using recorded ground motions and collected intensity data, and incorporating point-source and finite-fault simulations.

1.3.7 PEER NGA-East Adjustments to Median GMMs Report

PEER Report 2015/08 [PEER 2015b] documents a series of adjustments developed for the median GMMs as part of the NGA-East Project. The adjustments to median GMMs are necessary so that NGA-East (1) is applicable to rupture distances in the range from 0 to 1500 km; (2) allows source depth effects to be incorporated; and (3) is applicable to the vast CENA region to include the Gulf Coast and the Mississippi Embayment. The three corresponding adjustment models are documented in this report. This report can be considered as a supplemental report to the PEER Report 2015-/4 [PEER 2015a].

1.3.8 PEER NGA-East Sigma Report

In the study documented in PEER Report 2015/07 [Al Atik 2015] the empirical ground-motion data from CENA were used to analyze the components of ground-motion variability in CENA. Trends of ground-motion variability with parameters such as magnitude, distance, and V_{S30} were analyzed and compared to trends of ground-motion variability in other regions, particularly the Western United States (WUS) using the NGA-West2 dataset. The CENA dataset is limited in magnitude range to small-to-moderate magnitudes and in frequency content to frequencies between 1 and 10 Hz due to the bandwidth limitations of the recordings. Therefore, standard deviation models developed using the CENA ground-motion data cannot be reliably extrapolated to large magnitudes and to frequencies outside of 1 to 10 Hz. As a result, standard deviation models from other regions such as WUS and Japan were used to inform the extrapolation of CENA standard deviations and overcome data limitations. Candidate models for between-event standard deviation (τ), single-station within-event standard deviation (ϕ_{SS}), and site-to-site variability (ϕ_{S2S}) were developed for CENA. In turn, these models were combined to develop single-station sigma (σ_{SS}) and ergodic sigma models for CENA.

1.3.9 PEER NGA-East Report on Site-Correction Factors

In the PEER Report 2015/06 [Boore 2015] adjustment factors that can used to convert ground-motion intensity measures at sites with V_{S30} = 760 m/sec and V_{S30} = 2000 m/sec to a reference-rock site, defined as one with V_{S30} = 3000 m/sec, were provided as tables: (1) for moment magnitudes from 2 to 8; (2) rupture distances from 2 km to 1200 km; (3) response spectra at periods from 0.01 sec to 10.0 sec; and (4) PGA and PGV. Ten velocity models used in ground-motion studies in CENA with V_{S30} values very close to 760 m/sec were considered, and adjustment factors were provided for two of those models that effectively span the range of models; for the convenience of the user, adjustment factors were provided for an average of a representative set of models with V_{S30} = 760 m/sec. For models with this velocity, adjustment

factors were provided for four values of the diminution parameter κ, ranging from 0.005 sec to 0.030 sec. The adjustment factors were based on stochastic-method simulations of ground motion.

1.4 REPORT ORGANIZATION

The purpose of this report is to provide a set of ground motion models (GMMs) to be considered by the USGS for their NSHMs development for the CEUS region. The report contains 5 chapters as follows:

1. Chapter 1 provides an overview of the scope of this study as related to the larger NGA-East Project.
2. Chapter 2 provides a summary of the technical approach for capturing the median ground motion epistemic uncertainty in CENA.
3. Chapter 3 presents the implementation of principles introduced in Chapter 2 and the resulting median GMMs recommended for consideration by the USGS NSHMs.
4. Chapter 4 summarizes the CENA regionalization and the recommended approach for estimating ground motions in the Gulf Coast.
5. Chapter 5 presents the recommended appropriate ergodic aleatory models to use in conjunction with the median GMMs from Chapter 3 for the USGS NSHMs application.

2 NGA-East Model Development: Approach Overview

2.1 IMPORTANCE OF EPISTEMIC UNCERTAINTY QUANTIFICATION

This chapter summarizes the conceptual approach behind the ground-motion characterization (GMC) model building. The process is the same as followed for the SSHAC part of the Project, but adapted to the interim models for the USGS NSHMs application. The detailed implementation is described in Chapters 3–4. The current chapter is focused on the selected approach for the quantification of epistemic uncertainty in median ground motions. Generic notations for magnitude (**M**) and distance (R) are used throughout this chapter.

Epistemic uncertainty in the input parameters of probabilistic seismic hazard analysis (PSHA) studies is typically incorporated through the use of logic trees. In this format, epistemic uncertainty in the GMC is represented by a set of alternative ground-motion models (GMMs) with assigned weights. The epistemic uncertainty in median ground motions can be characterized separately from the epistemic uncertainty in the aleatory variability or the two can be linked. The alternative models for median motions and aleatory variability are assigned weights by the analyst(s) to represent the center, body, and range of the technically defensible interpretations (CBR of TDI). The uncertainty in the median ground motions and aleatory variability is propagated in the analysis by computing the hazard for each alternative GMM and assigning the associated GMM weight to the resulting hazard curve. The suite of weighted hazard curves is then used to compute the mean hazard and the hazard fractiles. Past experience has shown that the epistemic uncertainty distributions for seismic hazard are skewed such that the location of the mean hazard within the distribution is sensitive to the shape of the distribution. The proper definition and quantification of epistemic uncertainty is therefore of critical importance to hazard studies, and this recognition lead to the development of the SSHAC guidelines [Budnitz et al. 1997; NRC 2012[. The SSHAC process is intended to make the assessments of epistemic uncertainty transparent and defensible. We followed the same principles for the interim models documented in this report (for the USGS NSHMs application) and build on lessons learned from past SSHAC projects for the quantification of epistemic uncertainty.

2.2 OVERVIEW OF PREVIOUS APPROACHES

In the first application of the SSHAC process to GMC in the 1990s, the epistemic uncertainty was represented by a continuous distribution of ground motions in terms of peak ground acceleration (PGA) or pseudo-spectral acceleration (PSA). A discrete number of scalars,

combined into a logic tree, were used to represent the distribution for hazard calculations (Figure 2.1). Because logic trees were used to represent the epistemic uncertainty, it became automatic to think about them as the end product with the basis for the underlying distribution forgotten. The mathematical formulation behind the logic tree representation uses the axioms of probability such that, at a node of the tree, each branch must contribute information that aim to, at least conceptually, make the set of branches at that node mutually exclusive and collectively exhaustive (MECE). In other words, *the weights assigned to the branches are treated as probabilities*. When the underlying uncertainty is quantified by a well-defined distribution, then it can be represented discretely to varying degrees of accuracy (e.g., Miller and Rice [1983]) such that the individual discrete alternatives are mutually exclusive, and are collectively exhaustive to the extent the analyst wishes to capture the moments and fractiles of the underlying distribution. However, when the epistemic uncertainty is represented by a set of alternative models for a process with weights assigned often on the basis of relative merit, adherence to MECE may become problematic. As discussed in Bommer and Scherbaum [2008], it is often the case that the alternative models have been derived from the same or overlapping datasets using similar conceptual models such that there may be significant model redundancy. Bommer and Scherbaum [2008] argue that in these cases the epistemic uncertainty may not be fully captured, and the treatment of the alternative models as MECE in the calculation of the hazard distribution may not be appropriate. Moreover, there are other difficulties in this approach, such as potential lack of suitability of some or all of the models for the magnitude/distance/region of interest. These issues have resulted in a general understanding that in most cases the multiple-GMC approach will not actually meet the objective of describing the CBR of the TDI of the data [Atkinson et al. 2014].

The following sub-sections briefly summarize the strategies that were used in selected PSHA and GMC projects for the quantification of epistemic uncertainty in GMMs, with each sub-section corresponding to a specific project. All the projects referenced in this section were conducted as SSHAC Level 3 or 4. In all these examples, the epistemic uncertainty is quantified through logic trees, but the composition of each branch and the meaning of their associated weight evolved over time. We present a very short summary of each approach and an assessment of the degree to which MECE was achieved in order to provide the background for the proposed approach for the NGA-East Project, which is introduced in Section 2.3.

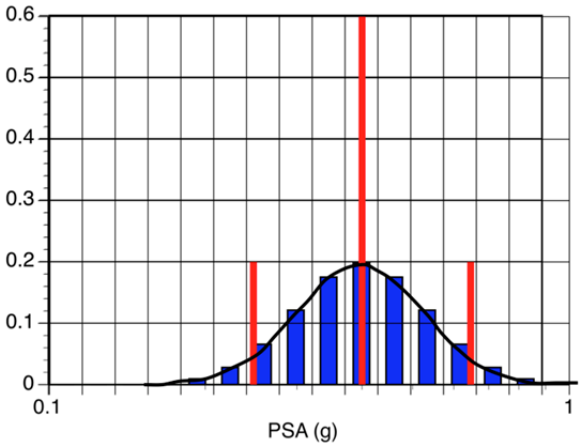

Figure 2.1 **Discrete representations (blue and red bars) of a continuous distribution (black line) of ground motions. The blue and red bars represent different levels of down-sampling, and when used in logic trees, the weights are selected to represent probabilities proportional to the area spanned by the discrete estimate.**

2.2.1 SSHAC Trial Implementation Project (1995–2002)

Purpose: The TIP Project was completed in the mid-late 1990s and documented in 2002 [Savy et al. 2002]. The project was launched to test the implementation of the SSHAC Level 4 guidelines for SSC and GMC projects, which were developed around the same time and published in 1997 [Budnitz et al. 1997].

Approach: The approach was based on expert elicitation using a panel of five experts. The experts were asked to assess the median ground motion and its uncertainty for 132 scenarios defined by magnitude, distance, and style of faulting for five frequencies. In addition, the experts were asked to assess the aleatory variability in ground motions for each scenario and its epistemic uncertainty. The experts were asked to provide distributions for these parameters defined by a median and standard deviation (σ) for each scenario. The resulting assessments were fit by algebraic expressions for the median ground motions and its epistemic uncertainty, along with algebraic expressions for the aleatory variability and its uncertainty for implementation in the PSHA calculations. The uncertainty distributions for median ground motions and aleatory variability were then represented by discrete three-point approximations in the PSHA calculations. Calculations were performed using each expert's assessment, and a composite model was derived from combining the assessments.

Through expert elicitation, they obtained scalar values of 5-Hz PSA for the scenario. These numerical estimates were scalars that corresponded to a continuous distribution. Three points (5^{th}, 50^{th}, and 95^{th} percentiles) were used to generate a simple, coarse MECE representation of a continuous distribution, similar to that shown in Figure 2.1.

2.2.2 Yucca Mountain PSHA (1998)

Purpose: This study was part of the analyses conducted for the Yucca Mountain (YM) Nuclear Waste Repository Project [CRWMS M&O 1998]. The PSHA conducted through expert elicitation was performed following a SSHAC Level 4 process.

Approach: The approach followed that utilized by Savy et al. [2002] using a panel of seven experts. The experts were asked to assess the median ground motion and its uncertainty for about 60 scenarios defined by **M**, *R*, and style of faulting, and nine frequencies for horizontal and vertical ground motions. In addition, the experts were asked to assess the aleatory variability in ground motions for each scenario and its epistemic uncertainty. The experts were asked to provide distributions (instead of a three-point estimate) defined by a median and standard deviation (σ) for each scenario. The resulting assessments were fit by algebraic expressions for the median ground motions and its epistemic implementation, along with algebraic expressions for the aleatory variability and its uncertainty for implementation in the PSHA calculations. The joint uncertainty distribution for median motion and aleatory variability was represented by a 10-point discrete approximation in the PSHA calculations.

The distributions were allowed to be asymmetric so that σ^+ could be different from σ^-. Such distributions can be down-sampled to be used in a logic tree, with each branch remaining MECE.

The number of requested distributions (~540) was too large to be practical. In the end, the experts used algorithms to define weights based on the merit of alternative models (e.g., empirical GMMs and simulations), straying away from the concept of probability. An additional limitation of such approach is that each (**M**, *R*) pair is treated independently; therefore, the correlation in ground motions is not preserved.

2.2.3 EPRI Ground Motion Study (2004, updated in 2013)

Purpose: The Electric Power Research Institute (EPRI) Ground Motion Study was conducted as a SSHAC Level 3 GMC for central and eastern North America [EPRI 2004]. The project organized the available GMMs into clusters based on their underlying technical basis (e.g., point-source simulations, hybrid-empirical, finite-fault simulations, etc.). Each cluster corresponded to a complete model and the ground motions were now correlated. The statistical uncertainty was addressed within each cluster.

Types of question addressed: "What is the weight of each GMM within a cluster? What is the weight of each cluster?"

Approach and discussion: The distributions were vectors of ground motions with (**M**, *R*) and frequency (f) correlated through GMMs. The cluster weights were assigned based on the merit of approaches, as assessed by a group of experts, and not based on the ground-motion space sampled by the GMMs. The cluster weights did not correspond to probabilities anymore: they were not an MECE discretization of the continuous ground-motion space.

2.2.4 PEGASOS PSHA (2004)

Purpose: This PSHA study for Switzerland nuclear power plants (NPPs) gets its name from the German acronym Probabilistische Erdbeben-Gefährdungs-Analyse für KKW StandOrte in der Schweiz [NAGRA 2004]. This SSHAC Level 4 study followed and learned from the YM-PSHA Project efforts. By then, it was recognized that experts were using GMMs to develop the large suite of ground motions required and to ultimately capture the epistemic uncertainty.

Type of question addressed: "What are the most appropriate weights for the GMMs for various (M, R) and frequency ranges?"

Approach and discussion: The distributions were again vectors of ground motions with (**M**, *R*) and f correlated through GMMs. Different weights could be applied to different sets of (**M**, *R*) and f. The correlation across scenarios was preserved through the magnitude and distance scaling built into the GMMs. The weights were again based on the relative merit of the GMMs and did not represent a discretization of a continuous ground-motion distribution. Therefore, the branches are not MECE. Although allowing the weights to change with (**M**, *R*) and f allowed more flexibility, it caused breaks in the PSA values at the boundaries that were propagated as breaks in the PSHA fractiles, leading to hazard curves that were not smooth.

2.2.5 BCHydro PSHA (2012)

Purpose: This PSHA study, led by British Columbia Hydro (BCHydro) power, was conducted as a SSHAC Level 3 project to assess seismic hazard from subduction events, for their dam portfolio [Addo et al. 2012]. Learning from other SSHAC projects, and in an attempt to return to logic tree weights representing discretized probabilities, the project adopted the scaled-backbone approach. The weights are again on GMMs, but assigning them as such that the branches are MECE and represent the full ground-motion space.

Types of question addressed: "How can we better define a suite of GMMs that span the full ground-motion space? What are the weights for the GMMs?"

Approach and discussion: As for EPRI and PEGASOS, the distributions were again vectors of ground motions with (**M**, *R*) and f correlated through GMMs. Instead of individual GMMs, a single "backbone" model was selected that was then scaled up and down to span the range of ground motions. The uncertainty in the scale factors increased for larger M events that were scarcely populated with data. The weights on the scaled GMMs allowed a complete MECE description of the ground-motion space, and the weights returned to representing discrete probabilities of a continuous distribution of ground motions. The drawback of this approach is that it doesn't allow different correlations of ground motions, i.e., the scaled GMM represents a single trend, or slope, for magnitude and distance scaling. It is noted that other implementations of the backbone concept that incorporate more refined magnitude and distance scaling are possible. The concept is illustrated in Figures 2.2 and 2.3.

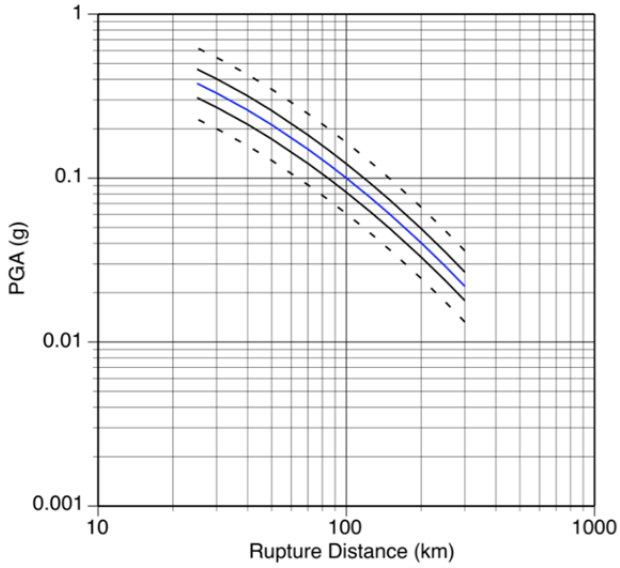

Figure 2.2 **Concept of backbone approach where a single GMM (blue line) is scaled up and down to capture the epistemic range in ground motions (solid and dashed black lines). The ground motions (PGA in this case) are represented by vectors, the values of which are correlated through magnitude and distance scaling terms built into the GMM.**

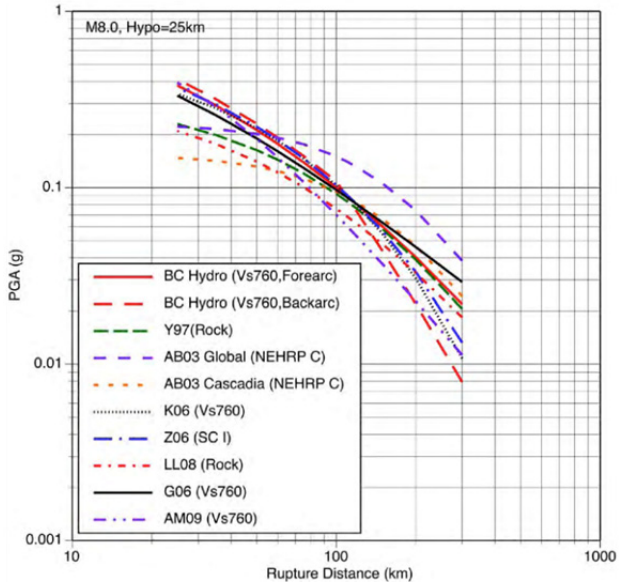

Figure 2.3 **Illustration of epistemic uncertainty in distance scaling approaches. Different models allow a different correlation of PSA with distance [Addo et al. 2012]. When the backbone approach is used with a single shape (Figure 2.2), this epistemic uncertainty in the interpretation of data and modeling of ground motions is not preserved.**

2.2.6 Hanford (2014)

Purpose: The Hanford Sitewide PSHA was conducted as a SSHAC Level 3 project for five hazard calculation sites at Hanford, Washington (Coppersmith et al. 2014). The purpose of the study was to update the PSHA for the U.S. Department of Energy (DOE) facilities as well as to fulfill the requirement from the U.S. NRC that Energy Northwest conduct a SSHAC Level 3 PSHA for the Columbia Generating Station (CGS). The PSHA results were provided for a defined base rock horizon. Ground-motion logic trees were developed for shallow crustal earthquakes and for subduction earthquakes. For both cases, the scaled-backbone approach was used to capture the distribution of median ground motions.

Types of question: "How can we define a suite of GMMs that span the full ground-motion space while allowing alternate correlations in magnitude and distance scaling? What are the weights for the GMMs?"

Approach and discussion: Project-specific criteria were defined for the selection of the backbone GMM for crustal earthquakes. As a result, four NGA-West2 GMMs (ASK14, BSSA14, CB14, and CY14) passed the selection criteria, and CY14 was selected as the backbone model. For subduction earthquakes, a GMM was developed for this project based on revisions to the BCHydro model [Addo et al. 2012]. These revisions were necessary to accommodate project-specific constraints, such as predictions from sources at distances of 200–400 km from the Hanford site, and to incorporate additional ground-motion data that have become available since the introduction of the BCHydro model.

The objective of the developed ground-motion logic trees was to capture the full range of epistemic uncertainty in median ground-motion predictions consisting of two components: inherent uncertainty in the predictions within the host region and uncertainty in the adjustments between the host and target regions.

For crustal earthquakes, the scaled-backbone model was developed in two steps. The first step consisted of developing the model for footwall conditions. This allowed for the development of appropriate factors to center the backbone model and capture the range in magnitude and distance scaling. The second step was to develop a separate distribution of hanging-wall effects using the hanging wall factors from Abrahamson et al. [2014], Campbell and Bozorgnia [2014], and Chiou and Youngs [2014]. Additional epistemic uncertainty was added to address other differences between host and target regions such as stress parameter.

2.2.7 SWUS (2015)

Purpose: The South-Western U.S. Utilities Project (SWUS) is a PSHA study funded by private utilities for NPP seismic hazard assessment of facilities in California and Arizona [GeoPentech 2015]. Like some of the projects above, SWUS was targeted to site-specific analyses. Building on previous efforts, SWUS was first to adopt and further develop a new approach based on visualization techniques of high-dimensional ground-motion space. The concept behind the approach is documented in Scherbaum et al. [2010].

Types of question: "How can we better define a suite of GMMs that span the full ground-motion space while allowing alternate correlations in magnitude and distance scaling? What are the weights for the GMMs?"

Approach and discussion: The SWUS approach aims to move beyond previous approaches towards true characterization and sampling of the ground-motion space, using a novel method described in the next paragraph. NGA-East largely built on the SWUS work, which is summarized below.

The basic idea of the method is to map the ground motions from each GMM into a high-dimensional (or multi-dimensional) space. This is done one frequency at-a-time, and each (**M**, *R*) pair corresponds to a dimension of the high-dimension space. Each GMM can then be represented by a single point in the high-dimension space. The key to the method is that differences in GMM can be assessed by their ground-motion distance in the high-dimension space. This ground-motion space distance is also referred to as a GMM-distance, and it is a measure of difference in ground motions (as opposed to a measure in the sense of travel distance). For a 3D space, the GMM-distance would be measured along a straight line. We can imagine computing GMM-distances between points for more than three dimensions in a curved Euclidian space. By taking those GMM-distances and projecting them on a 2D plane (using Sammon's [1969] maps), we can represent the complete ground-motion space, spanning the complete ground motion distribution for multiple (**M**, *R*) pairs for a specific frequency at once. By defining branches for specific regions or points on the Sammon's map and assigning weights to them, we can effectively re-discretize the ground-motion space and make each branch of the logic tree MECE. The principle is the same as originally used in the TIP [1995] Project, but applied to vectors (correlated sets of ground motions), as opposed to scalars (distribution of ground motions for a given (**M**, *R*) scenario).

There is no constraint on the GMMs magnitude and distance scaling, and the key is that a single GMM will produce a given set of ground motions following its built-in correlations. Following this process, multiple rules for scaling are considered. This approach, however, simply uses high-dimension visualization technique that relies on Sammon's map projections as a way to return to the original objective of *quantifying epistemic uncertainty as a discretization of a continuous ground-motion space*.

2.2.8 Summary and Motivation

Presented above was an overview of different approaches for quantifying the epistemic uncertainty in ground motions for GMC and PSHA projects. From the beginning of large PSHA projects in the 1990s, the epistemic uncertainty in ground motions was intended to represent a discretization of the ground-motion space. This can be achieved using logic trees if each branch of the logic tree represents parts of the distribution that are MECE. The various approaches discussed in this and the previous sections are summarized in Table 2.1.

For a simple scenario [e.g., a given (**M**, *R*) pair], this can be easily done through expert elicitation, as was shown schematically in Figure 2.1. When trying to consider multiple scenarios, as is usually required for PSHA, it becomes difficult to aggregate the information in a simple, meaningful way. To achieve this, the approach went from expert elicitation of expected ground-motion values (scalars) to expert elicitation of sets of values (vectors), which may or may not be correlated. As experts were confronted with a large number of scenarios, they started to use GMMs as algorithms for defining the ground motions. The epistemic logic tree branches now consisted of GMMs instead of ground motions, and the weights were a representation of the relative merit of each GMM approach as assessed by a group of experts. This approach has the

advantage of maintaining the correlation in magnitude and distance scaling between scenarios through the GMMs, but the concept of "weight as a probability" is lost. In other words, on the one hand, two GMMs may represent the same ground-motion space, or range, and not be mutually exclusive, allowing for some double-counting of the occurrence of certain ground-motion values. On the other hand, there may not be enough GMMs to capture the full range of ground motions, leading to gaps in ground motions or to incomplete distributions; the GMMs may not collectively exhaust the ground-motion space.

One solution to this problem was to use the backbone GMM approach [Bommer 2012; Addo et al. 2012; and Atkinson et al. 2014]. This is arguably a more principled approach to capture the center, body, and range of epistemic uncertainty associated with GMMs. In this case, a single GMM is selected as representative of the correlation of magnitude and distance scaling for a region. The GMM is scaled up and down to cover the range of ground motions; the scaling may be by a constant term (e.g., BCHydro), or may be dependent on magnitude and distance to represent modeling trade-offs (e.g., Atkinson and Adams [2013]). The distribution is now discretized, each branch is now associated with a scaling factor for the GMM, and all the branches are defined to be MECE of the full distribution of ground motions. The backbone approach represents an improvement relative to previous approaches in capturing the epistemic uncertainty, but may not fully capture the range of alternative interpretations of the data that affect magnitude and distance scaling.

The challenge for the quantification of epistemic uncertainty is to allow a discretization of the continuous ground-motion space into sets of GMMs that include alternative magnitude and distance-scaling correlations in a comprehensive way. The goal is to develop methods to generate, select, and combine discrete GMMs so that they represent the complete ground-motion space and are mutually exclusive, essentially treating GMM weights as probabilities. The proposed NGA-East approach summarized in this report aims to achieve this goal.

Table 2.1 Summary of approaches used in selected PSHA projects.

Project	Approach	Resulting Model Attributes
TIP	Point estimates (M,R,F)	MECE for each point estimate
Yucca Mtn	Point estimates (M,R,F)	MECE for each point estimate
EPRI	GMM clusters	Merit weights for clusters
	Suite of GMMs within cluster	MECE within cluster
PEGASOS	GMMs adjusted to site-specific conditions	Merit weights for GMMs
BCHYDRO	Scaled backbone	MECE, but ignores correlation of magnitude and distance scaling
Hanford	Scaled backbone with alternative magnitude scaling	MECE including correlation of M scaling
SWUS and NGA-East	Sampling GMMs from Sammon's maps, independent for each frequency	MECE including correlation of magnitude and distance scaling

2.3 NGA-EAST APPROACH TO MEDIAN GROUND MOTIONS AND EPISTEMIC UNCERTAINTY

2.3.1 Overview

This NGA-East approach to median ground motions is based on the understanding that the associated epistemic uncertainty can be described by a *continuous* probability distribution. This is a view that has been used in some previous approaches (e.g., TIP, BCHydro, and others), and that was recently emphasized again in Atkinson et al. [2014]. This key point is that it is not sufficient to put weights on a discrete number of *existing* GMMs to capture the *center*, *body,* and *range* of epistemic uncertainty associated with median ground-motion estimates.

There are different ways to model a continuous distribution for median ground motions. Working closely with the SWUS [GeoPentech 2015] Project since its inception, NGA-East followed a similar conceptual approach but with noted differences. The SWUS Project modeled a continuous distribution over GMMs, by estimating a (joint) distribution of coefficients assuming a single GMM functional form, which in turn led to a distribution of ground-motion values. In contrast, the NGA-East Project Team decided to estimate a distribution over ground-motion values directly, without the detour of a distribution over coefficients. In this approach, selected "seed" GMMs are used to generate ground-motion estimates, which then formed the probability distribution $P(\mathbf{Y})$, where $\mathbf{Y}$ is a vector of median ground-motion estimates at different ($\mathbf{M}$, R) scenarios, $\mathbf{Y}= \{Y_1, Y_2,...,Y_N\}$. Here, Y denotes the logarithmic response spectral value at a particular frequency, and the index goes over the magnitude, distance pairs $\{\mathbf{M}, R\}$. $\mathbf{Y}$ is a high-dimensional vector of ground motions, each dimension corresponding to a specific ($\mathbf{M}$, R) scenario.

In the context of the TIP Project, for example, the experts would have been asked to provide their estimate of the distribution for each Y_i individually, working with one dimension at-a-time. For NGA-East, both the Y_i marginal distributions and the full joint distribution $P(\mathbf{Y})$, which includes the correlations between the individual Y_i are considered. $P(\mathbf{Y})$ represents the epistemic uncertainty associated with median ground-motion estimates, and should therefore be the basis of the center, body, and range. This is different from the EPRI 2013 Project, for example, which was based on the 5% and 95% quantiles for different clusters on the marginal distributions at each ($\mathbf{M}$, R) scenario.

Ideally, for hazard calculations, one would work directly with the continuous distribution $P(\mathbf{Y})$; however this is computationally not feasible. Therefore, for practical reasons P($\mathbf{Y}$) needs to be discretized. Since $P(\mathbf{Y})$ is a distribution over a high-dimensional vector of ground-motion estimates $\mathbf{Y}$, it is not easy to discretize it using a small number of GMMs. The NGA-East approach is to discretize $P(\mathbf{Y})$ into a manageable number of representative GMMs based on drawing from a large number of samples from $P(\mathbf{Y})$, which are then evaluated to determine how well they cover the expected range. In this context, it is important to recall that a sample from $P(\mathbf{Y})$ is a vector of ground-motion values, but due to the correlation inherent in $P(\mathbf{Y})$, the entries of the vector behave like a GMM.

The assessment of the samples from $P(\mathbf{Y})$, each of which is a high-dimensional vector, is carried-out via high-dimensional visualization tools [Scherbaum et al. 2010], which makes it possible to collapse the analysis down to two dimensions. These tools provide a way to assess

the samples in a global sense—as opposed to a single scenario at-a-time—and allow a more intuitive definition of the center, body and range of $P(\mathbf{Y})$. Thus, the selection of a set of representative GMMs is based on these visualization tools. The visualization tools also provide a way to calculate weights for the set of representative GMMs, based on prior information and data.

2.3.2 Simple One-Dimensional Example

In this section, a simple one-dimensional (1D) problem is used to illustrate the NGA-East approach. The problem is centered around the quantification of epistemic uncertainty in median PSA (1 Hz) estimates for a $\mathbf{M} = 6$ and $R = 100$ km earthquake scenario. Assuming that epistemic uncertainty can be represented by a continuous distribution in ground-motion space, the following five steps are applied to capture it:

1. Develop a suite of seed GMMs
2. Develop continuous distributions of GMMs
3. Visualize the ground-motion space
4. Re-discretize the ground-motion space
5. Assign weights

For this 1D example, these steps are trivial, but their formal application serves as a simple entry to the problem in higher dimensions.

Step 1. Develop a suite of seed GMMs

This step involves evaluating available GMMs for suitability to the problem at hand. This example assumes that 20 (fictitious) GMMs were deemed applicable and selected as seed models. Figure 2.4 shows the median estimates from these 20 selected seed GMMs for a $\mathbf{M} = 6$, $R = 100$ km scenario and 1 Hz PSA. The figure also shows the estimated normal distribution describing the epistemic uncertainty, with mean $\mu_Y = -4.76$ and $\sigma_Y = 0.375$.

Step 2. Develop continuous distributions of GMMs

The characterization of the full ground-motion distribution is performed by estimating the means, variances, and correlations between median values at the different ($\mathbf{M}$, R) scenarios that are considered. For this single scenario, the estimation of the continuous distribution is obtained by calculating the mean and variance of the seed GMM estimates.

Step 3. Visualize the ground-motion space

The visualization step is critical in the real application of the NGA-East methodology. However, for the 1D example, it is mentioned only for completeness. The fitted probability density function (PDF) of the 1D normal distribution is shown as the blue line on Figure 2.4.

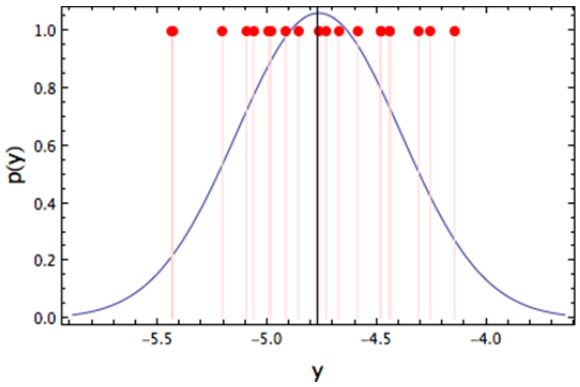

Figure 2.4 **Median estimates (red symbols) of seed models at M = 6, *R* = 100, for PSA (1 Hz), with *y* in ln units of PSA(*g*). The blue curve is the normal distribution fitted to the 18 median estimates**

Step 4. Re-discretize the ground-motion space

The next steps involve the definition of the range in ground-motion space, the partitioning of that range, and the selection of representative sets of GMMs in each partition. There are many tasks required to complete this step, which involve the Project Team's evaluation. The assumption for the 1D illustration is that the range of median ground motions to be captured is bounded by the mean plus/minus two standard deviations, and that the goal is to obtain a representative set of seven models at the end of the process.

Accordingly, the distribution $P[Y(\mathbf{M} = 6, R = 100)]$, is discretized into seven bins, as shown in Figure 2.5 (left). In this case, bins of equal widths were selected, but this is not a prerequisite. As a next step, 5000 "models" are sampled from $P[Y(\mathbf{M} = 6, R = 100)]$. Their histogram, together with the PDF and the bins, is shown in Figure 2.5 (right). Another assumption is made that the representative model can be defined as the mean of all the models in a particular bin. These values are also shown in Figure 2.5 (right) as blue dots.

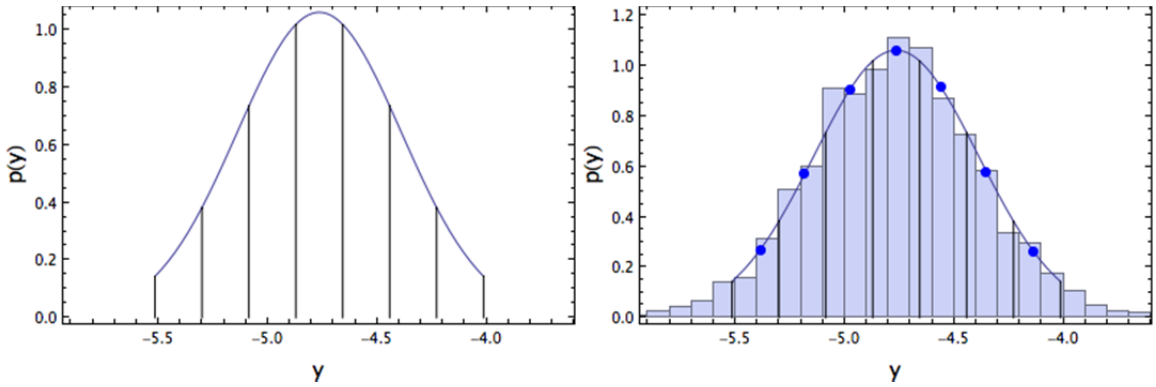

Figure 2.5 **Partitioned one-dimensional ground-motion distribution (left). Partitioned one-dimensional ground-motion distribution, histogram of 5000 sampled models, and selected models for each bin (blue points), calculated as mean over samples in each bin (right).**

Step 5. Assign weights

The next step is to calculate weights for the set of representative models. There are different ways to calculate weights: they can be based on information from the PDF of $P[Y(\mathbf{M} = 6, R = 100)]$, (i.e., "prior information") or on the model fit to existing data. Examples are presented below.

To calculate weights based on the PDF, two different approaches can be used. The first is to calculate the probability density for each bin by integrating over the PDF:

$$w_{PDF,i} \propto \int_{LB_i}^{UB_i} p(y)\, d(y) \tag{2.1}$$

where LB_i and UB_i are the lower bound and upper bound of the ith cell, and $p(y)$ is the PDF of $P[Y(\mathbf{M} = 6, R = 100)]$,. In this example, the distribution is essentially truncated and the weights calculated do not sum to one; they would need to be normalized.

Weights can also be obtained by calculating the number of samples in each bin,

$$w_{N,i} \propto N_i \tag{2.2}$$

where N_i is the number of models in the ith cell. The weights calculated this way are an approximation to the weights calculated with Equation (2.1).

An alternative weight computation process is based on the ability of the models to fit an observational dataset. To illustrate this approach, the "data" are simulated values extracted from a normal distribution with a mean slightly different from the mean of the GMMs ($\mu_{\text{data}} = \mu_Y + 0.5$), and a standard deviation $\sigma_T = 0.4$. This is a different standard deviation than the one for $P[Y(\mathbf{M} = 6, R = 100)]$ because the latter describes the epistemic uncertainty of the median estimates, while the former corresponds to aleatory variability of the data generating process. Since this is just an illustrative example, the actual value is not particularly important. Ten data points are simulated as shown in Figure 2.6. For each sampled model, we calculate the mean residual to the data, as well as the likelihood of the data under each model. The latter is computed by:

$$L_i = \prod_{j=1}^{N} p(y_j \mid m_i) \tag{2.3}$$

where N is the number of data points, $p(y_j \mid m_i)$ is the value of a normal density function with mean m_i, where i indexes the sampled models.

The log-likelihood and mean residual for each sampled model are plotted in Figure 2.7. They both exhibit a clear trend, which is not surprising, since each of the sampled models consists of only one parameter. The residuals cross the x-axis at the mean of the data; this is also where the curve of the log-likelihood has its maximum. The residuals and the likelihood can then be used to weigh the models selected earlier. Each of the selected models is representative of a given bin, so it needs to reflect the likelihoods and residuals of all sampled models in that particular bin. To calculate weights for each bin based on the data, the following rationale is used:

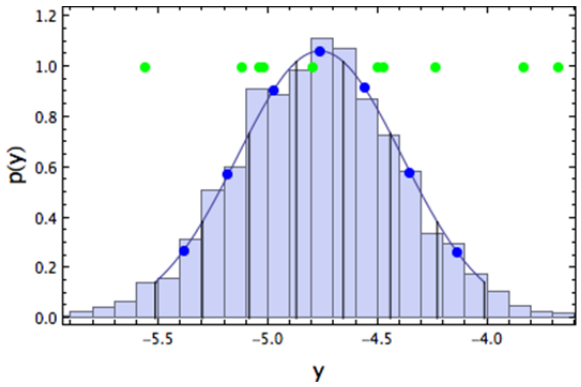

Figure 2.6 **Partitioned one-dimensional ground-motion distribution, histogram of 5000 sampled models, and selected models for each bin (blue points), calculated as mean over samples in each bin. Green dots are 10 simulated data points, which are used to evaluate the sampled models.**

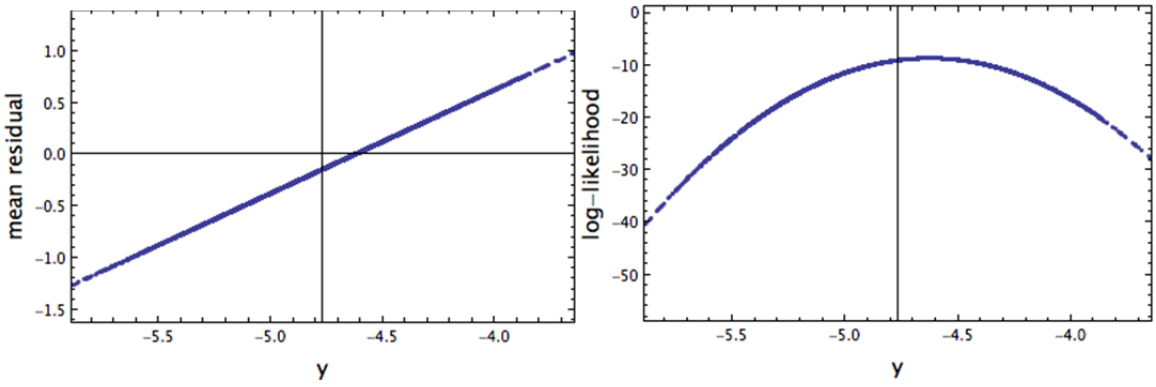

Figure 2.7 **Left: mean residual of each sample vs. the sampled value. Right: log-likelihood of data for each sample vs. sampled value. The axis is centered at the mean of the seed GMM distribution.**

1. Models with low residual should receive higher weight.
2. Models with high likelihood should receive higher weight.

Hence, weights are calculated based on the following formulae:

$$w_{\text{res},i} \propto \frac{A_i^1}{\left| \frac{1}{N_i} \sum_{j=1}^{N_i} r_j \right|} \tag{2.4}$$

$$w_{L,i} \propto A_i \frac{1}{N_i} \sum_{j=1}^{N_i} L_j \tag{2.5}$$

where N_i is the number of samples in the ith bin, A_i is its width, and j indexes over the samples in bin i. The weight based on residuals is inverse-proportional to the mean residual of one cell, whereas the weight based on the likelihood is proportional to the mean likelihood in one cell. Basically, the weights can be understood as an approximation to an expectation of a function over one particular bin:

$$w_{\text{res},i} \propto \sum_{LB_i}^{UB_i} f(y)\, p(y)\, d(y) \tag{2.5}$$

where LB_i and UB_i are again the lower bound and upper bound of the Ith cell, and $f(y)$ is the function over which the expectation is computed (such as the likelihood).

Figure 2.8 shows the weights calculated by the different approaches. As is expected, weights based on the PDF and the number of models are very close. They are also symmetric since they are based on the normal distribution inferred from the seed GMMs, and they favor (give highest weight to) the center model. Weights based on the data, on the other hand, are skewed because the mean of the data is not at the mean of the seed distribution.

It was now the decision of the TI-team to combine the weights based on the different approaches, by providing "weights on weights." If the data are deemed very reliable, one might argue to give very high weight to the likelihood and/or the residuals. On the other hand, if the data are thought to be uncertain or not very representative, one would give more weight to the weights based on the PDF.

This simple application considered a single (**M**, R) scenario. The case for two scenarios would also be simple to address, but as the number of (**M**, R) scenario increases, resulting in a high-dimensional ground-motion distribution $P(\mathbf{Y})$, the task becomes more difficult. For the NGA-East GMC model development, a large number of scenarios is considered. This leads to a vector of ground motions **Y**, whose entries correspond to the median predictions for each individual (**M**, R) scenario. Consequently, the associated epistemic uncertainty is described by a high-dimensional ground-motion distribution P(**Y**). Each entry of the vector **Y** can be thought of as a coordinate in a high-dimensional space, where the number of dimensions is the length of the vector (i.e., the number of (**M**, R) scenarios), just like a three-dimensional vector describes a point in three-dimensional space. Hence, a particular ground-motion vector **y** can be thought of as a point in a high-dimensional ground-motion space. To make this space accessible, high-dimensional visualization tools [Scherbaum et al. 2010] are used, in particular, Sammon's mapping [1969]. This is done to approximate the high-dimensional ground-motion space through projection in two dimensions. The resulting product is a 2D map representation of the ground-motion space, making it easy to follow the steps outlined in this section, with a slight modification to go from one dimension to two dimensions.

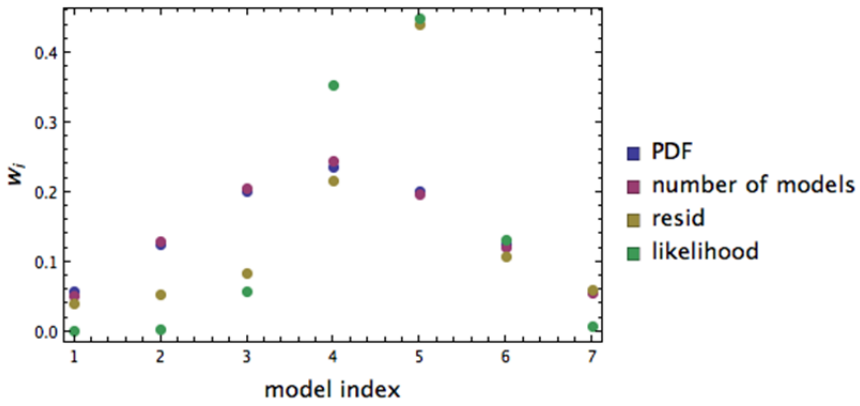

Figure 2.8 **Weights for the different bins, based on different approaches. Model index is from low to high *y*-values.**

2.3.3 Actual Process

The previous section provided a simple illustration of NGA-East's conceptual approach to epistemic uncertainty quantification. In this section, the same process is generalized for application to multiple dimensions (scenarios). The same five basic steps described above are followed, expanded upon, and illustrated in the flowcharts shown in Figure 2.9. In these charts, computations are shown as gray rectangles, while the Project Team (technical integration or TI team within the SSHAC framework) decisions are depicted as purple diamonds. Results of computations/decisions are in yellow parallelograms.

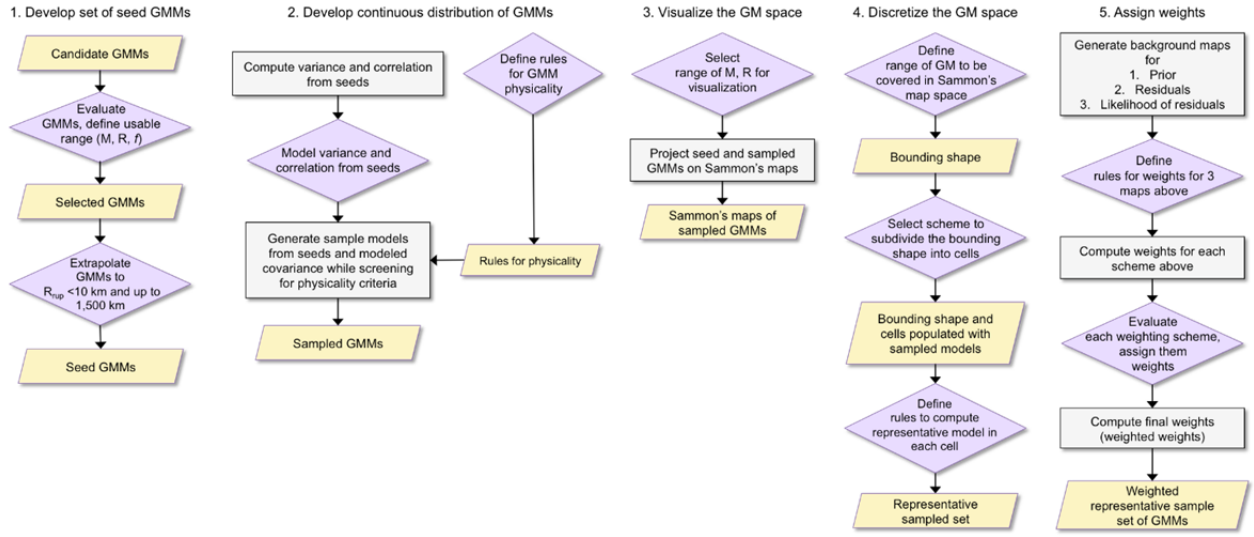

Figure 2.9 **Flowchart summarizing the Project Team (TI team in the figure) approach for capturing the epistemic uncertainty in median ground motions. The process used for the interim USGS models is described in Chapter 3.**

Step 1. Develop a suite of seed GMMs

The first step, described in detail in Section 3.1, is the compilation of a number of GMMs that are deemed applicable to CENA. These "candidate GMMs" are then evaluated to assess their scaling with magnitude, distance, and frequency, based on criteria developed by the Project Team. Following this initial screening, a set of feasible (technically defensible) GMMs is selected from the candidate models. The set of selected models may be different for different frequencies. It was found that for very short and large distances, most models needed to be adjusted/extrapolated to meet the {**M**, *R*} requirements of NGA-East. After these adjustments, sets of seed GMMs are selected to define the continuous distribution or ground motions over a large suite of (**M**, *R*) scenarios. This seed set is analogous to the red points in the 1D example (Figure 2.4).

Step 2. Develop continuous distributions of GMMs

The selected seed GMM set is used to generate ground-motion estimates. The variance and correlation (the covariance) between the different (**M**, *R*) scenarios can then be calculated. In the previous 1D example, a single variance was computed, but for a ground-motion vector **Y**, the correlations across the various (M, R) scenarios are required to ensure that a sample from $P(\mathbf{Y})$ will be a valid GMM.

The covariance model, together with the seed GMMs, defines the continuous distribution describing median ground motions, $P(\mathbf{Y})$. Hence, samples can be drawn from it (Figure 2.5). Generally, the correlation between different Y_i should ensure that a sample from $P(\mathbf{Y})$ is a physically valid GMM. However, it is still possible to generate samples that violate physical assumptions. This is not an issue in the 1D example, but it could happen even for a 2D problem. If, for example, Y_1 and Y_2 are the median estimates at $\mathbf{M} = 5$ and $\mathbf{M} = 6$ for $R = 10$ km for both cases, one would expect that $Y_2 > Y_1$. However, even if the mean of Y_2 is larger than that of Y_1, and the correlation is strong but not perfect, then there is a non-zero probability of drawing a sample with $y_2 > y_1$.

To avoid samples from $P(\mathbf{Y})$ that are unphysical, the Project Team defined criteria for physicality that a GMM needs to satisfy. In the sampling process, the samples are screened according to these criteria, and if they are not met, the sample is discarded, as described in Section 3.2.

Step 3. Visualize the ground-motion space

The result of Step 2 is a number of samples from $P(\mathbf{Y})$, each of which meets the physicality constraints and constitutes a valid GMM. Each sample from $P(\mathbf{Y})$ is a high-dimensional vector **y**, and thus is a point in a high-dimensional space. These points can be projected into 2D using visualization techniques. This process constitutes the essence of Step 3, which is described in detail in Section 3.3.

Step 4. Re-discretize the ground-motion space

Starting with the 2D projection of the high-dimensional ground-motion space from the step above, the center, body, and range are defined. The underlying assumption is that the 2D projection calculated in the previous step is a reasonable representation of the ground-motion space and hence of $P(\mathbf{Y})$. The Project Team's decision involves the definition of the bounding shape in two dimensions, corresponding to the upper and lower limits in Figure 2.5, for the 1D case, and the partitioning inside the bounding shape (i.e., the cells in Figure 2.5). The result is a

set of cells that cover the center, body, and range on the 2D representation of $P(\mathbf{Y})$. Each of the cells comprises several samples from $P(\mathbf{Y})$, which are combined into one representative model for that cell (Figure 2.5, right).

Step 5. Assign weights

This last step involves taking the selected set of representative GMMs from the previous step and assigning weights to them. The process is directly comparable to that of the 1D example. The total weights are a combination of weights based on "prior information" from the GMM distribution itself and from data.

As will be shown in Chapter 3, this process results in a suite of 13 GMMs per frequency, each with an assigned weight.

2.4 ALEATORY VARIABILITY OF GROUND MOTIONS

The model development for the aleatory variability (i.e., standard deviation) of ground motions followed a simpler process, consisting of two key steps: (1) model building, and (2) weight assignment. The model building part involved the analysis of the various components of ground-motion variability using recorded data from CENA. Trends of ground-motion variability with parameters such as magnitude, distance, and V_{S30} are analyzed and compared to observed trends of ground-motion variability in other regions, considering especially trends noted in the WUS using the NGA-West2 dataset.

The CENA dataset is limited in magnitude range to small-to-moderate magnitudes and in frequency content mainly to frequencies between 1 and 10 Hz due to the bandwidth limitations of the recordings. Therefore, aleatory variability models developed using the CENA ground-motion data cannot be reliably extrapolated to large magnitudes and to frequencies outside of 1 to 10 Hz. As a result, aleatory variability models from other regions such as WUS and Japan are used to inform the extrapolation of CENA models and overcome data limitations. Candidate models for between-event standard deviation (τ), single-station within-event standard deviation (ϕ_{SS}), and site-to-site variability (ϕ_{S2S}) are developed for CENA. In turn, these models are combined to develop single-station sigma (σ_{SS}) and ergodic sigma (σ) models for CENA.

The model-building phase is followed by the evaluation of the models and the weight assignment. This last task was performed by the Project Team and involved expert judgment informed by the available data.

2.5 COMPLETE MODEL DEVELOPMENT AND ORGANIZATION OF THE REPORT

The model development documentation is covered in Chapters 3 to 5 and with the following topic coverage.

Median ground motions – Figure 2.9 flowchart items

1. Step 1. Develop a suite of seed GMMs: Section 3.1
3. Step 2. Develop continuous distributions of GMMs: Section 3.2
4. Step 3. Visualize the ground-motion space: Sections 3.3 and 3.4
5. Step 4. Re-discretize the ground-motion space, select models: Sections 3.5-3.6
6. Step 5. Assign weights: Sections 3.7-3.9

Regionalization and Treatment of the Gulf Coast Region: Chapter 4

Standard deviation of ground motions: Chapter 5

3 Median GMM Development

The current chapter describes Steps 1–4 of the NGA-East approach to quantifying the epistemic uncertainty in median ground motions. The five steps are repeated here for convenience:

1. Develop a suite of seed ground-motion models (GMMs)
2. Develop continuous distributions of GMMs
3. Visualize the ground-motion space
4. Re-discretize the ground-motion space
5. Assign weights

The general principles were introduced in Chapter 2. This chapter summarizes the implementation of those principles to the development of GMMs for the USGS NSHMs.

3.1 DEVELOPMENT OF SEED MODELS

The section summarizes the candidate GMMs that were considered for use as seed models in developing the final median GMMs. Section 3.1.1 provides a brief description of the individual candidate GMMs along with the criteria utilized to screen the candidate models and to determine the usable bandwidth of those models passing the screening criteria. The selected candidate GMMS were then extended in distance to extend their range of capabilities. These extended models define the seed models utilized in the median ground-motion model development as discussed in Sections 3.2 and 3.3.

3.1.1 Candidate Median Ground-Motion Models

A total of 30 median GMMs were initially considered as candidate models. Ten of the models are from the recent EPRI Review Project [EPRI 2013] and are listed in Table 3.1. These models are described in detail in EPRI [2013] and are not summarized here. Ultimately, none of the EPRI [2013] models was used in the development of the final GMMs; this was primarily because they have been updated and replaced by more recent models (see Section 3.1.2).

The remaining 20 candidate GMMs were developed specifically for the NGA-East Project, and full descriptions of these models are provided in a PEER report [2015a]. Table 3.2 lists these 20 GMMs with specific reference to the title, authorship, and chapter number in the PEER report [2015a]. Table 3.2 also provides the acronym for each model used throughout the remainder of the current report. None of the models, in the form used here, includes a term for

source depth; rather, they were designed to be applicable to the range of depths expected in CENA. In addition, the candidate GMM developers have focused on limiting their developed models to the mid-continent region, i.e., the CENA region that excludes the Gulf Coast, as defined in Chapter 4. Adjustments to the models for the Gulf Coast region are also presented in Chapter 4.

In lieu of repeating the detailed documentation of the models, which is available in PEER [2015a], we summarize the key features of the models into a series of tables (Tables 3.3 to 3.12). Those tables aggregate the basic model development information—including key assumptions—and range of applicability. In this and the following chapters, the following notations are used: the moment magnitude is noted **M,** the Joyner-Boore distance (shortest distance to the horizontal projection of the rupture plane) is noted R_{JB}, and the rupture distance (shortest distance to the rupture plane) is noted R_{RUP}.

Table 3.1 EPRI [2013] Review Project GMMs.

Cluster	Model Type	Reference
1	Single corner Brune source	Silva et al. [2002], SCCS-Sat Silva et al. [2002], SCVS Toro et al. [1997] Frankel et al. [1996]
2	Complex/empirical source; $\sim R^{-1}$ geometrical spreading $R < 70$ km	Silva et al. [2002], DC-Sat A08′: Atkinson [2008] with modifications from Atkinson and Boore [2011] and EPRI
3	Complex/empirical source; $\sim R^{-1.3}$ geometrical spreading $R < 70$ km	AB06′: Atkinson and Boore [2006] with modifications from Atkinson and Boore [2011] Pezeshk et al. [2011]
4	Finite-source; Full waveform Green's functions	Somerville et al. [2001], two models for rifted and non-rifted regions

Table 3.2 Summary of NGA-East median GMMs.

Title (Authorship), chapter number in *PEER Report 2015/04* [2015a]	Acronym(s)
Point-Source Stochastic-Method Simulations of Ground Motions for the PEER NGA-East Project (D.M. Boore), Chapter 2.	Six GMMs from Boore, each based on a different Q and geometrical spreading model: B_a04 B_ab14 B_ab95 B_bca10d B_bs11 B_sgd02
Development of Hard Rock Ground-Motion Models for Region 2 of Central and Eastern North America (R.B. Darragh, N.A. Abrahamson, W.J. Silva, and N. Gregor), Chapter 3.	Four GMMs from DASG, each based single or double point source and on constant or variable stress parameter: 1CCSP 1CVSP 2CCSP 2CVSP
Regionally-Adjustable Generic Ground-Motion Prediction Equation based on Equivalent Point-Source Simulations: Application to Central and Eastern North America (E. Yenier and G.M. Atkinson), Chapter 4.	YA15
Ground-Motion Prediction Equations for Eastern North America using a Hybrid Empirical Method (S. Pezeshk, A. Zandieh, K.W. Campbell, and B. Tavakoli), Chapter 5.	Two GMMs from PZCT based on different large **M**-scaling (simulation- and empirical-based): PZCT15_M1SS PZCT15_M2ES
Ground-Motion Predictions for Eastern North American Earthquakes Using Hybrid Broadband Seismograms from Finite-Fault Simulations with Constant Stress-Drop Scaling (A. Frankel), Chapter 6.	Frankel
Hybrid Empirical Ground-Motion Model for Central and Eastern North America using Hybrid Broadband Simulations and NGA-West2 GMPEs (A. Shahjouei and S. Pezeshk), Chapter 7.	SP15
Empirical Ground-Motion Prediction Equations for Eastern North America (M.N. Al Noman and C.H. Cramer), Chapter 8.	ANC15
Ground-Motion Prediction Equations for the Central and Eastern United States (V. Graizer), Chapter 9.	Graizer
Referenced Empirical Ground-Motion Model for Eastern North America (B. Hassani and G.M. Atkinson), Chapter 10.	HA15
PEER NGA-East Median Ground-Motion Models (J. Hollenback, N. Kuehn, C.A. Goulet and N.A. Abrahamson), Chapter 11.	Two GMMs from PEER, based on alternate finite-fault models: PEER_GP PEER_EX

Table 3.3 Summary table: Boore GMMs

Boore Models: B_a04, B_ab14, B_ab95, B_bca10d, B_bs11, B_sgd02	
Key feature(s) of model	Suite of 6 GMM derived from point-source stochastic simulations and based on 6 different combinations of Q and geometrical spreading models. A single corner source spectral shape was used for all models. Stress parameter was estimated by inverting the PSA at 0.1 and 0.2 s from 9 ENA earthquakes recorded within 200 km. The geometric mean of the two stress parameters was used along with Yenier and Atkinson (2015) finite-fault factor, and the Boore and Thompson (2015) path duration.
Applicability	
Distance metric used	R_{RUP}
Site Conditions	V_{S30} = 3000 m/sec, κ = 0.006 sec
PSA metric predicted	Geometric mean of horizontal components.
GM Intensity Measures	PSA at 0.01–100Hz, PGA, PGV
Magnitude range	4.0–8.0
Distance range	0–1200 km
Constraints	
Summary of selected data used in model development.	Events: Nahanni, Saguenay, Mt. Laurier, Cap Rouge, St. Anne, Kipawa, Riviere du Loup, Val des Bois. V_{S30} = 2 km/sec, R_{RUP} < 200 km
Large M extrapolation	Point-source stochastic model, Brune spectrum.
Small distance extrapolation	Point-source stochastic model, Brune spectrum
Extrapolation to high frequencies (>15 Hz) and PGA	Point-source stochastic model, Brune spectrum
Constraints on Q	Used 6 preselected attenuation models
Constraints on geometrical spreading	Used 6 preselected attenuation models
Style of faulting	Not explicitly considered.

Table 3.4 Summary table: Darragh et al. (DASG) GMMs

Darragh et al [2015] Models: 1CCSP, 1CVSP, 2CCSP, 2CVSP	
Key feature(s) of model	Single and double corner point-source model with G(R), stress parameter, and Q(f) empirically constrained for NGA-East Region 2. Used both constant and variable stress models.
Applicability	
Distance metric used	R_{JB}
Site Conditions	V_{S30} = 3000m/sec, κ = 0.006 sec
PSA metric predicted	Geometric mean of horizontal components.
GM Intensity Measures	PSA at 0.01–100Hz, PGA, PGV
Magnitude range	4.5–8.2
Distance range	0–1000 km
Constraints	
Summary of selected data used in model development.	NGA-East database: Region 2, 53 events (Including 10 PIEs), $10 \le R_{HYP} \le 1000$ km all sites
Large M extrapolation	Magnitude scaling is determined from equivalent point-source simulations using NGA-West2 GMPEs.
Small distance extrapolation	Close distance scaling is determined from equivalent point-source simulations using NGA-West2 GMPEs.
Extrapolation to high frequencies (>15 Hz) and PGA	Point source, 1-, 2- corner.
Constraints on Q	Determined empirically from selected ground motions in Region 2.
Constraints on geometrical spreading	Geometrical spreading function features magnitude dependent attenuation based on NGA-West2 GMPEs
Style of faulting	Not explicitly considered.

Table 3.5 Summary table: Yenier and Atkinson (YA15) GMM.

Yenier and Atkinson [2015] Model: YA15	
Key feature(s) of model	Developed based on equivalent point-source simulations with parameters calibrated to California motions. Considers decoupled effects of magnitude, distance, stress parameter, geometrical spreading rate and anelastic attenuation coefficient. Adjusted to CENA based on the analysis of residuals between generic model predictions and observed motions.
Applicability	
Distance metric used	R_{RUP}
Site Conditions	Originally derived for V_{S30} = 760 m/sec, κ = 0.025 sec. Corrected to VHR site condition (V_{S30} = 3000 m/sec, κ = 0.006 sec) using site adjustment factors from Atkinson [2012, White Paper].
PSA metric predicted	RotD50
GM Intensity Measures	PSA at 0.01–100 Hz, PGA, PGV
Magnitude range	3.0–8.2
Distance range	1–600 km
Constraints	
Summary of selected data used in model development.	NGA-East database (2014-09-12): Earthquakes of **M** ≥ 3.0 that were recorded by at least three stations within 600 km (including PI Events). Excluded ground motions obtained in the Gulf Coast region. Maximum usable period as specified in the provided data table.
Large M extrapolation	Magnitude scaling is determined from equivalent point-source simulations using parameters calibrated to California motions.
Small distance extrapolation	Short distance scaling is determined from equivalent point-source simulations using parameters calibrated to California motions. Saturation effect is defined based on the recent findings of empirical studies.
Extrapolation to high frequencies (>15 Hz) and PGA	Determined from selected ground motions. No limit on high frequency considered for response spectra.
Constraints on Q	No constraints. Determined empirically from selected ground motions.
Constraints on geometrical spreading	Geometrical spreading function features magnitude- and period- dependent attenuation rates determined from equivalent point-source simulations where Fourier domain geometrical spreading is defined as $R^{-1.3}$ within the first 50 km and $R^{-0.5}$ at R > 50 km.
Style of faulting	Not explicitly considered.

Table 3.6 Summary table: Pezeshk et al. (PZCT) GMMs.

Pezeshk et al. [2015] Models: PZCT15_M1SS, PZCT15_M2ES	
Key feature(s) of model	Traditional Hybrid Empirical approach with NGA-West 2 GMM used to define the "host" region and the NGA-East Database used to calibrate the "host-to-target" adjustments.
Applicability	
Distance metric used	R_{RUP}
Site Conditions	V_{S30} = 3000 m/sec, κ = 0.006 sec
PSA metric predicted	RotD50
GM Intensity Measures	PSA at 0.01–100 Hz, PGA
Magnitude range	3.0–8.0
Distance range	0–1000 km
Constraints	
Summary of selected data used in model development.	Used 5 NGA-West2 GMPEs as the empirical ground motion models in the WNA host region. NGA-East database is used for comparison and calibration: 1. Excluded Gulf Coast 2. Excluded PIEs 3. Used V_{S30} > 180 m/sec (adjusted to 3000 m/sec) 4. Used data with quality flag of 0
Large M extrapolation	1. Used Hybrid Empirical Method (HEM) for **M** ≤ 6, then used magnitude scaling predicted by NGA-West2 GMPEs. 2. Used (HEM) for all magnitudes.
Small distance extrapolation	Used HEM (controlled by NGA-West2 GMPEs)
Extrapolation to high frequencies (>15 Hz) and PGA	Used HEM with point-source stochastic simulation model.
Constraints on Q	1. Used most recent database to determine Q for ENA. 2. Performed inversion of NGA-West2 GMPEs to determine Q for WNA.
Constraints on geometrical spreading	Same constraints that were used for Q
Style of faulting	Not explicitly considered.

Table 3.7 Summary table: Frankel GMM.

Frankel [2015] Model: Frankel	
Key feature(s) of model	Uses finite-fault deterministic synthetics at long periods and stochastic, finite-fault synthetics at short periods; combined with matched filter using a crossover frequency dependent on moment. Uses constant dynamic and static stress drops with moment. Method described in Frankel [2009 BSSA]. Uses 1/R geometrical spreading for stochastic part, for distances out to 70 km, based on Charlevoix observations (Frankel, submitted to BSSA).
Applicability	
Distance metric used	R_{RUP}
Site Conditions	V_{S30} = 2800 m/sec; κ = 0.006 sec
PSA metric predicted	Geometric mean of horizontal components.
GM Intensity Measures	PSA at 0.01–100 Hz, PGA, PGV
Magnitude range	4.5, 5.5, 6.5, 7.5, 8.0
Distance range	2–1000 km
Constraints	
Summary of selected data used in model development.	Observed PSA's for **M**4.5-5.5 were compared to PSA's from simulations
Large M extrapolation	Explicitly included in finite-fault simulations
Small distance extrapolation	Explicitly included in finite-fault simulations
Extrapolation to high frequencies (>15 Hz) and PGA	Explicitly included in stochastic finite-fault simulations
Constraints on Q	Q from Atkinson and Boore [1995]
Constraints on geometrical spreading	For stochastic portion, used geometrical spreading model of Atkinson and Boore [1995]. 1/R true geometrical spreading (< 70 km) based on observations of Charlevoix earthquakes [Frankel, submitted to BSSA]
Style of faulting	Simulations were done for vertical strike–slip fault and 45°dipping thrust fault

Table 3.8 Summary table: Shahjouei and Pezeshk (SP15) GMM.

Shahjouei and Pezeshk (2015) Model: SP15	
Key feature(s) of model	Hybrid empirical ground motion model developed based on the ratios of intensity measures of WNA and CENA regions and considering the empirical GMPEs developed in NGA-West2 Project. Synthetics are generated from the hybrid broadband simulation technique and the finite-fault method.
Applicability	
Distance metric used	R_{JB}
Site Conditions	V_{S30} = 3000 m/sec, κ = 0.006 sec
PSA metric predicted	RotD50
GM Intensity Measures	PSA at 0.01–100Hz, PGA, PGV
Magnitude range	5.0–8.0
Distance range	2–1000 km
Constraints	
Summary of selected data used in model development.	Used 5 NGA-West2 GMPEs as the empirical ground motion models in the WNA host region. NGA-East database is used for comparison and calibration: 1. Excluded Gulf Coast 2. Excluded PIEs 3. Used V_{S30} > 180 m/sec (adjusted to 3000 m/sec) 4. Used data with quality flag of 0
Large M extrapolation	Explicitly included in finite-fault simulations
Small distance extrapolation	Explicitly included in finite-fault simulations
Extrapolation to high frequencies (>15 Hz) and PGA	Explicitly included in stochastic finite-fault simulations
Constraints on Q	Equal weighting of Q models from Atkinson and Boore [2014] and Pezeshk et al. [2011], respectively: $Q = \max(1000, 893f^{0.32})$ $Q = 525f^{0.45}$
Constraints on geometrical spreading	Equal weighting of geometric spreading terms from Atkinson and Boore (2014) and Pezeshk et al. (2011), respectively: $Z(R) = R^{-1.3}$ for R < 50 km and $R^{-0.5}$ for R > 50 km $Z(R) = R^{-1.3}$ for R < 70 km, $R^{0.2}$ for 70 km < R < 140 km and $R^{-0.5}$ for R > 140 km
Style of faulting	Not explicitly considered.

Table 3.9 Summary table: Al Noman and Cramer (ANC15) GMM.

Al Noman and Cramer [2015] Model: ANC15	
Key feature(s) of model	Empirical model with intensity data converted to ground motion for M> 6
Applicability	
Distance metric used	R_{RUP}
Site Conditions	V_{S30} = 760 m/sec with correction term for other values
PSA metric predicted	RotD50
GM Intensity Measures	PSA at 0.01 - 10Hz, PGA, PGV
Magnitude range	3.0–8.2
Distance range	0–2000 km
Constraints	
Summary of selected data used in model development.	NGA East flatfile (2014-11-18) for earthquakes north of 35N and east of 100W and 1985 Nahanni eqks (4), plus 1976 **M**6.8 Gazli record and 2001 **M**7.6 Bhuj observations [Cramer and Kumar 2003, BSSA]. PIEs included if in selected area. Also used intensity data converted to ground motion estimates [Ogweno and Cramer 2014, ES-SSA abstract] for the 1925 **M**6.2 Charlevoix, 1929 **M**7.2 Grand Banks, 1886 **M**7.0 Charleston SC, Dec. 1811 **M**7.5 New Madrid, Jan. 1812 **M**7.3 New Madrid, and Feb. 1812 **M**7.7 New Madrid earthquakes. Magnitude for the 1886 and 1811–1812 earthquakes are from Cramer and Boyd [2014, BSSA].
Large M extrapolation	Historical earthquake intensities converted to ground motions as listed above.
Small distance extrapolation	Limited by few observations.
Extrapolation to high frequencies (>15 Hz) and PGA	Observations used for PGA. No values for frequencies above 10 Hz Sa provided by GMPE.
Constraints on Q	Selected data from Mid-continental regions avoiding Gulf Coast and WUS recordings and earthquakes. Bhuj Q is similar to ENA Q at distances less than 300 km [Bodin et al., 2004, BSSA], which corresponds to the Cramer and Kumar [2003, BSSA] dataset.
Constraints on geometrical spreading	Used unilinear model as most data beyond 50 km.
Style of faulting	Explicit terms for reverse, strike–slip, and undefined.

Table 3.10 Summary table: Graizer GMM.

Graizer (2015) Model: Graizer	
Key feature(s) of model	Model developed with modular filter based approach [Graizer and Kalkan (2007; 2009)], technique developed for the Western U.S.). Spectral shapes developed for the WUS are adjusted for CEUS using recorded data.
Applicability	
Distance metric used	R_{RUP}
Site Conditions	V_{S30} = 2800 m/sec, κ = 0.006 sec. Include adjustment to lower V_{S30}.
PSA metric predicted	RotD50
GM Intensity Measures	PSA at 0.01– 1000Hz, PGA
Magnitude range	4.0–8.2
Distance range	0–1000 km
Constraints	
Summary of selected data used in model development.	Used subset of the NGA-East database of Sept. 2014 for **M** > =3.75 and distances R_{RUP} < 1000 km with addition of 6 Kansas **M** = 4.8 records (5032 data points). All events, including PIE (if **M** >=3.75). All V_{S30} used.
Large M extrapolation	Scaling with the same approximation function type as for WUS [Graizer and Kalkan 2007] with coefficients adjusted based on a combination of (1) ratios of 3.5 < **M** <6 from the NGA-East database,(2) average stress-drop ratio between WUS and CEUS; and 3) checked against recent simulations of **M** >= 5.0.
Small distance extrapolation	Same approach as for the WUS. Used same corner distances (flat area in the near-fault area) as in WUS.
Extrapolation to high frequencies (> 15 Hz) and PGA	Based on info from EPRI 2013 and NGA-East database.
Constraints on Q	Used fixed Q_o = 650 [based on Erickson, D., D. E. McNamara, and H. M. Benz, 2004, Bull. Seism. Soc. Am., **94**, 1630-1643]. Potentially can be adjusted to other areas in CEUS with different Q_o.
Constraints on geometrical spreading	Geometrical spreading of R^{-1} is based on data.
Style of faulting	Not explicitly considered.

Table 3.11 Summary table: Hassani and Atkinson (HA15) GMM.

Hassani and Atkinson [2015] Model: HA15	
Key feature(s) of model	Referenced empirical approach was used to adjust the NGA-West2 BSSA14 model to the observed CENA data. Residuals were defined as the ration of the observed CENA data to the equivalent predicted values of BSSA14. Mixed-effect regression on residuals was used to estimate the adjustment factors coefficients.
Applicability	
Distance metric used	R_{JB}
Site Conditions	Originally derived for V_{S30}= 760 m/sec, κ = 0.025 sec. Corrected to VHR site condition (V_{S30} = 3000 m/sec, κ = 0.006 sec) using site adjustment factors from Atkinson [2012, White Paper].
PSA metric predicted	RotD50
GM Intensity Measures	PSA at 0.01–100Hz, PGA, PGV
Magnitude range	3.0–8.5
Distance range	0–400 km
Constraints	
Summary of selected data used in model development.	1. NGA-East database: All $R_{JB} \leq 400$ km and **M** ≥ 3. All events, including PIE. Exclude Gulf Coast. All V_{S30} used. Limited to usable bandwidth as specified in the flatfile, and only considered data in 0.1–20 Hz range. 2. Seismotoolbox and southern Ontario database. All $R_{JB} \leq 400$ km and **M** ≥ 3. All V_{S30} used. Limited to usable bandwidth as defined by Signal/Noise ≥ 2, Nyquist frequency, and 0.1–20 Hz range.
Large M extrapolation	Same magnitude scaling as BSSA14
Small distance extrapolation	Same close distance extrapolation as BSSA14.
Extrapolation to high frequencies (>15 Hz) and PGA	Adjustment factors defined up to 20 Hz and also PGA. Extrapolation above 20 Hz uses factors defined at f = 20 Hz.
Constraints on Q	No constraint, not solving for Q.
Constraints on geometrical spreading	No constraint, not solving for geometrical spreading.
Style of faulting	Not explicitly considered.

Table 3.12 Summary table: PEER GMMs.

PEER [Hollenback et al. 2015] Models: PEER_EX, PEER_GP	
Key feature(s) of model	Empirical mixed-effect regression on FAS, frequency-by-frequency. PSA predicted through RVT with a calibrated duration model. Extrapolation outside of data range using both finite fault simulations and point-source model. Two magnitude scaling models based on different finite fault simulations models.
Applicability	
Distance metric used	R_{RUP}
Site Conditions	Model centered at V_{S30} ~700 m/sec, analytically corrected to V_{S30} = 3000 m/sec, κ = 0.006 sec
PSA metric predicted	RotD50
GM Intensity Measures	PSA at 0.01– 100Hz, PGA
Magnitude range	4.0–8.2
Distance range	0–1200km
Constraints	
Summary of selected data used in model development.	1. NGA-East database: All $R_{RUP} < 300$ km and **M** > 2.5. All events, including PIE. Regions 2–5 (exclude Gulf Coast). All V_{S30} used. Limited to usable bandwidth, as specified in flatfile. 2. NGA-West2 database: subset of ~1400 records covering **M**3–7.9, $R_{RUP} < 250$ km. Used for duration model constraint.
Large M extrapolation	Finite-fault simulations for distance-dependent M-scaling up to **M**8 and up to 10 Hz. Point-source model for higher frequencies, using parameters from inversion.
Small distance extrapolation	Explicitly included in simulation model.
Extrapolation to high frequencies (>15 Hz) and PGA	Point Source, Brune spectrum
Constraints on Q	No constraint, not solving for Q.
Constraints on geometrical spreading	Tri-linear model; hinge locations fixed at 50 and 150 km, slope for 50 km > R_{RUP} and 50 km < R_{RUP} < 150 km regressed from data, slope for R_{RUP} > 150km fixed at $R^{-0.5}$ (for FAS).
Style of faulting	Not explicitly considered.

3.1.2 Criteria for Selecting Candidate Ground-Motion Models

The Project Team evaluation of candidate models was essentially completed in two passes. The first pass involved an initial screening (discussed in this section) of existing GMMs, and the second pass involved a more in-depth evaluation of the retained GMMs (Section 3.1.1). The Project Team developed a suite of criteria for the initial screening, and a candidate GMM was excluded from further consideration if it is fall in one or more of the following:

1. The model has been superseded by a more recent model (as confirmed by the model developer).
2. The model is more than 10 years old, unless the lead developer(s) can provide a compelling reason for its inclusion as a candidate model.
3. The model cannot cover, or be reasonably extrapolated, to the **M** = 4-8.2, R = 0–1200 km ranges.
4. The model cannot cover, or be reasonably interpolated, to cover the required range of frequencies (0.1 to 50 Hz plus PGA).
5. The model is not based on applicable data or utilizes data that is too uncertain to be diagnostic.
6. The model exhibits magnitude (**M**), distance and/or frequency scaling that appears unphysical or is inconsistent with the applicable data.

The initial screening removed from consideration the ten GMMs from the EPRI [2013] Review Project. The primary reason for excluding these models was that the models have been superseded by more recent versions; this applies to all eight GMMs in clusters 1, 2, and 3. The remaining two EPRI models [Somerville et al. 2001] were excluded because they had not been updated from their original form. The lead developer (Somerville) advised the Project Team that there were no plans to update these models in a time frame that would work for the NGA-East Project. In addition, one of the NGA-East PEER models includes simulations from the method developed for the Somerville et al. [2001] GMMs, capturing some of their important features.

3.1.3 Evaluation of Candidate Median Ground-Motion Models

For the remaining 20 GMMs that passed the initial screening process, the Project Team performed a more detailed and systematic analysis of the models to examine their behavior over a range of magnitudes, distances, and frequencies of interest to the NGA-East Project. This phase of the assessment focused on criteria (5) and (6) as listed in the previous section. Again, the objective of this process was not to make a critical assessment or ranking of individual models, but rather to ensure that all the selected models were grounded in physically sound and defendable principles for the region of interest (CENA), and that the data used to develop the models were appropriate, reproducible, and reliable. A key consideration was that all retained models need to be suitable for the specific purposes of this project.

Evaluation of Technical Bases and Range of Applicability

With 20 GMMs and such a wide range of magnitude, distance, and frequencies to consider, the Project Team focused the primary screening analysis on the magnitude range **M** = 4.5–7.5, distances $R < 200$ km, and frequency range $0.1 < f < 100$ Hz. The rationale behind this was as follows: if a model exhibited systematically unjustifiable behavior across this subset of key magnitudes and distances that was deemed unacceptable, it was likely the model would exhibit this behavior across other magnitudes and distances. Furthermore, throughout the entire model-building process, the behavior of the selected GMMs was continually checked to make sure that the results provided by these models were appropriate, understandable, and defendable. The plots shown below (Figures 3.1 to 3.20) capture the key features of the models that were identified during this interactive screening process and which are described in more detail below.

Additionally, this stage of the screening process determined the range of frequencies over which a candidate model could be used as a seed model across the entire range of **M** and R values. To ensure a practical, efficient and consistent model-building process, the Project Team excluded models that could only be used over a subset of **M** and/or R ranges. This constraint ensures a consistent number of (**M**, R) scenarios at each frequency, which simplifies the process described in Section 3.2.

Figures 3.1 to 3.20 present 5%-damped PSA as a function of oscillator frequency for the 20 candidate GMMs. The format of these figures is the same for each GMM. Each figure has four panels, one each for 20 km, 50 km, 100 km, and 200 km distance. The distance metric used is the same as provided by each model development team without any conversion at this point. Additionally, curves in each distance panel are plotted for magnitudes: **M** = 4.5, 5.5, 6.5, and 7.5. The red curves show the response of the individual GMM under consideration, and the grey curves show the response determined by averaging across all 20 GMMs. The grey curves have no special significance; they are simply included to provide a smooth, common reference from which to compare each of the individual GMMs.

The Project Team evaluated the GMMs' responses shown in Figures 3.1 to 3.20 to determine the frequency range over which each candidate model could be reliably used. In making these evaluations, a higher level of importance was given to the spectral shape than to the absolute level of the response. Additionally, the Project Team considered whether features seen in the relative shifts of the spectra across the ranges of magnitude and distance behave in a physically consistent and defendable manner.

Selection of Median Candidate Ground Motion Models

The majority of the candidate GMMs exhibit reasonable behavior over the complete range of magnitudes, distances, and frequencies considered in the evaluation process. Based on the TI-Team evaluations, 15 of the 20 candidate GMMs were selected to be "accepted as-is" over the full frequency range ($0.1 < f < 100$ Hz). Four candidate GMMs were selected for use over limited ranges of frequencies, and one GMM was not selected for use as a seed model as indicated previously.

Brief summaries for each GMM group ("groups" as defined in Table 3.2) are provided in the following sub-sections.

Boore Models

(B_a04, B_ab14, B_ab95, B_bca10d, B_bs11, B_sgd02)

This modeler provided a suite of six separate GMMs, which were developed at the request of the NGA-East Project Team. The intent of this request was to make sure that a minimum range of models representing the epistemic uncertainty in attenuation, as represented by the literature, would be made available to the Project Team. The primary difference among these six models is the form of the geometrical spreading and Q terms, the details of which are listed in Table 3.13.

The ground-motion spectra for the six Boore GMMs are shown in Figures 3.1 to 3.6. Since these models share several features, the computed spectra also show some similarities, e.g., they all produce relatively smooth spectra and do not exhibit any strong breaks in scaling as a function of distance or magnitude. Nonetheless, the differences in geometric spreading and Q used in these models (Table 3.13) do produce some noticeable differences. Note the tendency for the $R^{-1.3}$ models (B_ab04 and B_ab14) to produce relatively large motions at close distances (see 20-km panels in Figures 3.1 and 3.2) as compared to the other models. Also, the differences in Q can have a strong impact for the higher frequencies at larger distances, as seen in comparing the relatively low high-frequency motions at R = 200 km for B_bs11 (Figure 3.5) with the relatively large high-frequency motions at the same distance for B_sgd02 (Figure 3.6). All of these models are based on previously published geometric spreading and Q models, and thus provide a sampling of the epistemic uncertainty in these parameters. Based on the evaluations, all six of the Boore GMMs were accepted without restriction for use as seed models.

Table 3.13 Representative geometric spreading and Q models selected for the Boore GMMs development.

Model and Reference	Geometric Spreading G(R)	What is "R"?[1]	Attenuation $\exp(-\pi f R/Q\beta)$	Applicable Range[2]
B_ab95 Atkinson and Boore [1995]	$G(R) = \begin{cases} R^{-1}, & R \le 70 \text{ km} \\ C_0 R^{0}, & 70 \text{ km} < R \le 130 \text{ km} \\ C_1 R^{-0.5}, & R > 130 \text{ km} \end{cases}$ $C_0 = (1/70)$, $C_1 = (130^{0.5}/70)$	$R = R_{hyp}$	$Q(f) = 680f^{0.36}$ $\beta = 3.8$ km/sec	$4.0 \le \mathbf{M} \le 7.25$ $10 \le R \le 500$ km $0.5 \le f \le 20$ Hz
B_sgd02 Silva et al. [2002]	$G(R) = \begin{cases} R^{[a+b(\mathbf{M}-6.5)]}, & R \le 80\ km \\ C_0 R^{0.5[a+b(\mathbf{M}-6.5)]}, & R > 80\ km \end{cases}$ $a = 1.0296, b = -0.0422, C_0 = 80^{-0.5[a+b(\mathbf{M}-6.5)]}$	$R = R_{hyp}$	$Q(f) = 351\text{f}^{0.84}$ $\beta = 3.52$ km/sec	$4.5 \le \mathbf{M} \le 8.5$ $1 \le R \le 400$ km $0.1 \le f \le 100$ Hz
B_a04 Atkinson [2004]	$G(R) = \begin{cases} R^{-1.3}, & \text{R} \le 70 \text{ km} \\ C_0 \text{R}^{0.2}, & 70 \text{ km} < R \le 140 \text{ km} \\ \text{C}_1 \text{R}^{-0.5}, & R > 140 \text{ km} \end{cases}$ $C_0 = (70^{-0.2}/70^{1.3})$, $C_1 = C_0(140^{0.5}/140^{-0.2})$	$R = R_{hyp}$	$Q(f) = \max(1000, 893\text{f}^{0.32})$ $\beta = 3.7$ km/sec	$4.4 \le \mathbf{M} \le 6.8$ $10 \le R \le 800$ km $0.05 \le f \le 20$ Hz
B_bca10d Boore et al. [2010]	$G(R) = R^{-1}$ all R	$R = R_{PS}$	$Q(f) = 2850$ $\beta = 3.7$ km/sec	$4.4 \le \mathbf{M} \le 6.8$ $10 \le R \le 800$ km $0.05 \le f \le 20$ Hz
B_bs11 Boatwright and Seekins [2011]	$G(R) = \begin{cases} R^{-1}, & R \le 50 \text{ km} \\ C_0 R^{-0.5}, & R > 50 \text{ km} \end{cases}$ $\text{C}_0 = (50^{0.5}/50)$	$R = R_{hyp}$	$Q(f) = 410\text{f}^{0.5}$ $\beta = 3.5$ km/sec	$4.4 \le \mathbf{M} \le 5.0$ $23 \le R \le 602$ km $0.2 \le f \le 20$ Hz
B_ab14 Atkinson and Boore [2014]	$G(R) = \begin{cases} 10^{T_c C_{LF}} R^{-1.3}, & R \le 50 \text{ km} \\ C_0 R^{-0.5}, & R > 50 \text{ km} \end{cases}$ $T_c = \begin{cases} 1, & f \le 1 \text{ Hz} \\ 1 - 1.429 \log_{10}(f), & 1 \text{ Hz} < \text{f} < 5 \text{ Hz} \\ 0, & f \ge 5 \text{ Hz} \end{cases}$ $C_{LF} = \begin{cases} 0.2 \cos\left[\frac{\pi}{2}\left(\frac{R-h}{1-h}\right)\right], & R \le h \\ 0.2 \cos\left[\frac{\pi}{2}\left(\frac{R-h}{50-h}\right)\right], & h < R < 50 \text{ km} \end{cases}$ h = focal depth (km), $C_0 = (50^{0.5}/50^{1.3})$	$R = R_{PS}$	$Q(f) = 525f^{0.45}$ $\beta = 3.7$ km/sec	$3.5 \le \mathbf{M} \le 6$ $10 \le R \le 500$ km $0.2 \le f \le 20$ Hz

[1] R_{hyp} = hypocentral distance; R_{PS} = effective point source distance; $R_{PS} = [R_{hyp}^2 + h_{FF}^2]^{1/2}$, $\log_{10}(h_{FF}) = -0.405 + 0.235\mathbf{M}$ [Yenier and Atkinson 2015]

[2] When applicable range not explicitly stated in paper it was inferred from data comparisons.

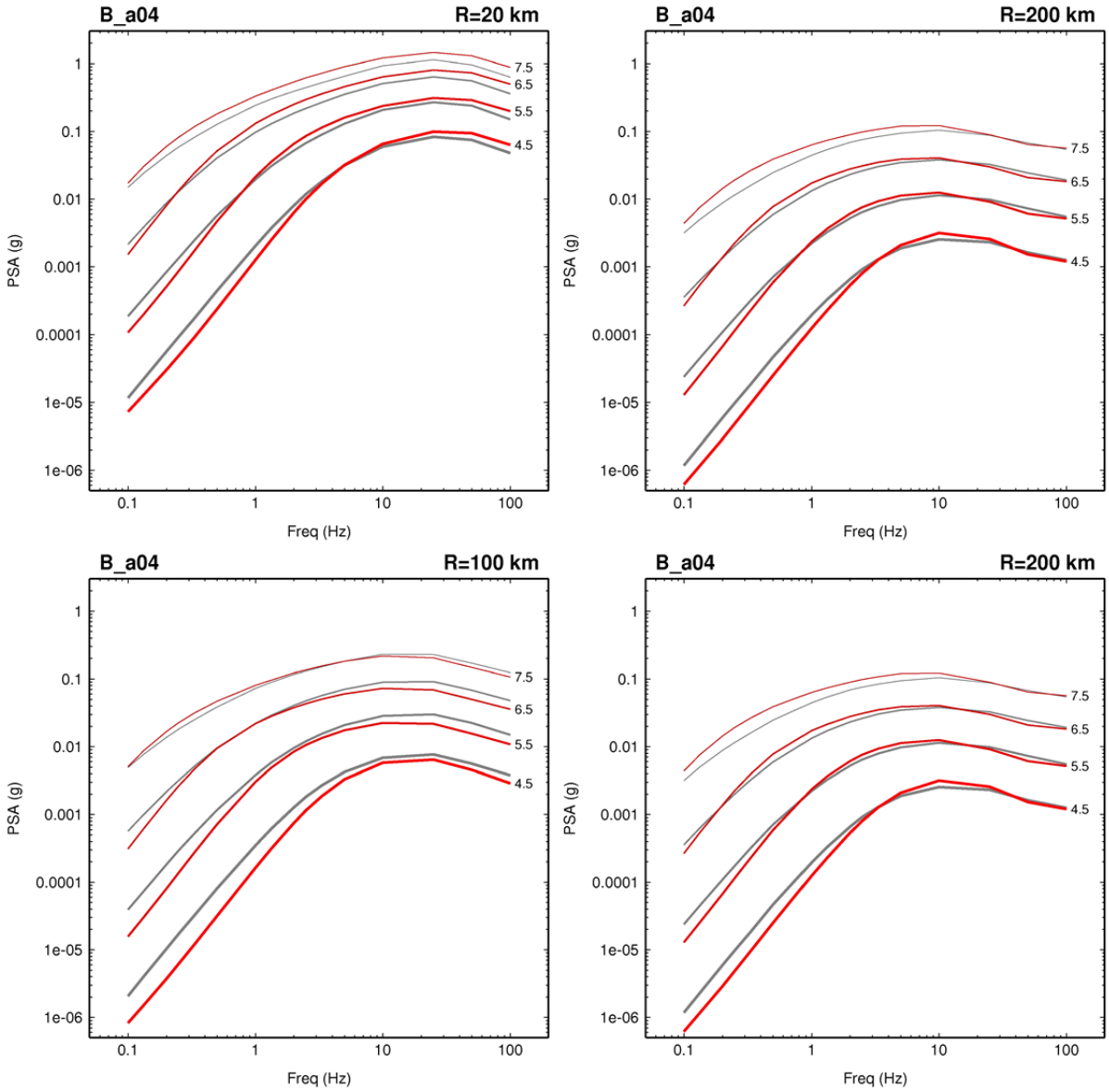

Figure 3.1 **Plots of 5% damped PSA for B_a04 GMM at distances of 20 km (upper left), 50 km (lower left), 100 km (upper right), and 200 km (lower right). In each panel, the response is shown for magnitudes M4.5, M5.5, M6.5, and M7.5, as indicated by the labels and line sizes. The red curves are for B_a04 GMM. The grey curves are the response determined by averaging over all 20 GMMs under consideration.**

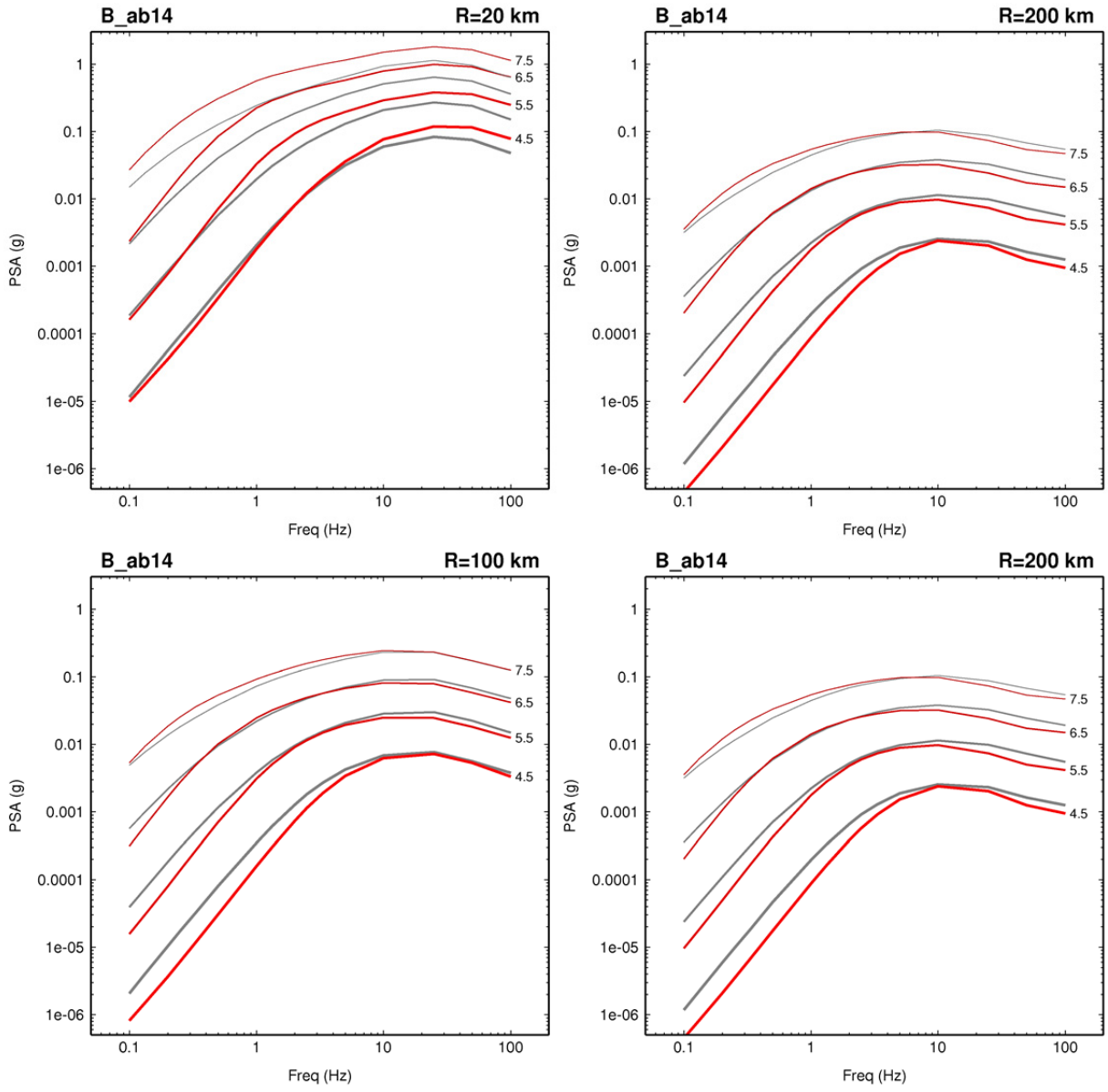

Figure 3.2 B_ab14 GMM. Format is same as Figure 3.1.

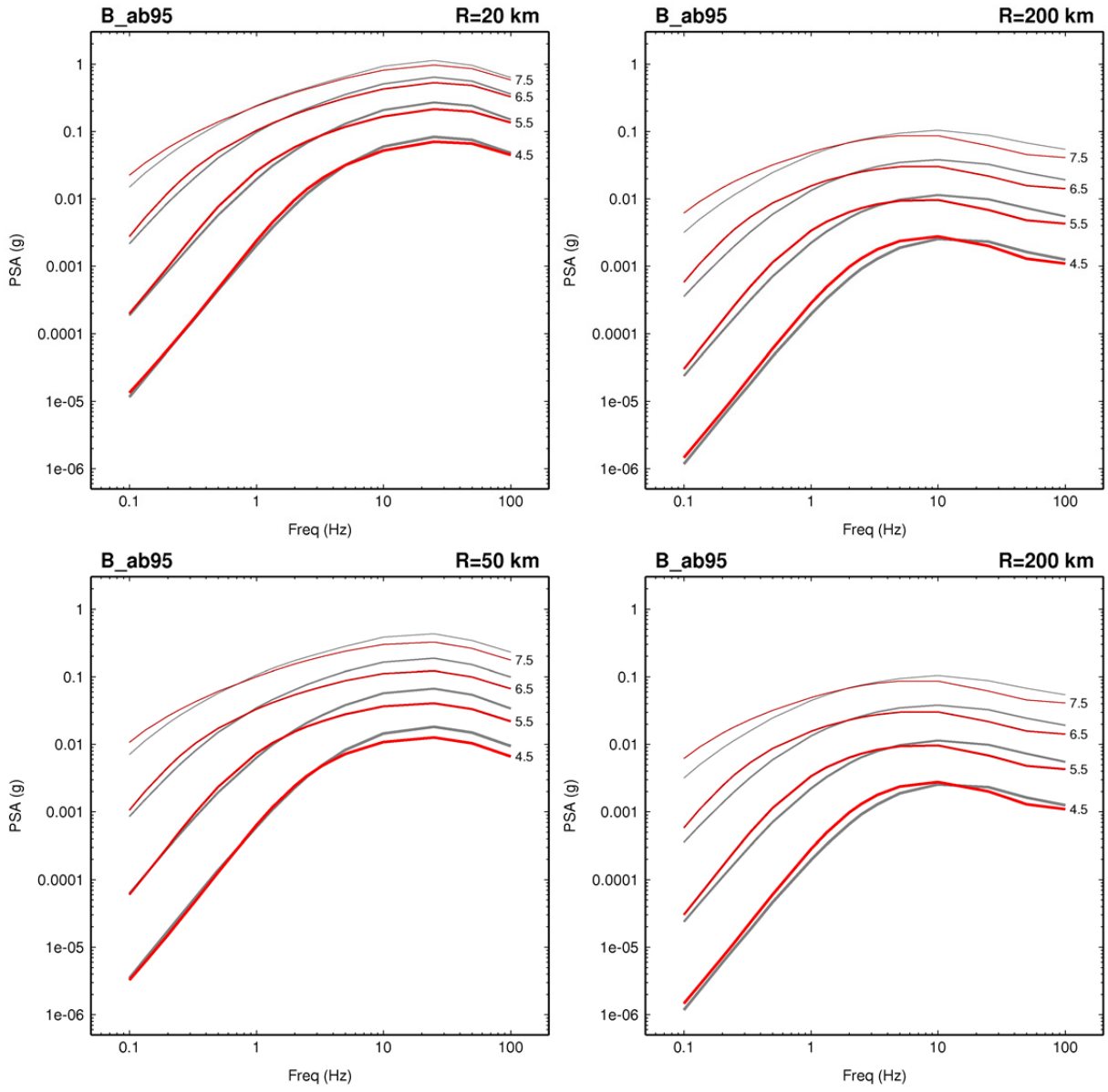

Figure 3.3 B_ab95 GMM. Format is same as Figure 3.1.

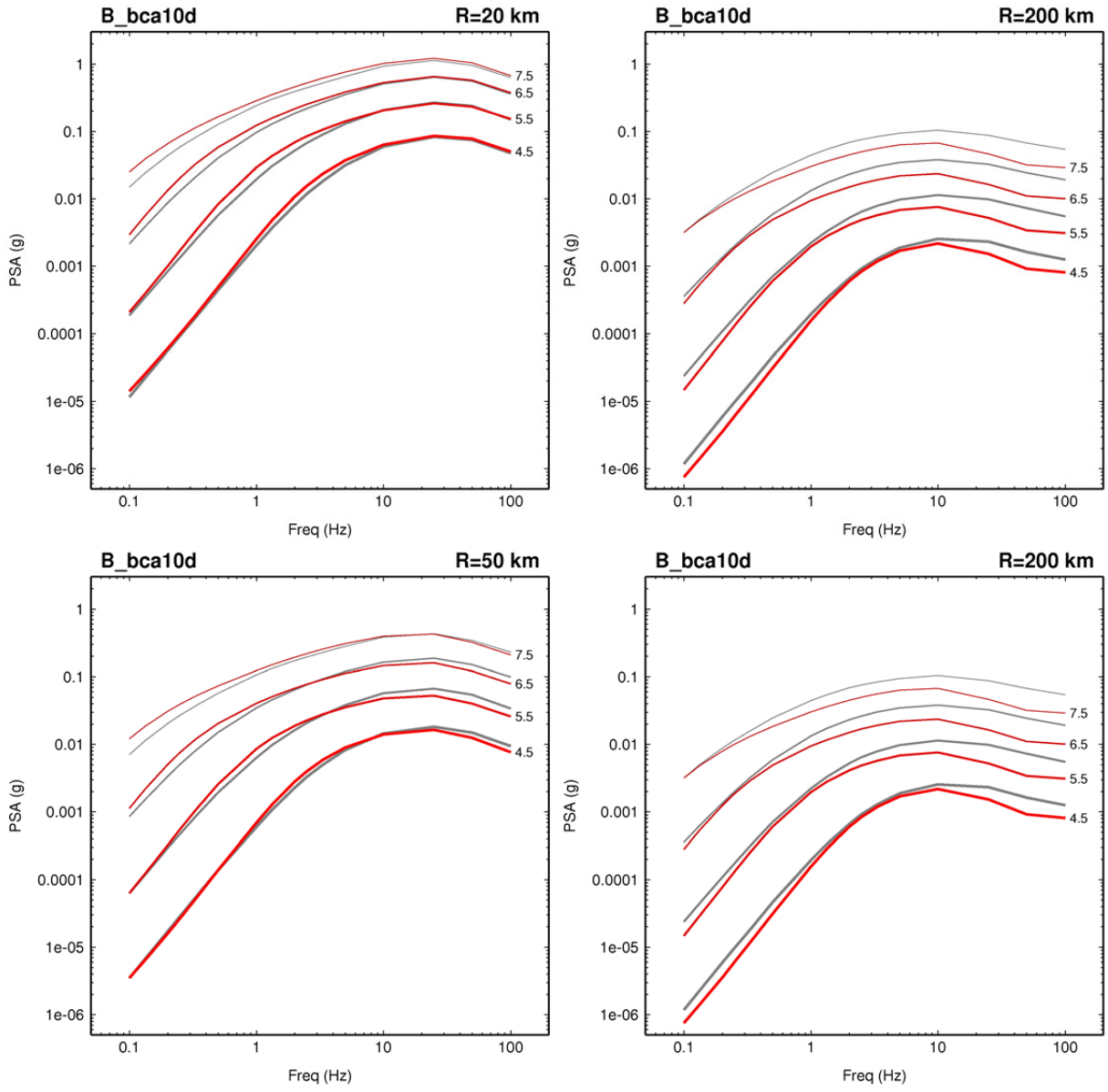

Figure 3.4 B_bca10d GMM. Format is same as Figure 3.1

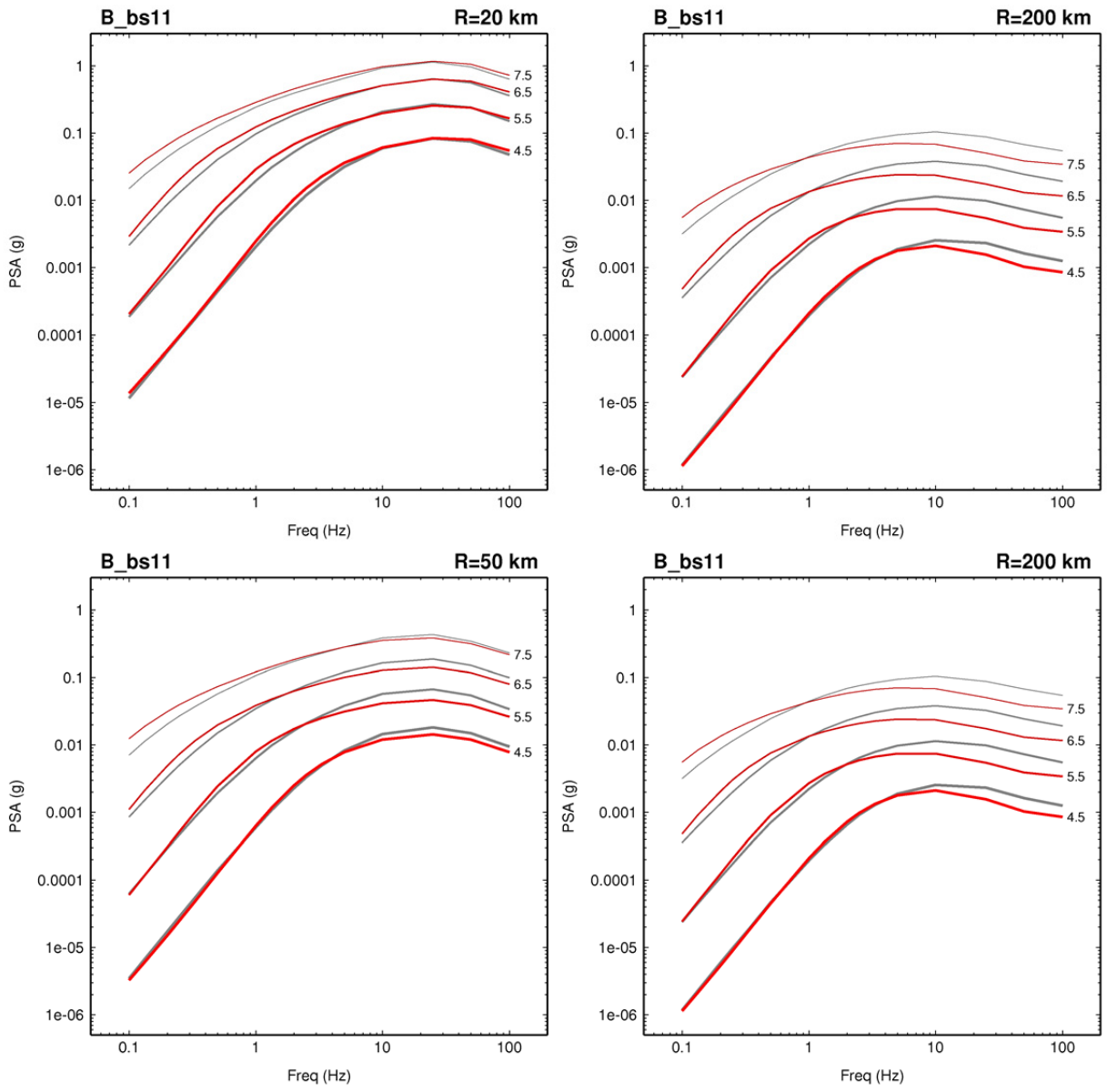

Figure 3.5 B_bs11 GMM. Format is same as Figure 3.1.

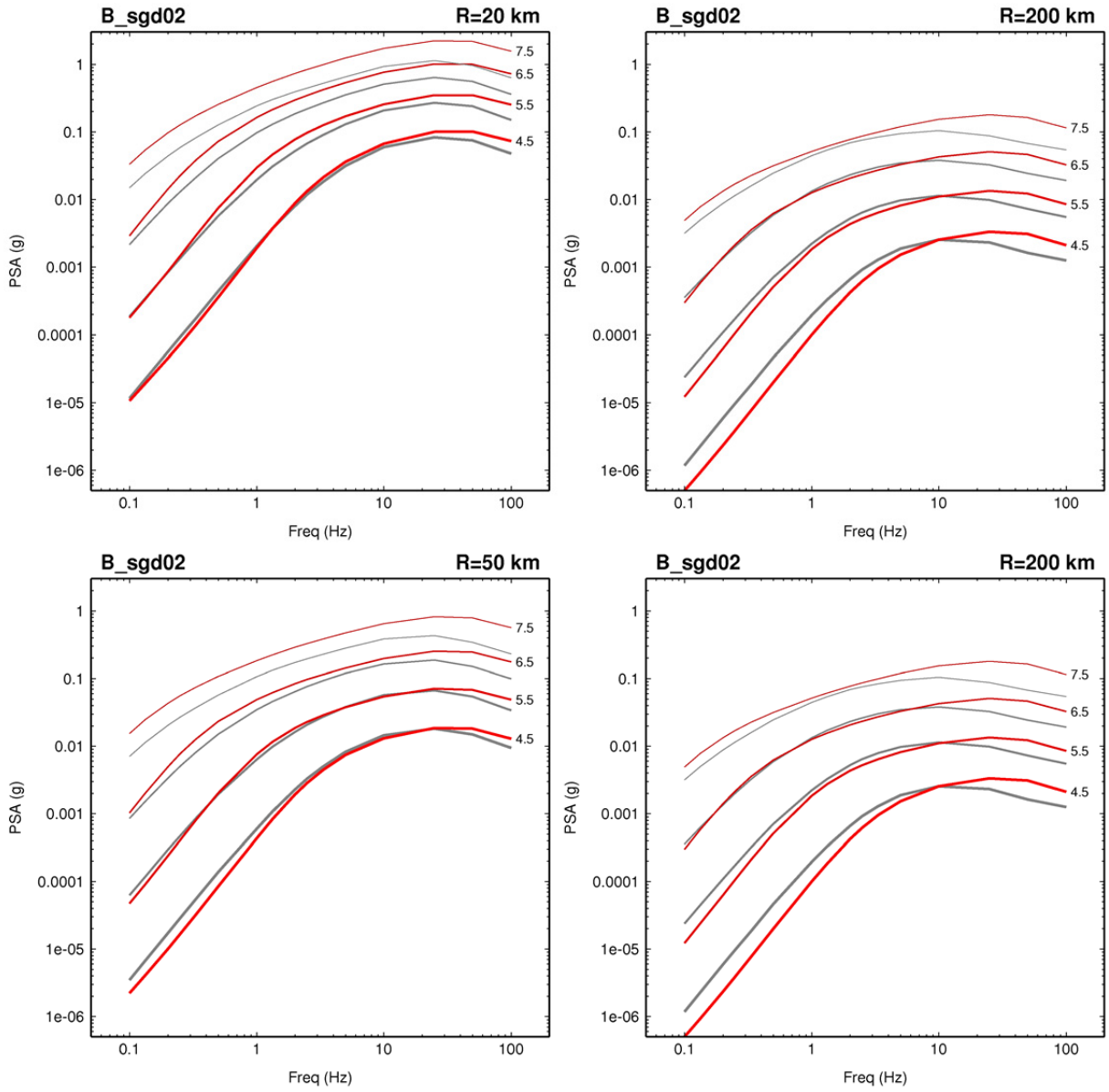

Figure 3.6 B_sgd02 GMM. Format is same as Figure 3.1.

Darragh, Abrahamson, Silva, and Gregor (DASG) Models

(1CCSP, 1CVSP, 2CCSP, 2CVSP)

The four models are grouped into single- and double-corner PS models (1C or 2C), with each group including a version with the stress parameter that is either constant or variable as a function of magnitude (CSP or VSP). The ground-motion spectra for the four DASG GMMs are shown in Figures 3.7 to 3.10. The primary difference among these models is the use of either a "single corner" (Figures 3.7 and 3.8) or "double corner" (Figures 3.9 and 3.10) for the stochastic point-source spectrum. The single-corner models (both constant and variable stress parameter

cases) tend to produce elevated levels of low-frequency (f < 1 Hz) ground motions, particularly for larger magnitudes (**M** > 6), which lead to a noticeable bump in the spectra. The developers have noted a similar feature for WNA single-corner models when compared against recorded ground motions. Their recommendation is to use the single-corner models only for frequencies above 1 Hz, and the Project Team agrees with this recommendation. The double-corner models do not exhibit this feature, and were accepted for use as seed models without any restrictions.

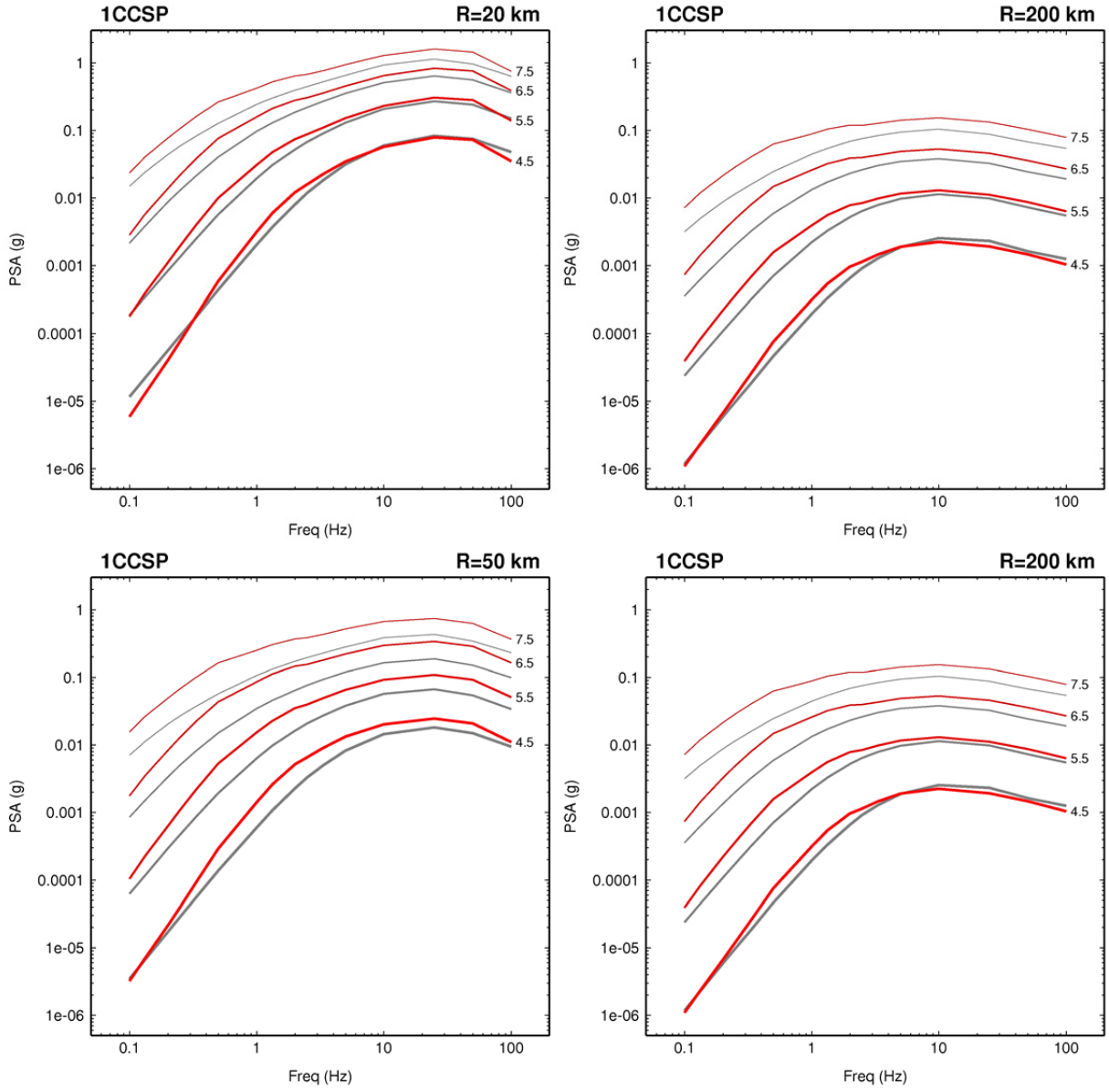

Figure 3.7 1CCSP GMM. Format is same as Figure 3.1.

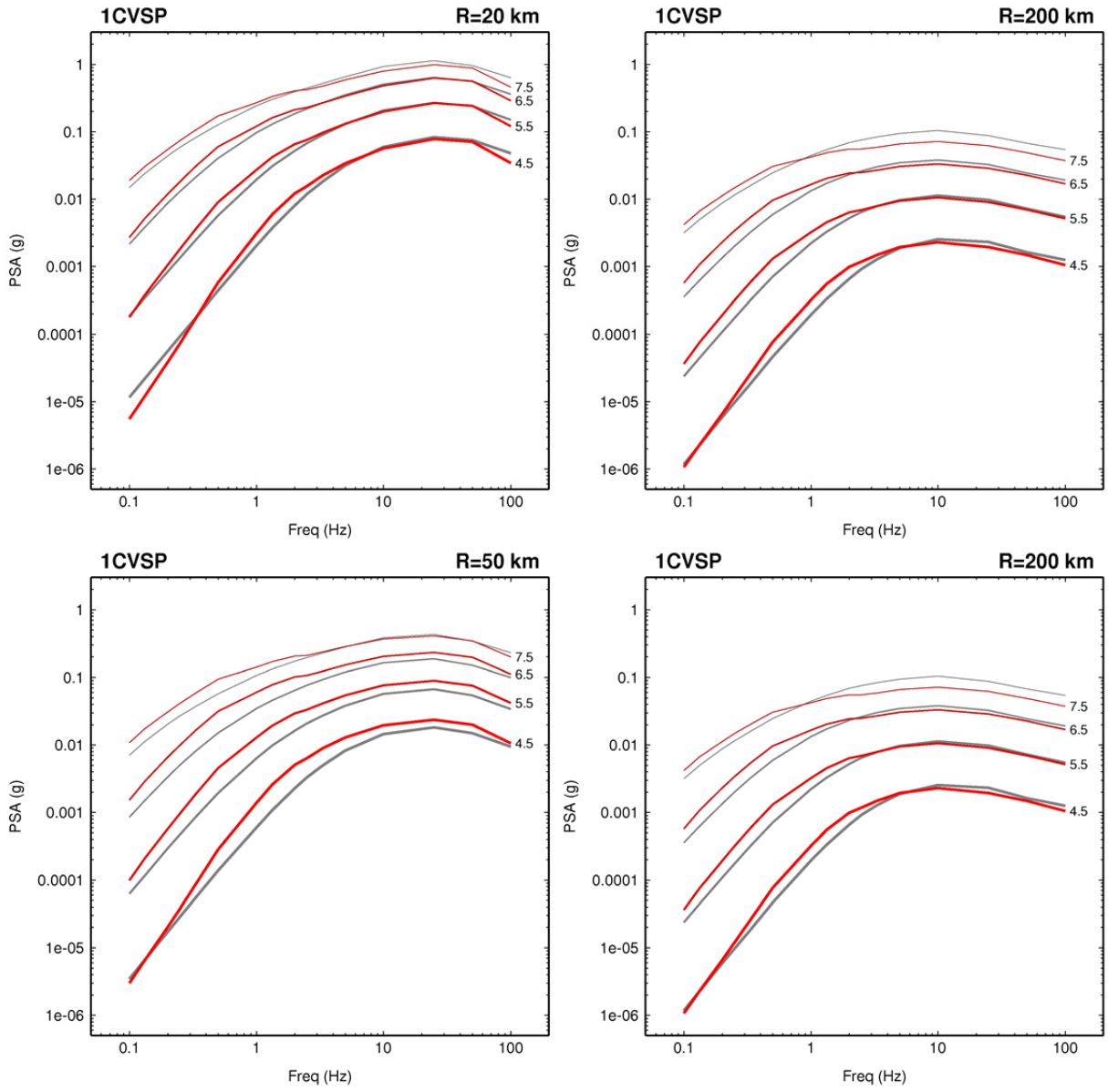

Figure 3.8 1CVSP GMM. Format is same as Figure 3.1.

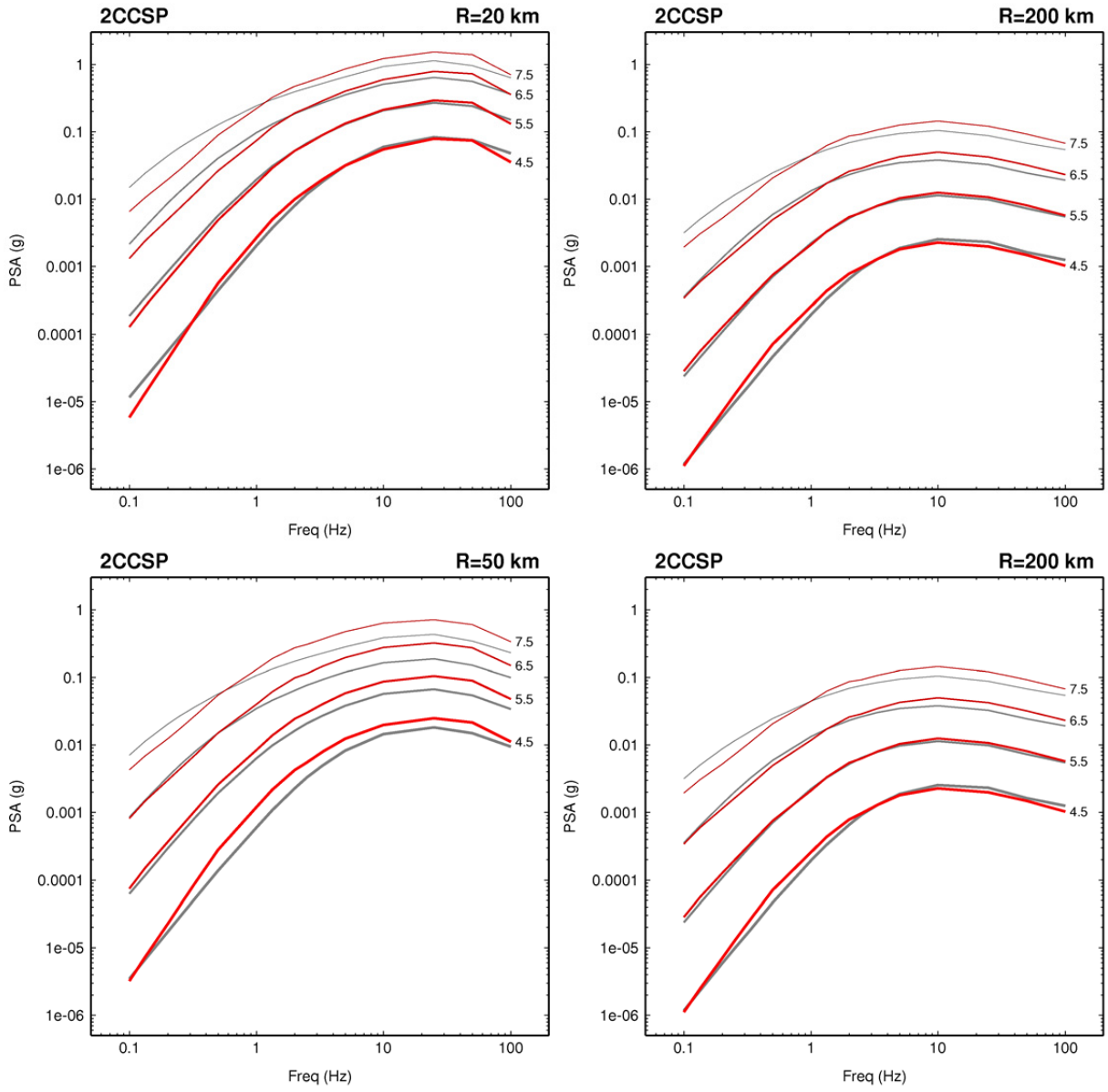

Figure 3.9 2CCSP GMM. Format is same as Figure 3.1.

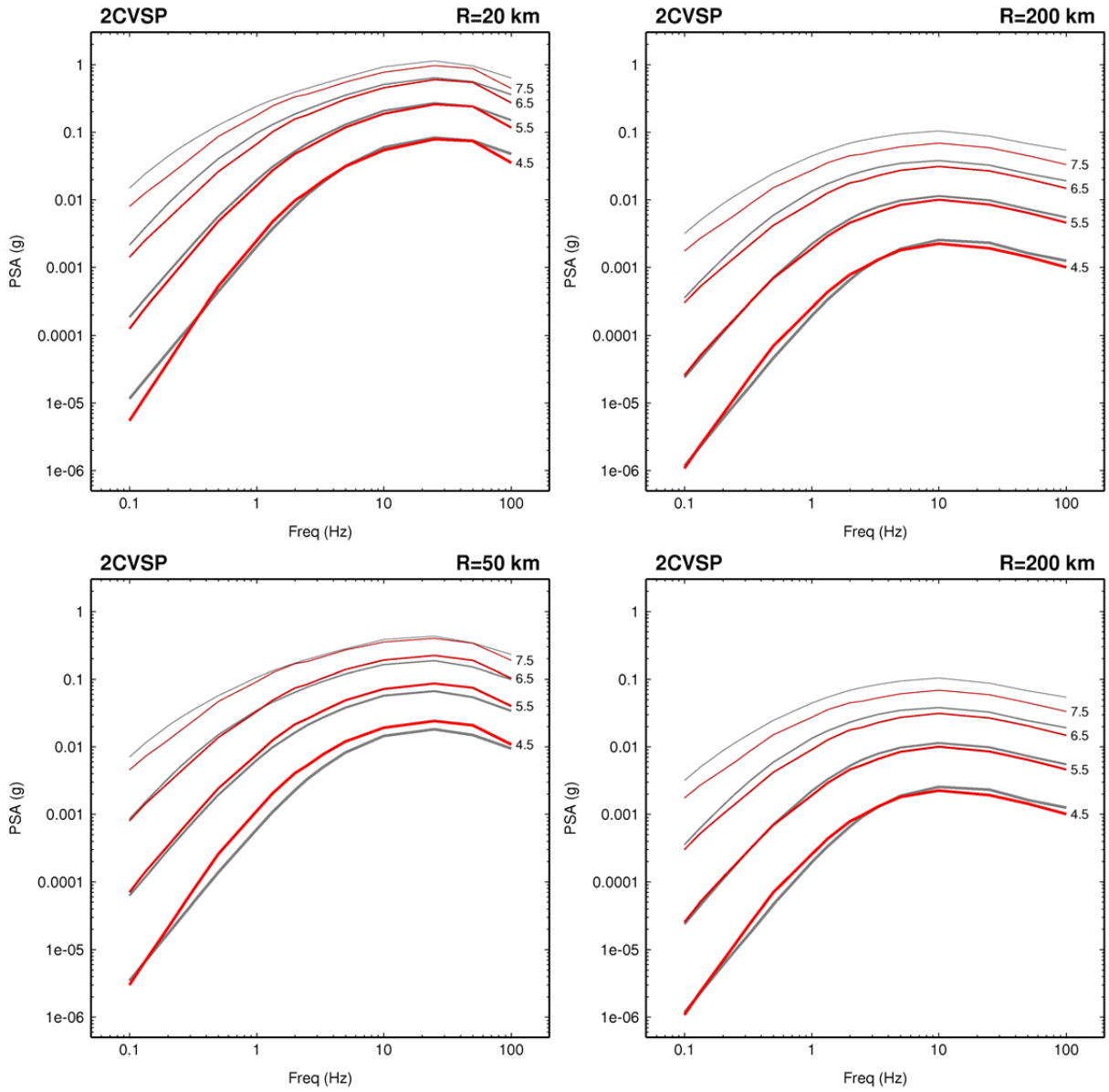

Figure 3.10 2CVSP GMM. Format is same as Figure 3.1.

Yenier and Atkinson (YA15) Model

The ground-motion spectra for the YA15 GMM are shown in Figure 3.11. This model generally produces relatively smooth spectra and does not exhibit any strong breaks in scaling as a function of distance or magnitude. The main feature identified in the evaluation process is the relative drop in ground motion level at 50 Hz, which was essentially set to PGA in the development process, because the model development focused on frequencies < 20 Hz. This was not considered to be a significant issue and accepted this model for use without any restrictions.

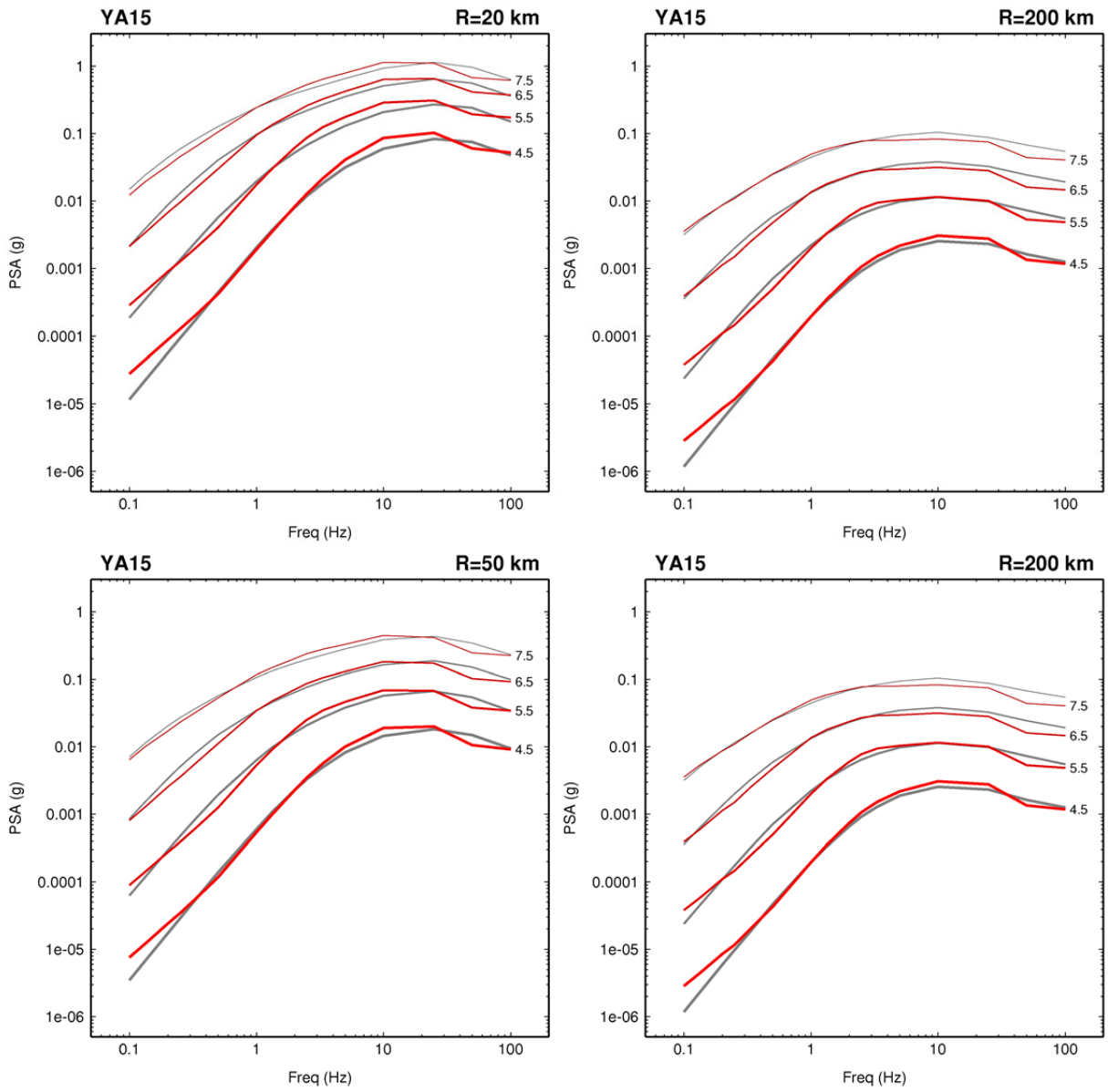

Figure 3.11 YA15 GMM. Format is same as Figure 3.1.

Pezeshk, Zandieh, Campbell, and Tavakoli (PZCT) Models

(PZCT15_M1SS, PZCT15_M2ES)

The ground-motion spectra for the PZCT GMMs are shown in Figures 3.12 and 3.13. These models produce relatively similar spectra across the range of magnitudes and distances considered for the evaluation. The main difference in the two models is the stronger high-frequency scaling for PZCT15_M2ES (Figure 3.13) for distances less than about 50 km. This difference is considered part of the epistemic uncertainty (the PZCT_M1SS large magnitude scaling is based on simulations and PZCT_M2ES is based on WUS data), and these models were accepted for use without any restrictions.

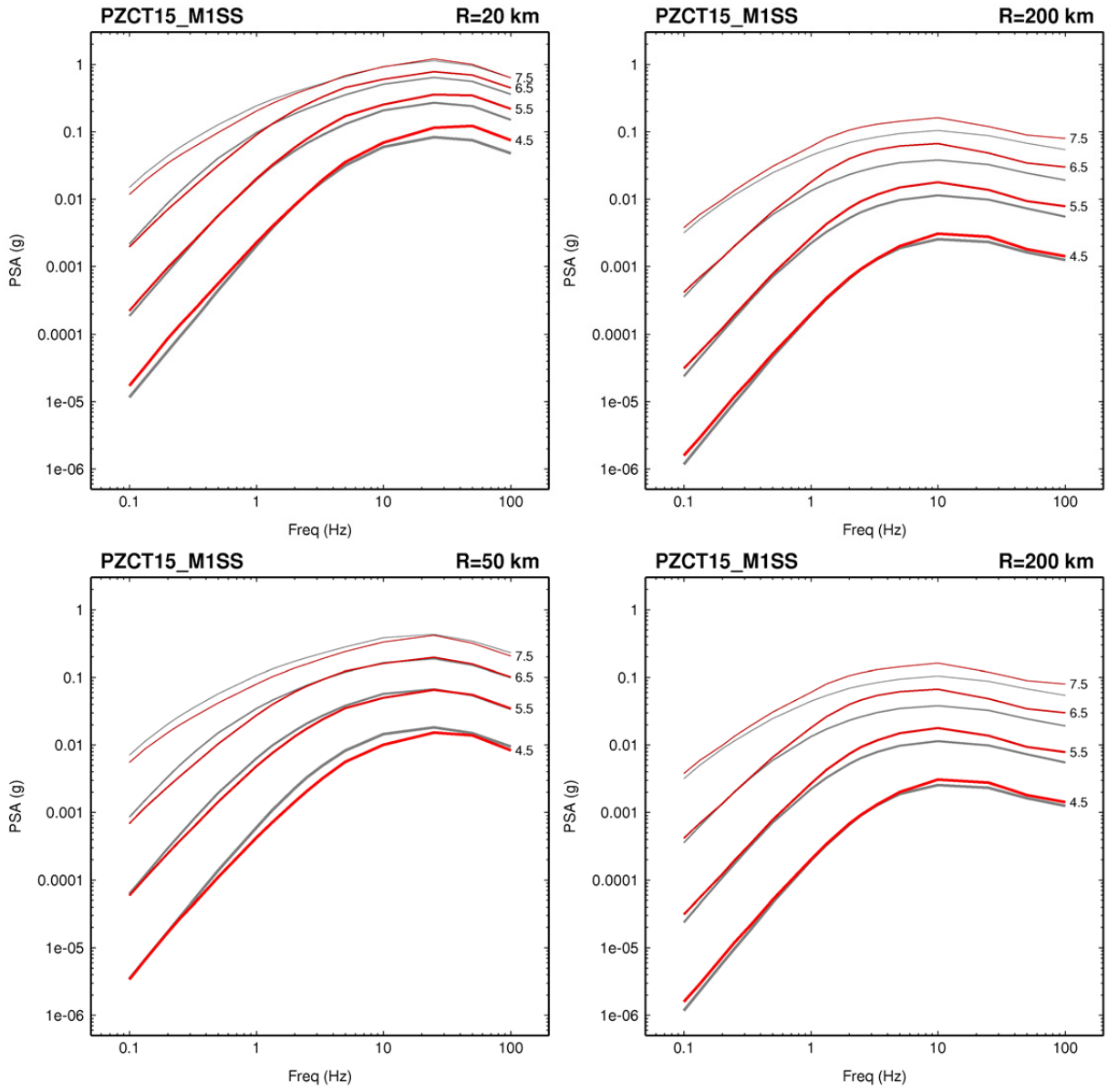

Figure 3.12 PZCT15_M1SS GMM. Format is same as Figure 3.1.

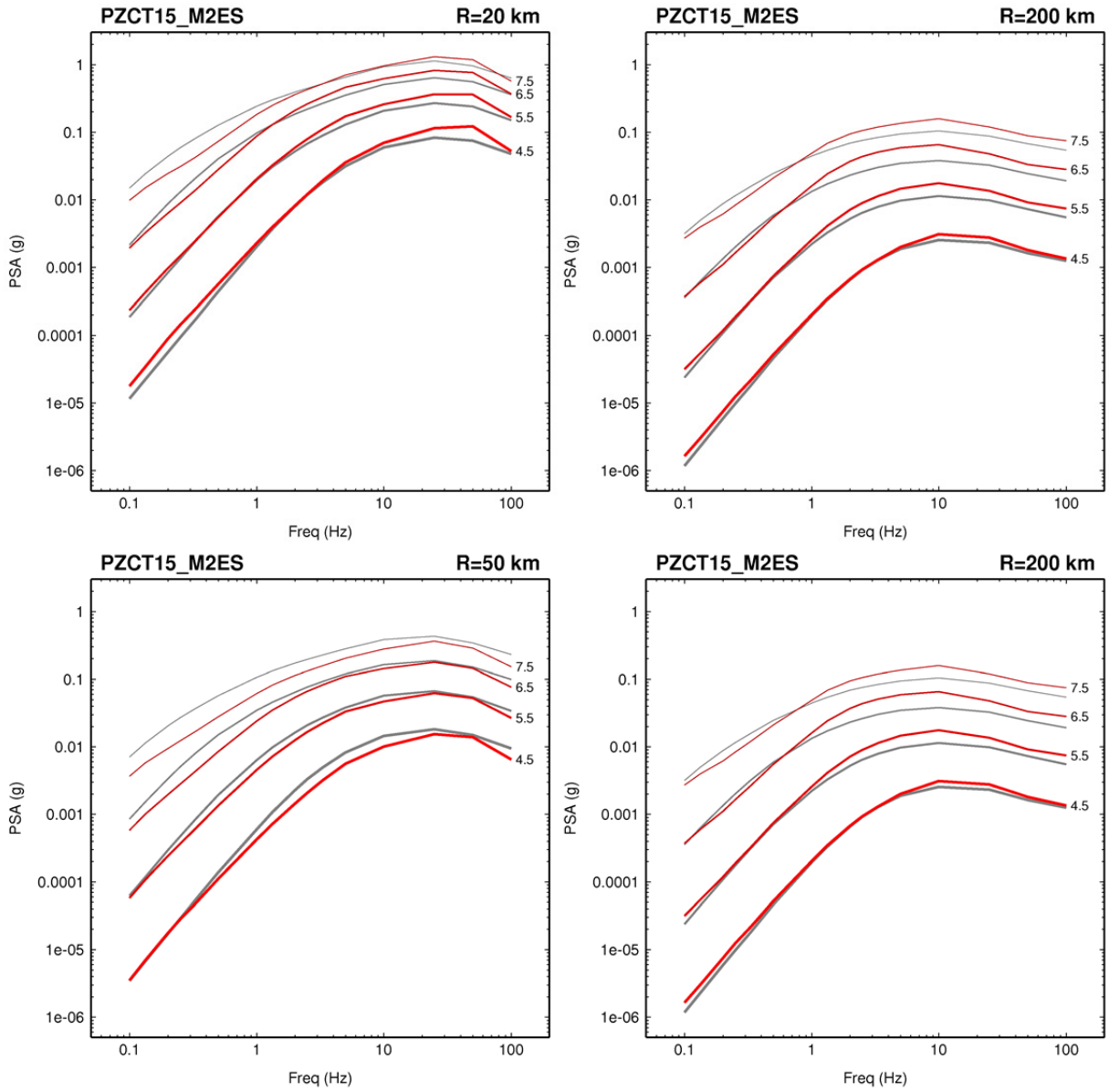

Figure 3.13 PZCT15_M2ES GMM. Format is same as Figure 3.1.

Frankel Model

The ground-motion spectra for the Frankel GMM are shown in Figure 3.14. This model produces spectra that are relatively jagged, particularly at the lower frequencies. This jaggedness primarily results from the limited number of realizations that were used in simulating the ground motions used to constrain the model. In addition, the use of full waveform Green's functions for the lower frequency portion of this model also contributes to the characteristics of the spectral shape, e.g., the elevation in lower frequency ($f < 0.5$ Hz) motions in the distance range 50–100 km is likely due to surface wave energy carried by these Green's functions. This feature is more prominent for the smaller magnitudes (which have spatially compact sources) and becomes washed-out at

larger magnitudes due to the much larger faults. These observations were not considered to be a significant issue and the model was accepted for use without any restrictions.

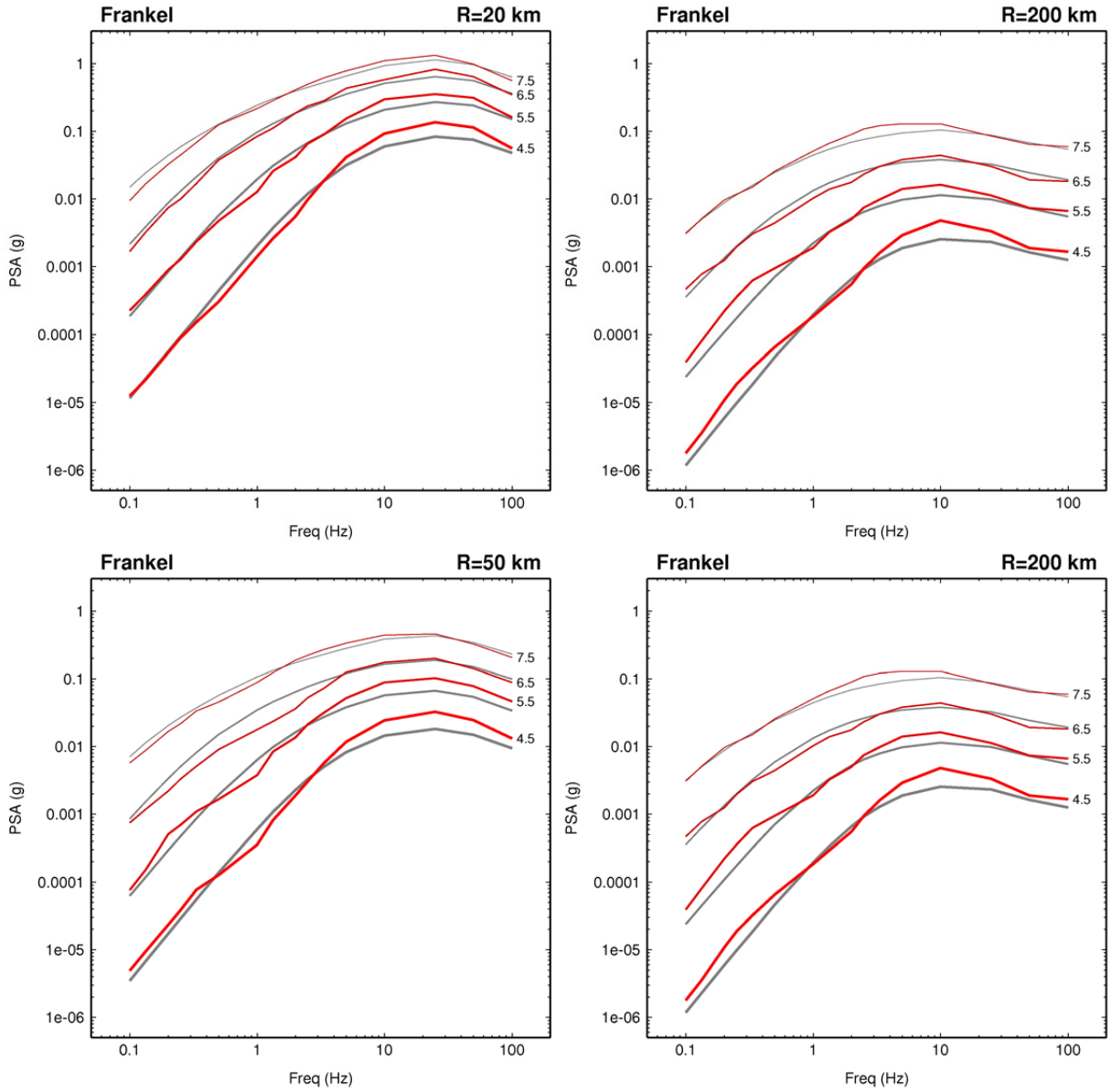

Figure 3.14 Frankel GMM. Format is same as Figure 3.1.

Shahjouei and Pezeshk (SP15) Model

The ground-motion spectra for the SP15 GMM are shown in Figure 3.15. This model produces relatively smoothly varying spectra across the range of magnitudes and distances considered for the evaluation. The Project Team noted the slight relative elevation in spectra around 10 Hz for distances of 50 and 100 km, which likely results from the choice of geometric spreading and attenuation used in generating the synthetic ground motions used to constrain this model. This

was not deemed to be a significant issue and the model was accepted for use without any restrictions.

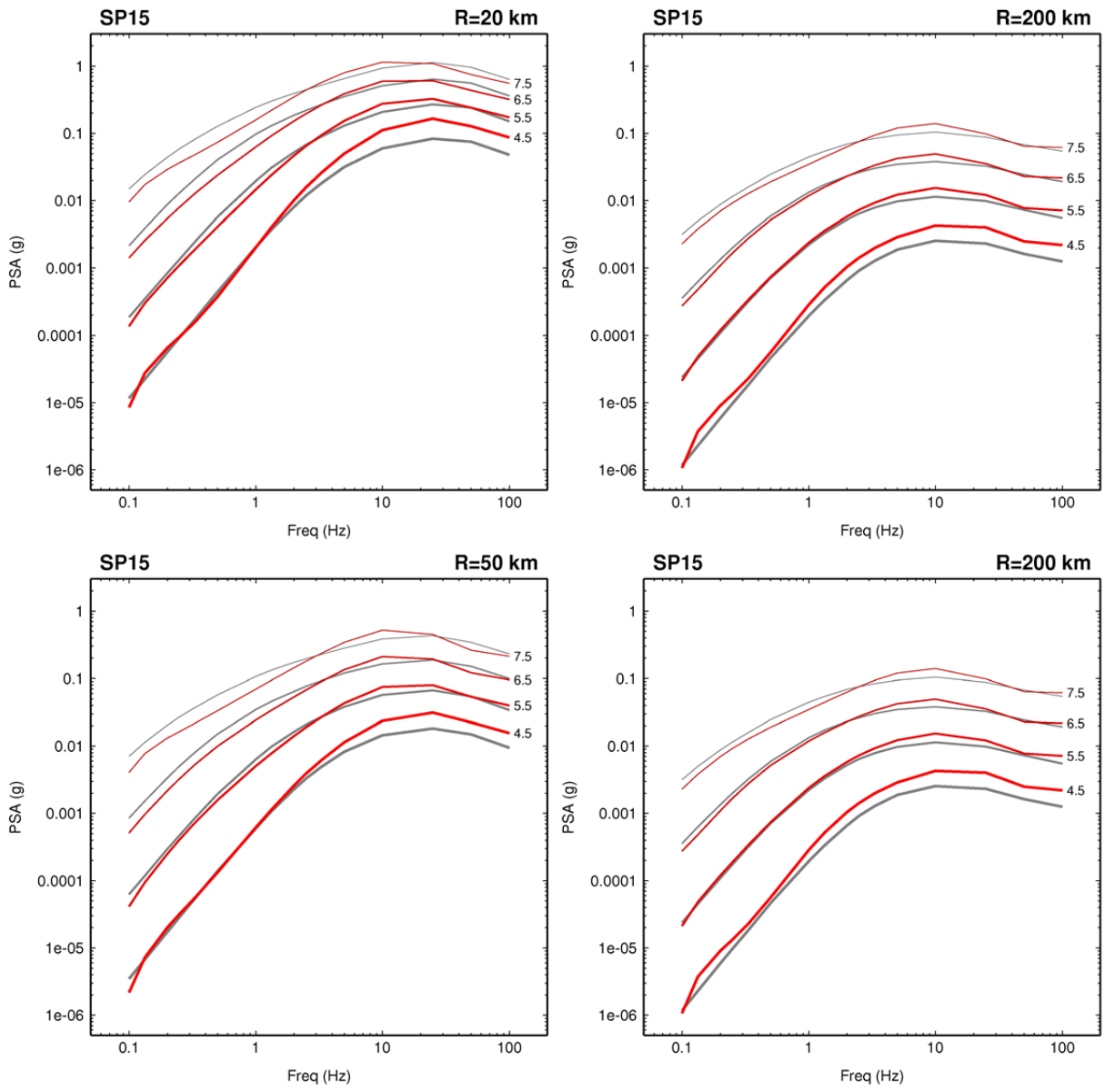

Figure 3.15 SP15 GMM. Format is same as Figure 3.1.

Al Noman and Cramer (ANC15) Model

The ground-motion spectra for the ANC15 GMM are shown in Figure 3.16. This model exhibits anomalous magnitude scaling at low frequencies, suggesting a possible bias due to the use of ground-motion intensity data used in constraining its development. The model uses a fixed "fictitious depth" term, and the developers believe this may limit the ability of the model to extrapolate well up to larger magnitudes. The developers and the Project Team deemed that the model was not ready to be used as a seed model for this project in its current form.

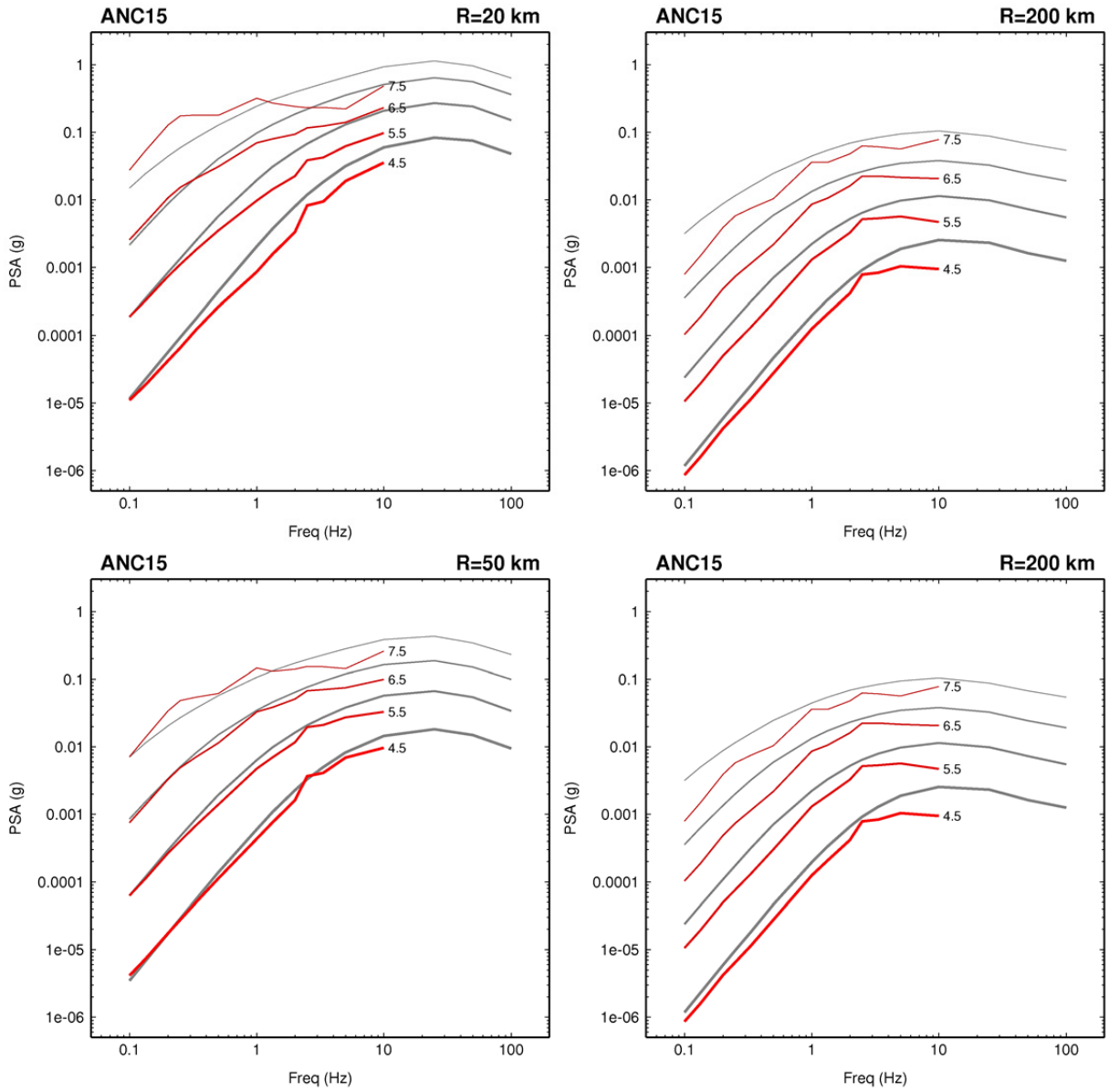

Figure 3.16 ANC15 GMM. Format is same as Figure 3.1.

Graizer Model

The ground-motion spectra for the Graizer [2015] GMM are shown in Figure 3.17. A key feature identified in this models is the spectral peak that occurs around 3–5 Hz for all magnitudes and distances, which is much lower than expected in CENA for a site condition of V_{S30} = 3000 m/sec and κ = 0.006 sec. This results in a noticeable drop in the ground-motion levels for frequencies above 10 Hz. Additionally, the scaling at low frequencies (f < 0.2 Hz) leads to relatively low ground-motion levels at large distances (R > 100 km) and large magnitudes (**M** > 7). Based on these observations, this model was limited for use in the bandwidth 0.2 ≤ f ≤ 5 Hz.

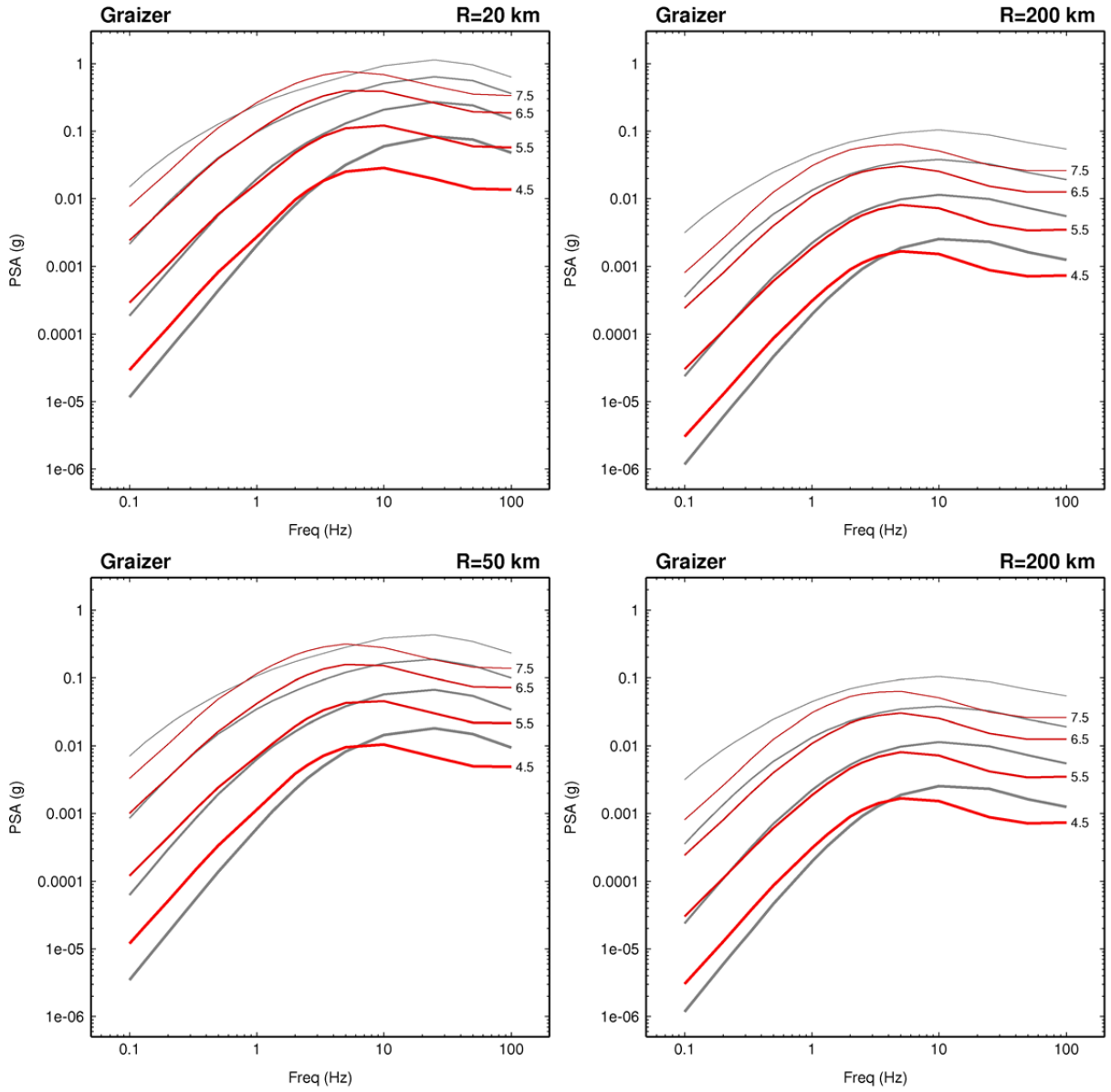

Figure 3.17 Graizer GMM. Format is same as Figure 3.1.

Hassani and Atkinson (HA15) Model

The ground-motion spectra for the Hassani and Atkinson (2015) GMM are shown in Figure 3.18. This model exhibits magnitude scaling inherent to the reference model (BSSA14 from NGA-West2, Boore et al. 2014b) that was used as basis for this GMM. These features include the relative reduction in spectral scaling for 0.2 Hz < f < 5 Hz at large magnitudes (**M** > 6), and the change in slope of magnitude scaling at **M** = 5.5 for high frequencies (f > 5 Hz). The developers of this model feel these features are warranted by the presence of such data trends in data-rich western regions (e.g., in the reference BSSA14 model), and they cannot be ruled out for CENA with the present set of observations. Therefore, this model was accepted for use without any limitations.

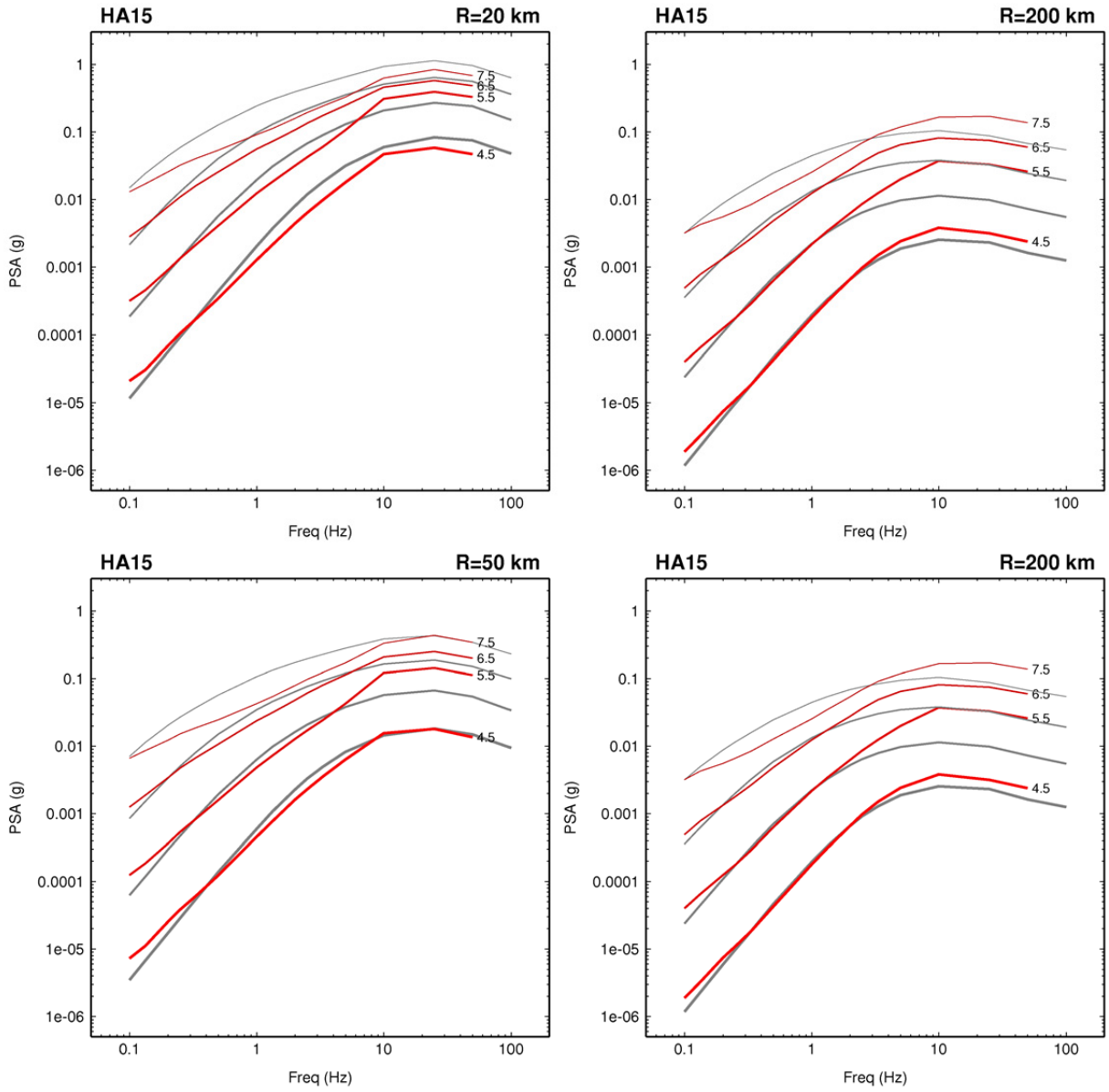

Figure 3.18 HA15 GMM. Format is same as Figure 3.1.

PEER Models

(PEER_EX, PEER_GP)

The ground-motion spectra for the PEER GMMs are shown in Figures 3.19 and 3.20. These two models differ only in the approach used to scale the results to $\mathbf{M} \geq 5.5$ (the developers felt this was the upper limit for which the CENA data can be used to constrain the model). PEER_EX uses EXSIM [Atkinson and Assatourians 2015] for this scaling, and PEER_GP uses the Graves and Pitarka [2015] simulation approach for the scaling. At higher frequencies, PEER_EX shows relatively stronger scaling with increasing magnitude compared to PEER_GP, particularly at larger distances. Nonetheless, both models produce reasonable high-frequency motions. At lower frequencies ($f < 2$ Hz), the models show larger differences. In particular, the spectra for

PEER_EX show a noticeable elevation beginning around 1 Hz and extending to lower frequencies. The developers felt that this feature was probably not well constrained by the simulation approach, and their recommendation was to only use the PEER_EX model for frequencies above 2 Hz. The Project Team agreed with this recommendation for the PEER_EX model. The PEER_GP GMM was accepted for use as a seed model without any restrictions.

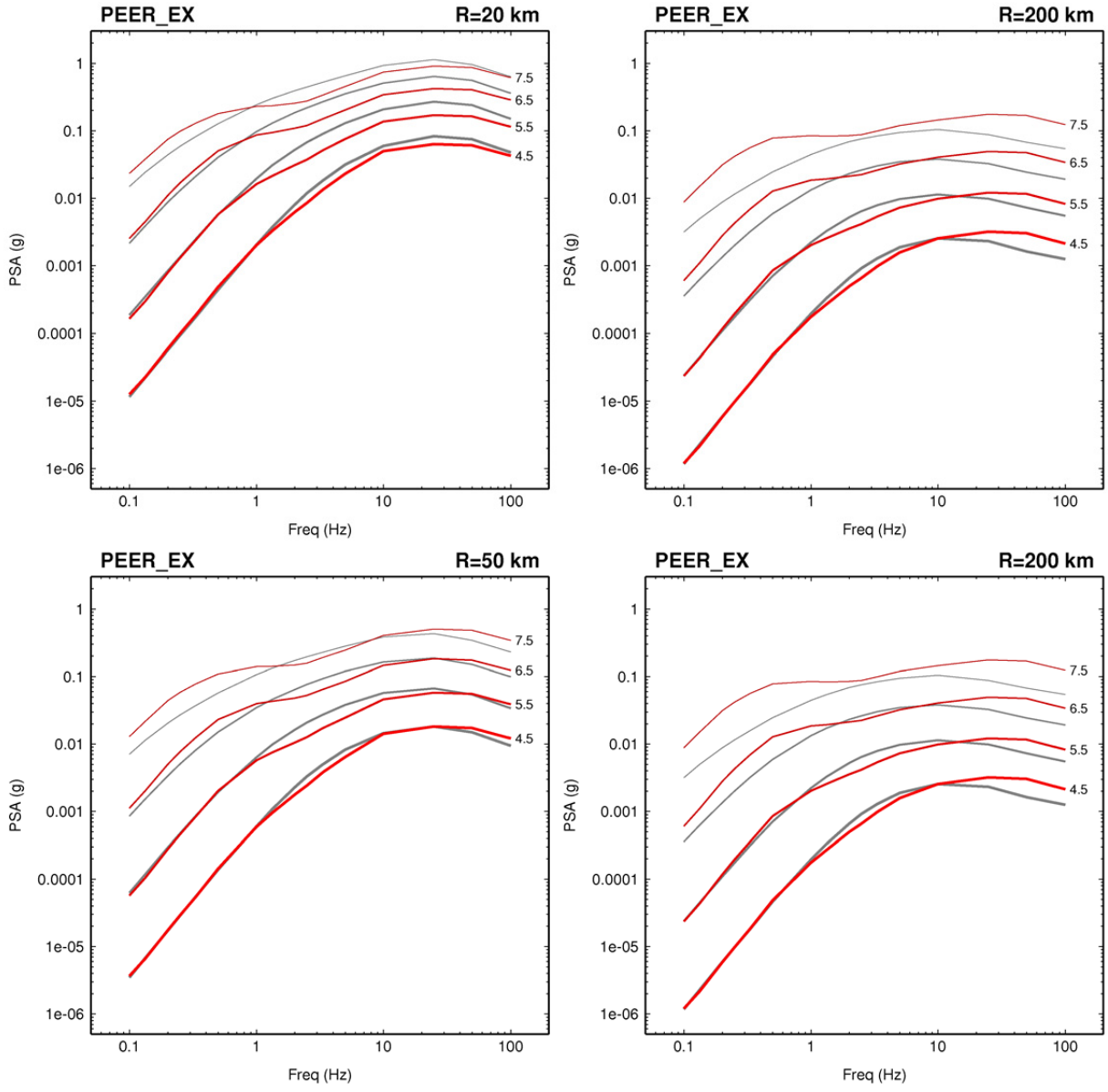

Figure 3.19 PEER_EX GMM. Format is same as Figure 3.1.

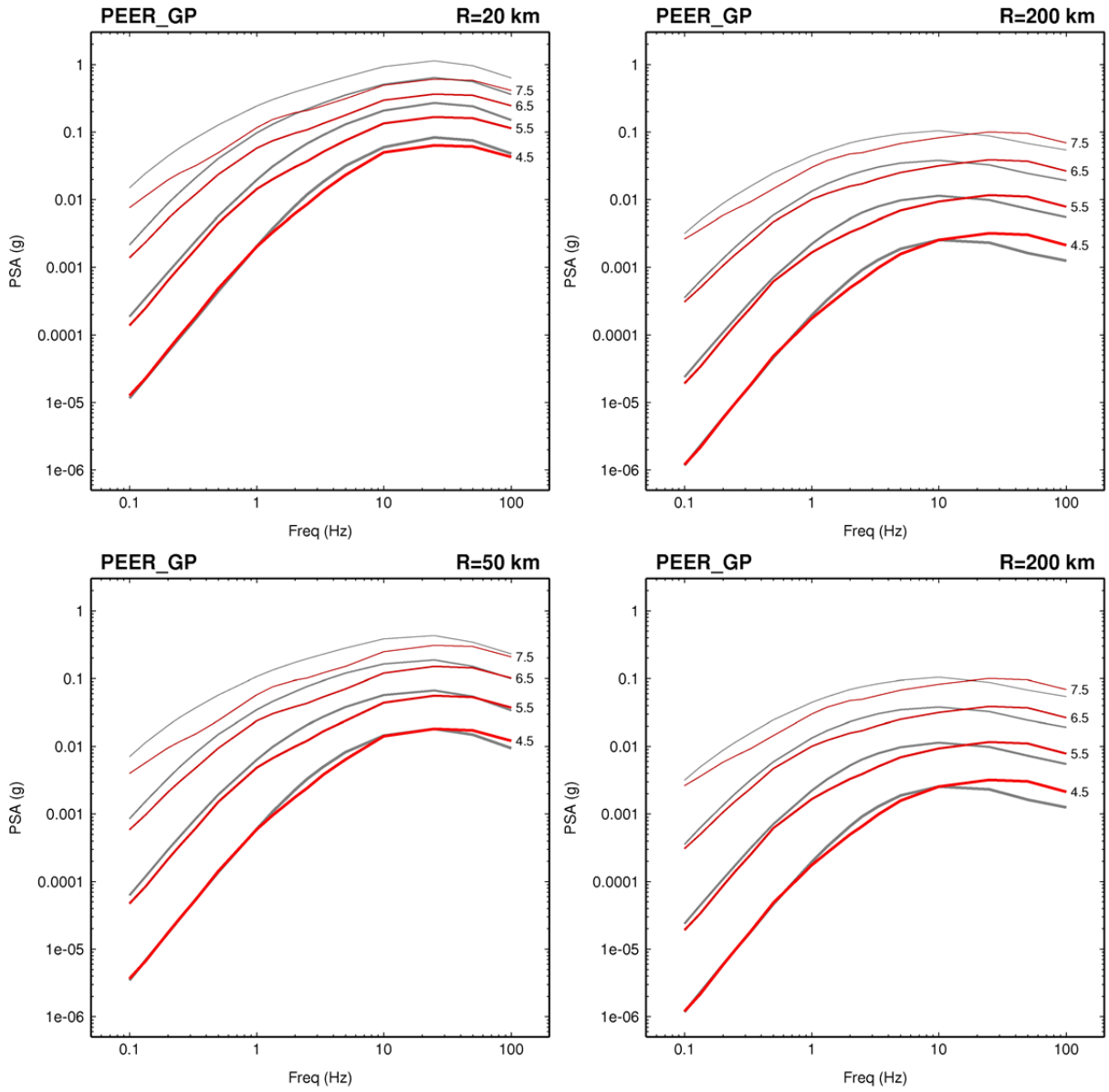

Figure 3.20 PEER_GP GMM. Format is same as Figure 3.1.

Summary of Evaluation

Table 3.14 summarizes the Project Team evaluations for each of the 20 candidate GMMs.

Table 3.14 Evaluation Summary of NGA-East median GMMs.

Model	Comments
B_ab04	Accepted as is.
B_ab14	Accepted as is.
B_ab95	Accepted as is.
B_bca10d	Accepted as is.
B_bs11	Accepted as is.
B_sgd02	Accepted as is.
1CCSP	Elevated level of low-frequency (f< 1Hz) spectra particularly for larger magnitudes (**M** > 6). Developers noted similar bias for WUS single-corner models when compared against recorded motions. Developers recommend only using f > 1 Hz.
1CVSP	Elevated level of low-frequency (f< 1Hz) spectra particularly for larger magnitudes (**M** > 6). Developers noted similar bias for WUS single-corner models when compared against recorded motions. Developers recommend only using f > 1 Hz.
2CCSP	Accepted as is.
2CVSP	Accepted as is.
YA15	Relative drop in response around 50 Hz (not considered an issue by Project Team). Accepted as is.
PZCT15_1MSS	Accepted as is.
PZCT15_M2ES	Accepted as is.
Frankel	Spectral shape a bit jagged due to limited number of simulations (not considered an issue by TI-Team). Accepted as is.
SP15	Accepted as is.
ANC15	Magnitude scaling at low-frequencies suggests possible bias due to use of intensity data, particularly at shorter distance range. Fixed h term (fictitious depth), doesn't extrapolate well with magnitude. Developers recommend not including this model as a seed model.
Graizer	Peak in the spectra occurs around 3–5 Hz for all magnitudes and distances, which is much lower than expected for CENA for site condition of V_{S30}=3000 and κ = 0.006 sec. Scaling of low frequency levels (f < 0.2 Hz) lead to relatively low values at large distance (R >100 km) and large magnitude (**M** > 7). Recommend using only in the bandwidth 0.2 <= f <= 5 Hz.
HA15	Magnitude scaling exhibits features inherent to the reference model [BSSA14] used as basis for this GMM. These features include relative reduction in scaling for 0.2 Hz < f < 5 Hz at large magnitude (M>6), and change in slope of magnitude scaling at **M**5.5 for high-frequencies (f >5 Hz). Developers feel these features are warranted by data used to develop reference model [BSSA14], and they cannot be ruled out for CENA with present set of observations. Accepted as is.
PEER_EX	Magnitude scaling at low-frequency suggests possible bias. Developers recommend only using f > 2 Hz.
PEER_GP	Accepted as is.

3.1.4 Adjustments to Median Ground-Motion Models

The GMMS are to be implemented in hazard analysis codes and should cover the complete range of distances in the Central and Eastern U.S. Seismic Source Characterization for Nuclear Facilities Project (CEUS SSC), including a distance of 0 km or very close to 0 km, in terms of closest distance to the rupture plane, R_{RUP}. As source depth tends to be magnitude-dependent, it is unlikely to have an **M** = 4 event rupture to the surface, but making this source depth and **M** combination possible and defined in the models may prevent computational problems in hazard codes.

The various GMMs listed in Table 3.2 cover a wide range of distances based on two main distance metrics: the Joyner-Boore Distance, R_{JB}, and the closest distance to the rupture plane, R_{RUP}. The R_{JB} distance is defined as the horizontal distance from the projection of the earthquake rupture plane on the Earth's surface. It is therefore zero everywhere above the rupture plane and does not include depth. However, the GMMs that use R_{JB} often incorporate a "fictitious depth" to allow for the near saturation of ground-motion levels at very short distances observed in empirical data. Note that GMMs that use R_{RUP} also include such terms to model ground-motion saturation at very short distances.

In the NGA-East Project, both R_{RUP} and source depth are included as parameters for the final GMC, implying that the ground motions from all the R_{JB}-based models had to be converted to R_{RUP}. This is a simple correction if the average depths used in the assumption of the models are known or are in the dataset used to constrain the models. However, when this simple conversion is applied, it is possible that the resulting extensions to R_{RUP} near and at 0 km may not be reasonable, depending on the specific modeling assumptions. For that reason, an extrapolation scheme based on fitting of ground-motion values with (converted) R_{RUP} values at larger distances, typically 10 km and larger, was developed.

As documented in the PEER report [2015a], the NGA-East team requested that all the GMMs provide ground motions up to 1200 km. Following subsequent hazard analysis runs and based on experience in assessment of hazard for nuclear facilities, the NGA-East Project Team extended the distance range to 1500 km. This large distance allows for application of the GMMs at sites in regions with low seismicity where ground motions from a large, distant earthquake (such as from the New Madrid seismic zone) contribute significantly to the site hazard. Because the intent for the NGA-East Project Team was to evaluate the model over the full range of distances to which it is likely to be applied, extrapolation of all the models to 1500 km was therefore required.

In addition, most models were not strongly calibrated for distances beyond about 400 or 600 km. The difficulty of calibration at large distances using the empirical data (NGA-East database) [Goulet et al. 2014] is primarily due to the lack of ground-motion records at large magnitudes. Because most of the dataset is from earthquakes smaller than **M** = 6, the ground motions at large distances are fairly weak and often below the noise threshold for a wide-frequency band. The only ground motions that remain are those motions that are "exceptionally high" for the given magnitude and distance, effectively biasing the dataset. This effect is denoted as distance censoring of the data and has been discussed in the literature with respect to development of GMPEs from empirical data; e.g., see Abrahamson et al. [2014] and Chiou and

Youngs [2014]. Therefore, NGA-East proposed to develop "reasonable" extrapolation rules for large distances as an alternative to the original GMM ground motions.

The adjustment of the GMMs to large distances was performed independently for each frequency. This sometimes led to an unphysical spectrum at large distances, with a trough at high frequencies beyond the peak of the spectrum. This observation was also made for some of the initial NGA-East GMMs (before extrapolation) and was noticed for large distances in some of the NGA-West2 GMMs [R.R. Youngs and N.A. Abrahamson, personal communication]. This effect is not observed for all models, but when it occurs, it is typically for distances larger than 400 km (the specific range is model dependent).

To correct these unphysical spectra, the high-frequency part is essentially replaced by a linear trend. If there is a trough at frequencies beyond the peak, the high-frequency ground-motion values are fixed to a specific value, following two possible cases. If there is a secondary peak beyond the trough, then the ground-motion values are fixed at the geometric mean of the trough value and the secondary peak value. Otherwise, the spectrum is fixed at the geometric mean of the trough value and the PGA value. After the distance extrapolation is completed, the process is applied systematically to all the spectra from all the GMMs. The conversion of R_{JB}-based models to R_{RUP}, the extrapolation at short and large distance, and the spectral adjustments to the GMMs are covered in details in Chapter 2 of PEER [2015b].

3.1.5 Summary of Selected Seed Median Models

The evaluation and selection processes described in the previous sub-sections led to a suite of 19 selected GMMs. The models were extended in distance their spectral shapes were modified following the rules described above. These models constitute the "seed models." The seed models are used in the development of the median GMMs, as described in Section 3.2. The seed models, as utilized in this project, are available in electronic appendices to PEER [2015b], which can be found online on the PEER website. They are not provided with the current report to avoid potential confusion with the models proposed for use by the USGS.

3.2 CONTINUOUS DISTRIBUTION OF GROUND-MOTION MODEL

One of the main assumptions behind the NGA-East approach to median ground motions is that the associated epistemic uncertainty can be described by a continuous distribution. This was illustrated for one particular moment magnitude and rupture distance ($\mathbf{M}$, R_{RUP}) scenario in Figure 2.4, where the (discrete) estimates from individual seed models were fitted by a continuous normal distribution. When going from one to multiple ($\mathbf{M}$, R_{RUP}) scenarios, the distribution describing median ground-motion values becomes a multivariate normal distribution, described by a mean and a covariance matrix.

Hence, for each of the NGA-East frequencies, the joint distribution of median ground-motion estimates at different ($\mathbf{M}$, R_{RUP}) scenarios is a multivariate normal distribution:

$$P(\mathbf{Y}) \sim N(\boldsymbol{\mu}, \Sigma) \tag{3.1}$$

where $\mathbf{Y} = \left\{ Y_1, \ldots Y_{N_D} \right\}$ is a vector of random variables describing the (uncertain) median ground-motion values at N_D different ($\mathbf{M}$, R_{RUP}) scenarios, $\boldsymbol{\mu}$ is a vector characterizing the mean of the

uncertainty distribution at each (**M**, R_{RUP}) scenario, and $\sum$ is the covariance matrix between the median ground-motion estimates at the different (**M**, R_{RUP}) scenarios. **Y** is a random variable whose probability distribution describes the epistemic uncertainty in median estimates, and it does not describe the ground-motion distribution that enters the hazard integral. The **Y** distribution can be written as

$$\begin{bmatrix} Y_1 \\ \vdots \\ Y_{N_D} \end{bmatrix} \sim N\left(\begin{bmatrix} \mu_1 \\ \vdots \\ \mu_{N_D} \end{bmatrix}, \left(\begin{bmatrix} \Sigma_{11} & \cdots & \Sigma_{1N_D} \\ \vdots & \ddots & \vdots \\ \Sigma_{N_D 1} & \cdots & \Sigma_{N_D N_D} \end{bmatrix} \right) \right) \tag{3.2}$$

where the entries of the covariance matrix are

$$\Sigma_{ij} = \rho_{ij} \sigma_i \sigma_j \tag{3.3}$$

with σ_i as the standard deviation of the ground-motion distribution for the ith (**M**, R_{RUP}) scenario, and ρ_{ij} describing the correlation between the *i*th and *j*th (**M**, R_{RUP}) scenario.

A sample from the distribution described by Equations (2.1) or (2.2) is a vector of median ground-motion estimates of **Y** at the considered (**M**, R_{RUP}) distributions. The evaluation of a more traditional equation (or physical model) at these (**M**, R_{RUP}) scenarios also leads to a vector of median ground-motion estimates **Y**. For a sufficiently large (ideally infinite) number of (**M**, R_{RUP}) scenarios, a sample from the median ground-motion distribution can be considered a continuous function of **M** and R_{RUP}; therefore, samples selected from P(**Y**) are GMMs.

The P(**Y**) distribution described by Equations (2.1) or (2.2) is a full description of the center, body, and range of epistemic uncertainty associated with median ground-motion estimates. The main task required to estimate the P(**Y**) distribution is to estimate its mean and to develop the covariance matrix, $\sum$, which consists of two parts:

- a model for the diagonal elements of $\sum$, which they are the variances σ_i^2 for the *i*th (**M**, R_{RUP}) scenario.
- a model for the correlation coefficients, ρ_{ij}, describing the correlation between median estimates for the *i*th and *j*th scenario.

The covariance model is inspired by a Gaussian process model. This concept is first introduced in the next subsection, followed by the development of the two parts indicated above.

Given the covariance model, and thus P(**Y**), the approach to discretize the median ground-motion distribution relies on drawing a large number of samples (e.g., a large number of sampled models; see the right side of Figure 2.5).

For the NGA-East Project, the (**M**, R_{RUP}) scenarios considered for the generation of new models are:

- **M** = 4, 4.5, 5, 5.5, 6, 6.5, 7, 7.5, 7.8, 8, 8.2

- R_{RUP} = 0,1, 5, 10, 15, 20, 25, 30, 40, 50, 60, 70, 80, 90, 100, 110, 120, 130, 140, 150, 175, 200, 250, 300, 350, 400, 450, 500, 600, 700, 800, 1000, 1200,1500

These magnitude and distance ranges were selected to capture important trends in scaling. The magnitude scaling for magnitudes up to about 7.5 follows a mostly linear trend, with a curvature at larger magnitudes. To capture the linear trend, we deemed bins of 0.5 magnitude units to be sufficient. For the large magnitudes, we reduced the bin with to 0.2, to capture the change in slope due to saturation. Scaling of ground motion with distance exhibits a more nonlinear behavior, especially within 50 km (due to effects such as geometrical spreading and near source saturation assumptions) and near the Moho bounce zone, which extends roughly from about 70 to 150 km. Thus, the distance bins are narrower in these zones. Beyond 500, the distance scaling is dominated by a linear trend, so fewer distance values needed.

In total, there are 374 ($\mathbf{M}$, R_{RUP}) scenarios at which the seed GMMs are considered and for which the sampled models are drawn.

3.2.1 Gaussian Processes

Gaussian processes (GPs) provide the theory behind the development of the covariance model introduced above. This section relies on Hermkes et al. [2014] and the descriptions in Rasmussen and Williams [2006]. Gaussian processes can be used in a regression setting, which typically have the form

$$y = f(\mathbf{x}) + \varepsilon \tag{3.4}$$

where y is the target variable, $\mathbf{x}$ denotes the predictor variables, and ε is the residual, usually assumed to be normally distributed with mean zero. Function f is a noise-free function, which connects the target and the predictors. A GP places a distribution over the noise-free function values:

$$f(\mathbf{x}) \sim GP[m(\mathbf{x}), k(\mathbf{x}, \mathbf{x}')] \tag{3.5}$$

which reads as "the function value at $\mathbf{x}$ is sampled from a GP with mean $m(\mathbf{x})$ and covariance function $k(\mathbf{x}, \mathbf{x}')$". Basically, the GP is an infinite-dimensional Gaussian distribution, and every finite subset is multivariate Gaussian as well. To obtain estimates at particular values of the predictor variables $\mathbf{x}$, the distribution [i.e., $m(\mathbf{x})$ and $k(\mathbf{x}, \mathbf{x}')$] is only evaluated at these values. Different covariance functions exist (see, e.g., chapter 4 of Rasmussen and Williams [2006]), and the one selected for the NGA-East Project is described below. In the NGA-East application, the function values are the median ground-motion estimates, and the distribution induced by the GP describes the associated epistemic uncertainty.

The covariance functions have parameters denoted by θ, which determine how the sampled functions behave. The parameters can be estimated using data. In the context of NGA-East, the data is given by the median ground-motions from the seed GMMs at different ($\mathbf{M}$, R_{RUP}) scenarios. The vector containing the target data is denoted as $\mathbf{y}$, and the vector containing the predictors [i.e., ($\mathbf{M}$, R_{RUP}) scenarios] as $\mathbf{X}$. The full "dataset" is denoted by $\mathbf{D} = \{\mathbf{X}, \mathbf{y}\}$. Then,

the parameters $\boldsymbol{\theta}$ can be estimated by maximizing the log marginal likelihood $p(\mathbf{y}|\mathbf{X},\boldsymbol{\theta})$ (see chapter 5 of Rasmussen and Williams [2006]), which can be written as

$$\ln p(\mathbf{y}|\mathbf{X},\boldsymbol{\theta}) = -\frac{1}{2}\mathbf{y}^T K_Y^{-1}\mathbf{y} - \frac{1}{2}\log|K_y| - \frac{N_D}{2}\ln 2\pi \tag{3.6}$$

where $K_y = K_f + \beta^2 I$, and I is the identity matrix (the β term is used to quantify the noise not captured by the GP). The matrix $K_f = k(\mathbf{x}_i, \mathbf{x}_j)$ is the covariance function evaluated at the predictor variables [the different (**M**, R_{RUP}) scenarios].

3.2.2 Variance Model

For one (**M**, R_{RUP}) scenario, it is easy to estimate a continuous normal distribution describing median estimates, given data from the seed GMMs. The normal distribution is described by the sample mean and sample variance of the seed GMMs (see Figure 2.4). For the multivariate case, the diagonal entries of the covariance matrix $\sum$ can be estimated by the sample variance:

$$\sigma_j = \frac{1}{N_S - 1} \cdot \sum_{i=1}^{N_D} (y_{ij} - \bar{y}_j)^2 \tag{3.7}$$

Here, σ_j is the sample variance for the jth (**M**, R_{RUP}) scenario, and N_S is the number of seed GMMs. Figure 3.21 shows two contour plots of the diagonal entries of the sample covariance matrix for two different frequencies. Each point in the contour plot corresponds to the sample variance. In other words, Figure 3.21 shows the epistemic uncertainty for each (**M**, R_{RUP}) scenario, contained in the set of seed GMMs. As one can see, the numbers vary greatly and are very small for some scenarios. In particular, the sample variances are counter-intuitive for some (**M**, R_{RUP}) scenarios. For example, they are quite small for large magnitudes, even though there is no Central and Eastern North America (CENA) data for these scenarios; cases for which the epistemic uncertainty associated with median ground-motion estimates is expected to be large. In addition, the variances do not vary smoothly with magnitude and distance. This is due to the finite sample size and strong differences in functional forms for some models, which accentuate differences in estimates at certain (**M**, R_{RUP}) scenarios, and thus, leads to higher variances.

The Project Team preferred a variance model that better addresses the "expected" variance given data-driven knowledge, and which would vary smoothly with magnitude and distance. The variance model expresses epistemic uncertainty in GMMs, considering the alternative GMMs developed during the project and other factors such as the data constraints and insights gained from analyses in more data-rich regions. The following guiding principles were used to develop the model.

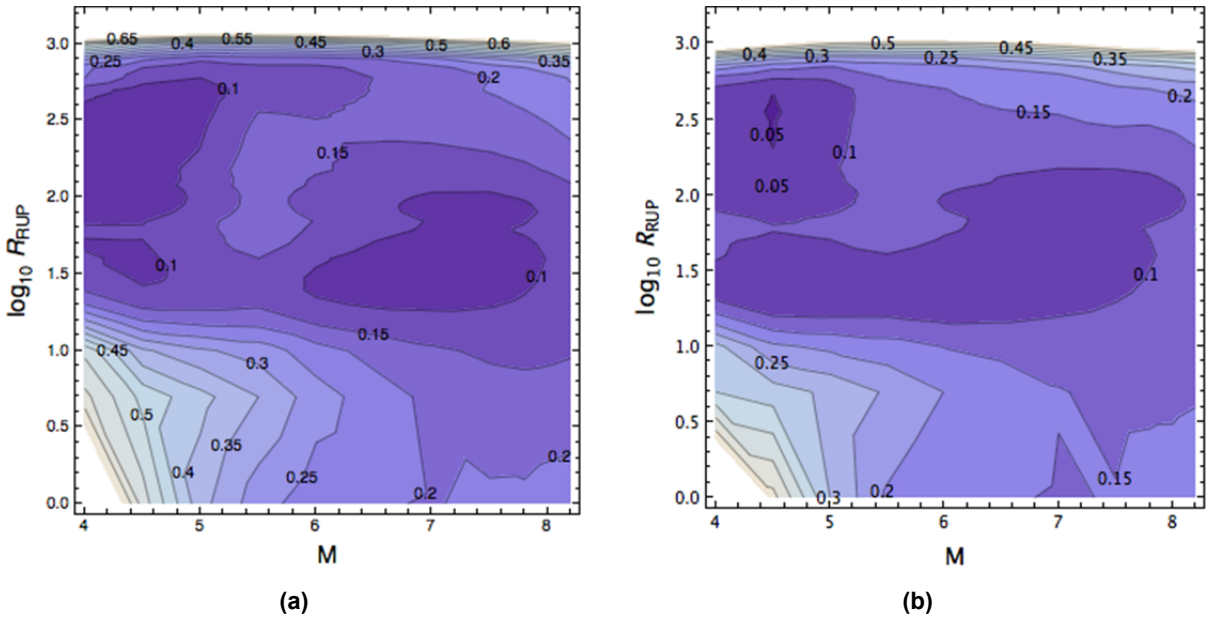

Figure 3.21 **(a) Diagonal entries of the sample covariance matrix for PGA, plotted against M and $\log_{10}R_{Rup}$; and (b) diagonal entries of the sample covariance matrix for f = 10 Hz, plotted against M and $\log_{10}R_{Rup}$.**

1. The epistemic uncertainty in GMMs in CENA is greater than the corresponding uncertainty in GMMs for shallow crustal events in active tectonic regions [such as Western North America (WNA)]. The rationale is that the database is much richer in WNA than CENA, especially in the magnitude-distance ranges of most interest; thus, knowledge of ground-motion behavior is greater in WNA than in CENA.
2. The epistemic uncertainty varies smoothly in magnitude-distance space, being larger in areas of this space where the data constraints are poor to develop CENA GMMs. The lowest epistemic uncertainty for GMMs in CENA is for small-to-moderate events (**M** = 4 to 5) at regional distances (R_{RUP} = 200–400 km).
3. The epistemic uncertainty is partly reflected by the observed variance between alternative GMMs. However, it is not perfectly captured this way, in either WNA or CENA. There are magnitude-distance ranges where alternative GMMs cross, providing a local minimum in variance; however, this does not imply low epistemic uncertainty. Conversely, there may be magnitude-distance ranges where alternative GMMs may push the variance to larger values.

First, a minimum variance based on GMMs in WNA was defined. The variance was estimated from a suite of GMMs that includes the NGA-West2 GMMs and other recent crustal GMMs for active regions (list of GMMs shown on Figure 3.23, as compiled for the South Western U.S. (SWUS) utilities project) [Geopentech 2015]. The inclusion of a range of GMMs

in addition to the NGA-West2 GMMs was deemed necessary as the NGA-West2 GMMs are based on a common database, come from a highly-collaborative GMM development project, and follow similar approaches, which could underestimate the expected epistemic uncertainty. The variance plot in Figure 3.22 shows the estimated variance in WNA for PGA, while Figures 3.23 and 3.24 show sample scaling with magnitude and distance to provide insight into the behavior seen in Figure 3.22. As shown in Figures 3.23 and 3.24 for example, the GMMs pinch together at **M**6.5 to 7 at close distances, in terms of their scaling behavior. This leads to the low variance patch in Figure 3.22, which is not generally representative of the spread between the models. Considering the overall behavior on Figure 3.22 and the fact that data for derivation of these GMMs are plentiful for **M** > 5.5 at R_{RUP} < 200 km, the Project Team concluded that a minimum realistic epistemic uncertainty in WNA GMMs is about 0.05 ln units, becoming larger at regional distances (>150 km): as much as 0.1 ln units in light of regional attenuation uncertainty. The extent to which the epistemic uncertainty is larger at regional distances depends, at least partly, on how uncertainty is partitioned between its epistemic and aleatory components.

The maximum variance for the CENA models should be for large events (**M** > 7) at close distances (R_{RUP} < 10 km). Based on initial variance plots for the developed GMMs (Figure 3.21), for high frequencies [10 Hz to peak ground acceleration (PGA)] this maximum variance is assigned a value of 0.4 ln units. For moderate events (**M** = 4 to 5) at close distance, the variance is assumed to be slightly smaller, at 0.3 ln units, because there are at least some data constraints.

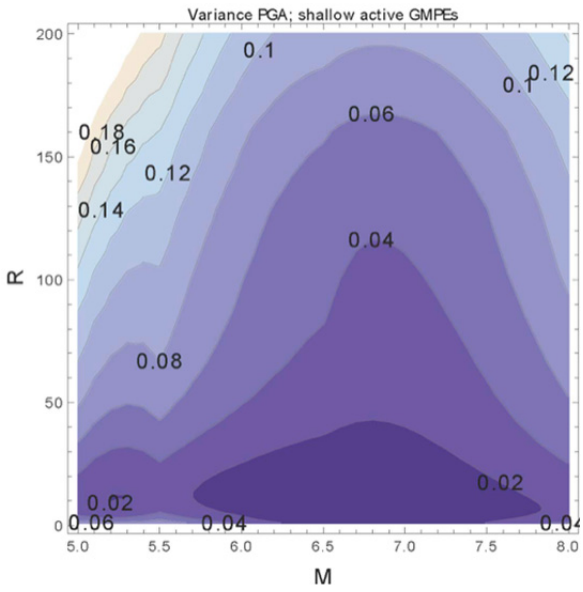

Figure 3.22 Variance in PGA for crustal GMMs in active tectonic regions (WNA).

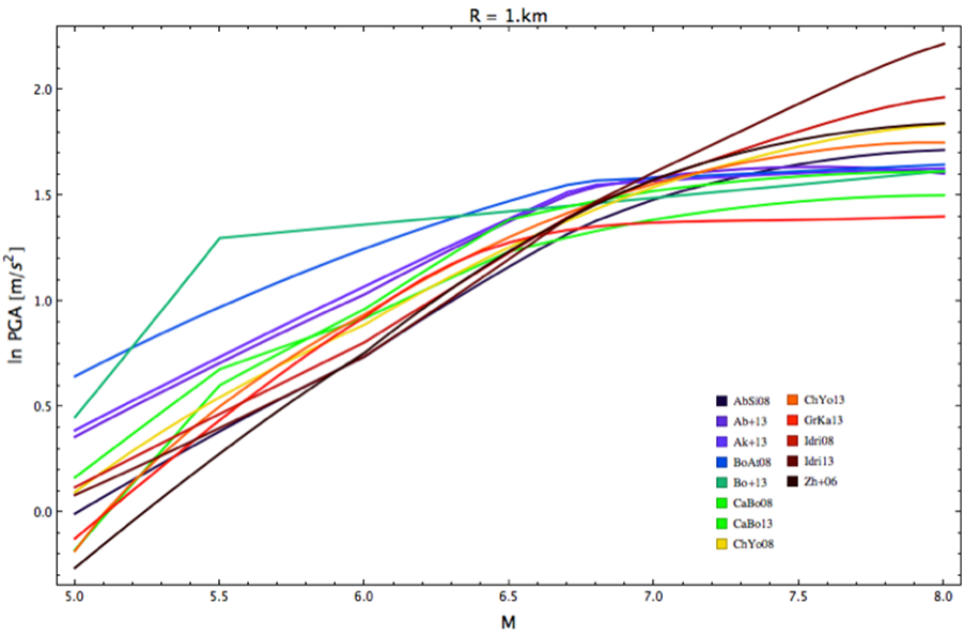

Figure 3.23 PGA scaling in magnitude for WNA GMMs

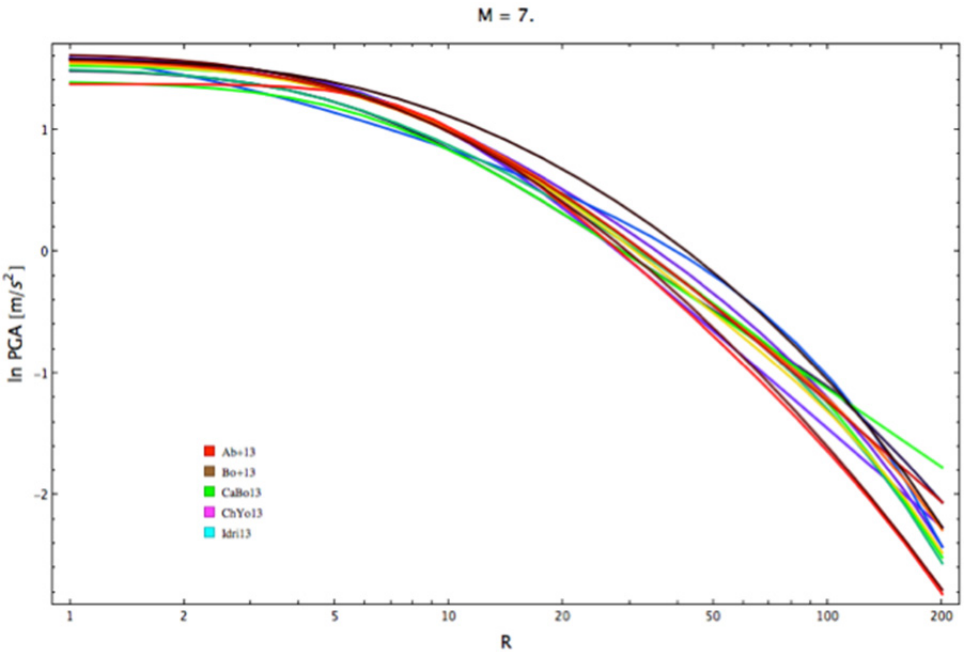

Figure 3.24 PGA scaling in distance for WNA GMMs.

At lower frequencies, it is possible that the variance might be either greater or lesser than that specified for the 10 Hz to PGA range. However, inspection of the plots of variance observed in the developed NGA-East GMMs did not reveal persistent trends in frequency. Moreover, the information upon which the models are based is not very rich for low and high frequencies, nor is the behavior of ground motion inherently better understood in one frequency band than another. Therefore, it is recommended to use the same model of variance for all frequencies.

The maximum value of 0.4 ln units is assigned over all magnitudes at R_{RUP} = 1000 km (and greater), in view of the large spread in GMMs, owing to attenuation sensitivity, at very large distances. Moreover, the maximum value of 0.4 ln units is assigned to **M** ≥ 7.5 events at all distances. Thus, the outer ranges of the variance plot are constrained by the maximum variance value of 0.4, while the inner range is constrained at 0.1 (similar to WNA GMMs at regional distances). For the remainder of the magnitude-distance space, a linear interpolation in [**M**, log(R_{RUP})] space, as shown in Figure 3.25 is performed. The final covariance model is plotted in Figure 3.26.

M,R_{RUP}	4	4.5	5	5.5	6	6.5	7	7.5	8	8.2
1200	0.4	0.4	0.4	0.4	0.4	0.4	0.4	0.4	0.4	0.4
1000	0.4	0.4	0.4	0.4	0.4	0.4	0.4	0.4	0.4	0.4
800	0.327	0.327	0.327	0.342	0.356	0.371	0.385	0.4	0.4	0.4
700	0.283	0.283	0.283	0.307	0.330	0.353	0.377	0.4	0.4	0.4
600	0.233	0.233	0.233	0.266	0.300	0.333	0.367	0.4	0.4	0.4
500	0.173	0.173	0.173	0.218	0.264	0.309	0.355	0.4	0.4	0.4
450	0.139	0.139	0.139	0.191	0.243	0.295	0.348	0.4	0.4	0.4
400	0.1	0.1	0.1	0.16	0.22	0.28	0.34	0.4	0.4	0.4
350	0.1	0.1	0.1	0.16	0.22	0.28	0.34	0.4	0.4	0.4
300	0.1	0.1	0.1	0.16	0.22	0.28	0.34	0.4	0.4	0.4
250	0.1	0.1	0.1	0.16	0.22	0.28	0.34	0.4	0.4	0.4
200	0.1	0.1	0.1	0.160	0.220	0.280	0.340	0.4	0.4	0.4
175	0.109	0.109	0.109	0.167	0.225	0.284	0.342	0.4	0.4	0.4
150	0.119	0.119	0.119	0.175	0.232	0.288	0.344	0.4	0.4	0.4
140	0.124	0.124	0.124	0.179	0.234	0.290	0.345	0.4	0.4	0.4
130	0.129	0.129	0.129	0.183	0.237	0.292	0.346	0.4	0.4	0.4
120	0.134	0.134	0.134	0.187	0.240	0.294	0.347	0.4	0.4	0.4
110	0.140	0.140	0.140	0.192	0.244	0.296	0.348	0.4	0.4	0.4
100	0.146	0.146	0.146	0.197	0.248	0.299	0.349	0.4	0.4	0.4
90	0.153	0.153	0.153	0.203	0.252	0.301	0.351	0.4	0.4	0.4
80	0.161	0.161	0.161	0.209	0.257	0.304	0.352	0.4	0.4	0.4
70	0.170	0.170	0.170	0.216	0.262	0.308	0.354	0.4	0.4	0.4
60	0.180	0.180	0.180	0.224	0.268	0.312	0.356	0.4	0.4	0.4
50	0.193	0.193	0.193	0.234	0.276	0.317	0.359	0.4	0.4	0.4
40	0.207	0.207	0.207	0.246	0.284	0.323	0.361	0.4	0.4	0.4
30	0.227	0.227	0.227	0.261	0.296	0.331	0.365	0.4	0.4	0.4
25	0.239	0.239	0.239	0.271	0.303	0.336	0.368	0.4	0.4	0.4
20	0.254	0.254	0.254	0.283	0.312	0.341	0.371	0.4	0.4	0.4
15	0.273	0.273	0.273	0.298	0.324	0.349	0.375	0.4	0.4	0.4
10	0.3	0.3	0.3	0.325	0.35	0.375	0.4	0.4	0.4	0.4
5	0.3	0.3	0.3	0.325	0.35	0.375	0.4	0.4	0.4	0.4

Figure 3.25 **CENA variance model for high frequencies, 10 Hz to PGA, to express epistemic uncertainty. The highlighted fields are assigned, while others interpolated linearly in magnitude-log distance.**

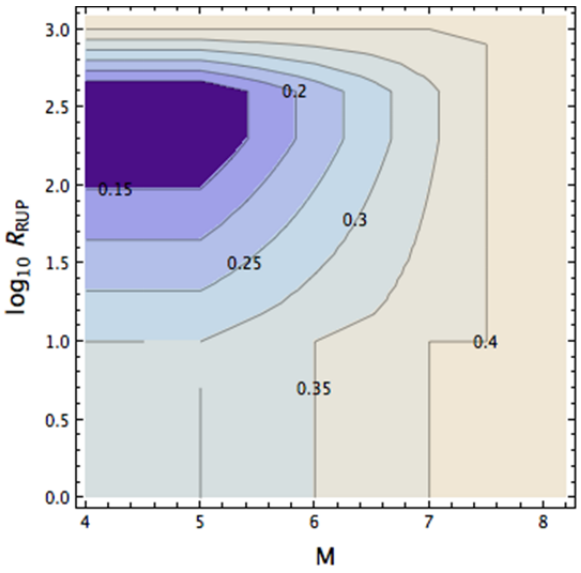

Figure 3.26 Variance model, plotted against M and $\log_{10}R_{RUP}$.

3.2.3 Correlation Model

In this section, the model for non-diagonal entries of the covariance matrix, i.e., the correlation coefficients ρ_{ij} [Equation (3.3)], is developed. As for the diagonal entries, it is possible to calculate the sample covariance—and hence the sample correlation—based on the set of seed models. The sample covariance can be calculated as

$$q_{jk} = \frac{1}{N_S - 1}\sum_{i=1}^{N_S}(y_{ij} - \bar{y}_j)(y_{ik} - \bar{y}_k) \tag{3.8}$$

and from q_{jk} the correlation coefficients ρ_{jk} can be computed. The sample correlation is shown in Figure 3.27, for three (**M**, R_{RUP}) scenarios and f =1 Hz. In each of those plots, the contours show the correlation between all (**M**, R_{RUP}) scenarios, with the reference scenario indicated by a black dot.

It is clear from Figure 3.27 that ground motions from scenarios that are close (in a **M**, R_{RUP} sense) to the reference scenario are highly correlated with ground motions from the reference scenario, whereas those which are farther away in (**M**, R_{RUP}) space are only loosely correlated. Hence, there is clearly structure in the correlation. However, as it was the case for the sample variance, the correlation coefficients do not change smoothly over the full (**M**, R_{RUP}) range due to the finite sample size provided by the seed GMMs; therefore, the approach selected involved modeling the correlation structure.

The modeling for the correlation coefficients is more involved than the one for the diagonal entries of the covariance matrix, requiring that the resulting covariance matrix be positive definite. This constraint can be achieved by modeling the correlation via a function that is a valid covariance function for a Gaussian process [Rasmussen and Williams 2006].

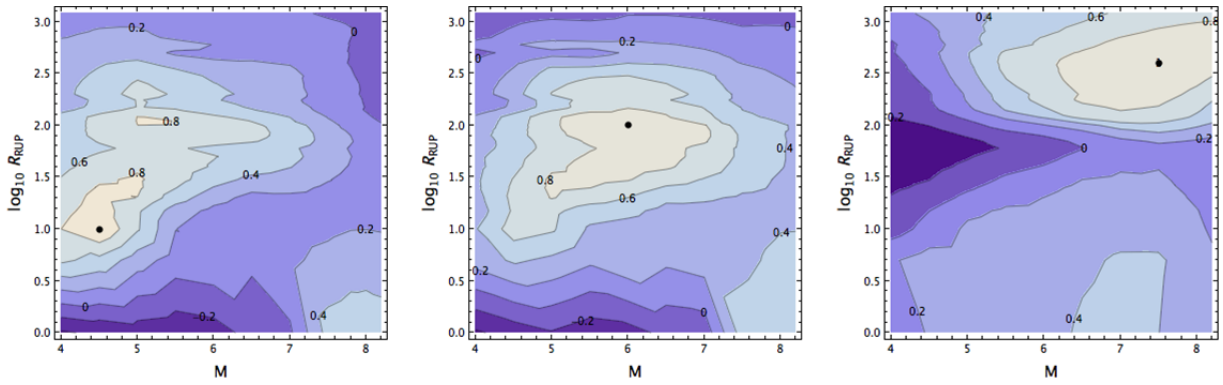

Figure 3.27 Sample correlation coefficients for *f* = 1Hz, plotted against M and $\log_{10}R_{Rup}$: (a) M = 4.5, *R* = 10; (b) M = 6, *R* = 100; and (c) M = 7.5, *R* = 400.

The covariance function that is used to model the correlation between median ground-motion estimates at different (**M**, R_{RUP}) values has the following form:

$$k(\mathbf{x},\mathbf{x}')^T = \theta_1\left[1+(\mathbf{x}-\mathbf{x}')\right]^T \begin{Bmatrix} \theta_2 & 0 \\ 0 & \theta_3 \end{Bmatrix} (\mathbf{x}-\mathbf{x}')/(2\theta_4)^{-\theta_4} + \mathbf{x}^T \begin{Bmatrix} \theta_5 & 0 \\ 0 & \theta_6 \end{Bmatrix} \mathbf{x}' \tag{3.9}$$

where $\mathbf{x} = \{\mathbf{M}, R_{RUP}\}$ is a vector describing the (**M**, R_{RUP}) scenario, and θ_i are parameters of the model that are estimated. This modeling form was selected to provide a compromise between assuming no correlation, i.e., independent expert elicitation for different (**M**, R_{RUP}) scenarios, and assuming full correlation (i.e., a scaled-backbone approach). It therefore allows for the spanning of a range of ground motions similar to that of the scaled backbone approach, while introducing differences in magnitude and distance scaling.

Equation (3.9) consists of two parts: an isotropic part that is a function of the difference $\mathbf{x}-\mathbf{x}'$ and a part that depends on the dot-product $\mathbf{x},\mathbf{x}'$. The isotropic part is called a rational quadratic covariance function and contains four parameters: $\theta_1,\theta_2,\theta_3$, and θ_4. Parameter θ_1 describes the amount of variance described by the rational quadratic part, θ_2 and θ_3 describe the two length-scales relative to magnitude and distance, respectively, and θ_4 describes a mixture of length-scales. The length-scale informally describes how much the correlation is preserved between two different values of the predictor variables (magnitude or distance). For example, considering two scenarios with **M** = 4 and 6: for a small length-scale, the ground motions corresponding to those two scenarios will be less correlated than if the length-scale was larger. If there is only one dimension, the rational-quadratic covariance function becomes:

$$k_{qr}(\mathbf{x},\mathbf{x}') = (1+\frac{r^2}{2L^2\alpha})^{-\alpha} \tag{3.10}$$

where $r = |x-x'|$, and the overall variance term is dropped. Figure 3.28 shows sampled functions from GPs with different length-scales *L*. Here, the covariance function of Equation (3.9) is

evaluated at $x_i \in \{0, 0.1, 0.2, \ldots, 10\}$, which results in a 101×101 dimensional covariance matrix. Then, function values are sampled from a multivariate normal distribution with mean zero and the calculated covariance matrix. These are plotted as functions at the x_i values. As one can see, with increasing length-scale L, the sampled functions become smoother. In other words, L controls the influence of a particular point x_i: the larger L, the larger the correlation at longer distances r. The dropped overall variance parameter controls the (point-wise) variability in the y-direction; a larger overall variance means a larger spread of the sampled function values at one particular x_i .

Figure 3.29 shows the effect of different values for α on the sampled function values. The effect of different values for α is smaller than for the length-scale parameter L. Figure 3.30 shows k_{qr} as a function of the input distance r for different values of L and α.

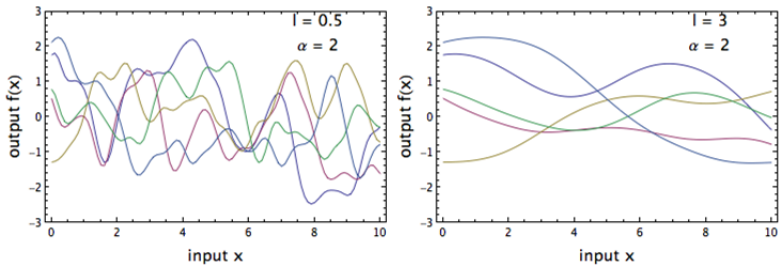

Figure 3.28 **Five sampled functions from a 1D GP with mean zero and rational-quadratic covariance function, for different value of the length-scale *L*.**

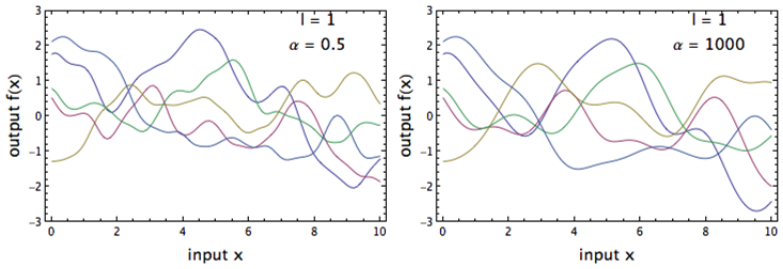

Figure 3.29 **Five sampled functions from a 1D GP with mean zero and rational-quadratic covariance function, for different value of *α* and *L* = 1.**

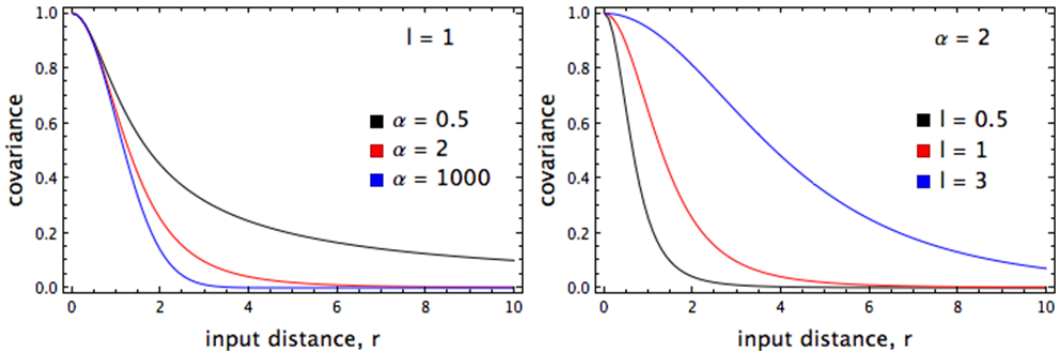

Figure 3.30 **Covariance function as a function of the input distance r=|x−x'|.**

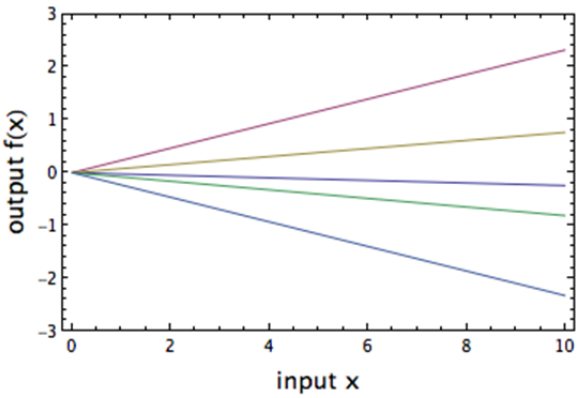

Figure 3.31 Five sampled functions from a GP with mean zero and linear covariance function with $\sigma_{lin}^2 = 0.10$.

The second part of the covariance function is a dot-product term, which models a linear dependence between the inputs and the outputs. This part is not isotropic, which means that the correlation does not depend on the distance between the inputs. For a one-dimensional input x this part reduces to

$$k_{lin}(x, x') = \sigma_{lin}^2 xx' \tag{3.11}$$

Figure 3.31 shows five sampled functions from a GP with linear covariance function. The sampled functions are straight lines, and the parameter σ_{lin}^2 controls the spread of the sampled function values at each x_i. In contrast to the rational quadratic covariance function (which is isotropic), the spread is different at each x_i. It is important to remember that the sampled functions in Figure 3.31 are sampled from a multivariate normal distribution with 101 dimensions; the function values at each x_i are sampled.

The covariance function used in NGA-East is a sum of a rational quadratic part and a linear part. This can be thought of as a superposition of a general linear trend of the function values (i.e., ground-motion values) with magnitude and distance, while the rational quadratic part models any nonlinearities. Parameters θ_2 and θ_3 control the influence of a particular **M** and R value and correspond to the length-scale L in Equation (3.10). Similarly, θ_5 and θ_6 control the possible slopes of the linear functions with **M** and R_{RUP}.

The rational quadratic covariance was chosen because it can be thought of as a mixture of squared exponential covariance functions and thus can accommodate several length-scales (Rasmussen and Williams 2006). The parameters $\theta = \{\theta_1, \ldots, \theta_6\}$ are estimated by maximizing the marginal likelihood $p(\mathbf{y}|\mathbf{X}, \boldsymbol{\theta})$ of the mean estimates of all the seed models (see, e.g., chapter 5 of Rasmussen and Williams [2006]). The marginal likelihood is calculated with Equation (3.6). For numerical stability, the predictors **X** and targets **y** are all standardized, such that they have a mean of zero and a standard deviation of one. Hence, the estimation of the parameters for the correlation model is done in the following way:

1. At the scenarios for NGA-East, calculate the mean of the seed set.

2. Standardize the magnitudes, distances and GM estimates.
3. Calculate K_f for some starting values of the parameters $\boldsymbol{\theta}$.
4. Calculate $\ln p(\mathbf{y}|\mathbf{X},\boldsymbol{\theta})$.
5. Maximize $\ln p(\mathbf{y}|\mathbf{X},\boldsymbol{\theta})\ \ln\left[p(\mathbf{y}|\mathbf{X},\boldsymbol{\theta})\right]$ with respect to $\boldsymbol{\theta}$ and β^2.

Given the estimated parameters $\boldsymbol{\theta}$, one can insert them into Equation (3.9) and calculate a covariance matrix for the (**M**, R_{RUP}) scenarios of interest [or any set of (**M**, R) values]; however, the parameters, in particular θ_1, are optimized to fit the mean of the seed set using a GP with a mean function of zero. Thus, the diagonal entries of the calculated covariance matrix reflect the spread of the estimates across the (**M**, R_{RUP}) scenarios but not across models; however, correlation coefficients can be calculated via Equation (3.3), which reflect the changing of estimates with magnitude and distance. Together with the covariance model, the correlation coefficients estimated in this section are combined to give the full covariance matrix.

3.2.4 Retaining the Scaling and Modeling Assumptions of the Original Seed Models

The selected correlation model is relatively strong (closer to full correlation than to zero correlation), leading to sampled models that do show some variation in their magnitude and distance scaling around the mean function. This behavior is a desired feature of the correlation model because it allows one to easily retain the characteristics of the members of the seed GMMs set. This is shown in Figure 3.32, which shows ten sampled functions each, using three different seed models as mean function. This can be written as:

$$\mathbf{f} \sim N(\boldsymbol{\mu}_S, \Sigma) \tag{3.12}$$

where **f** is a vector of (sampled) ground-motion values at the (**M**, R_{RUP}) scenarios of interest, Σ is the covariance matrix, calculated as described before, at these (**M**, R_{RUP}) scenarios, and $\boldsymbol{\mu}_S$ is a vector containing the estimates of the seed model that is used as the mean function. In each of the three cases, the sampled functions are randomized versions of their respective mean (seed) functions. Hence, this lends itself to an approach of sampling that produces sampled functions that are flexible in their scaling and follow the (point-wise) variance prescribed by the variance model (see Figure 3.16), but whose scaling on the other hand is bound by the original seed models. Basically, the ground-motion distribution P(**Y**) is a mixture distribution:

$$P(\mathbf{Y}) = \sum_{i=1}^{N_S} w_i N(\boldsymbol{\mu}_i, \Sigma) \tag{3.13}$$

where N_S is the number of seed models, and w_i are the weights of the individual seed model that need to sum up to one. Each individual distribution is a multivariate normal distribution with the same covariance matrix and a different mean.

The weights w_i are calculated to ensure that similar seed models do not bias the resulting ground-motion distribution P(**Y**). Such a bias could be introduced if two models are developed using very similar methods and subsets of data. These two models would give very similar

predictions; however, the similarity is not a confirmation that the predictions are more likely to be correct. Therefore, the weight of each seed model is proportional to how similar its predictions are to other models; if two models provide similar estimates, they receive less weight individually. The process of calculating weights for the individual seed models is based on Sammon's maps [1969] (Section 3.3), which provide aggregated information on how similar the estimates are for the seed GMMs. For each frequency, a Sammon's map is calculated for the seed models. The Sammon's map is partitioned into a grid of squares with length 0.25 ln units, and each square that contains a seed model is given the same weight. All models inside each square are given equal weight. The weights are computed by:

$$w_j = \frac{1}{N_{sq}} \frac{1}{N_j} \tag{3.14}$$

where N_{sq} is the number of squares that are occupied, and w_i is the number of seeds in the jth square. For example, if there are six squares that are occupied, and the Ith square contains four seed GMMs, then each of these four seed GMMs gets a weight of 1/24.

An example of the Sammon's map for the seeds, together with the grid that is used for defining clusters of models, is shown in Figure 3.33 for f = 1 Hz.

Figure 3.34 shows the result of sampling from the mixture distribution and compares samples from the mixture distribution in the top row with samples from a distribution where the mean function is the mean of the seed GMMs in the bottom row. In each case, 100 samples are drawn. In the top row, the samples follow the scaling of the individual GMMs, while in the bottom row there is less variability in scaling, due to having only one mean (no mixture distribution). On the other hand, the (point-wise) range covered at each (**M**, R_{RUP}) scenario is similar.

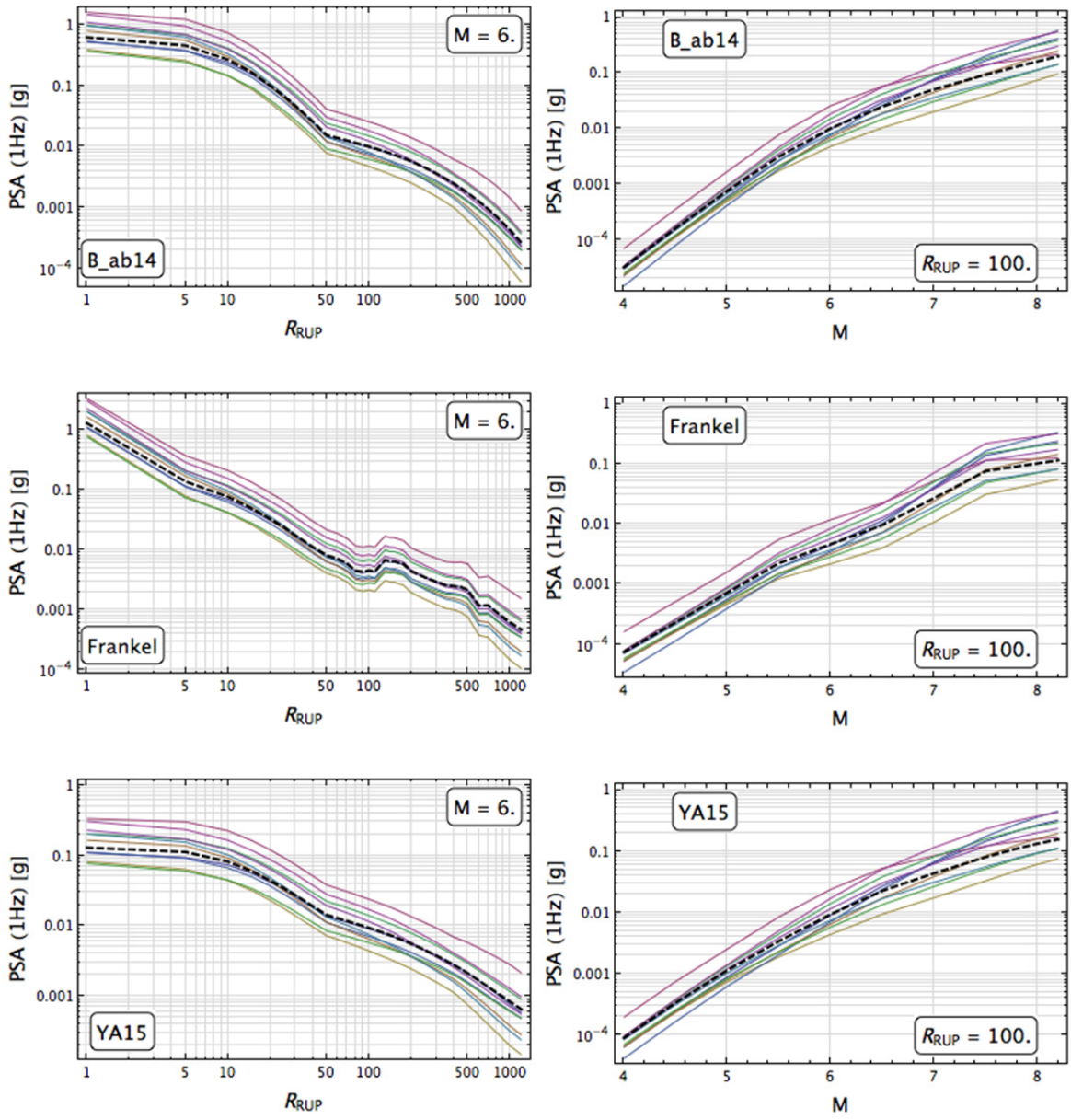

Figure 3.32 **Scaling of 10 sampled models with individual seed GMMs as mean function, for three different seed GMMs. The mean is plotted as a dashed black line.**

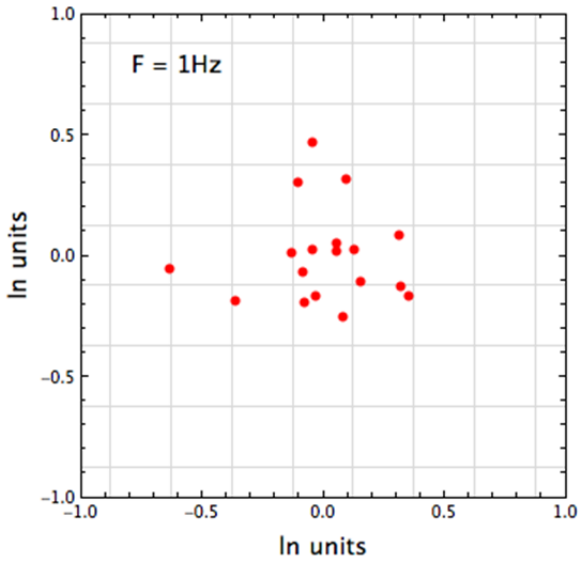

Figure 3.33 **Sammon's map of seed GMMs for 1Hz, together with grid used for calculating weights for the individual seed GMMs.**

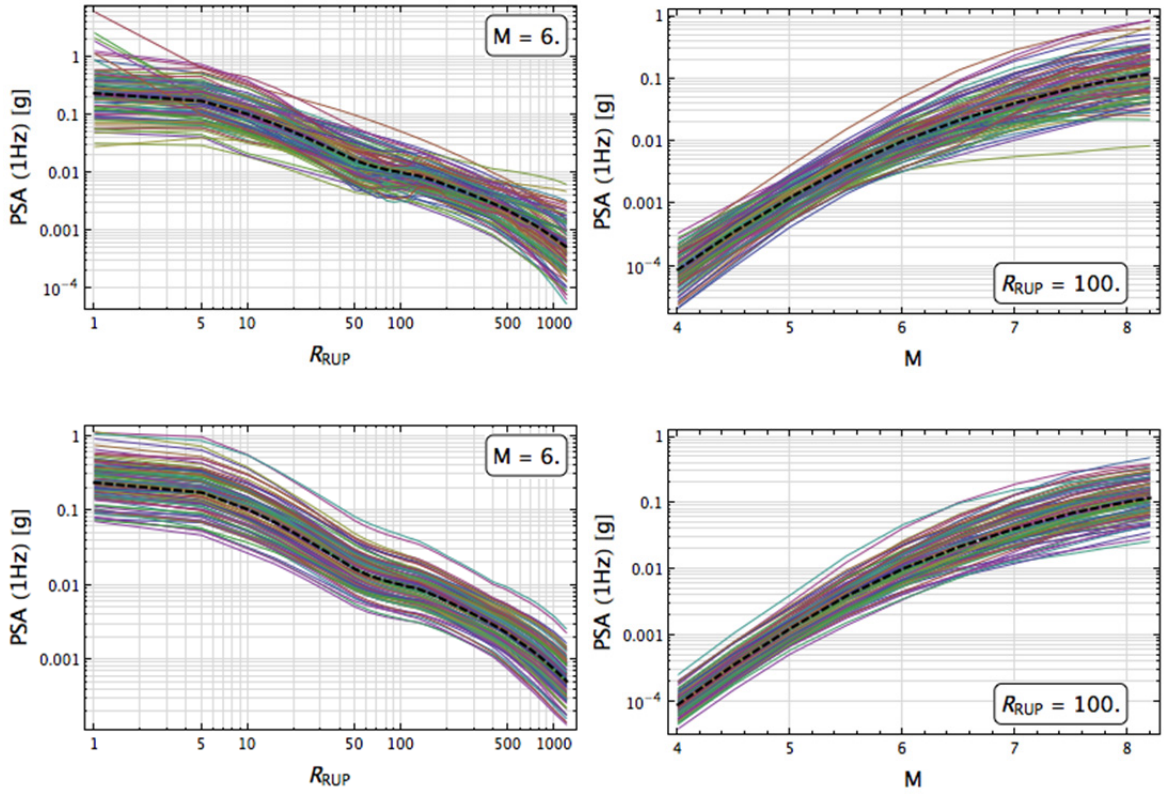

Figure 3.34 **Scaling of 100 sampled models with individual seed GMMs as mean function, for three different seed GMMs. The mean is plotted as a dashed black line.**

3.2.5 Screening Models for Physicality

In Figure 3.34 (top row), 100 sampled functions are shown, which are drawn from the mixture distribution defined in Equation (3.33). Each sample generally follows the respective seed model used to center it at the mean; however, because the samples are drawn from the distribution (correlation coefficients different than 1), there is no guarantee that every sample will exhibit a plausible physical behavior. An example of how an unphysical model could occur would be to draw from a seed model that exhibits a steep scaling with distance; if we were to sample the tail of the distribution for such a model, that sample might exhibit an attenuation so steep as to become unphysical. Such unphysical models must be screened out to prevent bias in the NGA-East GMC model. A set of constraints was defined which a sampled model needs to meet in order to be considered physical. These constraints are based on considerations regarding magnitude and distance scaling, and are defined as follows:

- The ground motion at **M** = 7 must be larger than the ground-motion at **M** = 6, for all distances where $R_{\text{RUP}} \geq 10$ km.
- The ground motion at **M** = 6 must be larger than the ground-motion at **M** = 5, for all distances where $R_{\text{RUP}} \geq 10$ Km.
- The ground-motion distance slope (sl) defined as $sl(R_{\text{RUP1}}, R_{\text{RUP2}}) = y(R_{\text{RUP1}}) - y(R_{\text{RUP2}}) / \ln R_{\text{RUP2}} - \ln R_{\text{RUP1}}$ between distance R_{RUP1} and R_{RUP2}, and must meet the following criteria:
  - sl(10,40)>0.4 (i.e., the distance slope in ground-motions between $R_{\text{RUP}} = 10$ and $R_{\text{RUP}} = 40$ must be larger than 0.4)
  - sl(40,150)>−0.2
  - sl(150,400)>min[0.45,0.9min(GMM)]

The values that are used for the constraints are based on physical considerations and expert judgment by the Project Team, as well as on the range implied by the seed models. The magnitude-scaling constraints are based on the general notion that larger magnitudes should generate larger ground motions, but allows for oversaturation at very large magnitudes, as is inherent in some of the seed models. The distance-scaling constraints allow for increasing ground motions with distance in the intermediate distance range of 40–150 km, related to the Moho bounce effect. Within 40 km and beyond 150 km, the constraints ensure that the scaling of the sampled models is negative with distance, but not too steep. For the slope beyond 150 km, it is assumed that the attenuation with distance must at least have a slope of 0.5, corresponding to the geometrical spreading; however, at some frequencies, some of the seed models do not adhere to these constraints. In those cases, the constraints are adjusted to be larger than the minimum value for the seed GMMs. The minimum slopes of the seed GMMs for the three different distance bins are shown in Figure 3.35. It can be seen that at low frequencies, the minimum slopes of the GMMs are lower than 0.5 for the small and large distance ranges.

Figure 3.35 also shows the minimum difference between estimates at **M** = 7 and **M** = 6 of the seed GMMs. For low frequencies, the differences are large, indicating a strong scaling with magnitude, whereas for higher frequencies the differences are very small, representing almost no scaling. Note that the values in Figure 3.35 are the extreme values obtained from the seed GMMs and do not represent the center or body of their distribution.

Any sampled model that does not meet the physicality criteria is rejected. Hence, the final algorithm to sample new models is as follows:

- Randomly select one of the seed GMMs using the weights defined in Equation (3.14)
- Sample from a multivariate normal distribution defined by a combination of the seed GMM (mean) and the covariance model.
- Check if sample passes criteria for physicality.
- If yes, proceed to step 4
- If no, go to step 1
- Add sample to list of sampled models.

This is repeated until a predefined number of physical samples are drawn. For NGA-East, the number of samples is set to 10,000.

Figure 3.36 shows the number of samples that fail the criteria for physicality at each frequency. For low frequencies, most samples are rejected due to a failure to meet the constraint on distance scaling, whereas for higher frequencies rejection is due to magnitude scaling. This is consistent with Figure 3.35, which shows that the minimum slopes of the seed GMMs are close to the constraint at low frequencies. For high frequencies, the minimum magnitude-scaling ratios of the seed GMMs are close to their respective constraint (Figure 3.35).

Figure 3.37 shows the number of samples, based on each seed model, in the final set of 10,000 sampled models, for f = 1 Hz. The weights defined in Equation (3.14) and Figure 3.33 lead to large differences in the number of models based on a specific seed. When models produce similar ground motions, they collectively share a weight. Models with fewer samples are also sometimes tied to the physicality constraints. An example of this is the PZCT_M2ES model, which contributes fewer samples. For this model, the distance scaling from 150 to 400 km is relatively flat and close to the physical constraint [$sl(150,400)_{PZCT\_M2ES} = 0.504$], leading to more rejections of (flatter) variants based on that model.

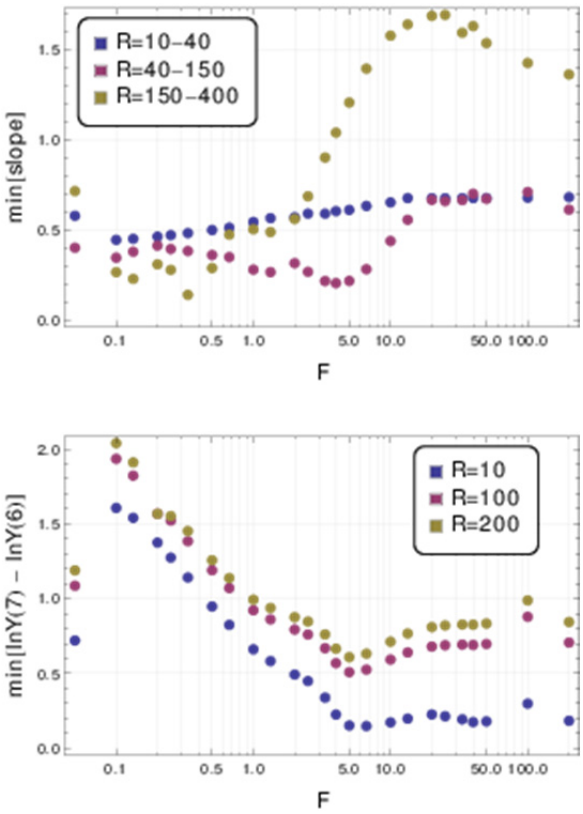

Figure 3.35 **Minimum distance slopes (left) and magnitude ratios (right) from seed GMMs.**

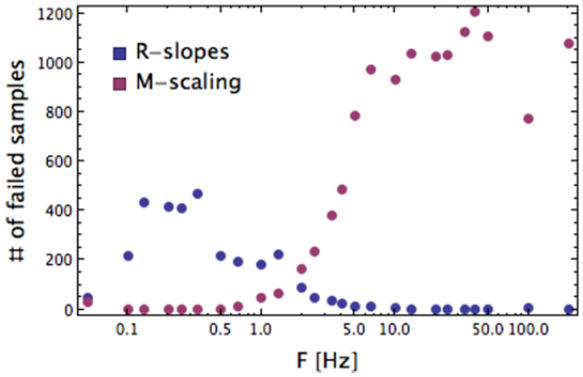

Figure 3.36 **Number of rejected models due to failing the constraints on either magnitude scaling or distance slopes, for the generation of 10,000 models.**

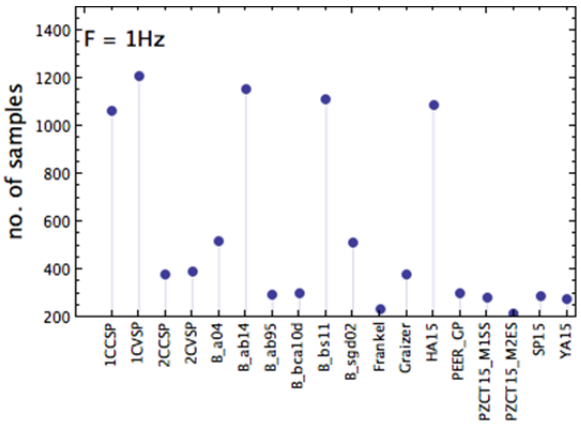

Figure 3.37 Number of samples using the different seed GMMs as mean function, for *f* = 1 Hz.

3.2.6 Discussion of the NGA-East Approach to Develop Continuous Distributions of GMM Median Predictions

The NGA-East approach is distinctly different from a scaled-backbone approach in many respects. As it was mentioned earlier, differences in scaling with magnitude and distance are captured with the NGA-East approach, whereas all the curves are parallel with the typical scaled-backbone concept. Another difference is that a "high" GMM, corresponding to the 95th percentile ground motions for a given (**M**, R_{RUP}) scenario, may not be classified as "high" for other scenarios that are far removed in magnitude-distance space. For example, when sampling 10,000 models from the NGA-East distribution, with the mean of the seed set as the mean, no single model is among the largest 500 models at all 374 (**M**, R_{RUP}) scenarios considered for NGA-East. This needs to be considered when selecting models and/or discretizing the distribution.

3.3 VISUALIZATION OF THE GROUND-MOTION SPACE

3.3.1 Challenges in Evaluation of Multiple GMMs

Whether hazard analysts choose to use different GMMs or a scaled-backbone approach, they are still faced with the task of assessing the center, body and range of epistemic uncertainty. Scherbaum et al. [2010] proposed using high-dimensional visualization techniques to provide a graphical representation of this uncertainty. They used tools such as self-organizing maps (SOMs) [Kohonen 2001] and Sammon's maps [1969] to project GMMs onto a two-dimensional map, which can be thought of as a two-dimensional projection of the GMM model space. Ultimately, the full, multidimensional GMM model space is the space upon which the assessment of center, body, and range should be based on.

High-dimensional visualization tools are a natural choice to compare different GMMs. This is illustrated in Figure 3.38 and it is closely related to the use of an ensemble of GMMs [Atkinson et al. 2014]. In Figure 3.38a, the estimates of the 18 candidate GMMs for one particular scenario are shown as a histogram, for f = 1 Hz. (There are a total of 19 seed GMMs; PEER_EX is used only above 2 Hz.)

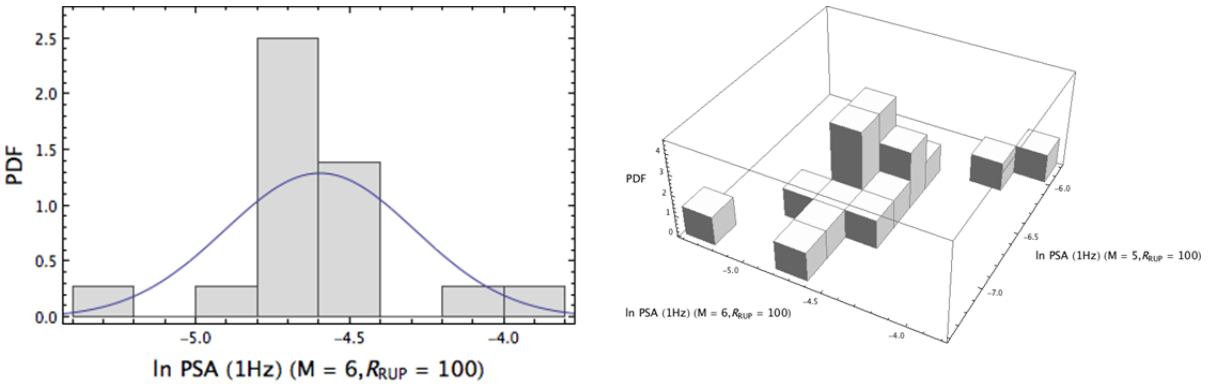

(a) (b)

Figure 3.38 Histogram of estimates of 18 GMMs, for one scenario (left) and two scenarios (right).

Since there are 18 discrete GMMs, there are 18 discrete median ground-motion estimates. However, as discussed previously, there should be a continuous distribution of estimates. The intermediate values are also likely valid, they are simply not generated with the given models. For a single scenario (one dimension) one can fit a continuous distribution to the estimates (in Figure 3.38 the best fitting normal distribution is shown) and evaluate the estimates and the continuous model graphically. Going to two scenarios, this is still possible, as shown in Figure 3.38b. For more than three scenarios, the simultaneous (graphical) evaluation of different GMMs becomes almost impossible. This poses a problem, because an assessment of the models and their corresponding continuous distribution is required for many different (**M**, R_{RUP}) scenarios [such as those sampled by probabilistic seismic hazard analysis (PSHA)].

For the single scenario case, the problem is easy: the difference between the GMMs is simply the difference between their estimates. If one keeps all predictor variables fixed and changes only the distance, one can plot the ground motion estimates versus distance. In that case, it is possible to distinguish trends and differences in distance scaling if only a few GMMs are evaluated. With an increasing number of GMMs, it becomes more difficult to assess differences between GMMs. As an example, Figure 3.39 shows the magnitude and distance scaling of the 18 aforementioned GMMs. Although the range in ground motions can be assessed, it is difficult to distinguish differences between individual models. A systematic evaluation would require plotting all the combinations of only two models at a time for one particular magnitude or distance, leading to a large number of plots. Even more plots are needed to compare the models at other magnitudes and distances.

To capture the center, body, and range of median GMM estimates, it is necessary to assess the similarity of GMMs over a wide range of magnitudes and distances that are relevant to the hazard at the site. Projecting the GMMs into two dimensions is a convenient way to achieve this. Basically, the GMMs are mapped onto a projection that allows them to be assessed *visually*.

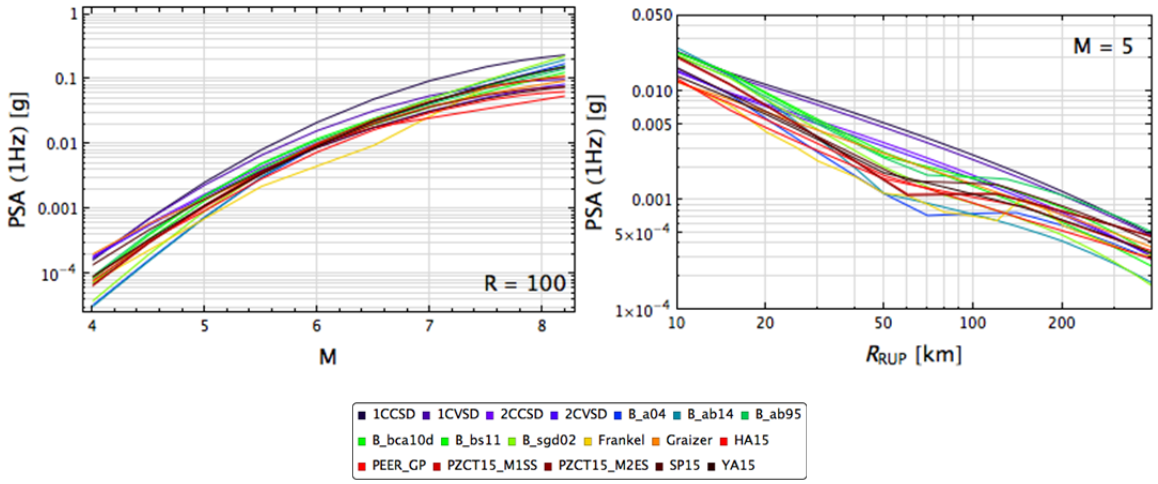

Figure 3.39 Magnitude and distance scaling for 18 GMMs used in this example.

The basic idea is that GMMs "live" in some abstract model space. This space can be thought of as the space of all the possible functions of magnitude and distance. The GMMs form a subspace associated the physically realizable instances of this function space. The basic assumption is that the GMMs occupy a lower dimensional manifold in the larger model space. If this manifold is two-dimensional, it is possible to plot it on a map and it is then easy to visualize.

The assessment of the model space involves the following assumptions:

- The median estimate from a GMM is a function.
- By evaluating the GMM at certain values of its predictor variables [(**M**, R_{RUP}) scenarios], it is discretized.
- If the GMM is evaluated at N_D different values of its predictor variables, it can be represented as an N_D -dimensional vector of ground-motions, one entry for each (**M**, R_{RUP}) pair.
- Each GMM is evaluated at the same N_D values of the predictor variables. This means that each GMM corresponds to a point in the N_D-dimensional ground-motion space. This is an approximation of the GMM model space.
- The N_D -dimensional space can be projected to two dimensions.

There are several different methods to project high-dimensional data onto a lower-dimensional space, such as those such as described in Hotelling [1933], Gianniotis and Riggelsen [2013], and Lawrence [2004]. Scherbaum et al. [2010] used SOMs [Kohonen 2001] and Sammon's mapping [1969]. NGA-East uses Sammon's mapping, which is described in the following sub-section. It is a relatively simple method, and in contrast to SOMs, it works on a continuous scale.

3.3.2 Introduction to Sammon's Maps

Sammon's mapping is a nonlinear dimensional reduction technique. In Sammon's mapping, a configuration of points in two dimensions is sought that resembles the distance distribution in high dimensions. In this case, distance describes the difference between coordinates (i.e., between their median estimates), and is not a physical distance like R_{JB} or R_{RUP}. Throughout this report, the term GMM-distance or $\overline{\Delta_{GM}}$ is used to describe differences between GMMs in ground-motion space. The misfit function is the difference between the GMM-distances in high dimensions and two dimensions (which is called Sammon's stress):

$$E = \frac{1}{\sum_{i<j} \overline{\Delta_{GM\,ij}}} \sum_{i<j} \frac{(\overline{\Delta_{GM\,ij}} - \overline{\Delta_{map\,ij}})^2}{\overline{\Delta_{GM\,ij}}} \tag{3.15}$$

where $\overline{\Delta_{GM\,ij}}$ is the GMM-distance between GMMs i and j in high-dimensions, and $\overline{\Delta_{map\,ij}}$ is the corresponding shortest distance on the map (in two dimensions), respectively. $\overline{\Delta_{map}}$ is the shortest path between two points on the map, which is the Euclidean distance in two dimensions. To produce a two-dimensional projection, E is minimized with respect to the positions in two dimensions through an iterative process, e.g., via gradient descent. As a starting configuration, a random set of points on the map can be used. Another common choice is to use the output of principal component analysis (PCA) as a starting configuration.

From the description of Sammon's mapping, one can appreciate that only the relative positions of GMMs on the map are important. The absolute coordinates depend on the starting configuration of the points on the map. On the other hand, relative positions and mapped GMM-distances do have a meaning; they correspond to the relative positions in high dimensions. They can be rotated and/or mirrored without changing the $\overline{\Delta_{map\,ij}}$.

Sammon's Map Conceptual Examples

A real-life analogy to this concept can be made by considering the geographical distribution of three cities. For example, the distance between San Francisco and Los Angeles is 552 km, the distance between San Francisco and Las Vegas is 662 km, and Los Angeles is 377 km away from Las Vegas. This is sufficient information to infer the relative geometry of those three cities on a map; however, it does not tell us which of the cities is the northernmost. For some applications, like estimating the cost of jet fuel, this can be all that is needed. If proper orientation is needed, the map can be mirrored and rotated without affecting the distances between the cities.

The following example is similar in spirit to the situation of comparing GMMs, but the map can be evaluated intuitively. We show an example visualization that exemplifies the power of high-dimensionalization tools. Figure 3.40 shows 18 pictures of rubber ducks as an intuitive example borrowed from Geusebroek et al. [2005]. The rubber ducks in the 18 individual pictures show the same duck, each time rotated by 20°. Each of the pictures is a grid of 32×32 pixels, and each pixel is associated with a red, green, and blue value. Hence, each picture can be represented by a 3072-dimensional vector, so each picture is a point in a 3072-dimensional "rubber duck"-

space. The analogy to the situation for a GMM is that each pixel corresponds to a particular magnitude/distance scenario. Figure 3.41 shows a Sammon's map calculated for the 18 pictures of the ducks. The map is easily interpretable: pictures that are close (one rotation apart) are close on the map. Hence, Figure 3.41 shows the potential of using visualization techniques to reveal structure in a high-dimensional dataset.

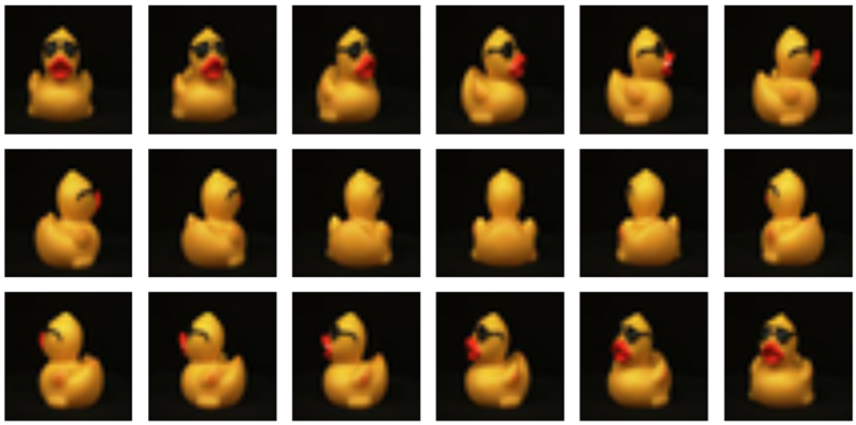

Figure 3.40 Pictures of rotated rubber ducks.

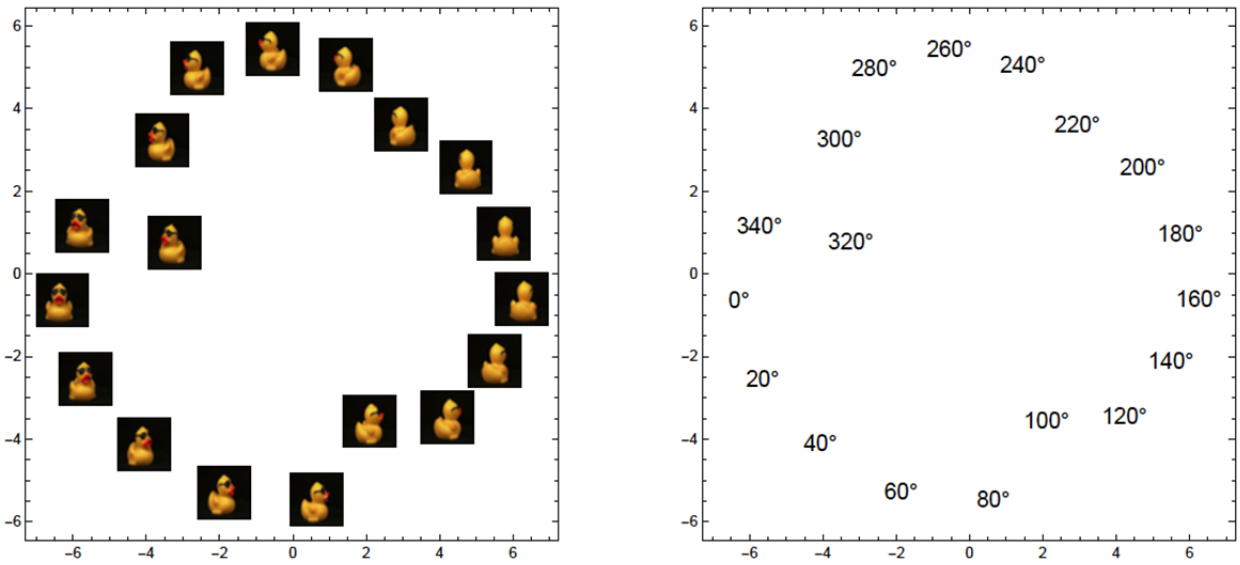

(a) (b)

Figure 3.41 (a) Sammon map of "rubber duck" space, with insets of pictures; and (b) same map, but with rotation angle of each picture at the respective coordinate.

Sammon's Maps or Ground-Motion Models.

In a Sammon's map for GMMs, the map distances correspond to high-dimensional GMM-distances, which have the same units as the ground-motion estimates themselves. As described earlier, the high-dimensional coordinates of a GMM correspond to its estimates at different values of the predictor variables. Hence, GMM-distances in high dimensions can be easily calculated from the differences in their estimates. There are, however, various GMM-distance metrics that one can use. As discussed in Scherbaum et al. [2010], the (symmetric) Kullback-Leibler divergence can be used to calculate differences between GMMs as a distribution. On the other hand, the median estimates and variability of a GMM are often separated in a PSHA. Therefore, when focusing on differences in median GMM estimates, it makes sense to use a GMM-distance metric that is tailored to this problem. For NGA-East, the Euclidean distance between two GMMs is used, which is based on the L_2-norm:

$$\overline{\Delta_{GM\,ij}}(L_2) = \sqrt{\frac{1}{N_D}\sum_{k}^{N_D}(GMM_{ik} - GMM_{jk})^2} \tag{3.16}$$

where k indexes the different values of the predictor variables, N is the number of dimensions, $\overline{\Delta_{GM\,ij}}(L_2)$ is the L_2-distance between GMMs i and j, and GMM_{ik} is the ground-motion prediction of the ith GMM corresponding to the kth predictor variable combination. The difference $\mathrm{GMM}_{ik} - \mathrm{GMM}_{jk}$ between two GMMs is illustrated in Figure 3.42. The factor $\sqrt{1/N_D}$ in the definition of the L_2-distance is there to normalize the GMM-distance so that it has units of ground motions and can be more easily interpreted.

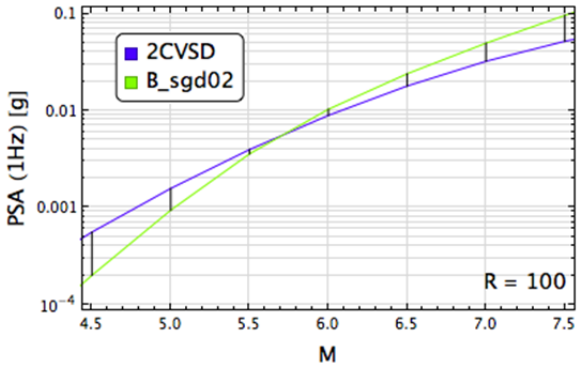

Figure 3.42 **Differences between two GMMs at different M-distance values, which go into the calculation of the (high-dimensional) distance $\overline{\Delta_{GMij}}$ between GMMs *i* and *j*.**

The Sammon's map for the 18 NGA-East GMMs (same ones that are shown in Figures 3.38 and 3.39) can then be generated. The input to the Sammon's map are the median prediction for PSA at a frequency of f = 1 Hz for magnitudes **M** =4.5, 5.,…,7.5 and distances R_{RUP} = 10, 20,…, 400 km. (This example has a different range than the one defined for the final computations.) Because each GMM is evaluated at 161 (**M**, R_{RUP}) scenarios, it can be

represented as a point in 161-dimensional ground-motion space, where each coordinate corresponds to the prediction for one particular magnitude/distance pair. Under the assumption that physically plausible GMMs reside on a two-dimensional manifold (i.e., a surface that is locally flat), we can estimate this manifold using Sammon's maps.

To facilitate interpretation of the map, reference models are added to the set of 18 GMMs:

- the arithmetic average of all model predictions (log-space), hereafter called the *mix*
- scaled versions of the average model: $mix+\ln\alpha$, with α = 0.67,0.8,1.25,1.5, called S−−, S−, S+, S++
- the average model with changed magnitude scaling: $mix + \beta(\mathbf{M}-6)$, with β =−0.4,−0.2, 0.2, and 0.4, called **M**−−, **M**−, **M**+, and **M**++
- the average model with changed distance scaling: $mix + \gamma(\ln R - \ln 100)$, with γ =−0.5,−0.25, 0.25, and 0.5, called *R*−−, *R*−, *R*+, *R*++

The scaling of these reference models is shown in Figure 3.43. The reference models can also be used to orient the maps in a consistent way. Figure 3.44 shows the following adjustments: the map is centered with the *mix* model at the point {0, 0}, the map is then rotated so that the model S++ is to the right and the line from S−− to S++ is horizontal. In a last step, the map is mirrored about the y-axis such that the **M**++ model is in the upper half of the model.

In general, the reference models help the interpretation of directions in which GMMs change in a systematic way. Because the different reference models (up/down-scaled, changed magnitude scaling, changed distance scaling) align in different directions, they allow a quick assessment of differences between GMMs over a wide magnitude/distance range–the range that was used to generate the map–in a qualitative manner. In particular, the three Boore models that have a distance scaling proportional to $R^{-1.3}$ line up in the upper half of the map, where also the reference model with *R*−− resides, which has a steeper attenuation.

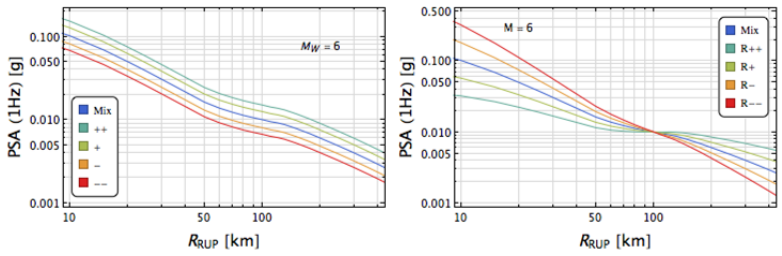

Figure 3.43 Difference in scaling of reference models that help the interpretation of the Sammon's maps.

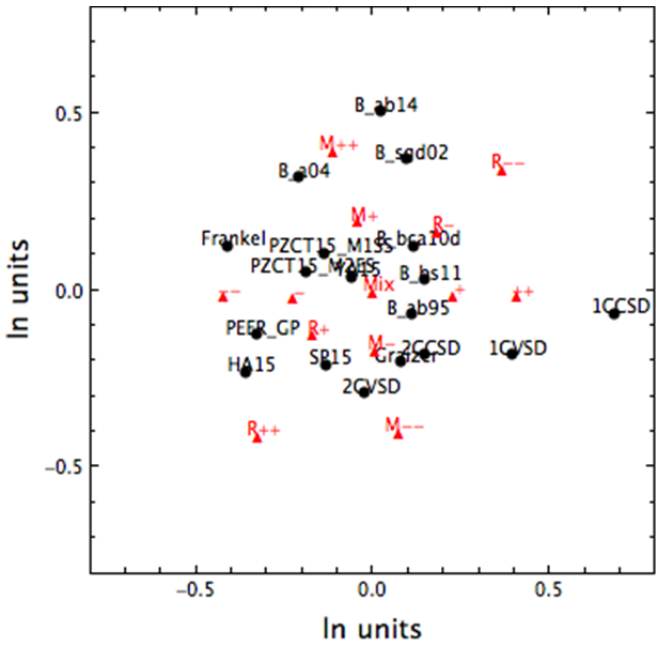

Figure 3.44 **Sample 1 Hz Sammon's map for 18 GMMs, together with reference models. GMM-distances in high dimensions are calculated using the L_2-distance.**

3.4 APPLICATION OF SAMMON'S MAPS TO DISTRIBUTION OF SAMPLED GMMS

For the NGA-East application, a suite of 10,000 models are projected onto Sammon's maps (one map per frequency) and used as a visual aid for the subsequent steps. These models are sampled from the mixture model defined in Equation 3-13. Figure 3.45 shows the magnitude and distance scaling of a subset of 200 sampled models, for $f = 1$ Hz. Even for this small subset of models, it is inconceivable to assess the center, body, and range by comparing the 200 samples based on scaling plots. However, there is structure in the high-dimensional ground-motion space that these models occupy. Each model is sampled at the 374 (**M**, R) scenarios, representing a point in a 374-dimensional (ground-motion) space, where each coordinate is the prediction at one particular (**M**, R_{RUP}) pair. In Figure 3.46, a three-dimensional subspace is plotted (three dimensions can be plotted), for {**M**, R_{RUP}} = {4, 10}, {**M**, R_{RUP}} = {5, 100}, and {**M**, R_{RUP}} = {7,400}. Each of the 10,000 sampled models is a point in this three-dimensional space and is plotted as a gray point. In addition, the 18 seed GMMs are plotted as red dots.

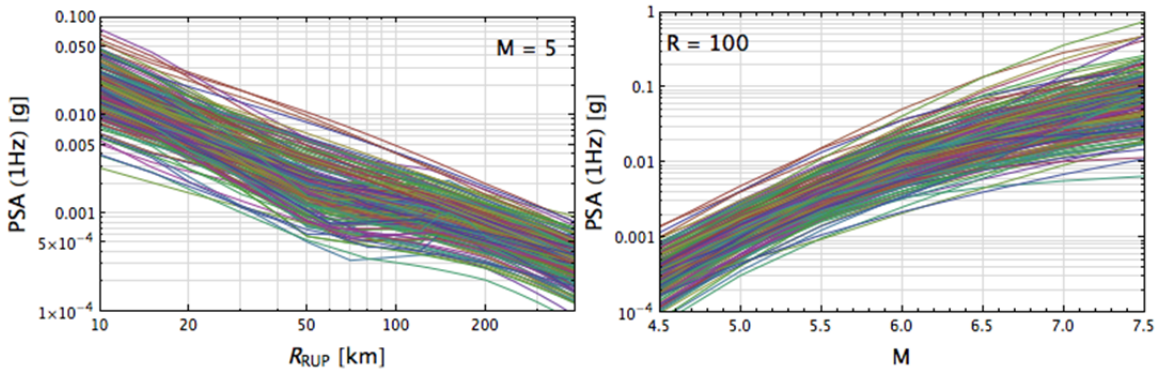

Figure 3.45 Distance and magnitude scaling for 200 sampled GMMs.

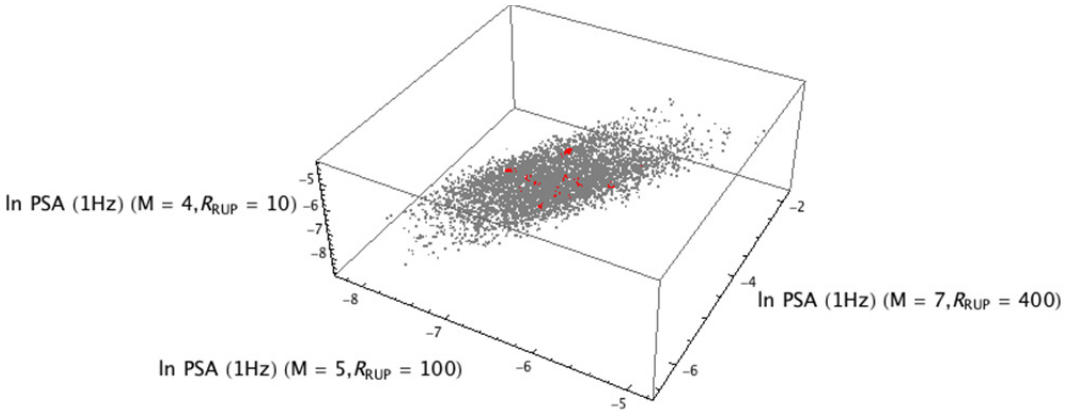

Figure 3.46 Three-dimensional ground-motion space, NGA-East correlation model, for 5000 sampled models (gray points) and the 18 seed GMMs (red points). The models form a plane (with non-zero thickness).

As shown in Figure 3.46, the sampled models and the 18 seed GMMs lie approximately on a plane in the three-dimensional ground-motion space, although this plane is not oriented in a clear way relative to the axes. However, Figure 3.46 also shows that there is structure in the ground-motion space; i.e., there is a two-dimensional manifold (plane) on which the sampled models lie, and thus the idea of using Sammon's mapping to visualize the models in two dimensions makes sense. By contrast, samples from a distribution where the correlation coefficients are zero ($\rho_{jk} = 0$) form a sphere in the three-dimensional ground-motion space (Figure 3.47); hence, they cannot be represented in two dimensions. On the other hand, samples from a scaled backbone model $\left(\rho_{jk} = 1\right)$) form 18 straight lines in ground-motion space, one for each model (Figure 3.48). In this context, because the NGA-East covariance is a compromise between the no-correlation and full-correlation distributions, the models reside on an intermediate high-dimensional shape. Hence, the plane from Figure 3.46 cuts the sphere $\left(\rho_{jk} = 0\right)$ and contains the straight lines $\left(\rho_{jk} = 1\right)$.

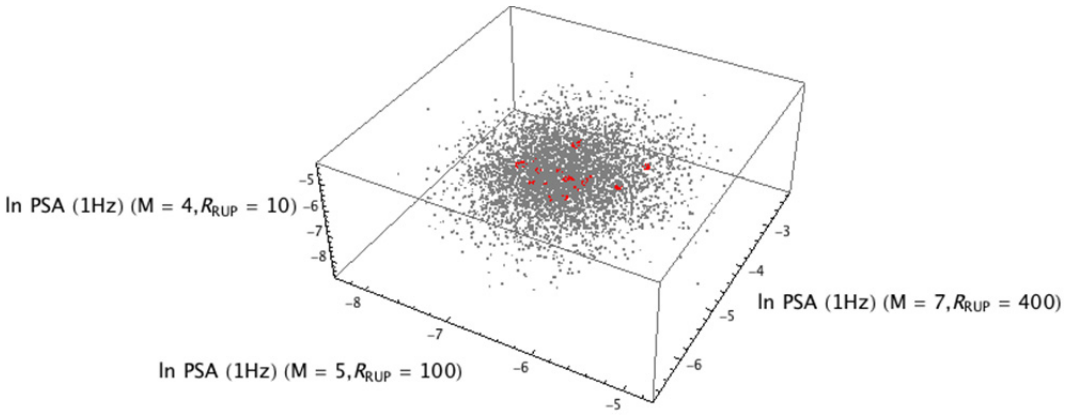

Figure 3.47 **Three-dimensional ground-motion space, no correlation, for 5000 sampled models (gray points) and the 18 seed GMMs (red points). The models form a sphere.**

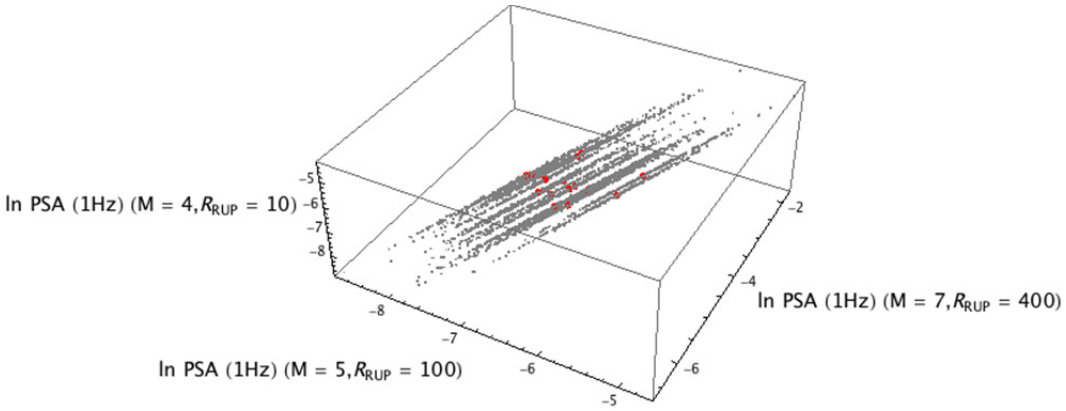

Figure 3.48 **Three-dimensional ground-motion space, full correlation, for 5000 sampled models (gray points) and the 18 seed GMMs (red points). The models reside on sets of lines.**

Capitalizing on the fact that there is structure in the ground-motion space, the 10,000 sampled models per frequency are projected to two dimensions using Sammon's mapping. For the NGA-East Project, the (**M**, R_{RUP}) scenarios considered for the Sammon's maps analyses are

- **M** = 4, 4.5, 5, 5.5, 6, 6.5, 7, 7.5, 7.8, and 8
- R_{RUP} = 0, 1, 5, 10, 20, 30, 40, 50, 70, 100, 130, 150, 200, 300, 400, 500, 600, 700, 800, 1000, 1200, and 1500

Hence, there are in total 210 (**M**, R_{RUP}) scenarios, at which the seed GMMs are considered, and the sampled models are drawn. This is a smaller subset than was considered for the generation of new models. This range comprises the bulk of hazard-relevant scenarios.

In addition to the 10,000 sampled models, the seed GMMs are also used to calculate the Sammon's maps. Three reference models are also added to this set: the mean of the seed GMMs, and the mean up and down-scaled by a factor of two. These reference models align on a straight line on the map (see Figure 3.44) and are used to orient the maps in the same way across

frequencies. The basic strategy for generating Sammon's maps that are comparable across frequencies is as follows:

1. For the set of selected models (sampled models, seed models, and reference models), select the ground-motion estimates at the defined relevant (**M**, R_{RUP}) scenarios.
2. Calculate GMM-distance or $\overline{\Delta_{GM}}$ between all models based on Equation (3.16).
3. Calculate Sammon's map, with PCA as the starting configuration.
4. Shift the resulting points in two dimensions such that the mean is at {0, 0}.
5. Rotate the resulting points such that the up/down-scaled mean models align horizontally (parallel to the *x*-axis); the rotation is carried out such that the up-scaled model has a larger *x*-value.
6. Mirror the resulting coordinates such that the "SP15" seed GMM has a positive *y*-value.

The last three steps are taken to ensure that the maps are comparable for different frequencies. (The map only preserves GMM distances; therefore, its orientation has no meaning.) The choice of the "SP15" seed GMM as a reference to orient the map vertically is because it has a distance and magnitude scaling that are consistently different from the mean scaling, so its coordinates on the map are consistently away from the origin on the *y*-axis.

As-is and rotated/mirrored maps are shown in Figure 3.49 for three different frequencies. The rotation and mirroring ensures that the up/down-scaled reference models are always at the same place for each frequency. Since models that are close in the high-dimensional space are close on the map, this means that sub-regions on the map can be traced across frequencies. This encourages the generation of smoother spectra. Additionally, Figure 3.49 shows that with increasing frequency, the distribution of samples in two dimensions becomes less like a circle and more like an ellipse. The reason for this is seen in Figure 3.50, where the variances of the seed models with respect to magnitude and distance scaling are shown. With increasing frequency, the variance of the magnitude scaling decreases, whereas in comparison the variance of the distance scaling stays relatively constant. Because differences in scaling are manifested in the *y*-direction on the map, the lower variance in magnitude scaling in the seed models for high frequencies leads to a lower variance in the sampled models and thus a lower variance in the y-direction on the map.

The up/down-scaled models in the rotated maps (see Figure 3.49a) have *x*-coordinates that are close to ln(2) = 0.693, which is the factor by which they are scaled. Hence, the maps can adequately capture the ground-motion distances in high-dimensional ground-motion space in two dimensions. The distribution of black points (corresponding to the seed GMMs) in the map for *f* = 1 Hz (see Figure 3.49b) is very similar to the corresponding Figure 3.44, which shows a map of the same seed models, but without the sampled set (gray points) and a slightly different ground-motion space.

Overall, the sampled set of GMMs captures the seed models on the maps and covers a continuous region in two dimensions. Thus, the conclusion is that the map is a reasonable representation of the continuous distribution of $P(\mathbf{Y})$.

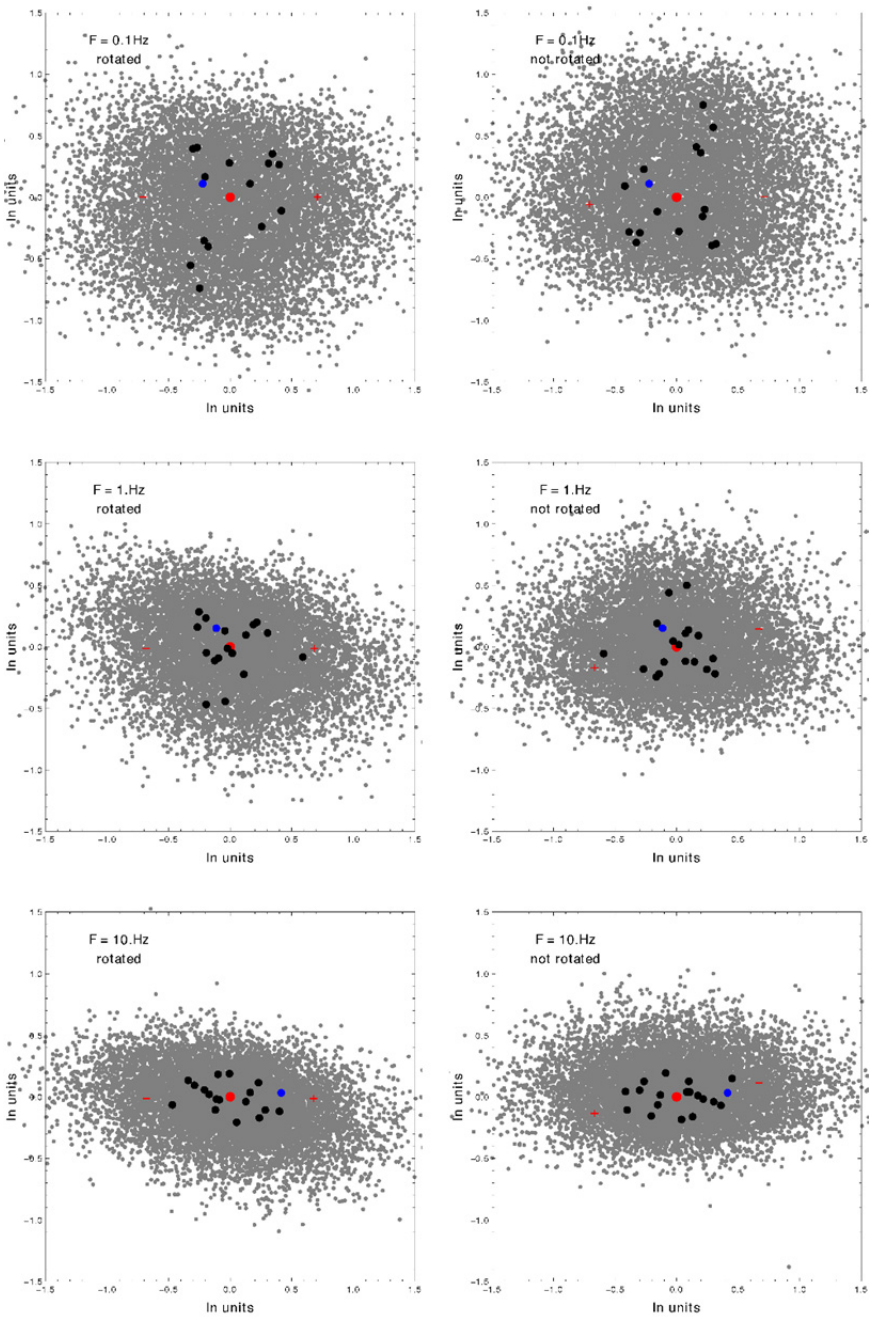

(a) (b)

Figure 3.49 **Sammon's maps for three different frequencies and 10,000 sampled models (gray points): (a) non-rotated and (b) rotated. The mean model is plotted as a red dot, the up/down-scaled models are plotted as + and −, respectively. The seed models are plotted as black dots. The reference model "SP15" is plotted as a blue dot.**

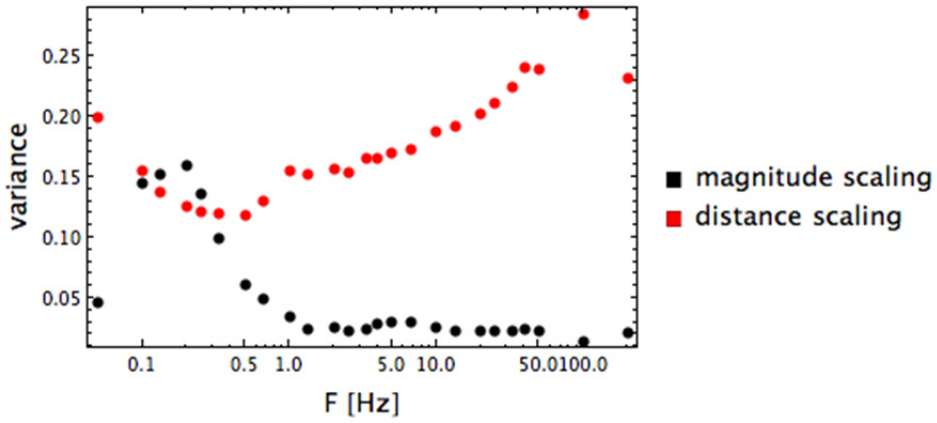

Figure 3.50 **Variance of magnitude and distance scaling of the seed GMMs. The magnitude scaling is approximated by the difference between estimates of the seed models at M = 7 and M = 6 for R_{RUP} = 10 km. The distance scaling is approximated by the difference in between estimates at R_{RUP} = 10 km and R_{RUP} = 40 km for M = 6.**

3.5 DISCRETIZATION OF GROUND-MOTION SPACE

3.5.1 Definition of Range in Ground-Motion Space

In the previous section, the visualization of the sampled models from the continuous ground-motion distribution $P(\mathbf{Y})$ was presented. This results in Sammon's maps, one for each frequency, which are a representation of the high-dimensional ground-motion model space. Hence, the center, body and range of $P(\mathbf{Y})$, which corresponds to the center, body, and range of epistemic uncertainty associated with median ground-motion estimates, can be defined on the map, i.e., in two dimensions. The definition of the range is done similar to a 1D distribution; in that case, often a range of $\pm 2\sigma$ is chosen (in the case of a normal distribution). Such a range covers 95.45% of the total probability of a normal distribution:

$$\int_{-2}^{2} N(x;\mu=0,\sigma=1)\,dx = 0.9545 \tag{3.17}$$

However, the Sammon's maps represent a two-dimensional distribution. Based on the definition of a two-dimensional normal distribution and the distribution of the sampled models (gray points in Figure 3.49), an ellipse was selected to represent the range on the map. The half-axes of the ellipses are determined by the standard deviations of the distribution of points in x- and y-direction. These are calculated and then scaled by a factor α = 2.273. Using this factor, an ellipse in two dimensions covers 95.45% of the total probability of a two-dimensional normal distribution. The ellipse is centered on the point {0,0}, which corresponds to the mean of the seed GMMs. Figure 3.51 shows the ellipse defining the range for two frequencies. This range covers a large portion of the map, and thus also in the ground-motion model space.

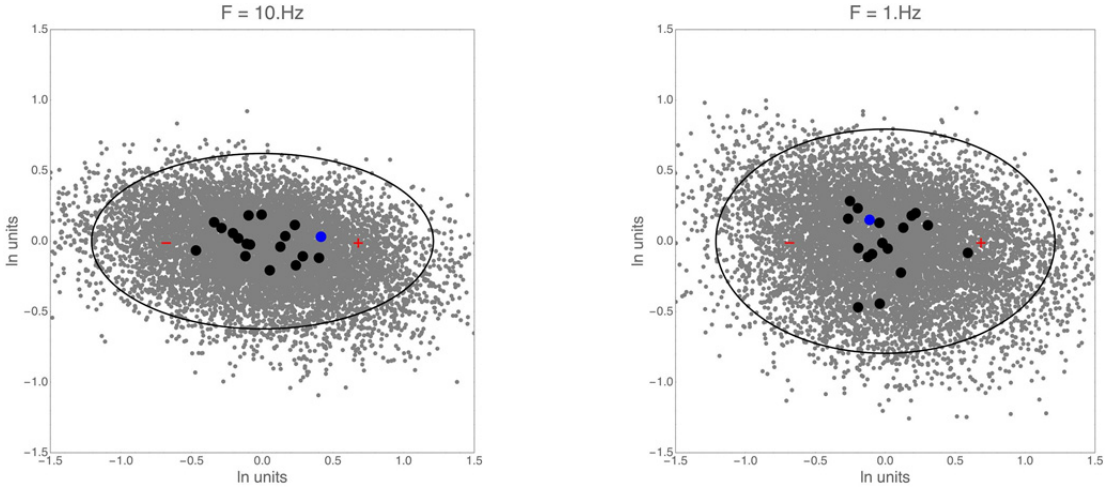

Figure 3.51 **Sammon's maps for two different frequencies and 10,000 sampled models (gray points). The range defined by the Project Team is a black ellipse. The mean model is plotted as a red dot, the up/down-scaled models are plotted as + and −, respectively. The seed models are plotted as black dots. The reference model "SP15" is plotted as a blue dot.**

3.5.2 Discretization of the Ground-Motion Space into Cells

With the range as defined in the previous section, the ellipse encloses the subset of ground-motion model space (Figure 3.51) that the Project Team intends to capture. As described above, this range covers 95.45% of the total probability on the map. The range needs to be discretized into a manageable number of GMMs. Therefore, the ellipse defining the range is partitioned into several cells, and a representative model for each cell is developed.

The range is first partitioned into three elliptical regions, each with half axes that are scaled by factors 0.25, 0.5, and 0.75 of the ellipse that spans the full range. This creates an inner ellipse and three elliptical bands. Each of these bands is then partitioned into a number of cells using an equal angular width, resulting in a larger number of cells in the outer bands. The Project Team concluded that there is not enough information to defend a more complex discretization, and that this scheme was appropriate to capture a range of ground-motion values, with alternate scalings represented in the space, away from the center.

An example of the discretized ground-motion space is shown in Figure 3.52, for two frequencies. Figure 3.53 shows model index numbers.

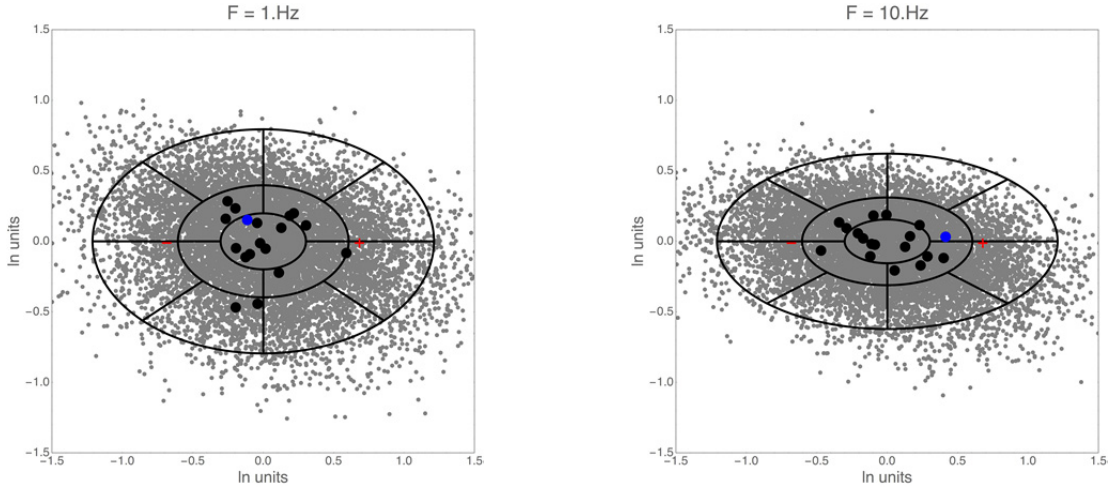

Figure 3.52 **Sammon's maps for two different frequencies and 10,000 sampled models (gray points). The partition of the ground-motion space defined by the Project Team are shown as black cells. The mean model is plotted as a red dot, the up/down-scaled models are plotted as + and −, respectively. The seed models are plotted as black dots. The reference model "SP15" is plotted as a blue dot.**

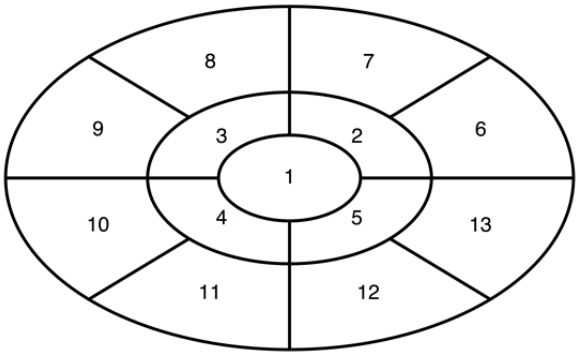

Figure 3.53 **Cell index numbers.**

3.5.2 Selection of Representative GMM for Each Cell

Each of the 13 cells defined above covers a fraction of the area on the map, which is the full representation of $P(\mathbf{Y})$. The next step is to define a representative GMM for each cell. Various candidate representative models were considered by the Project Team, with preference given to an approximation to the expectation of $P(\mathbf{Y})$ over each cell. Since $P(\mathbf{Y})$ is a distribution over vectors of ground-motion estimates (an approximation of a continuous GMM), this results in a valid GMM. The approximation to the expectation is calculated by averaging over all models inside one cell:

$$y_k = \frac{1}{N_k}\sum_{i=1}^{N_k} y_i \tag{3.18}$$

where k indexes the cell, and N_k is the number of samples inside a cell. This is an approximation of:

$$E[Y]_{A_k} = \int_{A_k} yP(y)dA \tag{3.19}$$

The representative model for each cell is therefore an average of samples from $P(\mathbf{Y})$, which allows the representation of the systematic trends in that cell. For example, if the representative model was randomly selected from any model in the cell, it could lead to extreme model realizations and larger variations from frequency to frequency (and very jagged spectra). Because the maps are all oriented the same way, the average metric has the advantage of producing smoother spectra.

All the samples passed the criteria of physicality established by the Project Team, ensuring that the selected models also pass the physicality constraints. Figure 3.54 shows the scaling of the 13 selected models against magnitude and distance.

The spectra of the selected models are shown in Figure 3.55, for a single ($\mathbf{M}$, R_{RUP}) values. For each frequency, the models with the same model index (see right-hand panel of Figure 3.53) are combined into one GMM. Considering that the process is performed for each frequency independently, the spectra are reasonably smooth. The smoothness is ensured by the fact that the Sammon's maps, on which the selected models are based, are all rotated and mirrored in the same way. Figure 3.54 shows an example 3D plot for two different frequencies. The three axes correspond to ground motions from three different ($\mathbf{M}$, R_{RUP}) scenarios. The seeds and samples align into plane-like cloud structures, one for each frequency. These two planes cover different ground-motion values, but the location of the seeds and samples remain in similar positions relative to each plane. This is especially true for close-by frequencies and can explain the relative smoothness of the spectra. Once the high-dimensional space is mapped in two dimensions, the structure is preserved across frequencies by the rotation and reflection of the Sammon's maps in a consistent way. Hence, the regions on the Sammon's maps for the different frequencies correspond roughly to the same scaling properties. However, smoother individual models may be desired for specific applications. The smoothing of the 13 models is described in the next section.

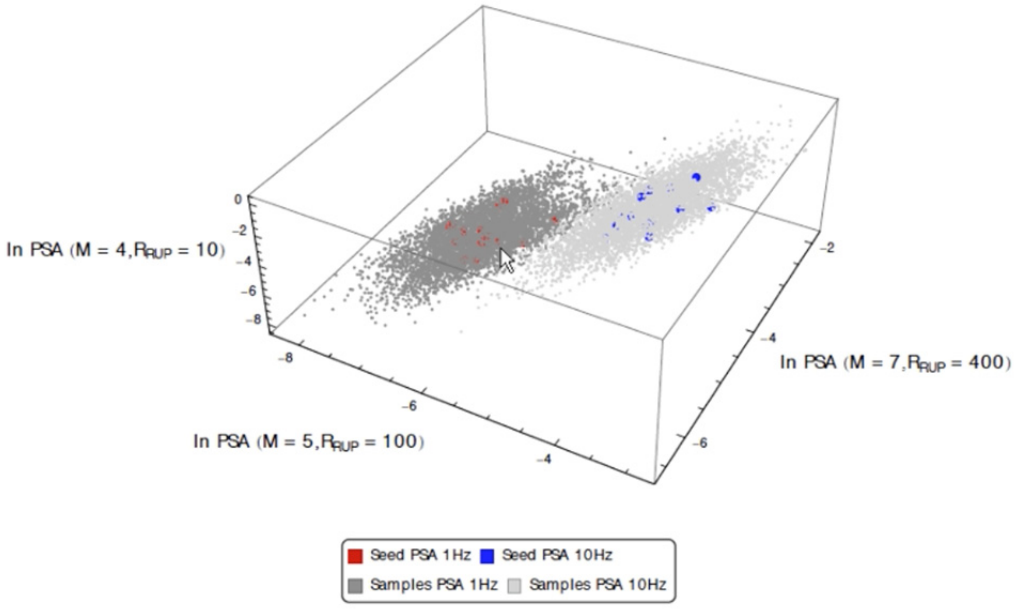

Figure 3.54 **Three-dimensional ground-motion space for seeds and samples at two frequencies (1 and 10 Hz).**

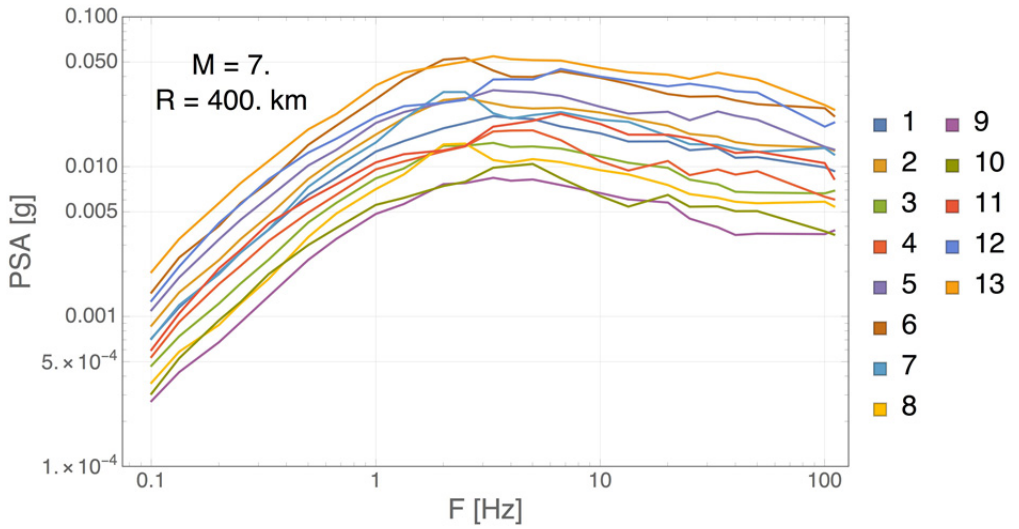

Figure 3.55 **Spectra of 13 selected models for a single (M, *R*) scenario.**

3.6 MODELS AND SMOOTHING PROCESS

Figure 3.56 shows that although the spectra are relatively smooth, they may be too jagged for certain applications. This is especially true for models near the tail ends of the distributions (the outer cells in ellipse) Therefore, the Project Team decided to smooth the 13 selected models to ensure a reasonable expected shape of all spectra for all (**M**, R_{RUP}) scenarios. This is done by fitting the spectra for all 13 models at each of the 374 (**M**, R_{RUP}) scenarios to the following function, modified from McGuire et al. [2001]:

$$\ln PSA_k(\mathbf{M}/R) = a_0 + \frac{a_1}{\cosh[a_2 f^{a_3}]} + a_4 \left[\frac{\exp(a_5 f)}{f^{a_6}} + \frac{a_7 \exp(a_8 f)}{f^{a_9}} \right]^{1/2} \quad (3.20)$$

where k indexes the 13 models.

In Equation 3.20, the coefficients a_4, a_6, a_7, a_8, and a_9 are function of magnitude and distance, with the dependency as described in Table 4-3 of McGuire et al. [2001]. The coefficients of the (**M**, R_{RUP})-dependency are estimated through regression. The coefficients a_0, a_1, and a_2 are different for each of the 374 (**M**, R_{RUP}) scenarios, whereas there is one value of a_3 and a_5 for each model. The coefficient a_0 is constrained to be close to the unsmoothed PGA value for each scenario. The frequency assigned to PGA for the fit is based on Boore (2017), with a lower limit of 110Hz.

Figure 3.56 shows the fit of one particular spectrum, and Figure 3.57 shows the smoothed version of the spectra from Figure 3.55. Figure 3.58 shows comparisons of the hazard curve distribution for f = 1 Hz, calculated the smoothed and unsmoothed models. Figure 3.59 shows a sample uniform hazard spectrum (UHS), calculated for both the smoothed and unsmoothed models. Although there are some differences at some frequencies, there is no defensible argument to maintain the "kinks," which are relatively small. The benefit of smooth spectra was deemed to outweigh the preservation of the actual spectral shapes. The 13 smoothed models are provided in Electronic Appendix A.

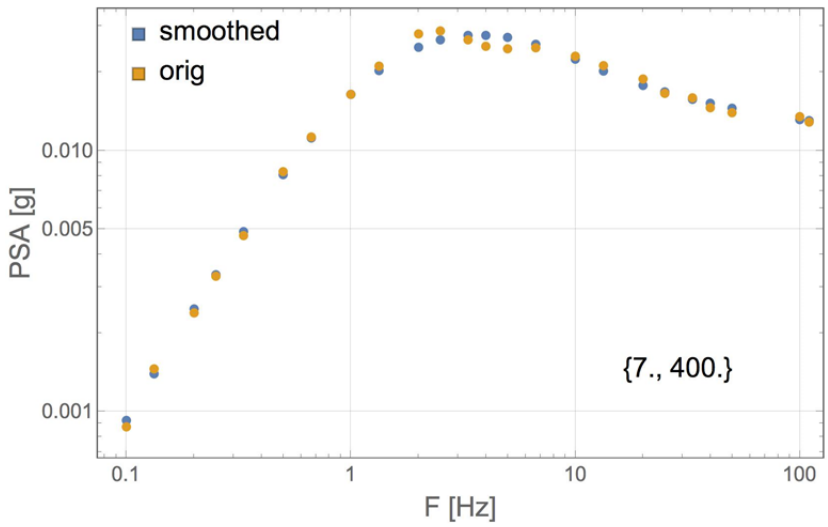

Figure 3.56 Example of a single scenario spectrum fit performed using Equation 3.20.

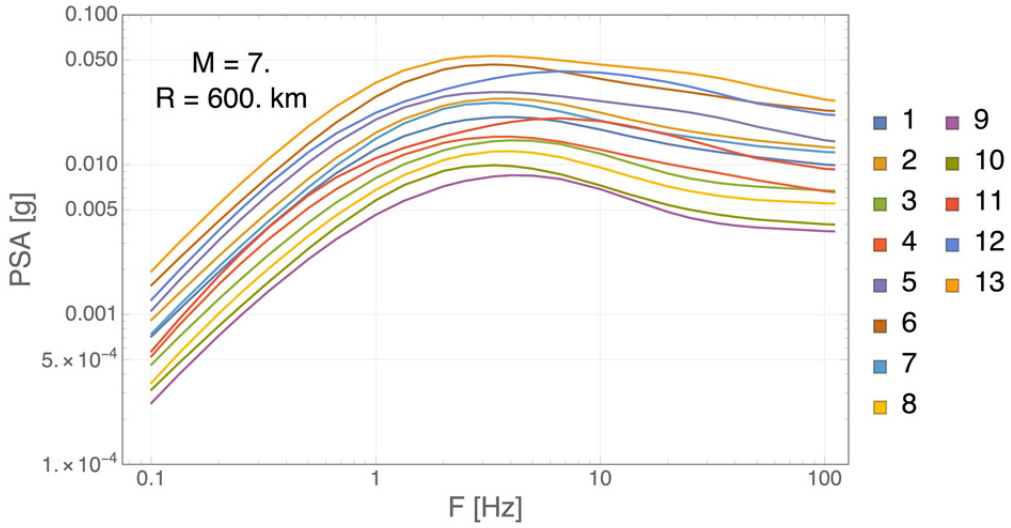

Figure 3.57 **Smoothed spectra of 13 selected models for a single (M, *R*) scenario (same models as in Figure 3.56).**

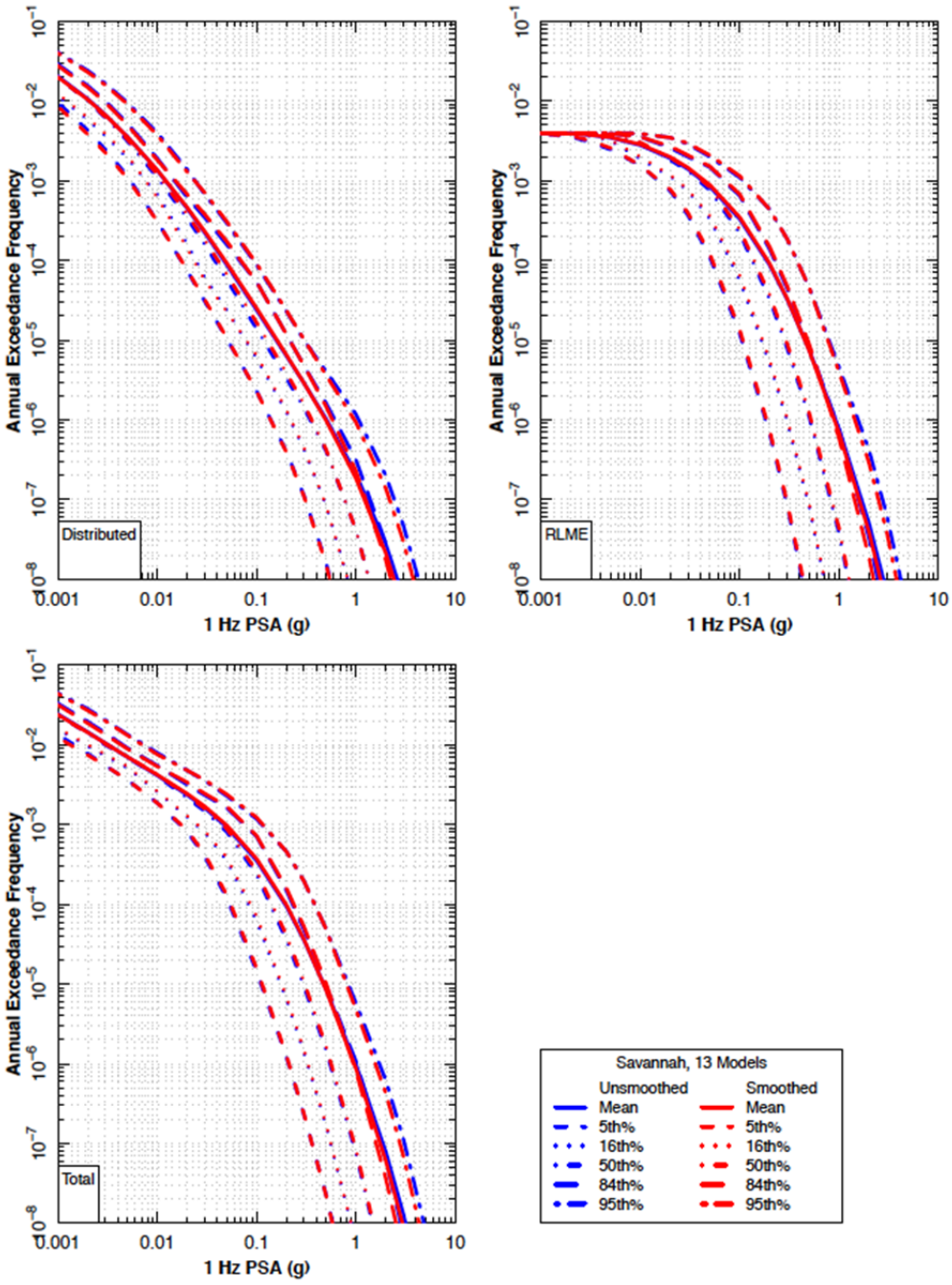

Figure 3.58 **Sample 1Hz hazard curves comparing results from the as-is and smoothed spectra.**

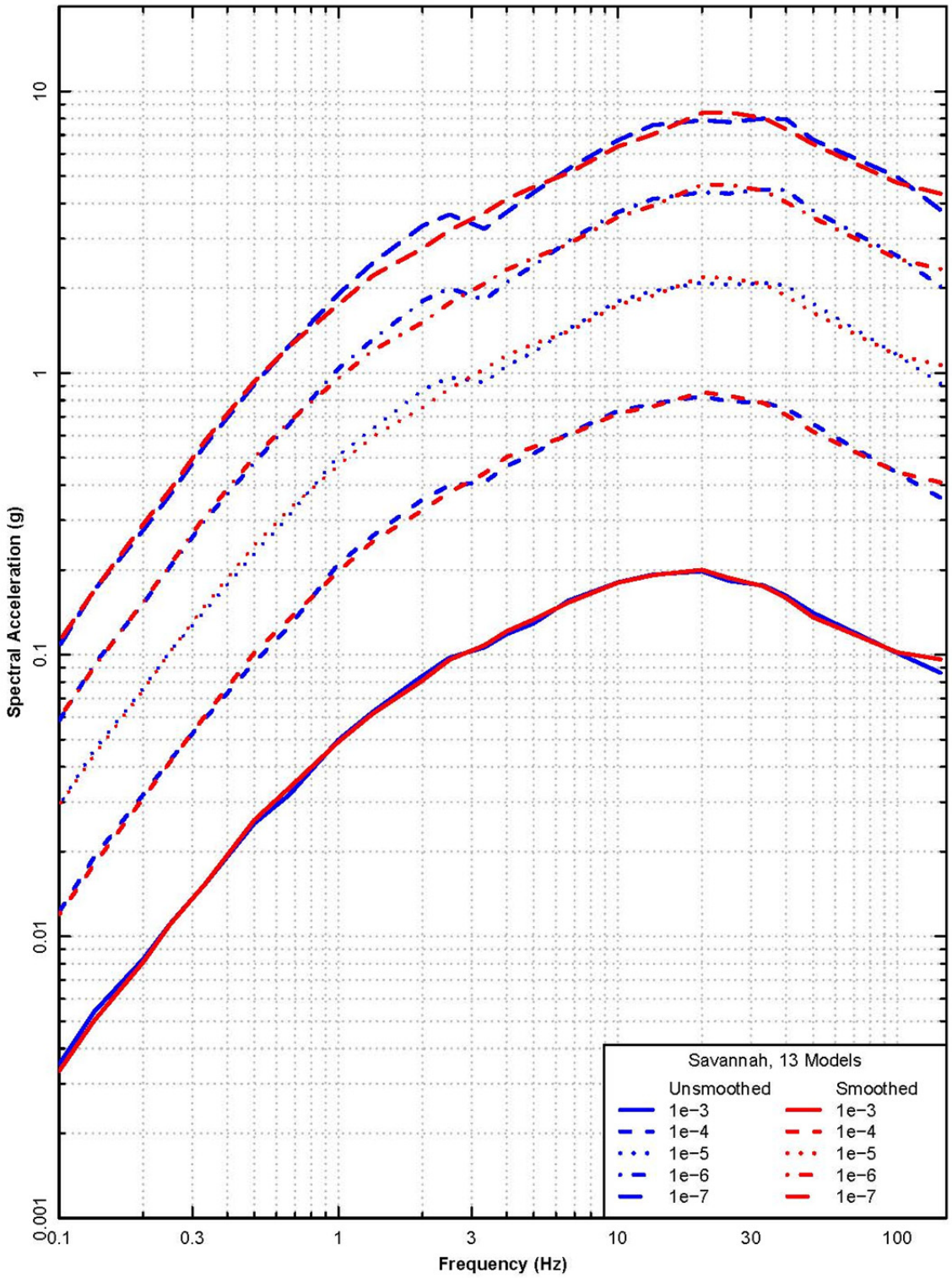

Figure 3.59 **Sample 1 Hz UHS comparing results from the as-is and smoothed spectra for various hazard levels, Manchester site.**

3.7 LOGIC TREE FOR MEDIAN GROUND MOTIONS

3.7.1 Logic Tree Structure – Median Ground-Motion Models

The median ground-motion logic tree consists of 13 branches, each corresponding to a different ground-motion model (GMM). The logic tree structure is therefore very simple, with a weight assigned to each branch. Because of the method used in the development of the 13 GMMs and the fact that they are selected independently for each ground-motion intensity measure (GMIM), the weights also change with frequency and for peak ground acceleration (PGA) and peak ground velocity (PGV). This is described in more detail below.

3.7.2 Weight Assignment Approaches

In the previous section we defined $P(\mathbf{Y})$ as the joint distribution of median ground-motion estimates at different ($\mathbf{M}$, R_{RUP}) scenarios, for a given frequency. This $P(\mathbf{Y})$ distribution is therefore the full description of the center, body, and range of epistemic uncertainty associated with median ground-motion estimates. The Project Team's approach to weighting the different median GMMs is based on two considerations:

- The weighting should reflect the distribution $P(\mathbf{Y})$.
- GMMs that better fit the data should receive higher weight.

The first point takes into account that the distribution $P(\mathbf{Y})$, estimated from the seed GMMs; therefore, it is a proper description of the epistemic uncertainty associated with median GMM estimates, and the weights for each model should reflect the likelihood with respect to that distribution. The second point takes into account that available data provide information about the models, and that models fitting the observed ground-motion data well should receive higher weights. Both of these approaches give a set of weights for the 13 median GMMs, and based on their relative merits, the Project Team assigns weights on the weighting approaches. Both approaches take into account that each selected GMM is representative of an area on the map, as described by the cells in Figure 3.61. Therefore, the weight of a GMM representing an individual cell represents the contribution of that cell in the ground-motion space.

Weights Reflecting the Median Ground-Motion Distribution

Earlier, the range of epistemic uncertainty was defined—at each frequency—by an ellipse in Sammon's map space that contains most of the 10,000 sampled GMMs. The ellipse represents a two-dimensional normal distribution with mean {0,0} and standard deviations estimated from the sampled models on the map. The ellipse was further re-discretized into 13 cells. Figure 3.60 shows all the example Sammon's maps [1969] with the cell definition and the seed and sampled GMMs. Two weights based on the distribution of sampled GMMs can be computed. Both weights are based on the assumption that the distribution of points on the Sammon's map is a representation of the high-dimensional distribution $P(\mathbf{Y})$.

Weight Based on the Fitted Two-dimensional Probability Density Distribution

In the following, the fitted 2D (elliptical) distribution is denoted by $P_{\text{Fitted-PDF}}(\mathbf{X})$, where $\mathbf{X}$ is the random variable describing the location on the Sammon's map. The weight for each cell is proportional to the density of $P_{\text{Fitted-PDF}}(\mathbf{X})$ inside each cell k

$$w_k(Fitted-PDF) \propto \int_{A_k} P_{Fitted-PDF}(\mathbf{x}) d\,\mathbf{x} \tag{3.21}$$

where A_k is the area of the kth cell. The weights are symmetric along the two axes of the ellipse, as is expected from the fitted distribution.

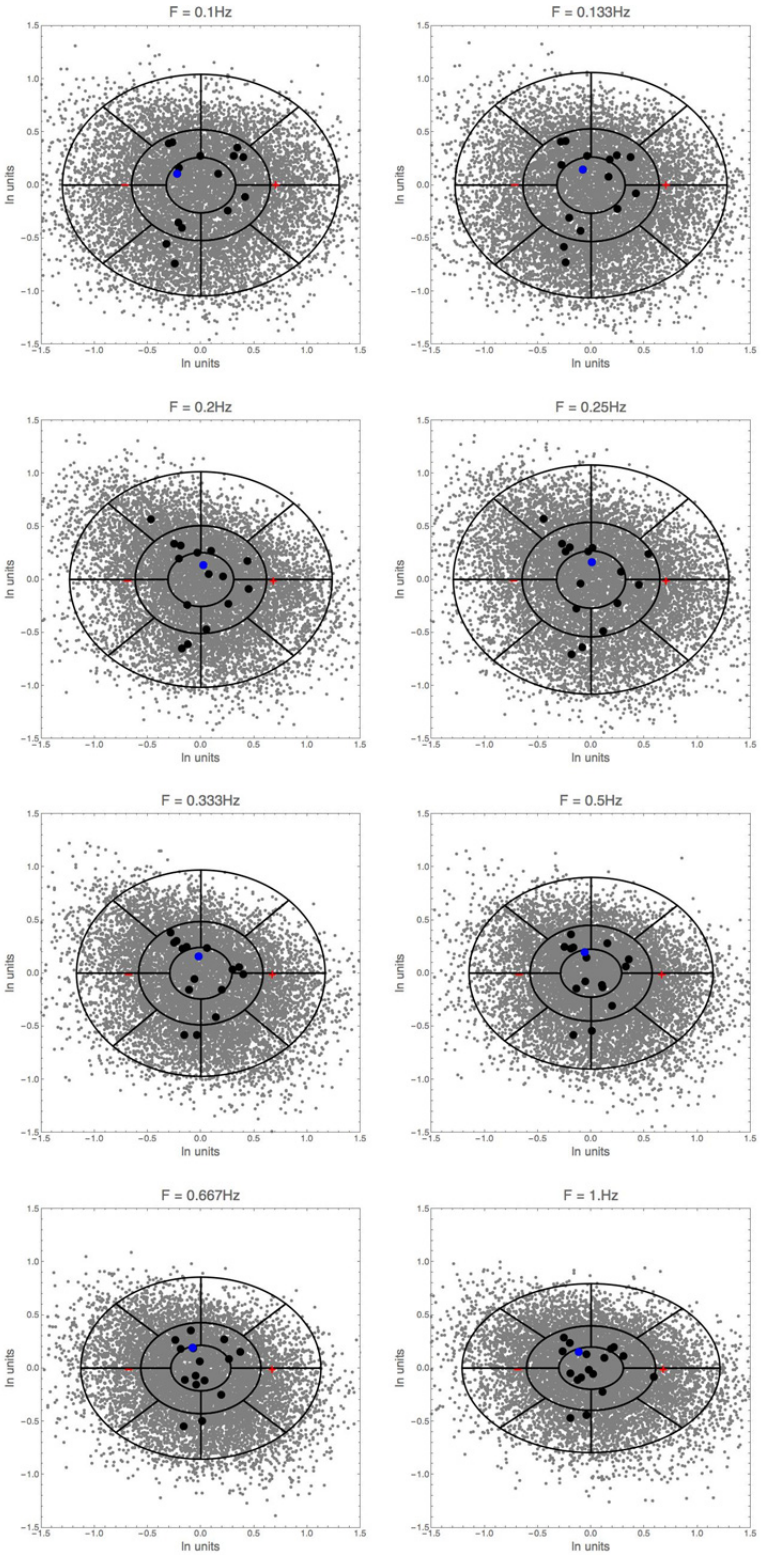

Figure 3.60(a) Sampled GMMs distribution on Sammon's maps. On each plot, the red dot is at the center (mean of GMMs), the black dots are seed GMMs, and the blue dot corresponds to the SP15 seed GMM (0.1-1 Hz).

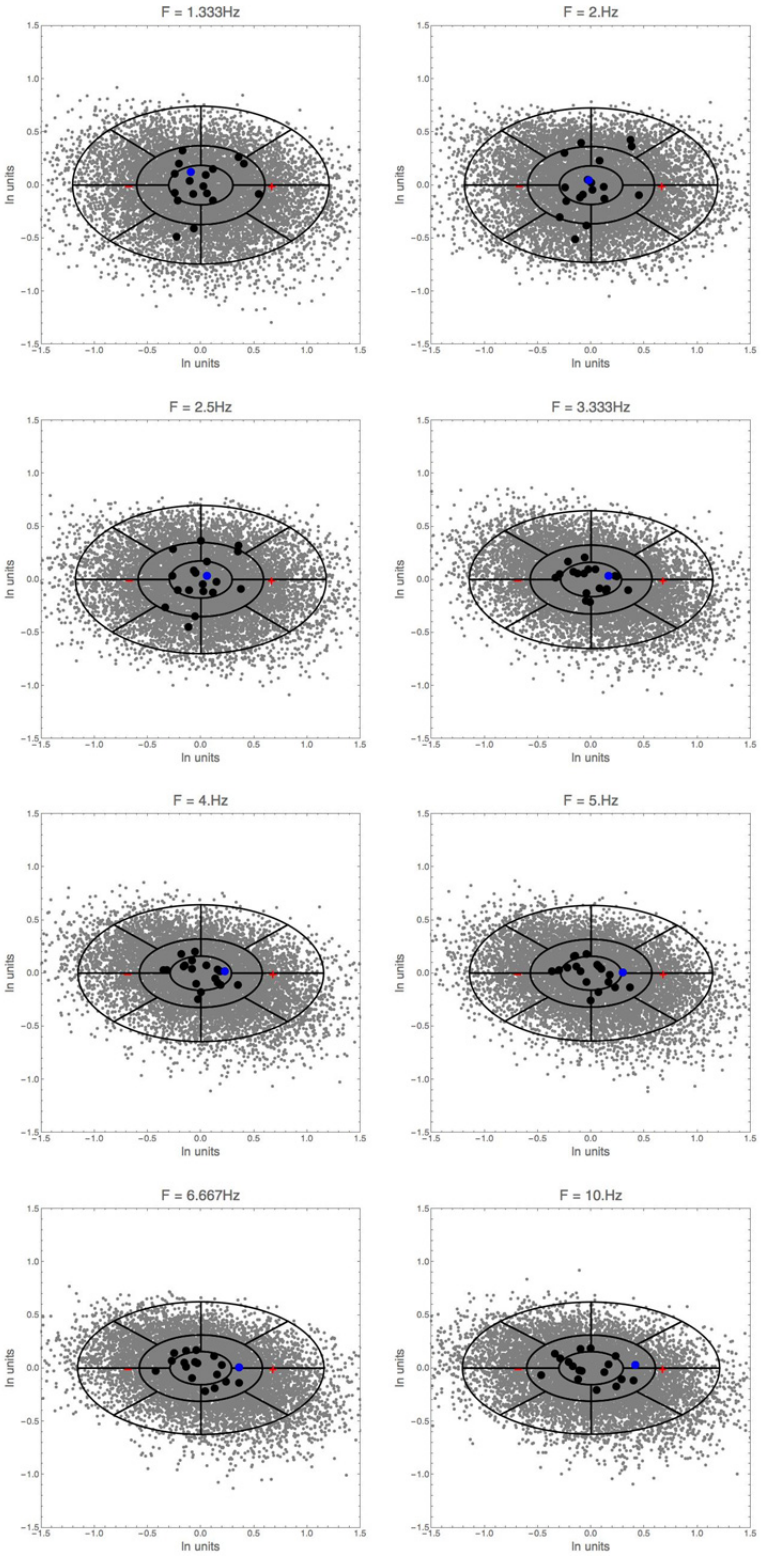

Figure 3.60(b) Sampled GMMs distribution on Sammon's maps. On each plot, the red dot is at the center (mean of GMMs), the black dots are seed GMMs, and the blue dot corresponds to the SP15 seed GMM (1.33-10 Hz).

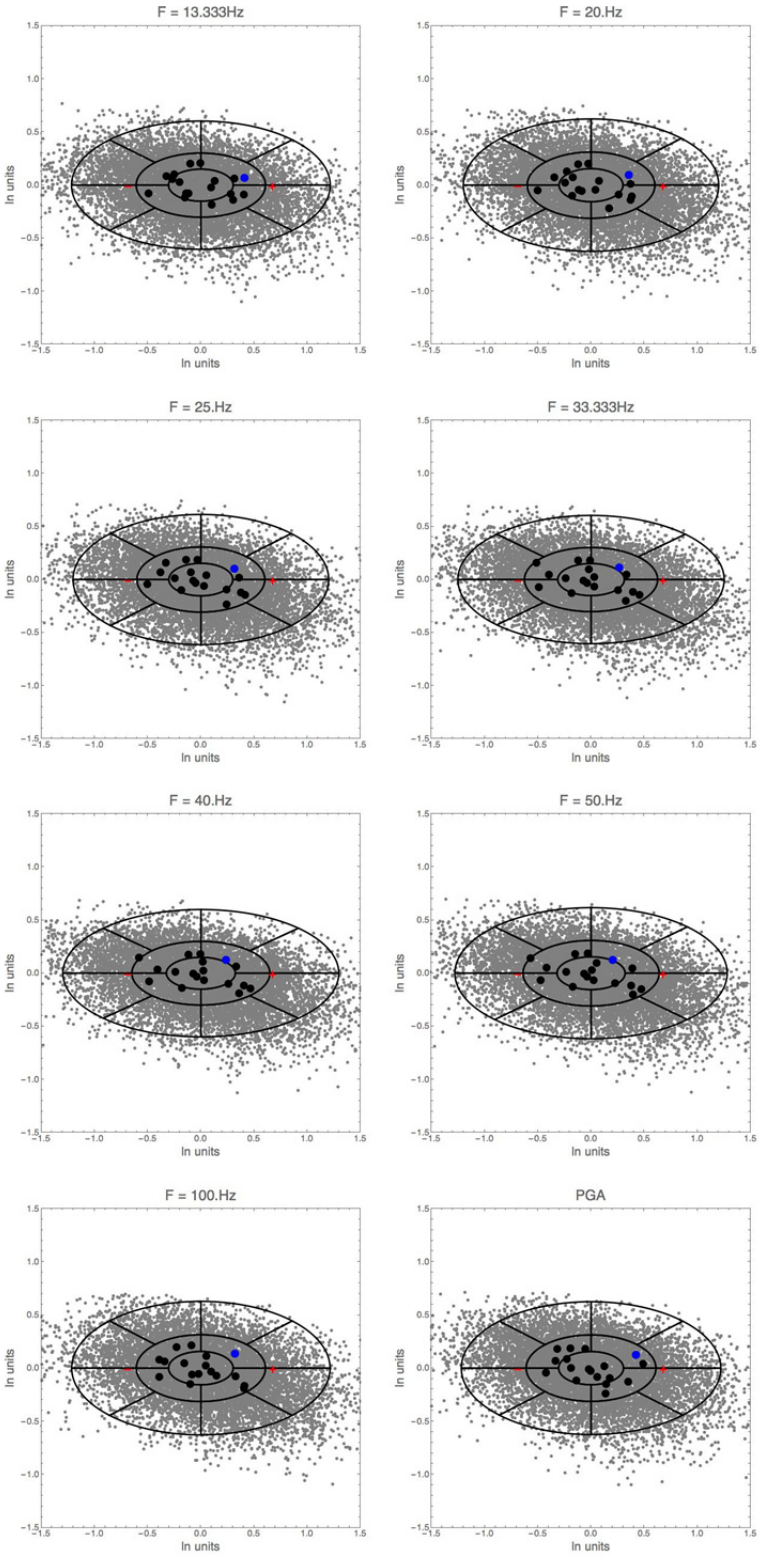

Figure 3.60(c) Sampled GMMs distribution on Sammon's maps. On each plot, the red dot is at the center (mean of GMMs), the black dots are seed GMMs, and the blue dot corresponds to the SP15 seed GMM (13.33-100 Hz, and PGA).

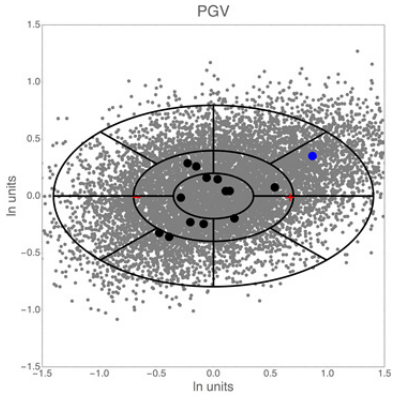

Figure 3.60(d) Sampled GMMs distribution on Sammon's maps. On each plot, the red dot is at the center (mean of GMMs), the black dots are seed GMMs, and the blue dot corresponds to the SP15 seed GMM (PGV).

Weight Based on the Number of Sampled GMMs in a Cell

Another way to account for the distribution of sampled GMMs is to compute the weight directly from the number of models inside each cell

$$w_k(N_{Samples}) \propto N_k \tag{3.22}$$

If the distribution of sampled GMMs was perfectly symmetric, the weights from Equations (3.21) and (3.22) would be identical (e.g., in the case of the one-dimensional example in Chapter 2). However, the weights based on Equation (3.22) take into account any skewness in the distribution of points on the map (Figure 3.60). Such skewness can be due to the characteristics of the seed GMMs themselves and/or to the application of the physicality criteria in screening the sampled GMMs. For example, Figures 3.36 and 3.37 showed that the number of rejected samples is different for the different seed GMMs, depending on how close the seed GMM is to the physicality criteria. This can translate into asymmetry in the two-dimensional distribution of sampled points on the map. Figure 3.61 compares the weights based on the two different approaches.

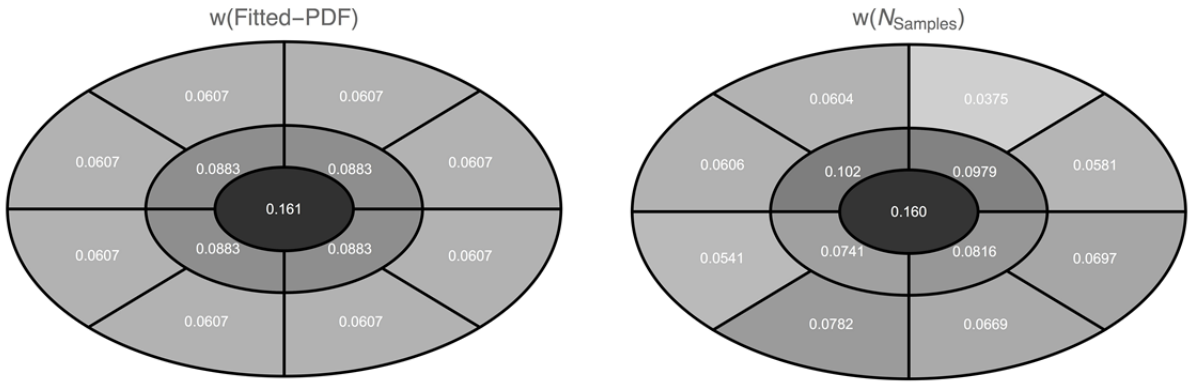

Figure 3.61 Comparison of weights: (a) w_k (Fitted—PDF) and (b) w_k ($N_{Samples}$), for the 1 Hz case.

Weights Reflecting the Fit to Data

The second approach to weighting takes into account that a model that fits the data better should receive a higher weight. Therefore, weights are calculated as an expectation over the area of the cell

$$w_k \propto \int_{A_k} f(\mathbf{x}, D) P(\mathbf{x}) d\mathbf{x} \tag{3.23}$$

where $f(\mathbf{x}, D)$ is a function that depends on the data **D**. The Project Team approach was to base weights on the mean residual with respect to data amplitudes, as well as the likelihood. To approximate the weights as calculated by Equation (3.23), the residuals and likelihood of data are calculated for each of the sampled models. The data are a subset of the NGA-East database, with the constraint of limiting records to within R_{RUP} = 400 km (to avoid data truncation issues discussed in Section 3.1). The dataset consists in 468 records from 21 events, including tectonic and potentially induced events (PIEs). The records span **M** = 4.03 to 5.85 and R_{RUP} = 4.2 to 400 km, with their distribution shown in Figure 3.62. The V_{S30} values range from 312 m/sec to 2000 m/sec. The distribution $P(\mathbf{Y})$ is based on seed GMMs that provide estimates for V_{S30} = 3000 m/sec and κ = 0.006 sec. The data were corrected for site conditions using the following steps:

- If the V_{S30} value of the recording station is lower than 760 m/sec, it is adjusted to V_{S30} = 760 m/sec using the BSSA14 [Boore et al. 2014] site-effects model. The resulting value is then adjusted to NGA-East conditions using adjustment factors developed by Boore [2015].
- If the V_{S30} value of the recording station is larger than 760 m/sec, the adjustment factors developed by Boore [2015] from V_{S30} = 760 m/sec to V_{S30} = 3000 m/sec are interpolated to find the factor suitable for the recording station V_{S30} value. This factor is then applied to the data.

For each of the 10000 sampled models, residuals to the data are calculated. These are partitioned into between-event residuals and within-event residuals using Equation 10 of Abrahamson and Youngs [1992] formulation, and the likelihood L is also calculated using the same reference. To calculate the likelihood, the average values of τ and ϕ from NGA-East are used [Al Atik 2015]. Then, weights are calculated with

$$w_k(res) \propto A_k \frac{1}{\mu_k\left(|res|\right) + \delta} \tag{3.24}$$

$$w_k(L) \propto \frac{1}{N_k} A_k \sum_{i=1}^{N_k} L_i \tag{3.25}$$

where A_k is the area on the map for the kth cell, and $\mu_k(|res|)$ is the mean absolute between-event residual of all models inside the kth cell, and L_i is the likelihood of the ith model within the kth cell. Parameter δ serves to penalize the weights based on residuals for cells with a mean residual of (close to) zero (that cell would get all the weight otherwise). It is set to a value δ = 0.0075.

Figure 3.63 plots contours of the mean between-event residuals and the likelihoods for each sampled model on the Sammon's maps for f = 1Hz. Figures 3.64 and 3.65 show the residual and likelihood maps for all the relevant GMIMs (PSA frequencies from 0.1 to 10 Hz and for PGV, respectively). Figure 3.66 shows example weights as calculated from Equations (3.24) and (3.25).

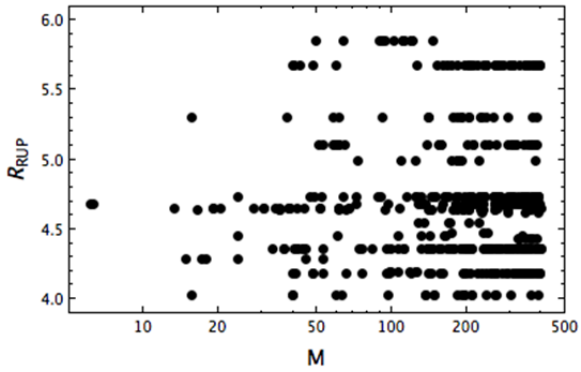

Figure 3.62 Magnitude and distance distribution of data used to calculate residuals.

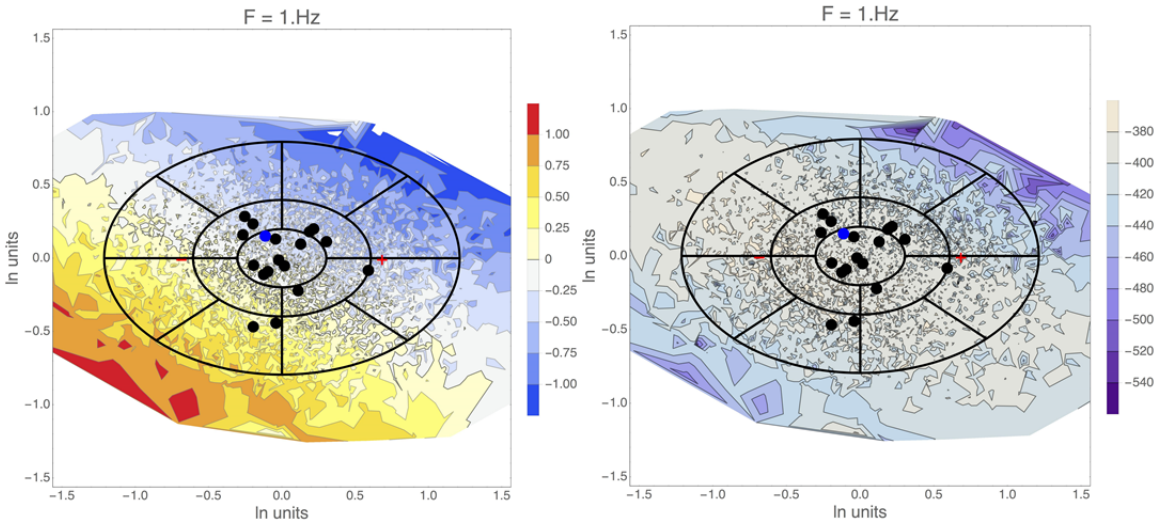

Figure 3.63 Contour plots of mean between-event residuals (left) and log-likelihood (right), for the 1 Hz case.

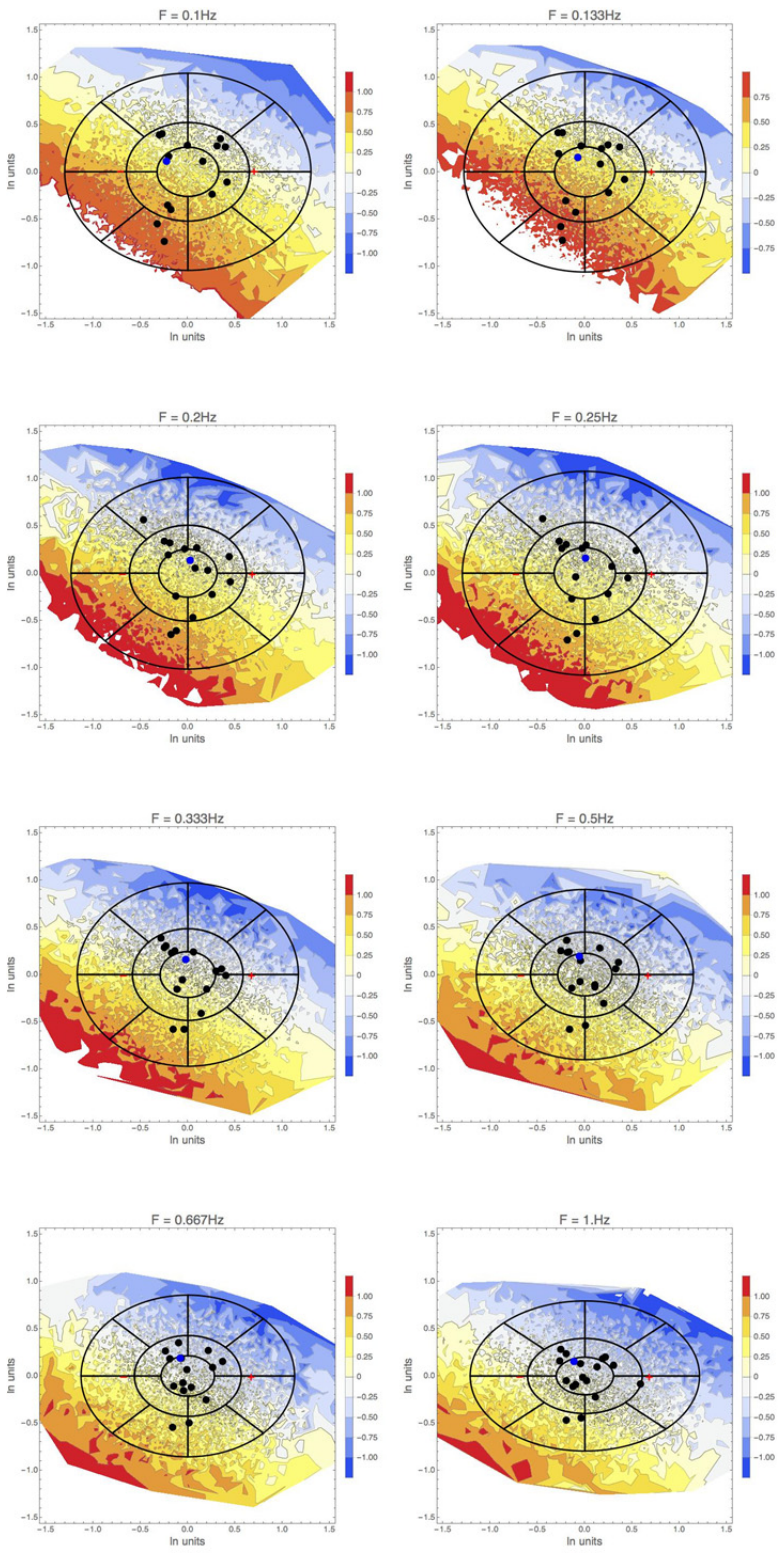

Figure 3.64(a) Contour plots of mean between-event residuals (0.1–1 Hz).

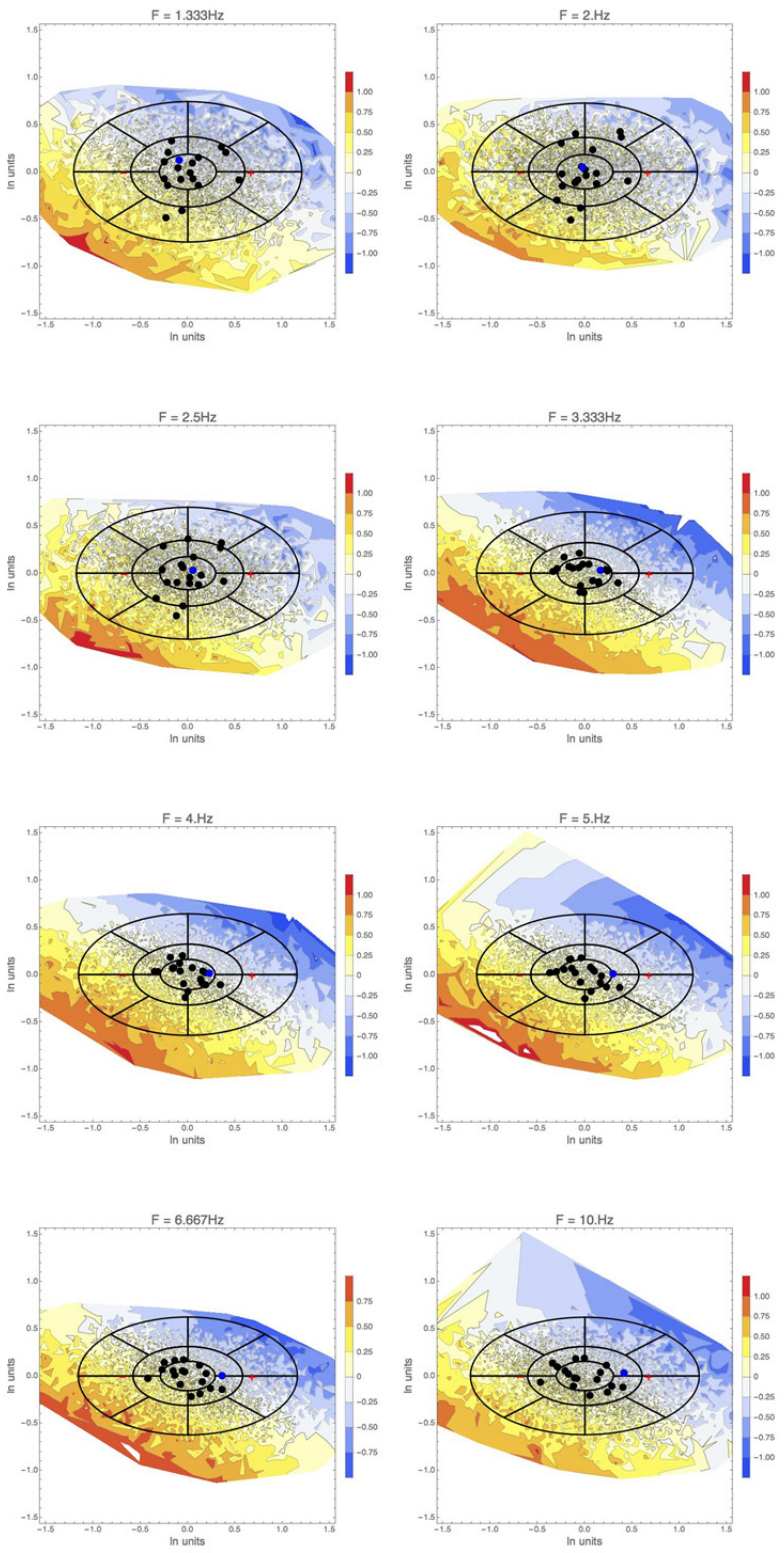

Figure 3.64(b) Contour plots of mean between-event residuals (1.33–10 Hz).

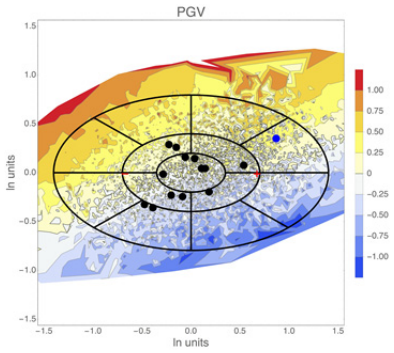

Figure 3.64(c) Contour plots of mean between-event residuals (PGV).

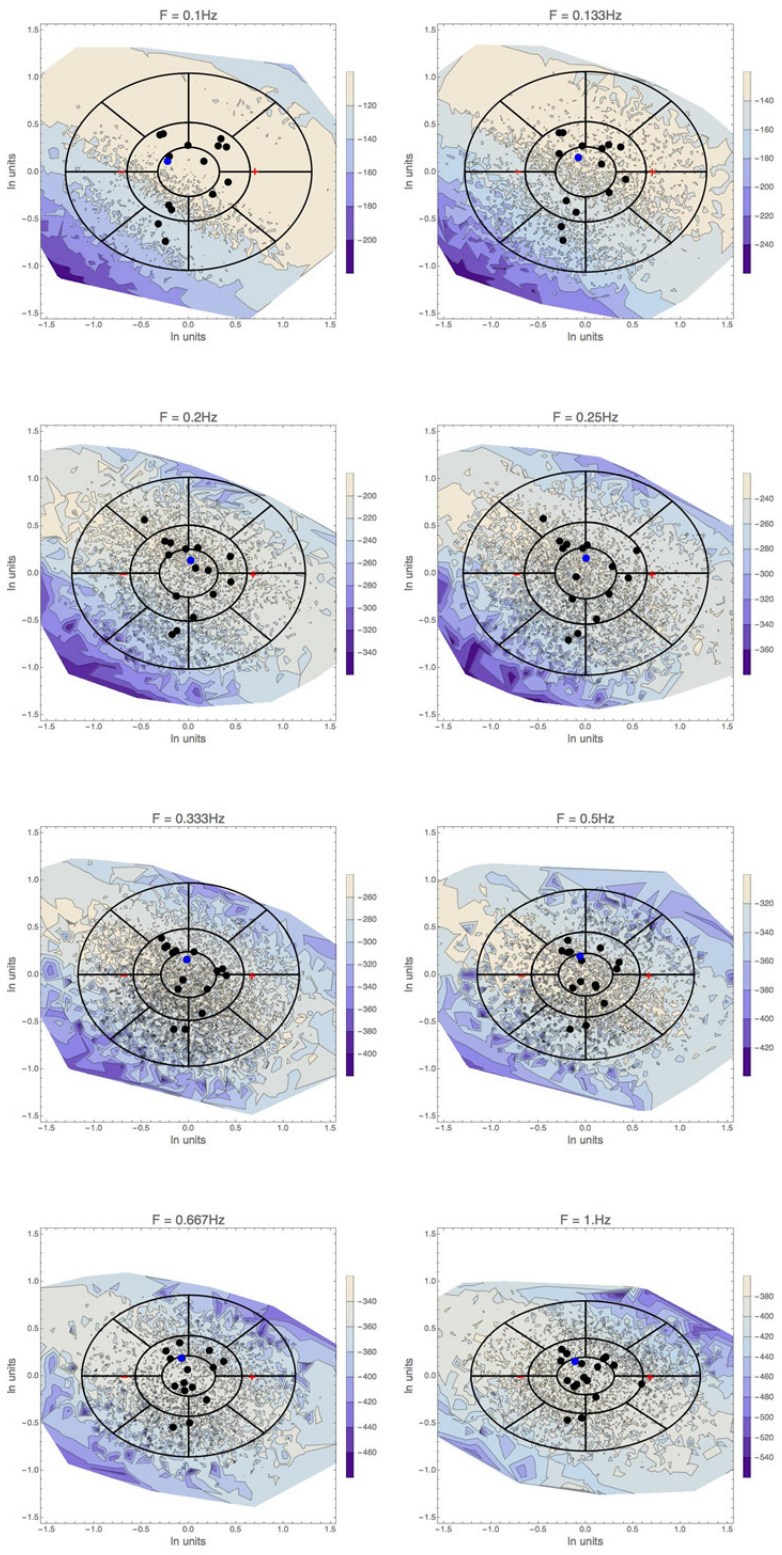

Figure 3.65(a) Contour plots of likelihood (0.1–1 Hz).

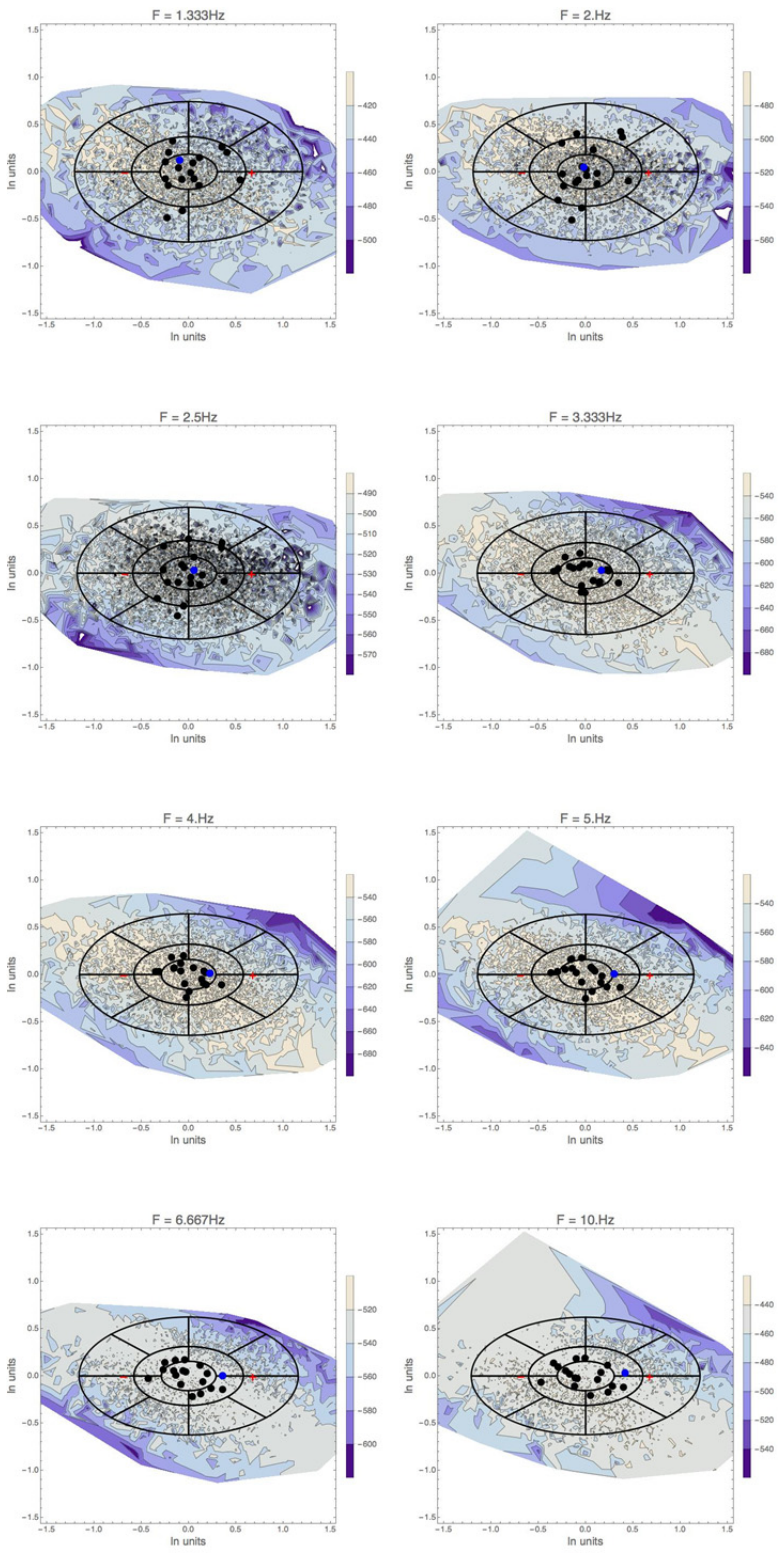

Figure 3.65(b) Contour plots of likelihood (1.33–10 Hz).

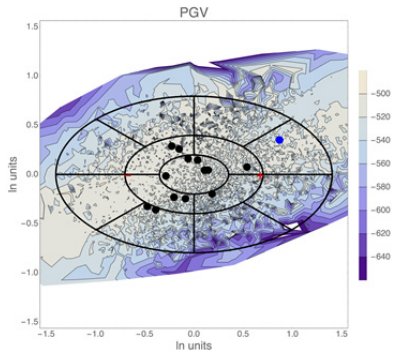

Figure 3.65(c) Contour plots of likelihood (PGV).

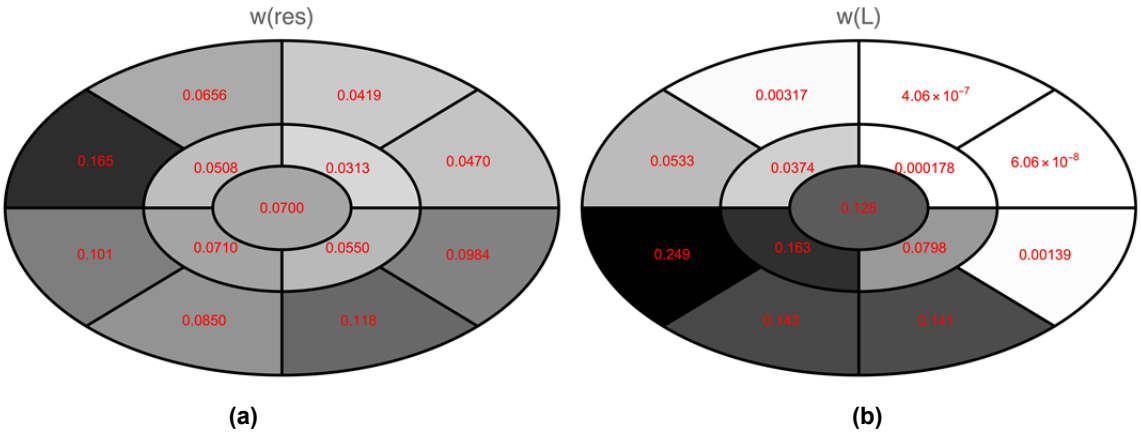

(a) (b)

Figure 3.66 Comparison of weights: (a) based on residual and (b) based on likelihood for the 1 Hz case.

Weights Combining the Distribution and Fit to Data

The third approach to assigning weights to the individual models is a combination of the previous two approaches, and takes into account both the GMM distribution and the fit to the data. It is based on calculating the posterior probability of each sampled model given the data. To calculate this probability, the value of the distribution $P_{\text{Fitted-PDF}}$ ($\mathbf{x}_i$) is multiplied with the likelihood L_i for the ith sample model m_i:

$$P(m_i \mid D) = P_{\text{Fitted-PDF}}(\mathbf{x}_i) L_i \tag{3.26}$$

Weights for each cell can then be calculated by averaging the values of the posterior distribution over the cell k

$$w_k(\text{post}) \propto \frac{1}{N_k} A_k \sum_{i=1}^{N_k} P(m_i \mid D) \tag{3.27}$$

3.8 EVALUATION OF WEIGHT ASSIGNMENT APPROACHES

3.8.1 Weights Reflecting the Median Ground-Motion Distribution

As mentioned earlier, the ellipse in the Sammon's map spans the epistemic uncertainty in the median GMM estimates. It is defined based on the dispersion of sampled GMMs along the horizontal and vertical axes. Therefore, the two-dimensional distribution represented by the ellipse does not contain the correlation sometimes visible in the sampled GMMs. For example, Figure 3.61 shows that the upper right and lower left cells contain fewer sampled GMMs than the lower right and upper left cells. This was described earlier as skewness in the distribution of the sampled GGMs. This correlation comes from the seed GMM estimates and should be preserved. The *wk*(Fitted-PDF) weights do not retain this correlation, but the $w_k(N_{\text{Samples}})$ weights do. Because of this, and because the two weighting schemes are otherwise similar, the Project Team preferred to give full weight to the weighting scheme based on $w_k(N_{\text{Samples}})$.

3.8.2 Weights Reflecting the Fit to Data

The weights based on residuals to the data, w_k(res), represent an assessment of how well a model (or the samples inside cell I) fits the ground-motion data on average. The likelihood based weights, $w_k(L)$, , take into account how well the variability of the data is captured. Both sets of weights provide similar insight into the data fit; thus, the Project Team assigned equal weights to these two sets.

3.8.3 Weights Combining the Distribution and Fit to the Data

The weights based on the posterior distribution given the data, w_k(post), are a combination of the "prior" distribution of the GMMs, $P_{\text{Fitted-PDF}}$ ($\mathbf{x}_i$), and the fit to the data via the likelihood. However, as seen from Figures 3.62 and 3.64, the weights based solely on these approaches favor a relatively small number of models, and, in particular, both give relatively high weight to the center model. Hence, their combination in terms of a posterior weight would enforce a stronger weight on the center model. The Project Team decided that this was not justified, since this would reduce the epistemic uncertainty for scenarios that are hazard-relevant but are not captured by the data. The posterior distribution leads to a concentration of the models, but although this is based on small magnitude data, it also leads to a concentration at large magnitudes, for which no data provides constraints.

In addition, the prior distribution is based on the fit of a normal distribution to the distribution of points on the Sammon's map, which does not take into account the skewness of the distribution as explained earlier in this chapter Therefore, the Project Team disregarded weights based on the posterior probability of the models.

3.9 SELECTED WEIGHTS

Figures 3.61 and 3.64 show the four types of weights presented above. The Project Team's task was to assign weights to these different weighting approaches. Ideally, for a region with ample empirical data coverage in terms of magnitude, distance, and bandwidth, higher importance would be assigned to weights based on goodness-of-fit to data. However, this is not the case for NGA-East. As shown in Figure 3.62, the magnitude/distance distribution of the data used for calculating the weights is far from ideal. In addition, a separate suite of analyses conducted for the standard deviation work showed that the data are only sufficient enough in the 0.1 to 10 Hz bandwidth. Therefore, both w_k(res), and $w_k(L)$, reflect an assessment of the models only over this limited range of magnitude, distance, and frequency. Moreover, models that are similar in this range can still be quite different for larger magnitudes. Hence, the available observations are not discriminative for models with respect to the most hazard-relevant scenarios. Based on these considerations, the Project Team assigned the following weights:

- Within 0.1-10 Hz bandwidth:
    - 80% for $w_k(N_{\text{Samples}})$ 10 % for and 10% for $w_k(L)$
- Everywhere else:
    - 100% to $w_k(N_{\text{Samples}})$

Figure 3.67 shows the total weights for all the GMIMs. There are variations in weights for a given cell with frequency, but the variations with frequency are relatively smooth and stable, which contributes to smoother response spectra. The total weights for each GMIM are provided in Table 3.15.

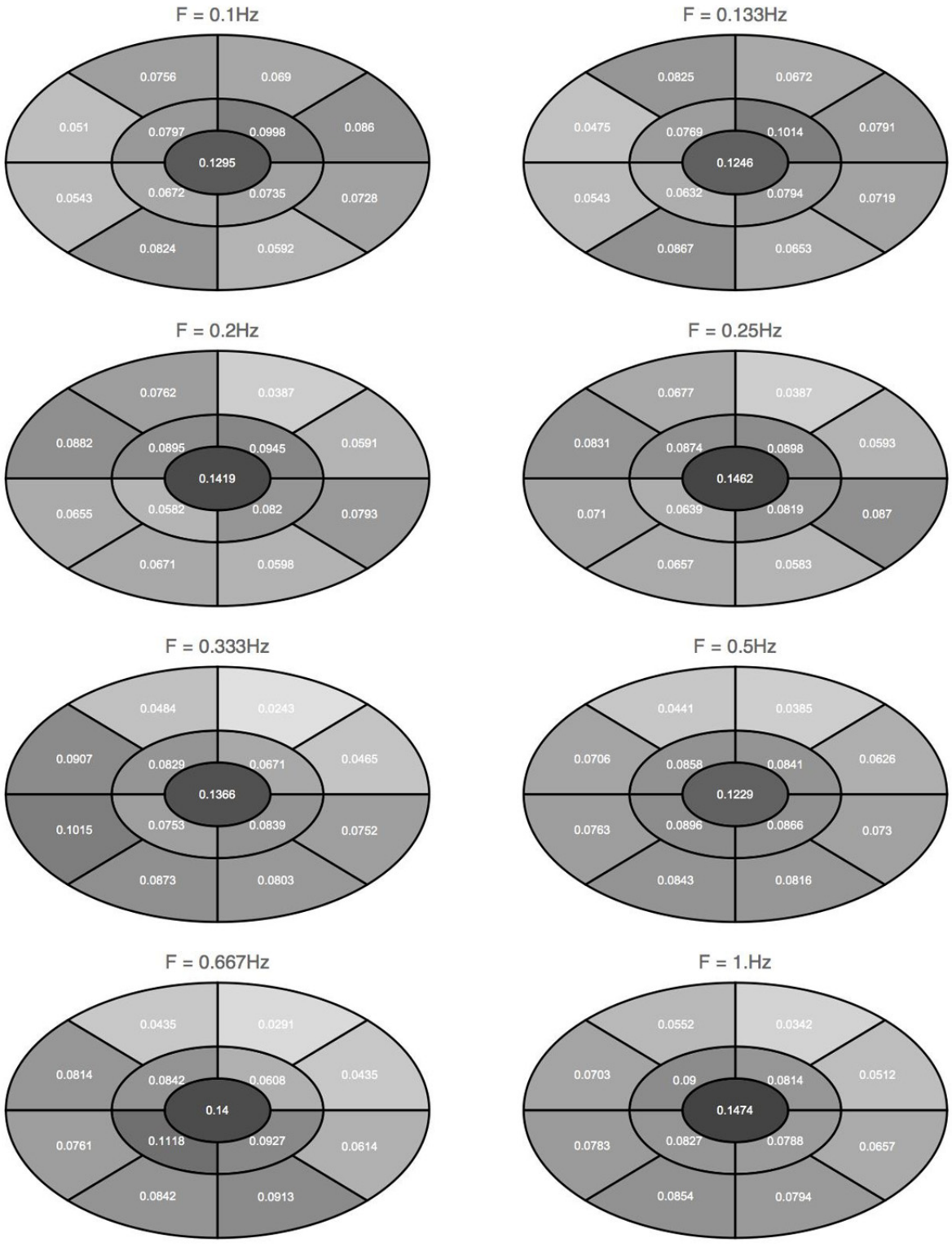

Figure 3.67(a) Total weights (0.1–1 Hz).

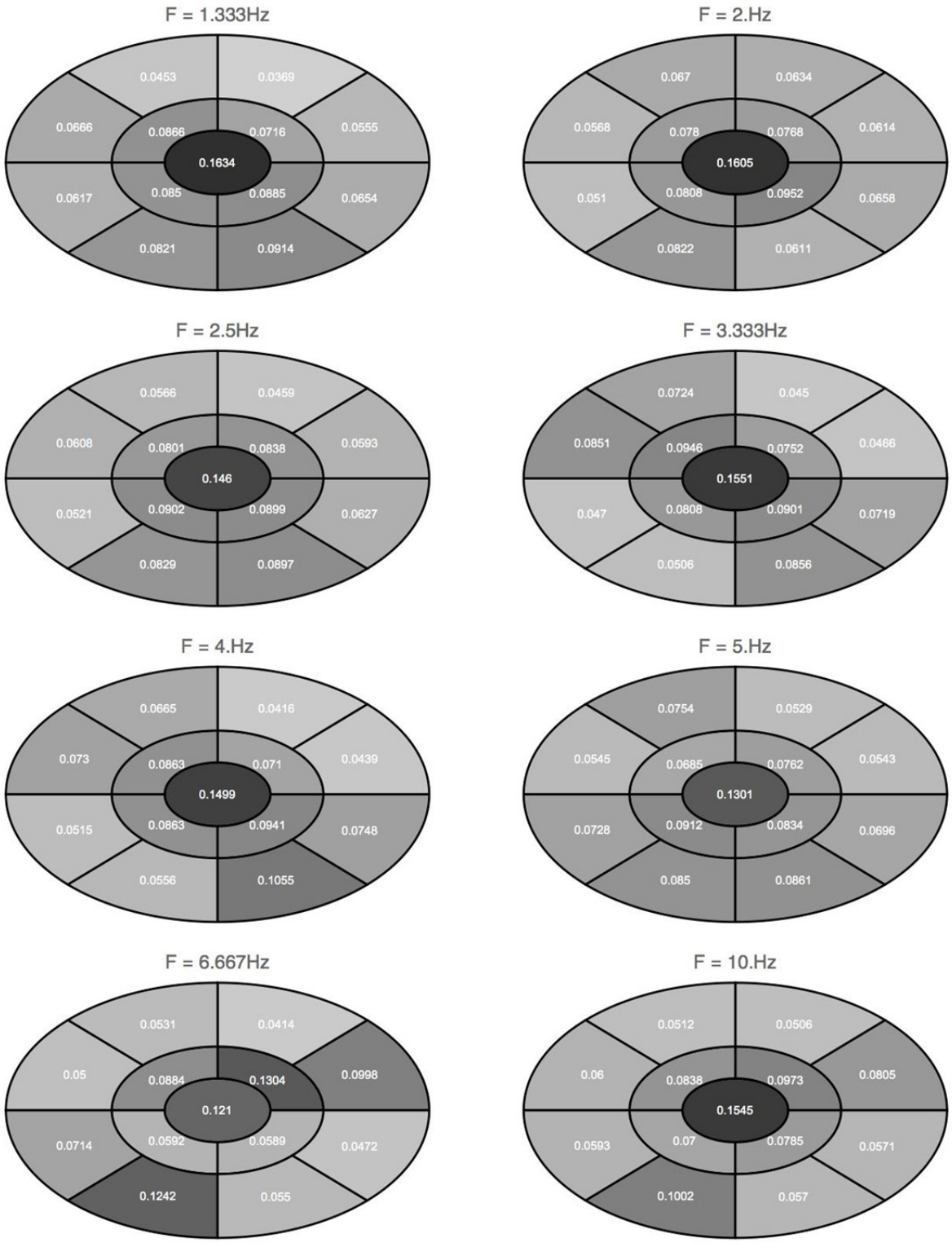

Figure 3.67(b) Total weights (1.33–10 Hz).

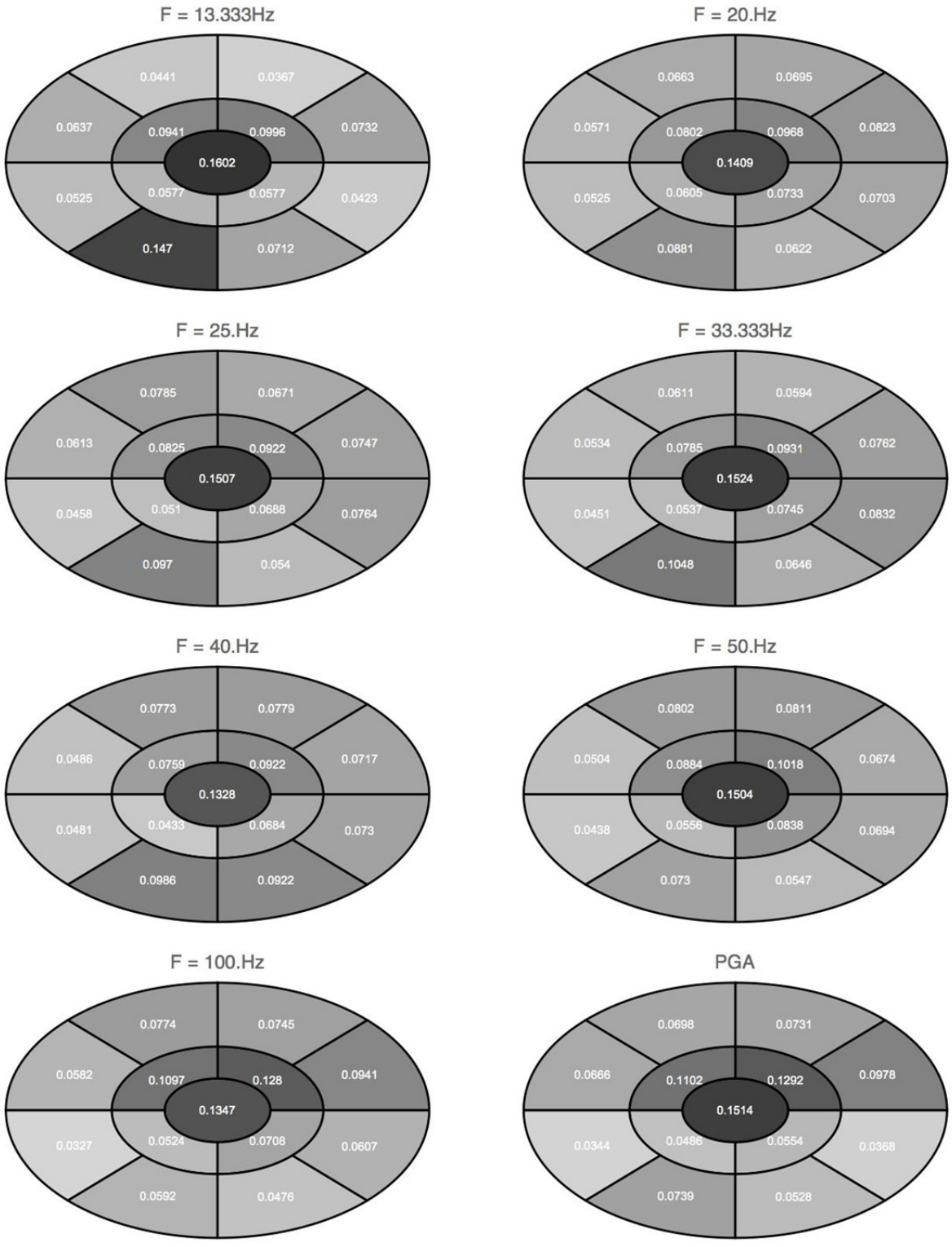

Figure 3.67(c) Total weights (13.33–100 Hz, and PGA).

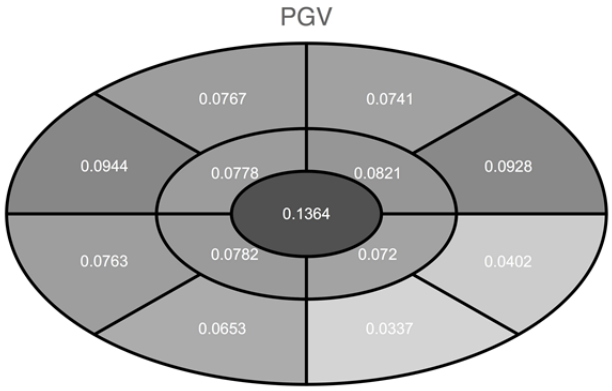

Figure 3.67(d) Total weights (PGV).

Table 3.15 Total weights for the 13 models, for all the GMIMs (oscillator frequencies, *f*, in Hertz).

Model	*f*=0.1	*f*=0.133	*f*=0.2	*f*=0.25	*f*=0.333	*f*=0.5	*f*=0.667	*f*=1.	*f*=1.333	*f*=2.	*f*=2.5	*f*=3.333	*f*=4.0	*f*=5.0	*f*=6.667	*f*=10.0	*f*=13.333	*f*=20.0	*f*=25.0	*f*=33.33	*f*=40.0	*f*=50.0	f=100.0	PGA	PGV
1	0.1295	0.1246	0.1419	0.1462	0.1366	0.1229	0.14	0.1474	0.1634	0.1605	0.146	0.1551	0.1499	0.1301	0.121	0.1545	0.1602	0.1409	0.1507	0.1524	0.1328	0.1504	0.1347	0.1514	0.1364
2	0.0998	0.1014	0.0945	0.0898	0.0671	0.0841	0.0608	0.0814	0.0716	0.0768	0.0838	0.0752	0.071	0.0762	0.1304	0.0973	0.0996	0.0968	0.0922	0.0931	0.0922	0.1018	0.128	0.1292	0.0821
3	0.0797	0.0769	0.0895	0.0874	0.0829	0.0858	0.0842	0.09	0.0866	0.078	0.0801	0.0946	0.0863	0.0685	0.0884	0.0838	0.0941	0.0802	0.0825	0.0785	0.0759	0.0884	0.1097	0.1102	0.0778
4	0.0672	0.0632	0.0582	0.0639	0.0753	0.0896	0.1118	0.0827	0.085	0.0808	0.0902	0.0808	0.0863	0.0912	0.0592	0.07	0.0577	0.0605	0.051	0.0537	0.0433	0.0556	0.0524	0.0486	0.0782
5	0.0735	0.0794	0.082	0.0819	0.0839	0.0866	0.0927	0.0788	0.0885	0.0952	0.0899	0.0901	0.0941	0.0834	0.0589	0.0785	0.0577	0.0733	0.0688	0.0745	0.0684	0.0838	0.0708	0.0554	0.072
6	0.086	0.0791	0.0591	0.0593	0.0465	0.0626	0.0435	0.0512	0.0555	0.0614	0.0593	0.0466	0.0439	0.0543	0.0998	0.0805	0.0732	0.0823	0.0747	0.0762	0.0717	0.0674	0.0941	0.0978	0.0928
7	0.069	0.0672	0.0387	0.0387	0.0243	0.0385	0.0291	0.0342	0.0369	0.0634	0.0459	0.045	0.0416	0.0529	0.0414	0.0506	0.0367	0.0695	0.0671	0.0594	0.0779	0.0811	0.0745	0.0731	0.0741
8	0.0756	0.0825	0.0762	0.0677	0.0484	0.0441	0.0435	0.0552	0.0453	0.067	0.0566	0.0724	0.0665	0.0754	0.0531	0.0512	0.0441	0.0663	0.0785	0.0611	0.0773	0.0802	0.0774	0.0698	0.0767
9	0.051	0.0475	0.0882	0.0831	0.0907	0.0706	0.0814	0.0703	0.0666	0.0568	0.0608	0.0851	0.073	0.0545	0.05	0.06	0.0637	0.0571	0.0613	0.0534	0.0486	0.0504	0.0582	0.0666	0.0944
10	0.0543	0.0543	0.0655	0.071	0.1015	0.0763	0.0761	0.0783	0.0617	0.051	0.0521	0.047	0.0515	0.0728	0.0714	0.0593	0.0525	0.0525	0.0458	0.0451	0.0481	0.0438	0.0327	0.0344	0.0763
11	0.0824	0.0867	0.0671	0.0657	0.0873	0.0843	0.0842	0.0854	0.0821	0.0822	0.0829	0.0506	0.0556	0.085	0.1242	0.1002	0.147	0.0881	0.097	0.1048	0.0986	0.073	0.0592	0.0739	0.0653
12	0.0592	0.0653	0.0598	0.0583	0.0803	0.0816	0.0913	0.0794	0.0914	0.0611	0.0897	0.0856	0.1055	0.0861	0.055	0.057	0.0712	0.0622	0.054	0.0646	0.0922	0.0547	0.0476	0.0528	0.0337
13	0.0728	0.0719	0.0793	0.087	0.0752	0.073	0.0614	0.0657	0.0654	0.0658	0.0627	0.0719	0.0748	0.0696	0.0472	0.0571	0.0423	0.0703	0.0764	0.0832	0.073	0.0694	0.0607	0.0368	0.0402

4 Regionalization and Treatment of Gulf Coast

4.1 INTRODUCTION

The ground motion characterization GMC developed in Sections 2 and 3 provides estimates of median ground motions as a function of magnitude and distance for a reference hard rock site condition defined by Hashash et al. [2014] and Campbell et al. [2014]. The model was developed to apply to the CEUS region covered by the EPRI/DOE/NRC [2012] CEUS SSC model. This region extends from the Rocky Mountains to the Atlantic coast and from southern Texas into southeastern Canada. The GMC developed in Sections 2 and 3 uses as a basis candidate GMMs developed for general application in the CENA region that encompasses eastern Canada along with the CEUS. The issue addressed in this section is the extent to which this model can be applied throughout the CEUS region and the necessary adjustments needed for application in specific sub-regions.

4.2 SUMMARY OF STUDIES OF GMC REGIONALIZATION IN THE CEUS

4.2.1 EPRI [1993]

Prior to the NGA East Project, the most comprehensive evaluation of GMC regionalization in the CEUS was performed as part of the EPRI [1993] study. EPRI [1993] investigated the effects of differences in crustal characteristics across the CEUS on the rate of attenuation of earthquake ground motions. The CEUS was divided into 16 regions on the basis of crustal velocity structure and 11 regions on the basis of differences in the intrinsic attenuation rate, as parameterized by the quality factor Q. Figure 4.1 shows the resulting regionalizations. EPRI [1993] performed numerical simulations to investigate the degree to which differences in crustal structure, Q, and earthquake focal depth in the various sub-regions shown on Figure 4.1 produce significant differences in the attenuation of earthquake ground motions. Based on analyses of these simulations, EPRI [1993] concluded that the CEUS should be separated into two primary sub-regions, a mid-continent region and a Gulf Coast region, as shown on Figure 4.2. The EPRI [1993] Gulf Coast region corresponded to their crustal region 4, shown on the top panel of Figure 4.1, and the mid-continent region encompasses the rest of the CEUS. EPRI [1993] then developed GMMs for these two regions. EPRI [1993] did note that a third sub-region could be defined (corresponding to crustal regions 7 and 13 on Figure 4.1) in which ground motion amplitudes may be significantly lower than those for the mid-continent region in the limited distance range of 80 to 150 km and suggested that this could be accounted for in site-specific studies. For application in cases where the source-to-site travel path crosses the sub-region

boundary, EPRI [1993] suggested comparing the results obtained using the models for the two sub-regions and using the highest of the two.

4.2.2 EPRI [2004]

EPRI [2004] developed an updated GMC for the CEUS in one of the first applications of the SSHAC Level 3 process defined in Budnitz et al. [1997]. The primary focus of the EPRI [2004] study was to incorporate the significant effort on ground motion model development that occurred since the completion of the EPRI [1993] study into an updated GMC. The EPRI [2004] study adopted the EPRI [1993] regionalization model shown on Figure 4.2 primarily on the basis of its acceptance by the participants in the project workshops. EPRI [2004] developed GMMs for the two sub-regions, with the Gulf Coast model created by applying scaling factors to the mid-continent model to account for differences in crustal structure and Q. EPRI [2004] indicated that for cases where the source-to-site path crosses the sub-region boundary one could either follow the suggestion of EPRI [1993] of using the highest of the two predictions or could select the model that was assessed to best represent the travel path.

4.2.3 EPRI [2013]

EPRI [2013] performed a SSHAC Level 2 study to update the EPRI (2004) GMC to incorporate the results of an additional decade of research on ground motion modeling, and the available results being developed as part of the NGA East project. The EPRI [2013] study adopted the concept developed by EPRI [1993] of two primary sub-regions, the mid-continent and Gulf Coast regions, but performed additional evaluations to refine the sub-region boundaries. EPRI [2013] found that the preliminary results of crustal regionalization of the CEUS being performed for the NGA East Project [Mooney et al. 2012], defined a Gulf Coast crustal region that corresponded closely with the boundaries of three seismotectonic source zones for distributed seismicity developed by EPRI/DOE/NRC [2012]. This result is not surprising as the EPRI/DOE/NRC [2012] seismotectonic source zones were characterized in part by differences in crustal structure. Accordingly, EPRI [2013] proposed the modified Gulf Coast GMM sub-region shown on Figure 4.3 for use in seismic hazard analyses in conjunction with the EPRI/DOE/NRC [2012] SSC model. One notable difference between the EPRI [2013] and EPRI [1993] Gulf Coast Regions is that the EPRI [2013] region encompasses all of the Mississippi Embayment extending to the New Madrid region. The EPRI [2013] Gulf Coast Region also encompasses all of Florida. Previously, the EPRI [1993] characterization was ambiguous about the regionalization in southern Florida.

EPRI [2013] performed analyses of the available ground motion data recorded by the Earthscope Transportable Array (TA) in the Mississippi Embayment and the central Gulf Coast Region, confirming differences in ground motion attenuation characteristics in this region compared to the surrounding regions of the central US. EPRI [2013] used the results of these analyses to develop adjustments to the updated mid-continent GMM for application in the Gulf Coast Region. For those cases where the source-to-site path crosses the sub-region boundary, EPRI [2013] suggested that one could compute a weighted logarithmic average of the ground motion predictions from the two sub-region GMMs based on the relative path lengths in the two sub-regions.

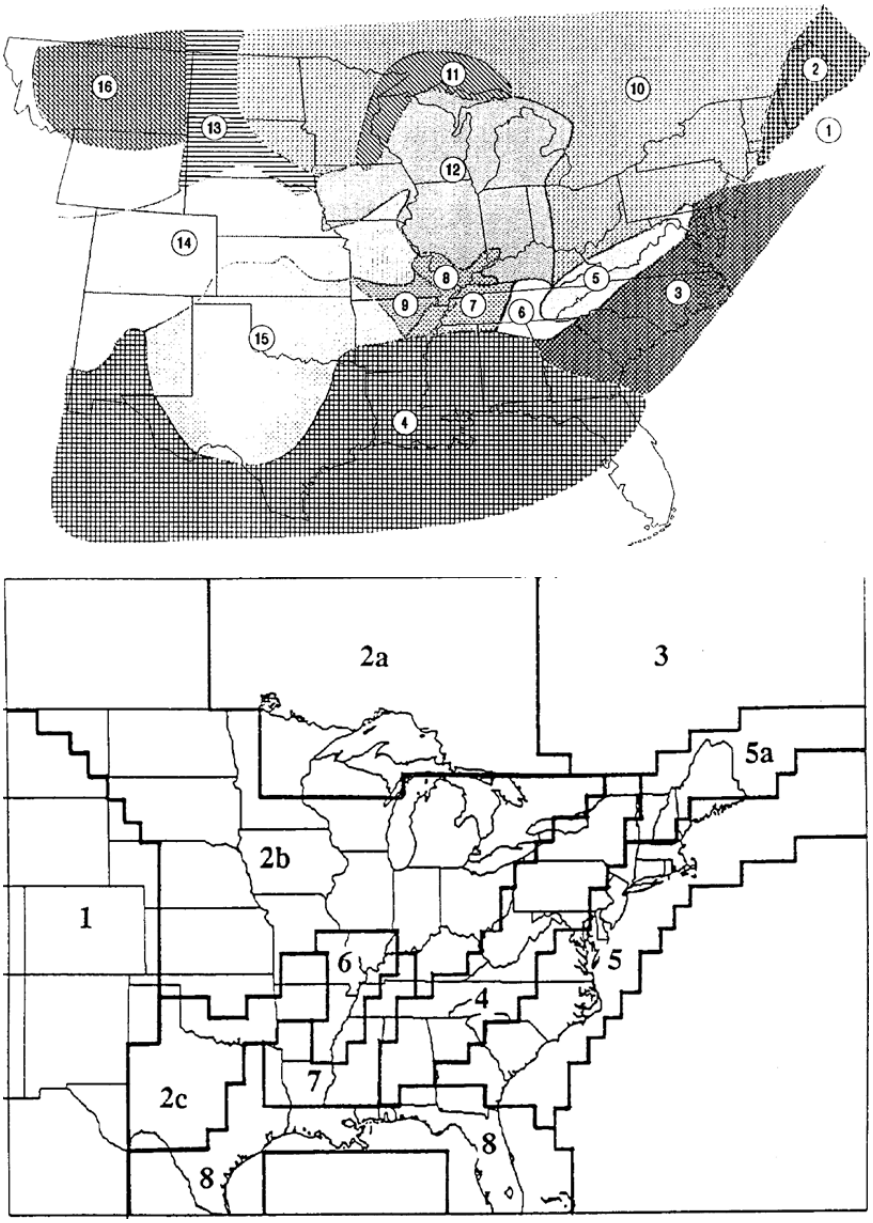

Figure 4.1 **Regionalization of the CEUS studied by EPRI [1993]. Top: regionalization of crustal seismic velocity structure into 16 regions. Bottom: Intrinsic seismic damping Q-value regionalization into eight regions.**

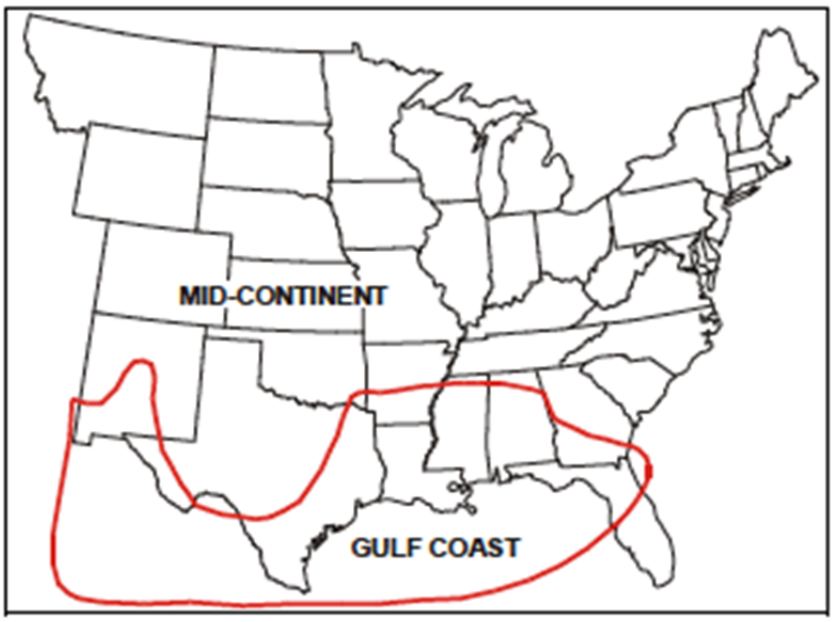

Figure 4.2 **Mid-continent and Gulf Coast GMC Regionalization defined by EPRI [1993], from EPRI [2004].**

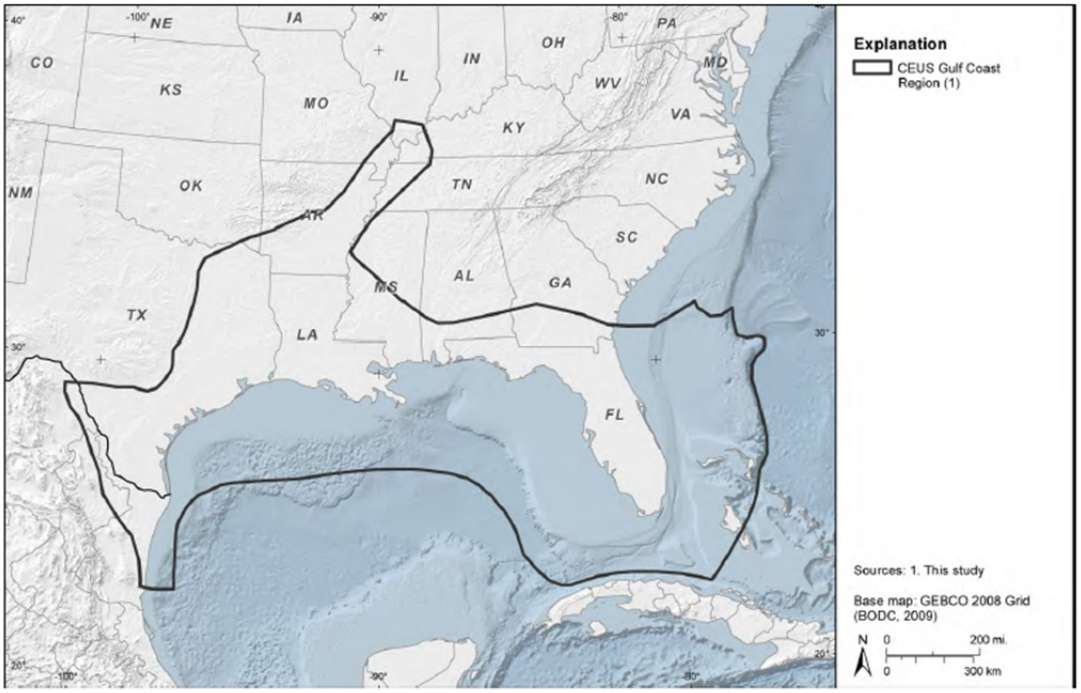

Figure 4.3 **Gulf Coast GMC Regionalization defined by EPRI [2013].**

4.2.4 Dreiling et al. [2014]

As part of the NGA East Project, Dreiling et al. [2014] performed an extensive evaluation of GMM regionalization following the general approach used by EPRI [1993]. The CEUS was divided into four primary sub-regions on the basis of differences in crustal structure and tectonic history. These regions are shown on Figure 4.4. Dreiling et al. [2014] developed assessments of crustal velocity structure and Q for each sub-region, including variability in these parameters. The distributions for crustal properties within each region as well as distributions of earthquake focal depths were used in ground motion simulations to develop distributions of earthquake ground motions for a range of magnitudes and distances. The ground motion distributions for the four sub-regions defined on Figure 4.4 were compared to determine if significant differences exist. The results of the analysis confirm past conclusions. The attenuation characteristics in the Atlantic Coastal Plain and Appalachian Province were found to be similar to those for central North America, while those for the Mississippi Embayment/Gulf Coast region were significantly different. Dreiling et al. [2014] conclude that differences in the seismic velocity structure of the crust, rather than the Q-factor, had the largest effect on the differences in attenuation of ground motions in the distance range they evaluated (35 to 500 km).

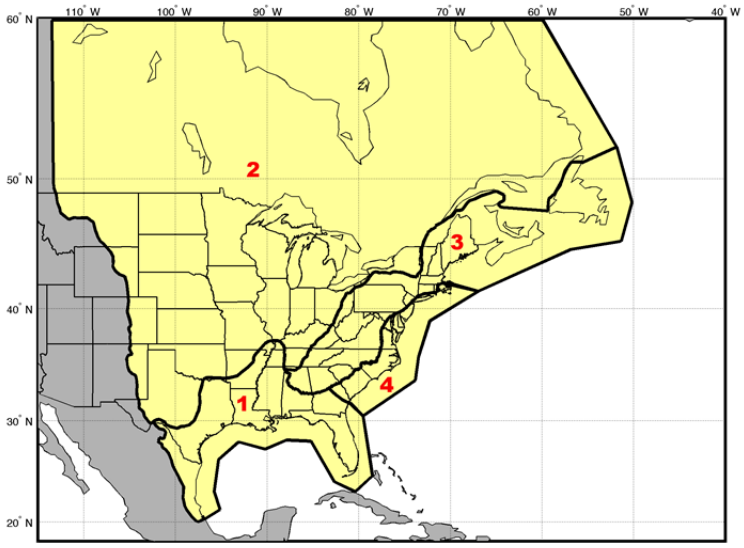

Figure 4.4 **Four regions defined for CENA by Dreiling et al. [2014]. The regions have been numbered as follows for the NGA-East database: (1) Mississippi Embayment/Gulf Coast region; (2) Central North America; (3) the Appalachian Province; and (4) the Atlantic Coastal Plain. Together, Regions 2, 3 and 4 form the larger mid-continent region.**

4.2.5 Gallegos et al. [2014]

Gallegos et al. [2014] performed a Q tomography study for the CEUS using the Earthscope TA recordings filtered to the narrow frequency band of 0.5 to 1.5 Hz. They produced the Q_0 maps shown in Figures 4.5 and 4.6 using the two-station method (TSM) and reverse two-station method (RTSM), respectively. Their Q_0 maps show low values along the Gulf Coast (GCP) and scattered areas of lower Q in other parts of the CEUS, including the Realfoot Rift region (RFR).

Gallegos et al. [2014] state that the TSM and RTSM results are generally similar, but there is lower resolution in the RTSM results due to less extensive ray-path coverage. They do indicate that both methods show lower Q in the GCP and RFR regions.

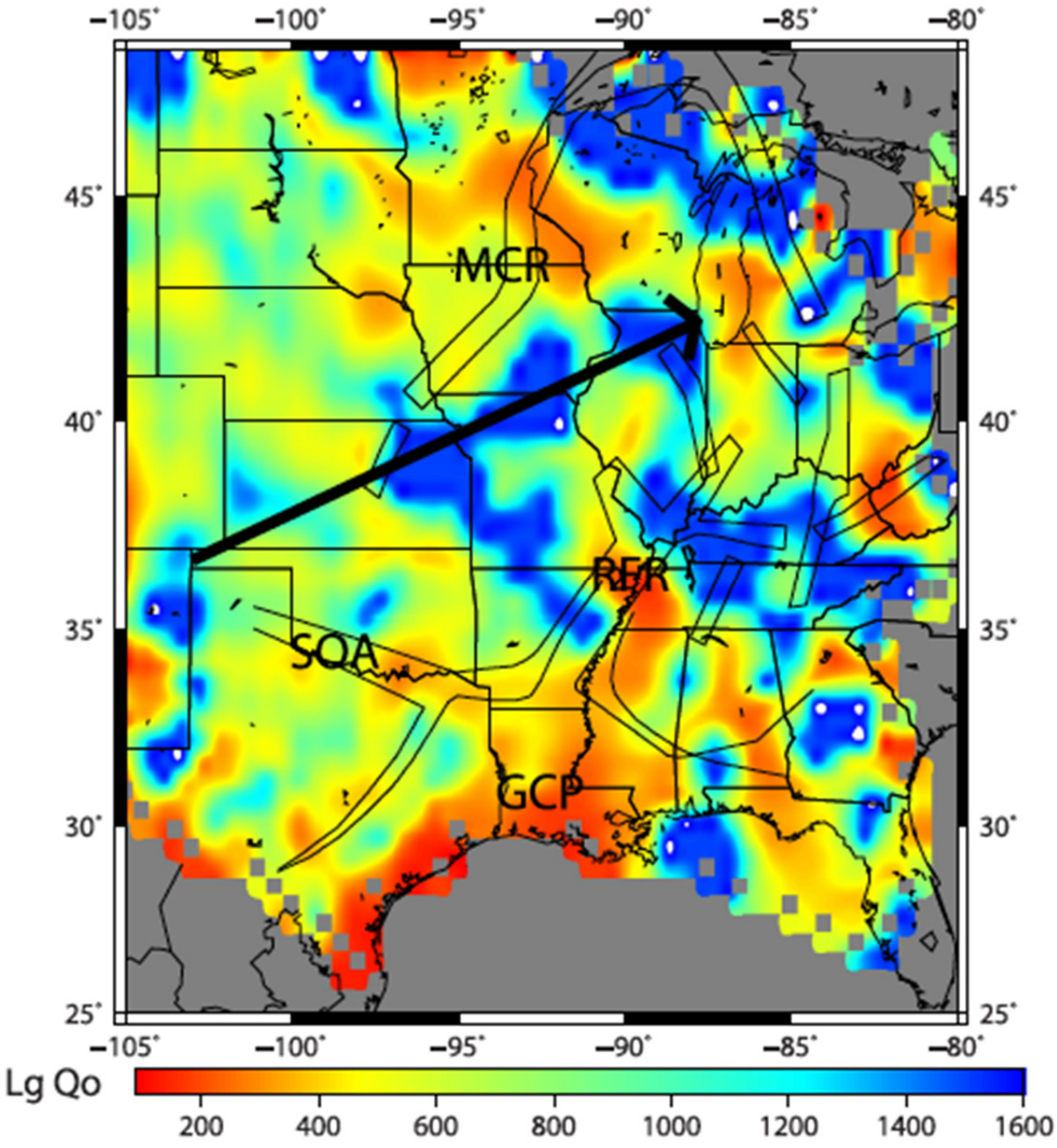

Figure 4.5 Two-station Lg attenuation map of the CEUS [Gallegos et al., 2014].

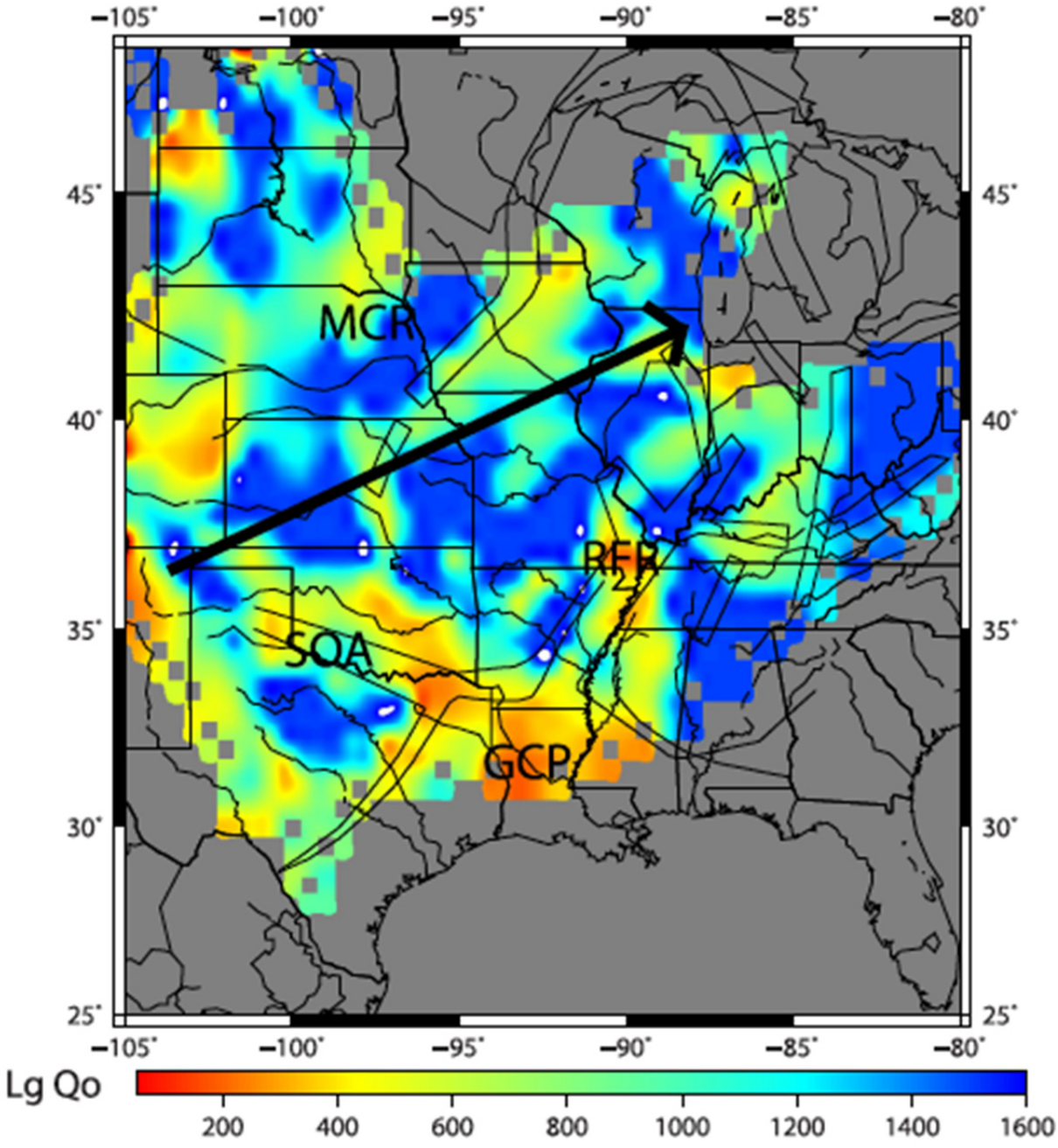

Figure 4.6 **Reverse two-station Lg attenuation map of the CEUS [Gallegos et al., 2014].**

4.2.6 Cramer and Al Noman [2016]

Cramer and Al Noman [2016] performed an analysis of TA recordings to identify regional differences in Q within the CEUS. The dataset used included recordings obtained over much of the southeastern US. They fit a model of the form:

$$\ln(PSA) = A + CR - 0.5\ln(R) \tag{4.1}$$

to 1 Hz and 5 Hz spectral accelerations recorded by the TA stations at distances beyond 150–200 km from the causative earthquakes., with the coefficients A and C determined by regression. The apparent Q as a function of frequency f is then computed by the relationship

$$Q(f) = -\pi f / C\beta \tag{4.2}$$

where β is the crustal shear wave velocity, taken to be 3.5 km/sec. Cramer and Al Noman [2016] use the dense grid of TA recordings to identify locations of significant changes in the slope parameter C of Equation (4.1) that indicate the transition from the higher Q of the mid-continent region to the lower Q of the Gulf Coast region. Figure 4.7 shows their proposed Q regionalization boundaries for earthquakes occurring outside of the Gulf Coast Region and Figure 4.8 shows their proposed Q boundaries for earthquakes occurring within or near the Gulf Coast Region. They define separate boundaries based on 1 Hz and 5 Hz motions. The Cramer and Al Noman [2016] Gulf Coast Q region is smaller than the Gulf Coast Region proposed by Dreiling et al. [2014], extending only part way up the Mississippi Embayment and including only the western portion of Florida.

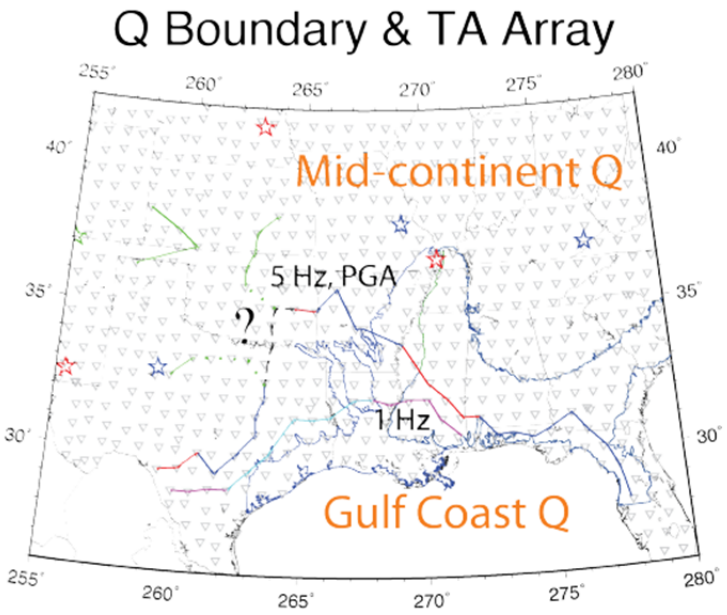

Figure 4.7 **Boundary between mid-continent and Gulf Coast *Q* regions for earthquakes occurring outside of the Gulf Region proposed by Cramer and Al Noman [2016] for 5 Hz and 1 Hz spectral accelerations.**

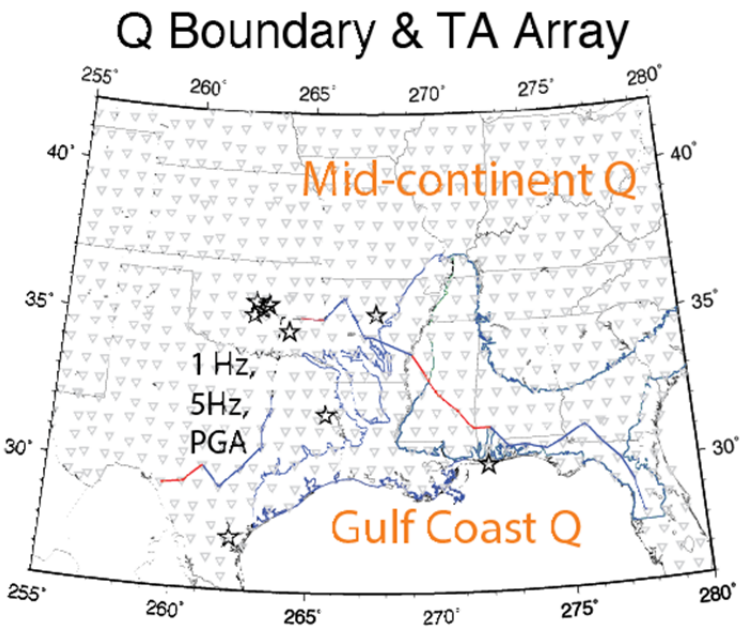

Figure 4.8 **Boundary between mid-continent and Gulf Coast *Q* regions for earthquakes occurring within or near the Gulf Region proposed by Cramer and Al Noman [2016] for 5 Hz and 1 Hz spectral accelerations.**

4.3 RECOMMENDATION FOR REGIONALIZATION

The studies summarized above consistently defined a division of the CEUS into two sub-regions with significant differences in attenuation characteristics, a Gulf Coast Region and a mid-continent region. The recent advances in mapping crustal structure and the dense recordings from the Earthscope TA project have produced refinements to the boundary between these two regions from those originally proposed by EPRI [1993] based on more limited data. The regionalization proposed by Dreiling et al. [2014] is based primarily on crustal structure, which they conclude is the most important factor in producing differences in attenuation. The Cramer and Al Noman [2016] regionalization is based solely on differences in Q derived from recorded ground-motion data from a more extensive coverage of the southeastern U.S. than was available at the time of the Dreiling et al. [2014] study. The Cramer and Al Noman [2016] Gulf Coast Region represents a subset of the Dreiling et al. [2014] Gulf Coast region in which the Reelfoot Rift portion of the upper Mississippi Embayment and the Florida Peninsula are considered to be part of the mid-continent region. Although Cramer and Al Noman [2016] state that their results are similar to those of Gallegos et al. [2014], one could argue that the Gallegos et al. [2014] Q_0 maps shown on Figures 4.5 and 4.6 indicate that the low Q region on the Gulf Coast extends up the Mississippi Embayment to the New Madrid region, consistent with the Dreiling et al. [2014] definition of the Gulf Coast region.

The difference in the proposed location of Gulf Coast/mid-continent boundary between the Dreiling et al. [2014] and Cramer and Al Noman [2016] studies is considered to be representative of the current state of epistemic uncertainty in GMM regionalization for the CEUS. This uncertainty should be taken into account in applying the Gulf Coast Region GMM adjustments presented in Section 4.4.

4.4 GROUND-MOTION ADJUSTMENT MODELS FOR THE GULF COAST REGION

4.4.1 Alternate Gulf Adjustment Models

The NGA-East GMMs documented in Chapter 3 were developed for the mid-continent region and the seed models were developed or calibrated using mostly Region 2 data (Figure 4.4). To account for the differences in crustal structures and Q estimates for the Gulf Coast, the NGA-East Project developed Gulf Coast adjustments models to be applied to the median GMMs. It is important that the NSHM hazard estimates capture these effects, which tend to be more pronounced when a large portion of the wave travel path is included in the Gulf Coast. The adjustment models are summarized in this section. The development of these adjustment models is described in detail in PEER [2015b] and is not repeated here.

Two groups built on their candidate median GMM work to develop Gulf Coast adjustment models. The first group is composed of R.B. Darragh, N.A. Abrahamson, W.J. Silva, and N. Gregor who developed the median DASG GMMs documented in Chapter 3 of PEER [2015a]. The second group consists of J. Hollenback, N. Kuehn, C.A. Goulet, and N.A. Abrahamson who developed the PEER GMMs documented in Chapter 11 of PEER [2015a].

The model development was based on the assumption that the Gulf Coast boundary was as described in Dreiling et al. [2014]. The data available in the NGA-East database [Goulet et al. 2014] with both the earthquake source and the site located in the Gulf Coast are relatively sparse. Figures 4.9 and 4.10 summarize the magnitude and distance ranges covered in the NGA-East database for the Gulf Coast region. Both DASG and PEER used this dataset in their model development (see PEER [2015b] for details on data selection from each group). The regionalization assumption implies that at least some of the data includes paths sampling the Mississippi Embayment Region (Figure 4.9) but not paths sampling the Florida area. The inclusion of paths spanning the Mississippi Embayment may slightly bias expected Gulf Coast results if another region boundary is considered (such as the Al Noman and Cramer [2016] model).

The two groups adopted slightly different approaches, which were consistent with their original candidate median GMM development. DASG uses a theoretical-based approach based on the point-source stochastic model, constraining the point-source parameters by data inversions from the Gulf Coast region. The PEER group used their empirically based Fourier amplitude spectrum (FAS) functional form, which they recalibrated with the Gulf Coast data. Both groups considered alternative formulations to model ground motions from the Gulf Coast from which they selected a preferred model. Once their respective Gulf Coast models were developed, both groups computed ratio of response spectra for various **M** and R_{RUP} conditions and defined models as a distance-dependent ratio of PSA of the form:

$$f(\theta) = \frac{\mathrm{PSA}_{GC}}{\mathrm{PSA}_{MC}} \tag{4.3}$$

where PSA_{GC} and PSA_{MC} are the PSA values from the Gulf Coast and Mid-Continent regions, respectively, and θ is the set of predictive parameters. The models are shown in Figure 4.10 for a subset of frequencies (the PEER model is frequency independent). Both models show ratios essentially equal to unity for roughly the first 100 km: the DASG ratio decays very slowly from

distance zero and the PEER model is exactly 1 until 100 km. The unit ratio close in and the monotonic decrease in ratios with distance implied that only differences in attenuation are captured by the models. This may appear counter-intuitive given the deep sediment deposits present in the Gulf Coast. However, the ratios were computed for the same hard rock conditions as the candidate medians GMMs (V_{S30} =3000 m/sec and kappa (κ =0.006 sec), thus neglecting expected site effects from the geological conditions. It is expected that defining an alternate set of reference site conditions for the Gulf Coast, which would involve additional work on kappa, would be more appropriate in capturing regional differences in ground motions for a wide range of site conditions (tasks could include extending the work from Chapman and Conn [2016] to shear waves). Estimation of kappa and regional site conditions outside of for the reference rock conditions was not part of the NGA-East Project scope.

The ratios from each group are provided in Electronic Appendix B in tabular form. To adjust ground-motion values from the mid-continent to the Gulf Coast region requires multiplying the original median GMM predictions by the Gulf Coast ratios provided in Appendix B.

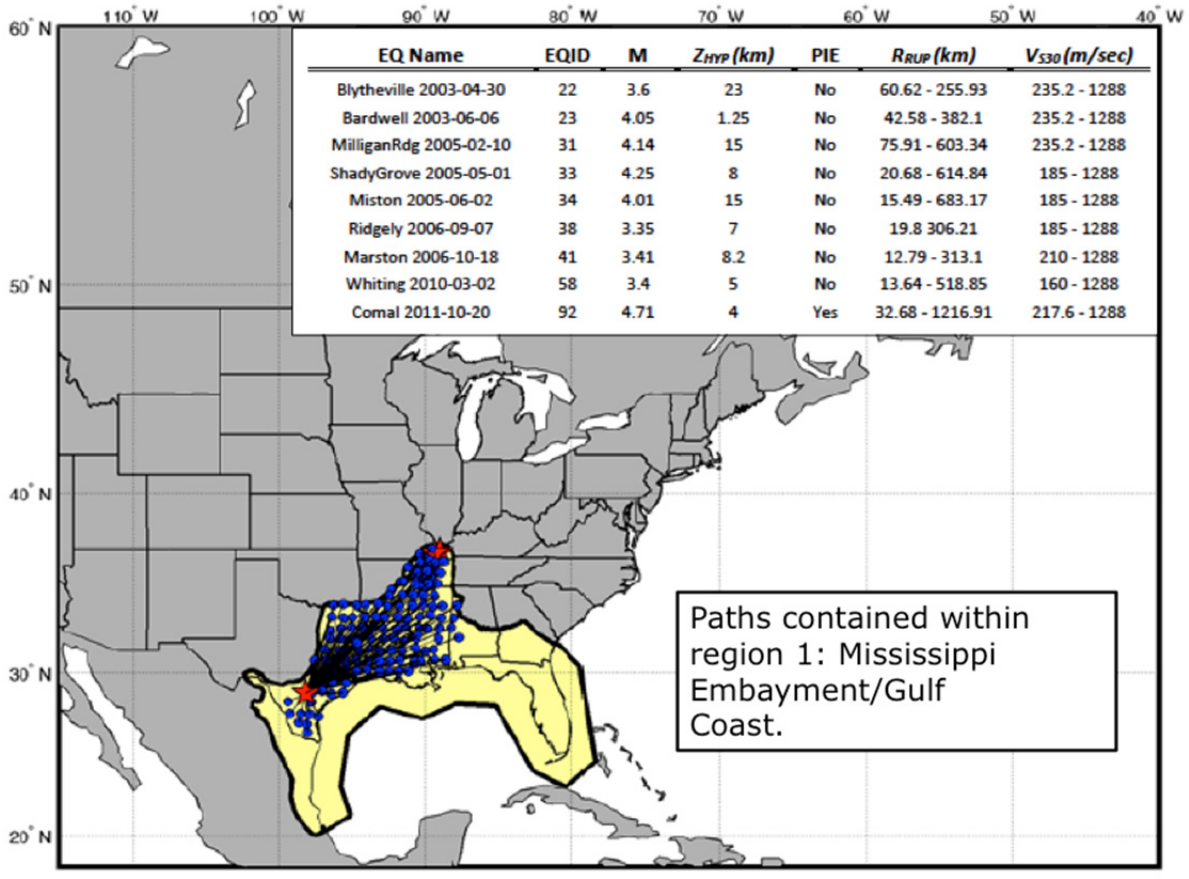

EQ Name	EQID	M	Z_{HYP} (km)	PIE	R_{RUP} (km)	V_{S30} (m/sec)
Blytheville 2003-04-30	22	3.6	23	No	60.62 - 255.93	235.2 - 1288
Bardwell 2003-06-06	23	4.05	1.25	No	42.58 - 382.1	235.2 - 1288
MilliganRdg 2005-02-10	31	4.14	15	No	75.91 - 603.34	235.2 - 1288
ShadyGrove 2005-05-01	33	4.25	8	No	20.68 - 614.84	185 - 1288
Miston 2005-06-02	34	4.01	15	No	15.49 - 683.17	185 - 1288
Ridgely 2006-09-07	38	3.35	7	No	19.8 306.21	185 - 1288
Marston 2006-10-18	41	3.41	8.2	No	12.79 - 313.1	210 - 1288
Whiting 2010-03-02	58	3.4	5	No	13.64 - 518.85	160 - 1288
Comal 2011-10-20	92	4.71	4	Yes	32.68 - 1216.91	217.6 - 1288

Figure 4.9 **List of earthquake events used in the Gulf Coast adjustment models. Red stars show the events locations, blue dots show station locations and the blue lines show the sampled wave propagation paths.**

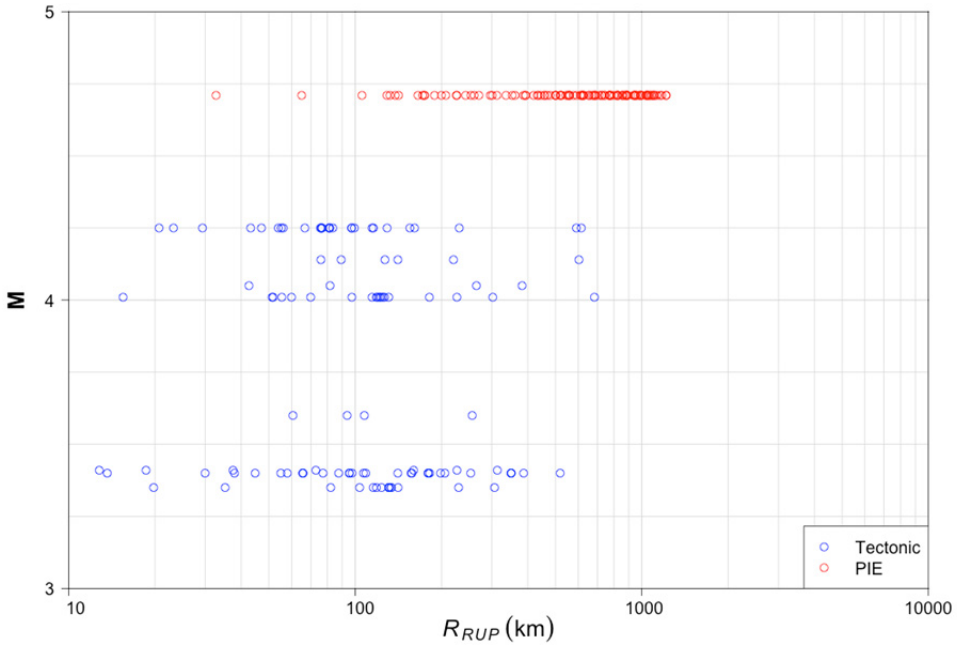

Figure 4.10 **Magnitude (M) and rupture distance (R_{RUP}) ranges for records in the NGA-East database from Path Region 1 (i.e., both the earthquake source and the site are located in the GC region).**

4.4.2 Application Recommendation

Both adjustment models are based on limited datasets and yet provide alternate estimates for the Gulf Coast adjustment. The USGS NSHMs team will have to consider this as a source of epistemic uncertainty.

The Gulf Coast models can be used as-is when the complete path (source-to-site) is contained in the Gulf Coast. Rules for the treatment of paths including a regional boundary crossing are available in EPRI [1993] for site-specific analyses.

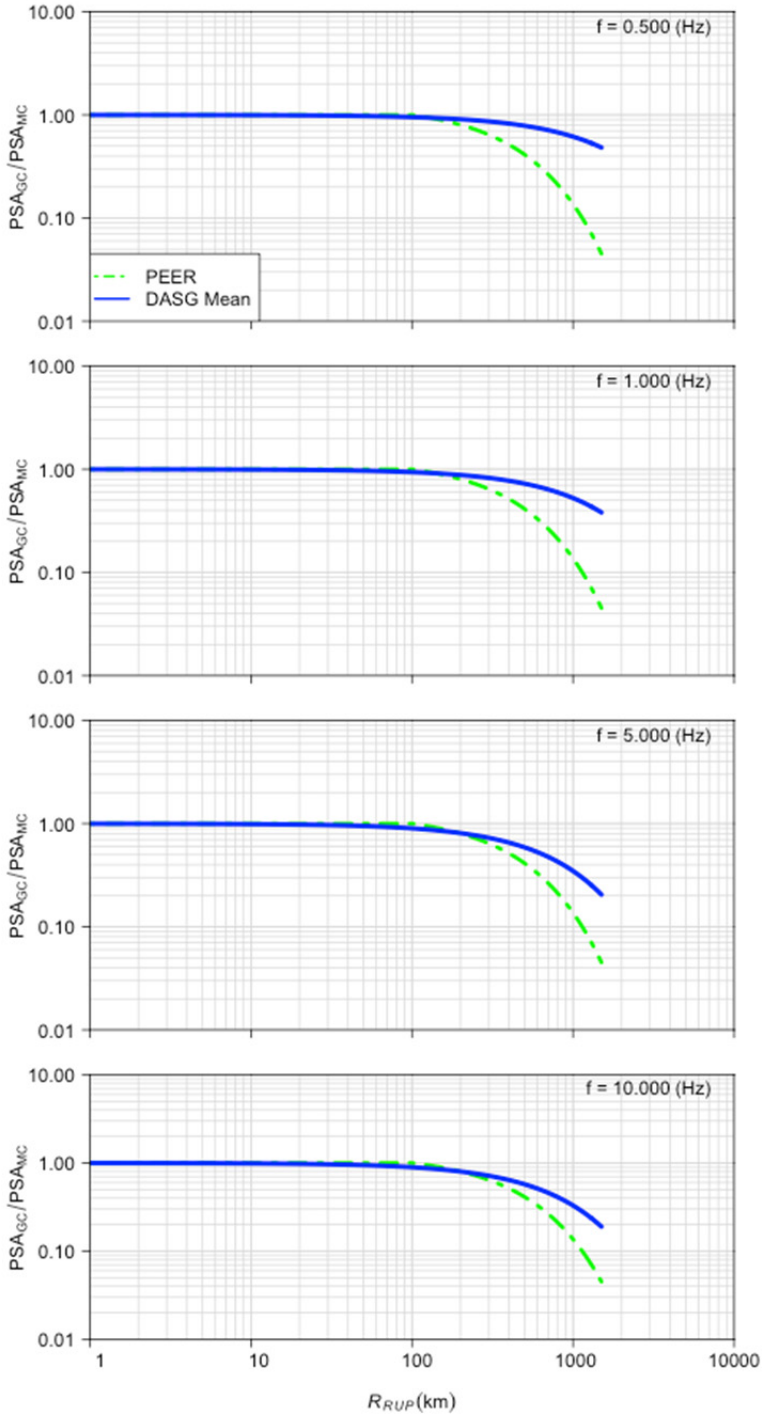

Figure 4.11 **Comparison of Gulf Coast adjustment ratios between DASG model (blue) and the PEER model (green) plotted against distance for PSA at frequencies 0.5, 1.0, 5.0, and 10.0 Hz.**

5 Aleatory Variability

5.1 OVERVIEW

Empirical ground motion data from CENA were used to analyze the components of ground motion variability (τ, ϕ, ϕ_{SS}, and ϕ_{S2S}) in CENA. Trends of ground motion variability with parameters such as magnitude, distance, and V_{S30} were analyzed and compared to trends of ground motion variability in other regions, particularly the Western United States (WUS) using the NGA-West2 dataset. The CENA dataset is limited in magnitude range to small-to-moderate magnitudes and in frequency content to frequencies between 1 and 10 Hz due to the bandwidth limitations of the recordings. Therefore, standard deviation models developed using the CENA ground-motion data cannot be reliably extrapolated to large magnitudes and to frequencies outside of 1 to 10 Hz. As a result, standard deviation models from other regions such as WUS and Japan were evaluated for applicability to CENA and to inform the extrapolation of CENA standard deviations and overcome data limitations. A detailed description of the components of ground motion variability is presented in Al Atik et al. [2010] and Al Atik [2015]. This chapter uses the terminology described in Al Atik et al. [2010] to refer to the components of ground motion variability.

Analysis of the components of the ground motion variability (τ, ϕ, ϕ_{SS}, and ϕ_{S2S}) using the NGA-East CENA dataset and the development of candidate aleatory variability models for CENA are described in Al Atik [2015]. Candidate standard deviation models were developed for CENA for each of the components of the ground motion variability. Three models were presented for τ to address the uncertainty in the large magnitude extrapolation: CENA constant model, CENA magnitude-dependent model, and global model. Similarly, three models were presented for ϕ_{SS}: CENA constant model, CENA magnitude-dependent model, and global model. Data from CENA were used to derive a CENA ϕ_{S2S} extrapolated to frequencies outside of 1 to 10 Hz using results from analysis of Japanese data. Mean and standard deviations of each of the candidate models were quantified. Standard deviation models for single-station σ and ergodic σ are obtained by combining the appropriate components of the ground motion variability.

This chapter summarizes the evaluation of the candidate aleatory variability models for CENA performed by the NGA-East Technical Integration (TI) Team. This evaluation is presented separately for the components τ, ϕ_{SS}, and ϕ_{S2S} of the ground motion variability. The limitations of the developed models are discussed. Finally, a recommendation is presented for the total ergodic standard deviation model to be used in the development of the USGS NSHMs for Central and Eastern US.

5.2 SUMMARY OF NGA-EAST MODELS

5.2.1 Between-Event Variability (Tau)

The NGA-East Project Team evaluated 3 candidate models for τ:

Global τ model,
CENA constant τ model (homoscedastic), and
CENA magnitude-dependent τ model.

The derivation of the 3 candidate τ models (mean and SD[τ^2]) is described in Al Atik [2015] and a brief description is given here.

The global τ model is based on the average of the variance of τ for the four NGA-West2 models: Abrahamson et al. (2014) (ASK14), Boore et al. (2014) (BSSA14), Campbell and Bozorgnia (2014) (CB14), and Chiou and Youngs (2014) (CY14). The Idriss (2014) model was not used because ground motion residuals were not partitioned into between-event and within-event residuals for this GMPE. These models were chosen based on the general similarity of τ for CENA and the NGA-West2 models in the limited magnitude and frequency range of the CENA data. Moreover, the NGA-West2 τ models were derived from a large and uniformly-processed global dataset and are applicable to a wide magnitude range (**M**3.0 to 8.0 or 8.5). The global τ model is period-independent but magnitude-dependent with 4 magnitude breaks at **M** 4.5, 5.0, 5.5, and 6.5. The standard deviation of the global τ model considers both the between-model variability (standard deviation of τ^2 for the four underlying models) and within-model variability calculated as part of the regressions conducted for the CY14 model (Bob Youngs, personal communication).

CENA tectonic data with **M** greater than 3.0 were used to construct a τ model. Since CENA data are limited in magnitude range to a maximum **M** of about 5.5, two alternative models (constant and magnitude-dependent) were evaluated using the CENA data to address the uncertainty in the extrapolation of τ to magnitudes larger than 5.5. Because CENA data suffer from frequency bandwidth limitations, CENA τ values were averaged in the frequency range of 1 to 10 Hz to obtain the proposed CENA constant τ model (τ = 0.37 natural log units) which is magnitude-independent and period-independent. The variability in τ^2 was evaluated using the CENA data. This variability in τ^2 was smaller than that observed for the global τ^2 model which is based on a bigger dataset. As a result, the variability in the global τ^2 model at **M** = 5.0 was adopted as the variability in the constant CENA model.

Because studies of between-event variability based on large datasets that cover a wide magnitude range generally note a magnitude-dependent trend in τ whereby τ decreases as **M** increases and reaches a constant value at **M**6 to 7.5 (ex. NGA-West2 models), a CENA τ model was developed to incorporate the magnitude-dependence observed in the global τ models. This model has 3 magnitude breaks (**M**5.0, 5.5, and 6.5). CENA data was used to derive the coefficient of τ for **M** less than or equal to 5.0 while the magnitude scaling for the larger magnitudes was based on the magnitude scaling of the global τ model. The variability of the magnitude-dependent CENA τ model was evaluated and the SD[τ^2] values were adopted based on the CENA data for **M** less than or equal to 5.0 and the global model for the larger magnitudes.

All three candidate τ models are frequency-independent. A comparison of these models as a function of magnitude is shown in Figure 5.1. In the evaluation of the three candidate τ models, the Project Team strongly favored the global model over the two CENA models. This is due to three factors:

The global model is built using a large uniformly-processed global and broad dataset while the CENA dataset used to build the τ models (**M** larger than 3.0 and tectonic events only) is significantly smaller.
CENA dataset is limited to **M** less than 5.5 and therefore does not extrapolate reliably to large magnitudes. On the other hand, the global model is based on data from a wide magnitude range and is reliable at large magnitudes.
CENA dataset is limited to the frequency range of 1 to 10 Hz. Beyond this range, the model is simply extrapolated with a constant.

The statistical significance of the difference between global and the CENA τ for **M** less than 5.0 was evaluated by the Project Team using the F-test of equality of variance. The results of this test indicated that the equality of τ^2 between CENA and NGA-West2 for **M** less than or equal to 5.0 cannot be rejected at 5% significance level. Based on these results, the Project Team decided to give the CENA τ models zero weights and to fully adopt the global τ model. The logic tree for τ is shown in Figure 5.2. Values of τ for the global model can be calculated using equation (5.1) and the model coefficients at PGV and frequencies of 0.1 to 100 Hz are presented in Table 5.1for the central, high, and low branches.

$$\tau = \begin{cases} \tau_1 & \text{for } \mathbf{M} \le 4.5 \\ \tau_1 + (\tau_2 - \tau_1) * (\mathbf{M} - 4.5) / 0.5 & \text{for } \mathbf{M} \le 5.0 \\ \tau_2 + (\tau_3 - \tau_2) * (\mathbf{M} - 5.0) / 0.5 & \text{for } \mathbf{M} \le 5.5 \\ \tau_3 + (\tau_4 - \tau_3) * (\mathbf{M} - 5.5) / 1.0 & \text{for } \mathbf{M} \le 6.5 \\ \tau_4 & \text{for } \mathbf{M} > 6.5 \end{cases} \quad (5.1)$$

Table 5.1 Coefficients of the global τ model for the central, high and low branches.

	Period (sec)	Frequency (Hz)	τ_1	τ_2	τ_3	τ_4
Central	0.01 to 10	0.1 to 100	0.4436	0.4169	0.3736	0.3415
	PGV		0.3633	0.3532	0.3340	0.3136
Low	0.01 to 10	0.1 to 100	0.3280	0.2928	0.2439	0.2343
	PGV		0.2488	0.2370	0.2278	0.2081
High	0.01 to 10	0.1 to 100	0.5706	0.5551	0.5214	0.4618
	PGV		0.4919	0.4845	0.4535	0.4333

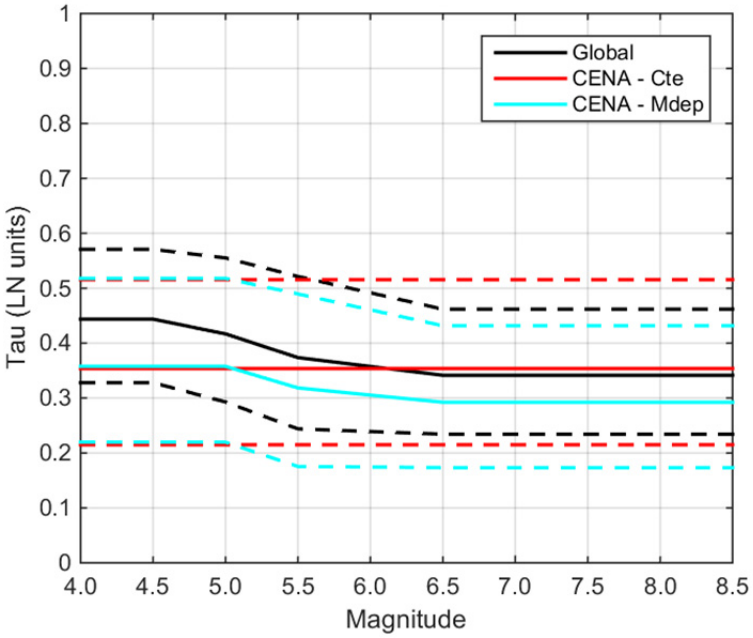

Figure 5.1 **Comparison of candidate τ models for CENA. Dashed lines represent the 5th and 95th percentiles of the models.**

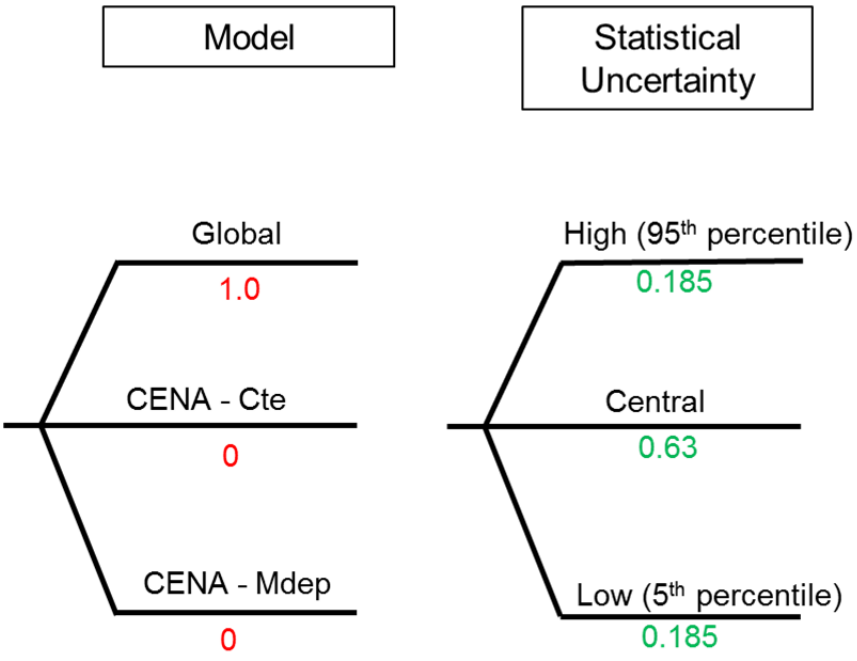

Figure 5.2 **Logic tree for τ.**

5.2.2 Single-Station Within-Event Variability (PhiSS)

In a fashion similar to the case of τ, the NGA-East Project Team evaluated three candidate ϕ_{SS} models to overcome the limitations in the magnitude range and frequency bandwidth of the CENA ground motion data. These models are:

Global ϕ_{SS} model,
CENA constant ϕ_{SS} model (homoscedastic), and
CENA magnitude-dependent ϕ_{SS} model.

The derivation of the three candidate ϕ_{SS} models (mean and SD[ϕ_{SS}^2]) is described in Al Atik [2015] and a brief description is given here.

The global ϕ_{SS} model is derived from the single-station within-event residuals of the four NGA-west2 models: ASK14, BSSA14, CB14, and CY14. The global ϕ_{SS} model is magnitude-dependent reflecting the trend observed in the binned ϕ_{SS} values with magnitude. At short spectral period, a clear dependence of ϕ_{SS} with magnitude is observed. At long spectral periods, this magnitude dependence becomes weaker and ϕ_{SS} become magnitude-independent. The uncertainty in the global ϕ_{SS} model incorporates the station-to-station variability in ϕ_{SS}, the statistical uncertainty in the ϕ_{SS} estimates, and the error in the fit of model to the binned ϕ_{SS} values with magnitude. The global ϕ_{SS} model has magnitude breaks at **M** 5.0 and 6.5 and has the following form:

$$\phi_{SS} = \begin{cases} a & \text{for } \mathbf{M} \le 5.0 \\ a + (\mathbf{M} - 5.0) * (b - a) / 1.5 & \text{for } \mathbf{M} \le 6.5 \\ b & \text{for } \mathbf{M} > 6.5 \end{cases} \quad (5.2)$$

Coefficients a and b of the model were smoothed while preserving their trend as a function of frequency. Table 5.2 lists the values of coefficients a and b for PGV and frequencies between 0.1 and 100 Hz for the central (median), high (95th percentile), and low (5th percentile) branches of ϕ_{SS}.

CENA tectonic data with minimum **M** of 3.0 and maximum R_{RUP} distance of 300 km were used to construct ϕ_{SS} models. Since CENA data are limited in magnitude range to a maximum **M** of about 5.5, two alternative models (constant and magnitude-dependent) were developed using the CENA data to address the uncertainty in the extrapolation of ϕ_{SS} to **M** greater than about 5.5. The constant CENA ϕ_{SS} model is magnitude-independent and period-independent developed using the constant ϕ_{SS} values averaged between frequency of 1 and 10 Hz (ϕ_{SS} = 0.51 natural log units). The uncertainty in the CENA constant ϕ_{SS} model is based on the station-to-station variability in ϕ_{SS} observed in the WUS and the statistical uncertainty in the ϕ_{SS} estimates from the CENA data. The values of the constant ϕ_{SS} model for the central (median), high (95th percentile), and low (5th percentile) are listed in Table 5.3.

The CENA magnitude-dependent ϕ_{SS} model was developed to incorporate the magnitude-dependence in ϕ_{SS} observed in the global ϕ_{SS} model and other large global datasets that cover a wide magnitude range. The CENA magnitude-dependent model as the same functional form as equation (5.2), whereby coefficient a was derived from the CENA tectonic data with minimum **M** of 3.0 and maximum R_{RUP} distance of 300 km. The ratios of b/a were constrained to those of the global ϕ_{SS} model. Based on the average values of coefficients a and b and their uncertainty

(station-to-station variability and statistical uncertainty in ϕ_{SS}), the coefficient of the central (median), high (95th percentile), and low (5th percentile) branches of the CENA magnitude-dependent model were derived and are listed in Table 5.4.

In the evaluation of the three candidate ϕ_{SS} models, the Project Team strongly favored the global model over the CENA models. This is due to the following factors:

Global model is developed based on a large uniformly-processed global dataset while the CENA dataset used to build the ϕ_{SS} models (**M** larger than 3.0, R_{RUP} less than 300 km, and tectonic events only) is significantly smaller.
CENA dataset is limited to **M** less than 5.5 and therefore does not extrapolate reliably to large magnitudes. On the other hand, the global model is based on data from a wide magnitude range and is reliable at large magnitudes.
CENA dataset is limited to the frequency range of 1 to 10 Hz. Beyond this range, the model is extrapolated.

Furthermore, the statistical significance of the difference between global and CENA ϕ_{SS} for **M** between 3.0 and 5.0 was evaluated by the Project Team using the F-test of equality of variance between the CENA and NGA-West2 single-station within-event residuals. Results of this test indicated that, for a significance level of 5%, the variances cannot be assumed to be equal between the CENA and NGA-West2 data at four spectral periods between 1 and 10 Hz. Based on these results and the favoring of the global model as discussed above, the Project Team assigned weights of 0.8, 0.1, and 0.1 to the global, CENA magnitude-dependent, and CENA constant ϕ_{SS} models, respectively. The logic tree of ϕ_{SS} for CENA is shown in Figure 5.3. A comparison of the three ϕ_{SS} models as a function of magnitude is given in Figure 5.4 for PGV and frequencies of 100, 10, 1, 0.2, and 0.1 Hz.

Table 5.2 Coefficients of the global ϕ_{SS} model for the central, high and low branches.

Period (sec)	Frequency (Hz)	*Global ϕ_{SS}* Model					
		Central		*High*		*Low*	
		a	*b*	*a*	*b*	*a*	*b*
0.01	100	0.5423	0.3439	0.6553	0.4446	0.4367	0.2525
0.02	50	0.5410	0.3438	0.6537	0.4452	0.4357	0.2518
0.03	33.33	0.5397	0.3437	0.6521	0.4459	0.4347	0.2510
0.04	25	0.5382	0.3436	0.6503	0.4466	0.4334	0.2503
0.05	20	0.5371	0.3435	0.6489	0.4473	0.4326	0.2496
0.075	13.33	0.5339	0.3433	0.6450	0.4489	0.4301	0.2478
0.1	10	0.5308	0.3431	0.6412	0.4505	0.4277	0.2461
0.15	6.67	0.5247	0.3466	0.6338	0.4561	0.4229	0.2478
0.2	5	0.5189	0.3585	0.6266	0.4673	0.4182	0.2600
0.25	4	0.5132	0.3694	0.6196	0.4776	0.4137	0.2712
0.3	3.33	0.5077	0.3808	0.6129	0.4879	0.4093	0.2831
0.4	2.5	0.4973	0.4004	0.6002	0.5057	0.4010	0.3037
0.5	2	0.4875	0.4109	0.5884	0.5161	0.3932	0.3142
0.75	1.33	0.4658	0.4218	0.5622	0.5264	0.3757	0.3253
1	1	0.4475	0.4201	0.5403	0.5217	0.3607	0.3263
1.5	0.67	0.4188	0.4097	0.5068	0.4985	0.3367	0.3271
2	0.5	0.3984	0.3986	0.4836	0.4818	0.3189	0.3208
3	0.33	0.3733	0.3734	0.4565	0.4556	0.2958	0.2969
4	0.25	0.3604	0.3604	0.4436	0.4437	0.2832	0.2831
5	0.2	0.3538	0.3537	0.4374	0.4381	0.2764	0.2757
7.5	0.13	0.3482	0.3481	0.4325	0.4337	0.2703	0.2691
10	0.1	0.3472	0.3471	0.4317	0.4329	0.2692	0.2679
PGV		0.4985	0.3548	0.6010	0.4296	0.4027	0.2850

Table 5.3 Values of the CENA constant ϕ_{SS} model for the central, high and low branches.

		CENA Constant ϕ_{SS} Model		
Period (sec)	**Frequency (Hz)**	***Central***	***High***	***Low***
0.01 to 10	0.1 to 100	0.5076	0.6192	0.4037
PGV		0.5461	0.6502	0.4483

Table 5.4 Coefficients of the CENA magnitude-dependent ϕ_{SS} model for the central, high, and low branches.

Period (sec)	Frequency (Hz)	*CENA Magnitude-Dependent ϕ_{SS}* Model					
		Central		*High*		*Low*	
		a	***b***	***a***	***b***	***a***	***b***
0.01	100	0.5135	0.3263	0.6267	0.4198	0.4081	0.2412
0.02	50	0.5135	0.3271	0.6267	0.4206	0.4081	0.2420
0.03	33.33	0.5135	0.3279	0.6267	0.4215	0.4081	0.2427
0.04	25	0.5135	0.3288	0.6267	0.4224	0.4081	0.2436
0.05	20	0.5135	0.3296	0.6267	0.4231	0.4081	0.2443
0.075	13.33	0.5135	0.3316	0.6267	0.4252	0.4081	0.2463
0.1	10	0.5135	0.3336	0.6267	0.4272	0.4081	0.2482
0.15	6.67	0.5135	0.3413	0.6267	0.4351	0.4081	0.2555
0.2	5	0.5135	0.3569	0.6267	0.4514	0.4081	0.2702
0.25	4	0.5135	0.3717	0.6267	0.4671	0.4081	0.2839
0.3	3.33	0.5135	0.3870	0.6267	0.4837	0.4081	0.2979
0.4	2.5	0.5135	0.4150	0.6267	0.5145	0.4081	0.3230
0.5	2	0.5135	0.4344	0.6267	0.5362	0.4081	0.3401
0.75	1.33	0.5135	0.4665	0.6267	0.5726	0.4081	0.3680
1	1	0.5135	0.4836	0.6267	0.5922	0.4081	0.3827
1.5	0.67	0.5135	0.5026	0.6267	0.6141	0.4081	0.3988
2	0.5	0.5135	0.5135	0.6267	0.6267	0.4081	0.4081
3	0.33	0.5135	0.5135	0.6267	0.6267	0.4081	0.4081
4	0.25	0.5135	0.5135	0.6267	0.6267	0.4081	0.4081
5	0.2	0.5135	0.5135	0.6267	0.6267	0.4081	0.4081
7.5	0.13	0.5135	0.5135	0.6267	0.6267	0.4081	0.4081
10	0.1	0.5135	0.5135	0.6267	0.6267	0.4081	0.4081
PGV		0.5575	0.3957	0.6789	0.4950	0.4445	0.3041

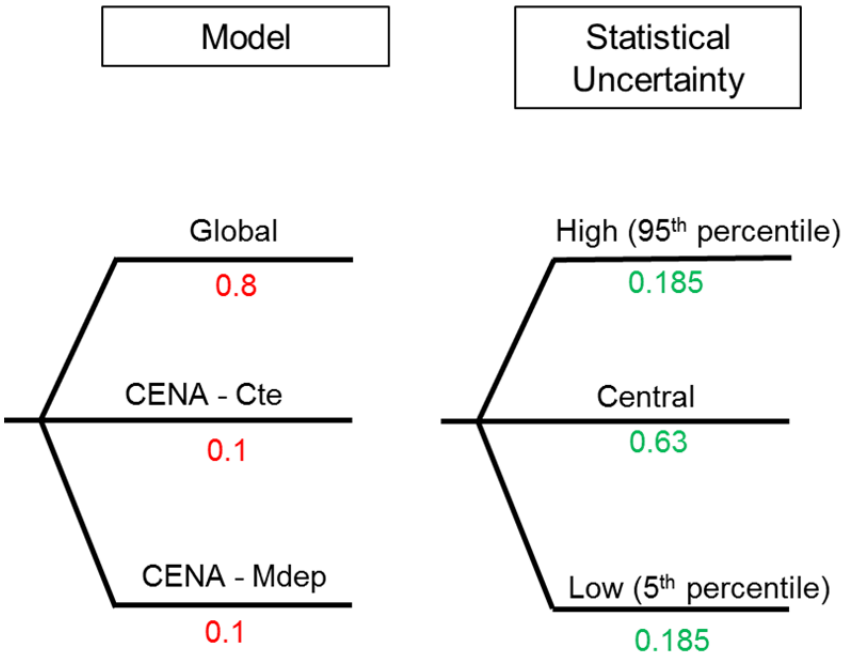

Figure 5.3 **Logic tree for ϕ_{SS}.**

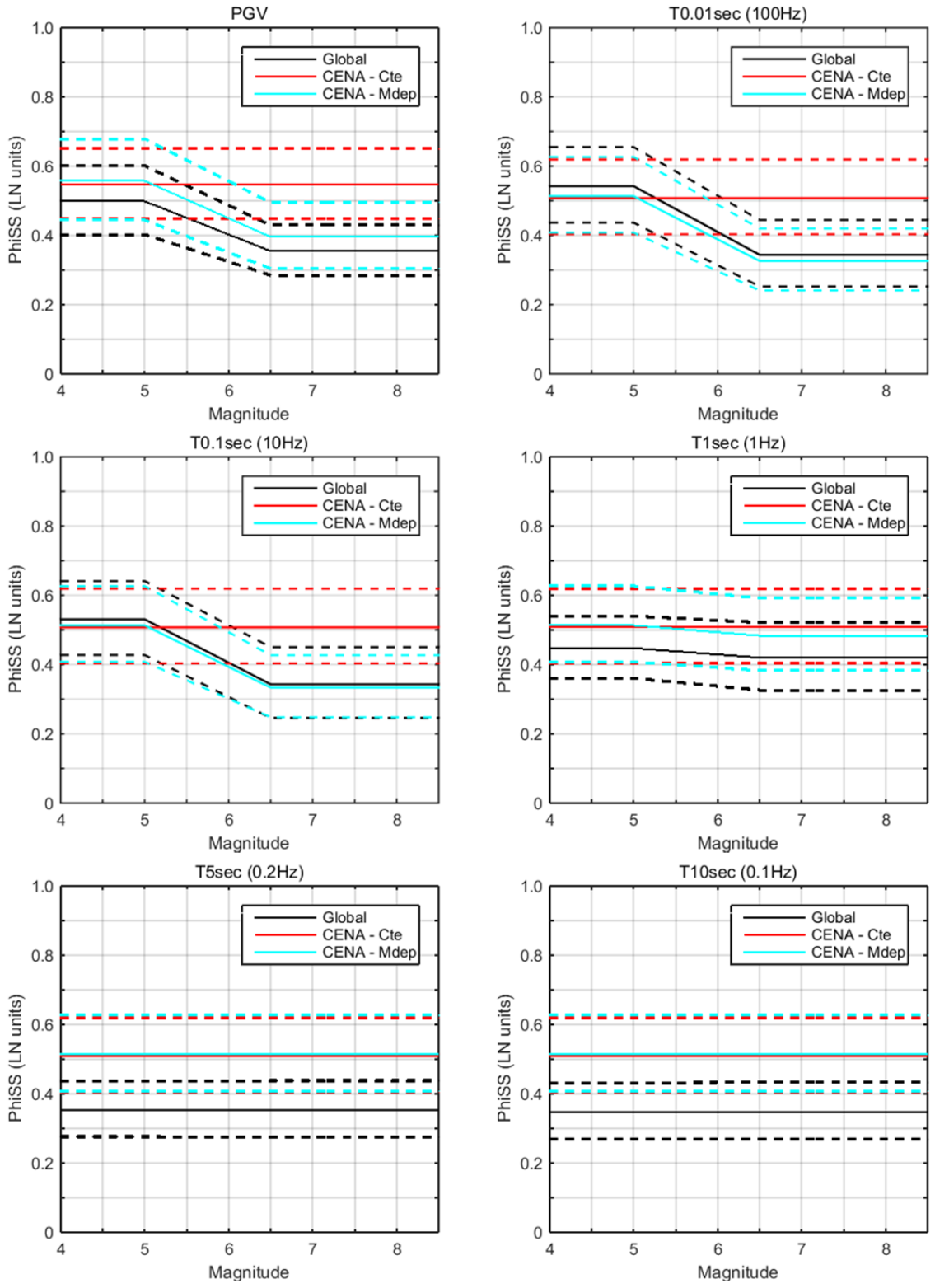

Figure 5.4 **Comparison of ϕ_{SS} models for CENA versus magnitude at PGV, and F = 100, 10, 1, 0.2, and 0.1Hz. Dashed lines represent the 5th and 95th percentiles of the models.**

5.2.3 Station-to-Station Variability (PhiS2S)

Values of ϕ_{S2S} obtained from the regression analysis of all the CENA data (Potentially-induced events, PIE and tectonic events) with a minimum of three recordings per station were used for the purpose of deriving a CENA ϕ_{S2S} model. Both tectonic events and PIE were used in order to maximize the number of stations in the analysis. Additionally, the F-test of equality of variance was conducted to test the equality ϕ_{S2S}^2 using the PIE and tectonic data versus tectonic data alone. This test indicated that the equality of variance cannot be rejected for 5% significance level for most frequencies between 1 and 10 Hz. Therefore, the use of PIE and tectonic data to derive ϕ_{S2S} for CENA was considered appropriate.

Figure 5.5 presents a comparison of the CENA ϕ_{S2S} values to those for the NGA-West2 GMPEs as well as for Japanese data [Dawood and Rodriguez-Marek 2015]. These comparisons indicate that ϕ_{S2S} for CENA is larger than that for the NGA-West2 models for frequencies greater than about 2 Hz. For the low frequencies (long spectral periods), Figure 5.5 indicates that CENA ϕ_{S2S} is smaller than NGA-West2 ϕ_{S2S}. This trend, however, at low frequencies is not reliable since the CENA data is considered useable only between 1 and 10 Hz. The small ϕ_{S2S} values at low frequencies for CENA are likely an artifact of the sharp drop in the number of stations.

Figure 5.5 also indicates that CENA ϕ_{S2S} values are comparable to Japanese ϕ_{S2S} both in terms of amplitude as well as general spectral shape. Al Atik [2015] describes additional analyses performed to investigate the impact of other factors such as regression approach, errors in assigned V_{S30}, PIE/tectonic events, and regional trade-offs on the ϕ_{S2S} results and concludes that these factors are unlikely to have controlled the CENA ϕ_{S2S} results. Based on the similarity of ϕ_{S2S} for CENA and Japan, the Project Team initially concluded that for site conditions with relatively shallow soil cover over hard rock such as typical Japanese and CENA sites, V_{S30} may not a good parameter for capturing the site response. This could explain the relatively large ϕ_{S2S} values for both CENA and Japan.

More recently, analyses were conducted to evaluate the impact of magnitude on ϕ_{S2S}. These analyses were motivated by recent observations that site response estimated using small magnitude data may not result in linear trends, as commonly assumed, and may be dependent on the magnitude and distance of the earthquake scenario. Regression analyses were performed using the within-event residuals of BSSA14 to estimate ϕ_{S2S} for three cases: using all their subset of the NGA-West2 data (**M** greater than 3.0), **M** less than 5.5, and **M** greater than 5.5. Figure 5.6 shows the resulting ϕ_{S2S} for BSSA14 and indicates a significant difference in the ϕ_{S2S} obtained using the small versus large magnitude subsets of the BSSA14 within-event residuals. ϕ_{S2S} obtained using the subset of data with **M** less than 5.5 is up to 40% smaller than ϕ_{S2S} obtained with the **M** greater than 5.5 dataset. We note that the small values of ϕ_{S2S} observed for the small magnitude dataset at long periods are affected by the small number of stations available in the small magnitude dataset at long periods (ex., 157 stations in the **M** less than 5.5 dataset versus 271 stations in the **M** greater than 5.5 dataset at $\boldsymbol{F}$ = 0.1 Hz).

The same magnitude-dependence analysis of ϕ_{S2S} was repeated using the Japanese data. We note that the minimum magnitude in the Japanese dataset is around 4.0. Figure 5.7 presents ϕ_{S2S} obtained using all the Japanese data versus two subsets of the data with **M** less than and greater than 5.5. Similar to the WUS data, Figure 5.7 indicates that ϕ_{S2S} obtained using the smaller magnitude subset of the Japanese data is generally larger than ϕ_{S2S} obtained for **M** greater

than 5.5. At long periods, the small magnitude subset of the Japanese data suffers from a limited number of stations, which could explain the reduction of ϕ_{S2S} for the small magnitude data at long periods.

The magnitude-dependence of ϕ_{S2S} observed in the WUS and the Japanese data has a significant impact for the CENA ϕ_{S2S}. The results obtained from the WUS and Japanese data indicate that ϕ_{S2S} values obtained from small magnitude data is larger than ϕ_{S2S} results for the large magnitude earthquakes, which are important for hazard analyses. Figure 5.8 shows a comparison of the CENA ϕ_{S2S} to ϕ_{S2S} obtained from BSSA14 and the Japanese data with **M** less than 5.5. We note that the CENA dataset used to estimate ϕ_{S2S} ranges in magnitude between **M** 2.57 and 5.81. Figure 5.8 indicates a similarity, both in terms of amplitude and spectral shape, between the CENA ϕ_{S2S} and ϕ_{S2S} obtained using the BSSA and the Japanese data with **M** less than 5.5.

While the mechanism behind the magnitude dependence of ϕ_{S2S} is not fully resolved and is subject to further analyses, this trend of magnitude dependence of ϕ_{S2S} is clear in datasets that span a wide magnitude range. As a result, the NGA-East Project Team concluded that CENA ϕ_{S2S} values obtained entirely from small magnitude data may not be appropriate for use in hazard analyses where earthquake scenarios with **M** larger than or equal to 5.0 are typically used. The NGA-West2 ϕ_{S2S} values, which are better constrained in terms of magnitude range and frequency bandwidth, are more appropriate for use in CENA for the development of the USGS NSHMs.

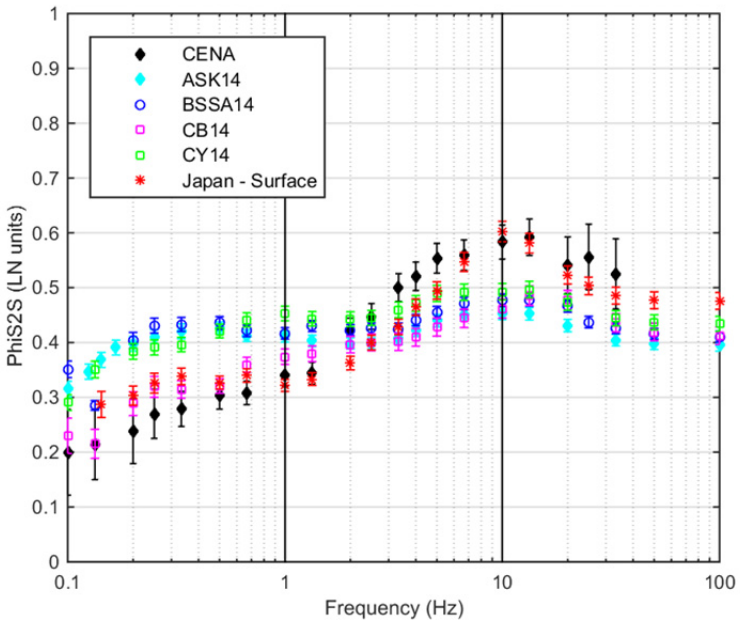

Figure 5.5 Comparison of ϕ_{S2S} for CENA, NGA-West2, and Japan.

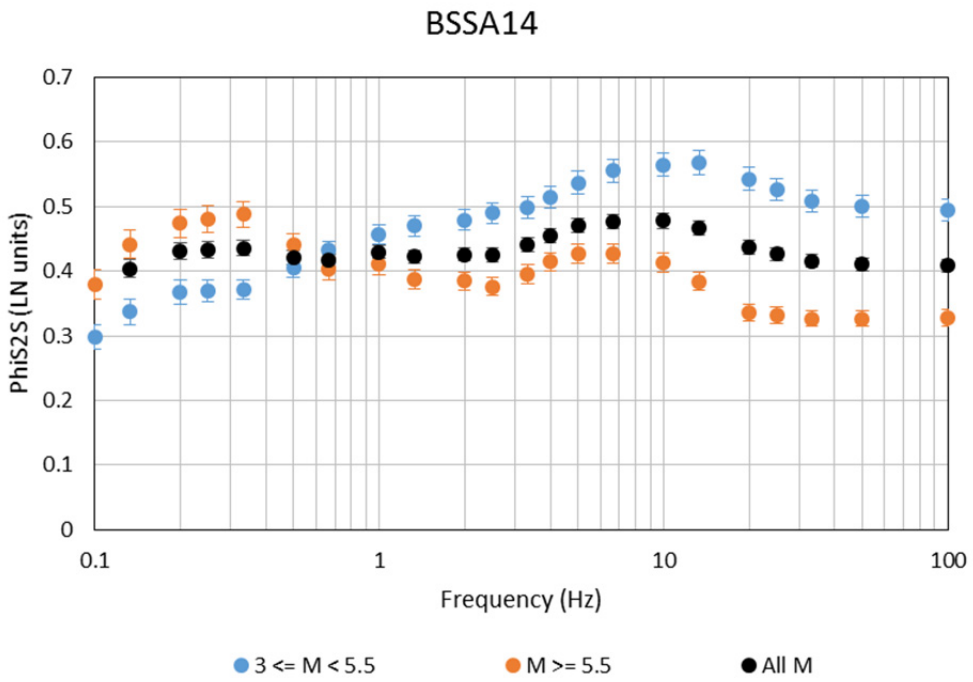

Figure 5.6 **Dependence of ϕ_{S2S} on magnitude observed using the BSSA14 within-event residuals.**

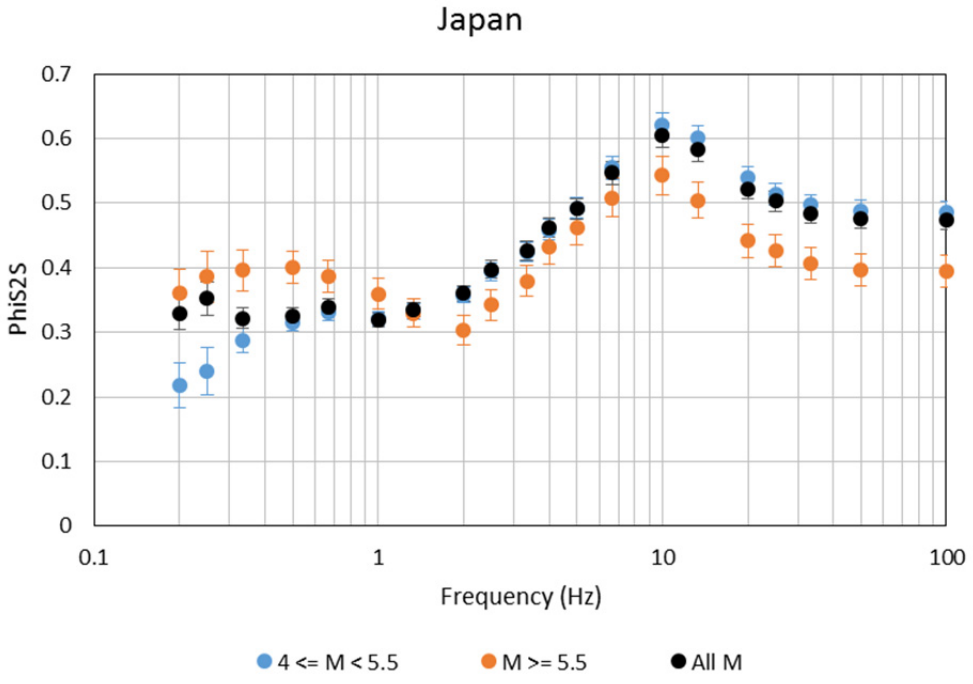

Figure 5.7 **Dependence of ϕ_{S2S} on magnitude observed using the Japanese within-event residuals.**

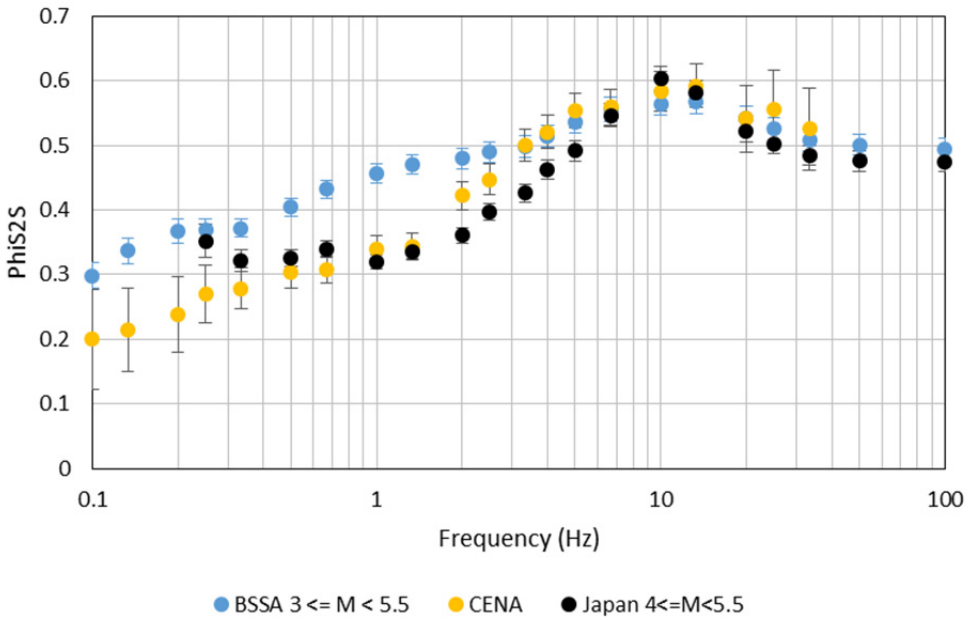

Figure 5.8 **Comparison of CENA ϕ_{S2S} to ϕ_{S2S} obtained using the BSSA14 and the Japanese data with magnitude less than 5.5.**

5.3 RECOMMENDED MODEL FOR TOTAL ERGODIC STANDARD DEVIATION (SIGMA) FOR THE USGS NSHMS

Based on the description of the models developed for the components τ, ϕ_{SS}, and ϕ_{S2S} of the ground motion variability for CENA and their evaluation by the NGA-East Project Team summarized in the Section 5.2, this section presents a recommended total ergodic standard deviation model for use in the development of the USGS NSHMs for CEUS. The total ergodic standard deviation can be calculated as:

$$\sigma = \sqrt{\phi_{SS}^2 + \phi_{S2S}^2 + \tau^2} \tag{5.3}$$

$$\sigma = \sqrt{\phi^2 + \tau^2} \tag{5.4}$$

Based on the discussion presented in Section 5.2, the Project Team adopted a global τ model and the highest weighted branch for ϕ_{SS} is also the global model (weight of 0.8). Both global τ and ϕ_{SS} models are based on the corresponding variability in the four NGA-West2 models (ASK14, BSSA14, CB14, and CY14). Moreover, the Project Team recommended against using the ϕ_{S2S} values obtained from the analysis of the CENA data in deriving a CENA ϕ_{S2S} model due to the latest observations that ϕ_{S2S} appears to be overestimated using small magnitude data. Because CENA models for both τ and ϕ_{SS} are mostly based on the NGA-West2 residuals analysis and standard deviation models and WUS ϕ_{S2S} being better constrained than CENA ϕ_{S2S} as a result of the wide magnitude range in the NGA-West2 dataset, the Project Team

recommends a total ergodic standard deviation model based on the NGA-West2 total ergodic standard deviations.

The 2013 EPRI study based their aleatory variability model on the average of preliminary version of aleatory variability values of four NGA-West2 models (not including Idriss [2014]) [EPRI 2013]. This aleatory variability model has magnitude breaks in the magnitude dependence at M at 5.0, 6.0, and 7.0. Similar to the 2006 study [EPRI 2006], the 2013 study increased τ by 0.03 natural log units to adjust the values derived for active tectonic regions for application in CEUS. In addition, the values of τ and ϕ between 10 Hz and PGA were set equal to the value at 10 Hz to account for the increase in high-frequency content of the CEUS ground motions. We recommend using a total ergodic standard deviation model based on the 2013 EPRI updated to use the published aleatory variability models of the four NGA-West2 GMPEs instead of the preliminary values used in the 2013 EPRI study. The estimated V_{S30} flag was used to estimate the standard deviations of ASK14 and CY14. The total ergodic standard deviation can be calculated according to Equation (5.4) with the components τ and ϕ listed in Table 5.5. The values of τ and ϕ at **M** between 5.0 and 6.0, and **M** between 6.0 and 7.0 can be obtained by linear interpolation between the listed values of τ and ϕ at **M**5.0, 6.0, and 7.0.

Figure 5.9 shows a comparison of the recommended total ergodic sigma models (updated version of EPRI 2013 models) to the original models published in EPRI [2013]. Figure 5.9 indicates that using the published NGA-West2 standard deviation models lead to an increase in the total sigma models compared to the EPRI [2013] models that used a preliminary version of the NGA-West2 aleatory variability models. The increase in total sigma is observed for frequencies greater than 1 Hz. For lower frequencies, a small decrease in the total sigma is observed.

We note that for the SSHAC NGA-East Project, the τ and ϕ_{SS} models will be largely based the ones described in Sections 5.2.1 and 5.2.2. The recommendation for the ϕ_{S2S} model will likely be different for the SSHAC NGA-East Project due to the different target applicability of the NGA-East Project (hard rock sites with V_{S30} = 3000 m/sec). On the other hand, for the USGS NSHMs, the seismic hazard will be evaluated for a wide range of site conditions. Hence, a total ergodic sigma model based on the updated EPRI [2013] sigma model is recommended.

Al Atik [2015] evaluated the difference in the components of ground motion variability (τ, ϕ_{SS}, and ϕ_{S2S}) between the Gulf Coast and Mississippi Embayment region (referred to here as the Gulf Coast region) and the rest of CENA. Al Atik [2015] concluded that the difference in τ, ϕ_{SS}, and ϕ_{S2S} between the Gulf Coast region and the rest of CENA is not statistically significant at most frequencies between 1 and 10 Hz. As a result, we recommend the use of the updated EPRI [2013] model described in this section for the total ergodic sigma model for the Gulf Coast region.

Table 5.5 Recommended total ergodic sigma model.

Period (sec)	Frequency (Hz)	*Components of the Total Ergodic Sigma Model*					
		M 5.0		*M 6.0*		*M >= 7.0*	
		τ	ϕ	τ	ϕ	τ	ϕ
0.01	100	0.4320	0.6269	0.3779	0.5168	0.3525	0.5039
0.02	50	0.4710	0.6682	0.4385	0.5588	0.4138	0.5462
0.03	33.33	0.4710	0.6682	0.4385	0.5588	0.4138	0.5462
0.04	25	0.4710	0.6682	0.4385	0.5588	0.4138	0.5462
0.05	20	0.4710	0.6682	0.4385	0.5588	0.4138	0.5462
0.075	13.33	0.4710	0.6682	0.4385	0.5588	0.4138	0.5462
0.1	10	0.4710	0.6682	0.4385	0.5588	0.4138	0.5462
0.15	6.67	0.4433	0.6693	0.4130	0.5631	0.3886	0.5506
0.2	5	0.4216	0.6691	0.3822	0.5689	0.3579	0.5566
0.25	4	0.4150	0.6646	0.3669	0.5717	0.3427	0.5597
0.3	3.33	0.4106	0.6623	0.3543	0.5846	0.3302	0.5727
0.4	2.5	0.4088	0.6562	0.3416	0.5997	0.3176	0.5882
0.5	2	0.4175	0.6526	0.3456	0.6125	0.3217	0.6015
0.75	1.33	0.4439	0.6375	0.3732	0.6271	0.3494	0.6187
1	1	0.4620	0.6219	0.3887	0.6283	0.3650	0.6227
1.5	0.67	0.4774	0.5957	0.4055	0.6198	0.3819	0.6187
2	0.5	0.4809	0.5860	0.4098	0.6167	0.3863	0.6167
3	0.33	0.4862	0.5813	0.4186	0.6098	0.3952	0.6098
4	0.25	0.4904	0.5726	0.4144	0.6003	0.3910	0.6003
5	0.2	0.4899	0.5651	0.4182	0.5986	0.3949	0.5986
7.5	0.13	0.4803	0.5502	0.4067	0.5982	0.3835	0.5982
10	0.1	0.4666	0.5389	0.3993	0.5885	0.3761	0.5885
PGV		0.3925	0.5979	0.3612	0.5218	0.3502	0.5090

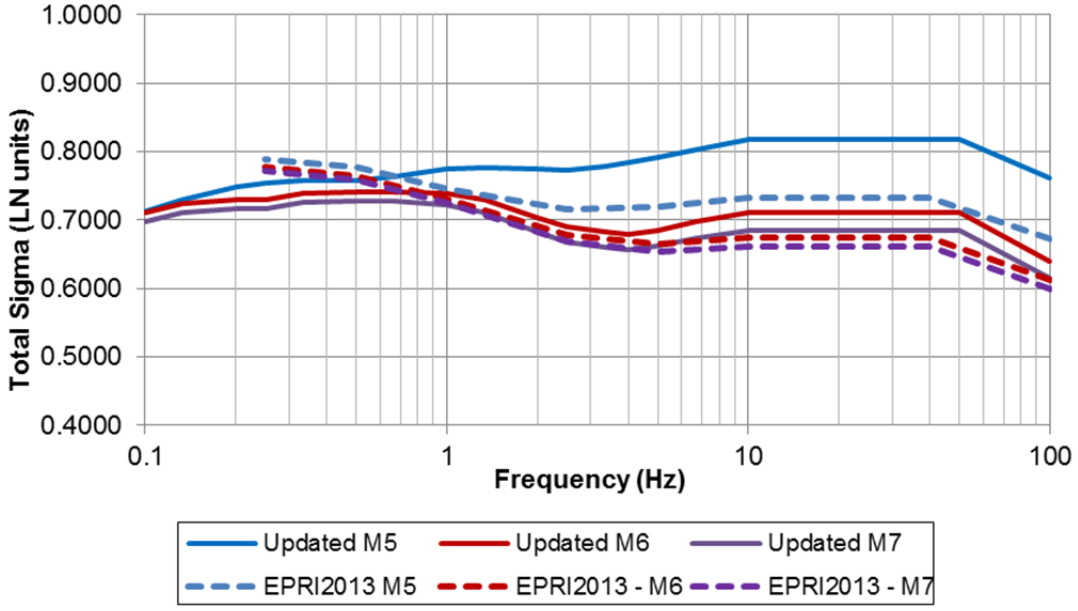

Figure 5.9 **Comparison of recommended total ergodic sigma models at M5.0, 6.0, and 7.0 to the models published in EPRI [2013].**

REFERENCES

Abrahamson N.A., Silva W.J., Kamai R. (2014). Summary of the ASK14 ground-motion relation for active crustal regions, *Earthq. Spectra*, 30(3): 1025–1055,

Abrahamson N.A., Youngs R.R. (1992). A stable algorithm for regression analysis using the random effects model, *Bull. Seismol. Soc. Am*., 82(1): 505–510.

Addo K.O., Abrahamson N.A., Youngs R.R. (2012). Ground motion characterization (GMC) model, *BCHydro SSHAC Level 3 Probabilistic Seismic Hazard Analysis Report*.

Al Atik L. (2015). NGA-East: Ground motion standard deviation models for Central and Eastern North America, *PEER Report No. 2015/09,* Pacific Earthquake Engineering Research Center, University of California, Berkeley, CA.

Allmann B.P., Shearer P.M. (2009). Global variations of stress drop for moderate to large earthquakes, *J. Geophys. Res.*, 114, B01310.

Ancheta T.D., Darragh R.B., Stewart J.P., Seyhan E., Silva W.J., Chiou B.S.-J., Wooddell K.E., Graves R.W., Kottke A.R., Boore D.M., Kishida T., Donahue J.L. (2014). NGA-West2 database, *Earthq. Spectra*, 30: 989–1005.

Atkinson G.M. (2004). Empirical attenuation of ground-motion spectral amplitudes in southeastern Canada and the northeastern United States, *Bull. Seism. Soc. Am*., 94, 1079–1095.

Atkinson G.M. (2008). Ground motion prediction for eastern North America from a referenced empirical approach: Implications for epistemic uncertainty, *Bull. Seismol. Soc. Am*., 98(3): 1304–1318.

Atkinson G.M., Adams J. (2013). Ground motion prediction equations for application to the 2015 national seismic hazard maps of Canada, *Can. J. Civil Eng*., 40: 988–998.

Atkinson G.M., Assatourians K. (2015). Implementation and validation of EXSIM (a stochastic finite-fault ground-motion simulation algorithm) on the SCEC broadband platform, *Seismol. Res. Lett*., 86(1): 48–60.

Atkinson G.M., Bommer J.J., Abrahamson N.A. (2014). Alternative approaches to modeling epistemic uncertainty in ground motions in probabilistic seismic-hazard analysis, *Seismol. Res. Lett*., 85(6): 1141–1144.

Atkinson G.M., Boore D.M. (1995). Ground motion relations for eastern North America, *Bull. Seismol. Soc. Am.* 85(1): 17–30.

Atkinson G.M., Boore D.M. (2006). Earthquake ground-motion prediction equations for eastern North America, *Bull. Seismol. Soc. Am*., 96, 2181–2205. (also see the erratum published in Vol. 97, No. 3, p. 1032).

Atkinson G.M., Boore D.M. (2011). Modification to existing ground-motion prediction equations in light of new data, *Bull. Seismol. Soc. Am*., 101(3): 1121–1135.

Atkinson G.M., Boore D.M. (2014). The attenuation of Fourier amplitudes for rock sites in eastern North America, *Bull. Seismol. Soc. Am*., 104: 513–528.

Bent A.L. (1992). A re-examination of the 1925 Charlevoix, Quebec, earthquake, *Bull. Seismol. Soc. Am*., 82: 2097–2113.

Bent A.L. (1995). A complex double-couple source mechanism for the Ms 7.2 1929 Grand Banks earthquake, *Bull. Seismol. Soc. Am.*, 85: 1003–1020.

Boatwright J., Seekins L. (2011). Regional spectral analysis of three moderate earthquakes in northeastern North America, *Bull. Seismol. Soc. Am.,* 101(4): 1769–1782.

Bommer J.J. (2012). Challenges of building logic trees for probabilistic seismic hazard analysis, *Earthq. Spectra*, 28(4): 1723–1735.

Bommer J.J., Douglas J., Scherbaum F., Cotton F., Bungum H., Fah D. (2010). On the selection of ground-motion prediction equations for seismic hazard analysis, *Seismol. Res. Lett*., 81(5): 783–793.

Bommer J.J., Scherbaum F. (2008). The use and misuse of logic trees in probabilistic seismic hazard analysis, *Earthq. Spectra*, 24(4): 997–1009.

Boore D.M. (1996). SMSIM-Fortran programs for simulating ground motions from earthquakes: version 1.0, *U.S. Geol. Survey Open-File Rept. 96-80-A*, Menlo Park, CA, 73 pgs.

Boore D.M. (2015). Adjusting ground-motion intensity measures to a reference site for which V_{S30} = 3000 m/sec, *PEER Report No. 2015/06*, Pacific Earthquake Engineering Research Center, University of California, Berkeley, CA.

Boore D.M., Campbell K.W., Atkinson G.M. (2010). Determination of stress parameters for eight well-recorded earthquake in eastern North America, *Bull. Seismol. Soc. Am*., 100(4): 1632–1645.

Boore D.M., Di Alessandro C., Abrahamson N.A. (2014). A generalization of the double-corner-frequency source spectral model and its use in the SCEC BBP validation exercise, *Bull. Seismol. Soc. Am.,* 104: 2387–2398.

Boore D.M., Stewart J.P., Seyhan E., Atkinson G.M. (2014). NGA-West 2 equations for predicting PGA, PGV, and 5%-damped PSA for shallow crustal earthquakes, *Earthq. Spectra*, 30(3): 1057–1085.

Boore D.M., Thompson E.M. (2015). Revisions to some parameters used in stochastic-method simulations of ground motion, *Bull. Seismol. Soc. Am*., 105: 1029–1041.

Bora S.S., Scherbaum F., Kuehn N., Stafford P. (2014). Fourier spectral- and durations models for the generation of response spectra adjustable to different source-, propagation-, and site conditions, *Bull. Earthq. Eng.,* 12: 467–493.

Bozorgnia, Y. (2008). A roadmap for the Next Generation Attenuation models for Central and Eastern North America (NGA-East), Letter report to the U.S. Nuclear Regulatory Commission, Pacific Earthquake Engineering Research Center, University of California, Berkeley, CA.

Bozorgnia, Y., Abrahamson N.A., Al Atik L., Ancheta T.D., Atkinson G.M., Baker J., Baltay A., Boore D.M., Campbell K.W., Chiou B.-S.J., Darragh R.B., Day S., Donahue J.L., Graves R.W., Gregor N., Hanks T., Idriss I.M., Kamai R., Kishida T., Kottke A.R., Mahin S.A., Rezaeian S., Rowshandel B., Seyhan E., Shahi S., Shantz R., Silva W.J., Spudich P., Stewart J.P., Watson-Lamprey J., Wooddell K.E., Youngs R.R.. (2014). NGA-West2 research project, *Earthq. Spectra*, 30(3): 973–987.

Budnitz R.J., Apostolakis G., Boore D.M., Clu L.S., Coppersmith K.J., Cornell C.A., Morris P.A. (1997). Recommendations for probabilistic seismic hazard analysis: Guidance on uncertainty and use of experts, *Report NUREG/CR-6372*, U.S. Nuclear Regulatory Commission, Washington D.C.

Campbell K.W., Bozorgnia Y. (2014). NGA-West2 ground motion model for the average horizontal components of PGA, PGV, and 5% damped linear acceleration response spectra, *Earthq. Spectra*, 30(3): 1087–1115.

Campbell K.W., Hashash Y.M.A., Kim B., Kottke A.R., Rathje E.M., Silva W.J., Stewart J.P. 2014. Reference-rock site conditions for Central and Eastern North America: Part II – Attenuation Definition, *PEER Report 2014-12*, Pacific Earthquake Engineering Research Center, University of California, Berkeley, CA, 80 pgs.

Chapman M., Conn A. (2016). A model for Lg propagation in the Gulf Coastal Plain of the Southern United States. *Bull. Seismol. Soc. Am.*, 106 (2): 349–363.

Chapman M.C, Pezeshk S., Hosseini M., Conn A.. (2014). Regional study of Fourier amplitude drop of Lg-wave acceleration in central United States, *Proceedings, Seismological Society of America Annual Meeting*, Anchorage, AK.

Chiou, B.S.-J., Youngs R.R. (2008). NGA model for average horizontal component of peak ground motion and response spectra, *PEER Report No. 2008/09*, Pacific Earthquake Engineering Research Center, University of California, Berkeley, CA.

Chiou B.-S.J., Youngs R.R. (2014). Update of the Chiou and Youngs NGA model for the average horizontal component of peak ground motion and response spectra, *Earthq. Spectra*, 30(3): 1117–1153.

Coppersmith K.J., Bommer J.J., Hanson K., Coppersmith R., Unruh J.R., Wolf L., Youngs R.R., Al Atik L., Rodriguez-Marek A., Toro G., Montaldo-Falero. V. (2014). Hanford sitewide probabilistic seismic hazard analysis, *PNNL- 23361*, Pacific Northwest National Laboratory, Richland, WA.

Cramer C.H., Boyd O.S. (2014). Why the New Madrid earthquakes are M7-8 and the Charleston earthquake is ~M7, *Bull. Seismol. Soc. Am*., 104: 2884–2903.

Cramer C.H., Al Noman, N. (2016). Improving regional ground motion attenuation boundaries and models in the CEUS and developing a Gulf Coast empirical GMPE using Earthscope US Array data for use in the National Seismic Hazards Mapping Project. *US Geological Survey External Grants Program Final Technical Report, Award Number G14AP00049*, August, 52 pgs.

CRWMS M&O (1998). Probabilistic seismic hazard analyses for fault displacement and vibratory ground motion at Yucca Mountain, Nevada, *Milestone SP32IM3*, three volumes. Las Vegas, NV.

Dreiling J., Isken M.P., Mooney W.D., Chapman M.C., Godbee R.W. (2014). NGA-East regionalization report: Comparison of four crustal regions within Central and Eastern North America using waveform modeling and 5%-damped pseudo-spectral acceleration response, *PEER Report No. 2014/15,* Pacific Earthquake Engineering Research Center, University of California, Berkeley, CA.

EPRI (1993) Guidelines for determining design basis ground motions. Volume 1: Method and guidelines for estimating earthquake ground motion in Eastern North America. Electric Power Research Institute, *Technical Report*, Palo Alto, CA.

EPRI (2004). CEUS ground motion project final report, *EPRI Report 1009684*, Electric Power Research Institute, Palo Alto, CA.

EPRI (2006). Program on Technology Innovation: Truncation of the lognormal distribution and value of the standard deviation for ground motion models in the Central and Eastern United States, Electrical Power Research Institute, *EPRI Rept. 1013105*, Technical Update, Palo Alto, CA.

EPRI (2013). EPRI 2004–2006 ground-motion model (GMM) review project, *Final Report Project 3002000717*, Electric Power Research Institute, Palo Alto, CA.

EPRI/USDOE/USNRC. (2012). Central and Eastern United States seismic source characterization for nuclear facilities, *U.S. Nuclear Regulatory Commission Report, NUREG-2115; EPRI Report 1021097*, *6 Volumes; DOE Report# DOE/NE-0140,* Washington, D.C.

Frankel A. (2009). A constant stress-drop model for producing broadband synthetic seismograms—Comparison with the Next Generation Attenuation relations, *Bull. Seismol. Soc. Am*., 99: 664–681.

Gallegos, A., Ranasinghe, N., Ni, J., and Sandvol, E. (2014). Lg attenuation in the central and eastern United States as reveales by the Earthscope Transportable Array, *Earth and Planetary Science Letters*, 402, 187-196.

GeoPentech (2015). *Southwestern United States ground motion characterization SSHAC Level 3 – Technical Report Rev. 2*.

Geusebroek J.M., Burghouts G.J., Smeulders A.W.M. (2005). The Amsterdam library of object images, *Int. J. Comput. Vision*, 61(1): 103–112.

Gianniotis N., Riggelsen C. (2013). Visualisation of high-dimensional data using an ensemble of neural networks, *Proceedings, IEEE Symposium on Computational Intelligence and Data Mining,* SSCI 2013, Singapore.

Goulet C.A., Kishida T. Ancheta T.D., Cramer C.H., Darragh R.B., Silva W.J., Hashash Y.M.A., Harmon J., Stewart J.P., Wooddell K.E., Youngs R.R. (2014). PEER NGA-East database, *PEER Report No. 2014/17*, Pacific Earthquake Engineering Research Center, University of California, Berkeley, CA.

Graizer V., Kalkan E. (2007). Ground-motion attenuation model for peak horizontal acceleration from shallow crustal earthquakes, *Earthq. Spectra*, 23(3): 585–613.

Graizer V., Kalkan E. (2009). Prediction of response spectral acceleration ordinates based on PGA attenuation, *Earthq. Spectra*, 25(1): 39–69.

Graves R.W., Pitarka A. (2015). Refinements to the Graves and Pitarka (2010) broadband ground motion simulation method, *Seismol. Res. Lett*., 86(1): 75–80.

Hartzell S.W., Langer C., Mendoza C. (1994). Rupture histories of Eastern North American earthquakes, *Bull. Seismol. Soc. Am*., 84(6): 1703–1724.

Hashash Y.M.A., Kottke A.R., Stewart J.P., Campbell K.W., Kim B., Rathje E.M., Silva W.J. (2014). Reference rock site condition for central and eastern North America, *Bull. Seismol. Soc. Am*., 104: 684–701.

Hassani B., Atkinson G.M. (2015). Referenced empirical ground-motion model for Eastern North America, *Seismol. Res. Lett*., 86(2): 477–491.

Hermkes M., Kuehn N.M., Riggelsen C. (2014). Simultaneous quantification of epistemic and aleatory uncertainty in GMMs using Gaussian process regression, *Bull. Earthq. Eng.,* 12(1): 449–466.

Hotelling H. (1933). Analysis of a complex of statistical variables into principal components, *J. Educ. Psychol.,* 24(6): 417–441.

Idriss I.M. (2014). An NGA-West2 empirical model for estimating the horizontal spectral values generated by shallow crustal earthquakes, *Earthq. Spectra,* 30(3): 1155−1177.

Joyner W.B., Boore D.M. (1993). Methods for regression analysis of strong motion data, *Bull. Seismol. Soc. Am.,* 83: 469–487.

Joyner W.B., Boore D.M. (1994). Errata: Methods for regression analysis of strong-motion data, *Bull. Seismol. Soc. Am*., 84: 955–956.

Kohonen T. (2001). *Self-Organizing Maps*. Springer Verlag, New York.

Lawrence N.D. (2004). Gaussian process latent variable models for visualization of high dimensional data, *Adv. Neur. In.*, 16: 329–336.

Leonard M. (2010). Earthquake fault scaling self-consistent relations of rupture length, width, average displacement and moment release, *Bull. Seismol. Soc. Am*., 100: 1971–1988.

McGuire R.K., Silva W.J., Costantino C.J. (2001). Technical basis for revision of regulatory guidance on design ground motions: hazard- and risk-consistent ground motion spectra guidelines, *NUREG/CR-6728*, U.S. Nuclear Regulatory Commission, Washington, D.C.

Miller A.C., Rice T.R. (1983). Discrete approximations of probability distributions, *Management Sci*., 29: 352−362.

Mooney W.D., Chulick G., Ferguson A., Radakovich A., Kitaura K, Detweiler S. (2012). *NGA-East: Crustal Regionalization*, presentation at NGA-East Workshop on Path and Source Issues, University of California, Berkeley, October 16,; available at http://peer.berkeley.edu/ ngaeast/2012/08/working-meeting-path-and-source-issues-oct-16-2012/.

NAGRA (2004). Probabilistic seismic hazard analysis for Swiss nuclear power plant sites (PEGASOS Project), *Report to Swiss Nuclear prepared by Nationale Genossenschaft für die Lagerung radioaktiver Abfälle*, Wettingen, 358 pgs.

NRC (2012). Practical implementation guidelines for SSHAC Level 3 and 4 hazard studies, *Technical Report NUREG-2117*, U.S. Nuclear Regulatory Commission, Washington D.C.

Ogweno L.P., Cramer C.H. (2014). Regression relationships between modified Mercalli intensities and ground motion parameters (abstract), *Program and Abstracts, 86th Annual Meeting, Eastern Section of the Seismological Society of America*, Charleston, SC.

PEER (2015a). NGA-East: Median ground-motion models for the Central and Eastern North America region, PEER *Report No. 2015/04*, Pacific Earthquake Engineering Research Center, University of California, Berkeley, CA.

PEER (2015b). NGA-East: Adjustments to median ground-motion models for Central and Eastern North America, *PEER Report No. 2015/08*, Pacific Earthquake Engineering Research Center, University of California, Berkeley, CA.

Pezeshk S., Zandieh A., Tavakoli B. (2011). Hybrid empirical ground-motion prediction equations for Eastern North America using NGA models and updated seismological parameters, *Bull. Seismol. Soc. Am*., 101(4): 1859–1870.

Rasmussen C.E., Williams C.K.I. (2006). *Gaussian Processes for Machine Learning*, MIT Press, Cambridge, MA.

Sammon J.W. (1969). A nonlinear mapping for data structure analysis, *IEEE Trans. Computers*, C-18: 401–409.

Savy J.B., Foxall W., Abrahamson N.A., Bernreuter D. (2002). Guidance for performing probabilistic seismic hazard analysis for a nuclear plant site: example application to the southeastern United States, *Report NUREG/CR-6607*, Lawrence Livermore National Laboratory (UCRL-ID-133494), Livermore, CA.

Scherbaum F., Kuehn N.M., Ohrnberger M, Koehler K. (2010). Exploring the proximity of ground-motion models using high-dimensional visualization techniques, *Earthq. Spectra*, 26(4): 1117–1138.

Silva W.J., Gregor N., Darragh R.B. (2002). *Development of Regional Hard Rock Attenuation Relations For Central And Eastern North America*, Pacific Engineering and Analysis Report, El Cerrito, CA.

Somerville P.G. (2014). Scaling relations between seismic moment and rupture area of earthquakes in stable continental regions, *PEER Report No. 2014/14*, Pacific Earthquake Engineering Research Center, University of California, Berkeley, CA.

Somerville P.G., Collins N., Abrahamson N.A., Graves R.W., Saikia C. (2001). Ground motion attenuation relations for the Central and Eastern United States, *Report to U.S. Geological Survey, NEHRP Award No. 99HQGR0098*, 36 pgs.

Stewart J.P., Parker G.A., Harmon J.A., Atkinson G.M., Boore D.M., Darragh R.B., Silva W.J., Hashash Y.M.A. (2017). Expert Panel-Recommendations for Ergodic Site Amplification in Central and Eastern North America, *PEER Report No. 2017/04,* Pacific Earthquake Engineering Research Center, University of California, Berkeley, CA.

Toro G.R. (2002). Modification of the Toro et al. (1997) attenuation equations for large magnitudes and short distances, *Risk Engineering Technical Report*, 10 pgs.

Yenier, E., Atkinson G.M. (2015). Regionally-adjustable generic ground-motion prediction equation based on equivalent point-source simulations: Application to Central and Eastern North America, *Bull. Seismol. Soc. Am*., 105: 1989–2009.

Electronic Appendix A

The 13 smoothed median GMMs are provided in tables as an electronic appendix to this report. There is one Excel workbook per GMM, with each worksheet corresponding to a specific GMIM.

Electronic Appendix B

The two Gulf Coast adjustment models described in Chapter 4 are provided as electronic appendices in Excel workbooks.

B.1 PEER Gulf Coast Adjustment Model

B.2 DASG Mean Culf Coast Adjustment Model

PEER REPORTS

PEER reports are available as a free PDF download from http://peer.berkeley.edu/publications/peer_reports_complete.html. Printed hard copies of PEER reports can be ordered directly from our printer by following the instructions at http://peer.berkeley.edu/publications/peer_reports.html. For other related questions about the PEER Report Series, contact the Pacific Earthquake Engineering Research Center, 325 Davis Hall, Mail Code 1792, Berkeley, CA 94720. Tel.: (510) 642-3437; Fax: (510) 642-1655; Email: clairejohnson@berkeley.edu.

PEER 2017/03 *NGA-East Ground-Motion Models for the U.S. Geological Survey National Seismic Hazard Maps*. Christine A.Goulet, Yousef Bozorgnia, Nicolas Kuehn, Linda Al Atik, Robert R. Youngs, Robert W. Graves, and Gail M. Atkinson. March 2017.

PEER 2017/02 *U.S.–New Zealand–Japan Workshop: Liquefaction-Induced Ground Movements Effects, University of California, Berkeley, California, 2–4 November 2016*. Jonathan D. Bray, Ross W. Boulanger, Misko Cubrinovski, Kohji Tokimatsu, Steven L. Kramer, Thomas O'Rourke, Ellen Rathje, Russell A. Green, Peter K. Robinson, and Christine Z. Beyzaei. March 2017.

PEER 2017/01 *2016 PEER Annual Report*. Khalid Mosalam, Amarnath Kasalanati, and Grace Kang. March 2017.

PEER 2016/11 *Seismic Design Guidelines for Tall Buildings*. Members of the Committee for the Tall Buildings Initiative. December 2016.

PEER 2016/10 *Performance-Based Robust Nonlinear Seismic Analysis with Application to Reinforced Concrete Bridge Systems*. Xiao Ling and Khalid M. Mosalam. December 2016.

PEER 2016/09 *Resilience of Critical Structures, Infrastructure, and Communities***.** Gian Paolo Cimellaro, Ali Zamani-Noori, Omar Kamouh, Vesna Terzic, and Stephen A. Mahin. December 2016.

PEER 2016/08 *Processing and Development of Iran Earthquake Ground-Motion Database*. Tadahiro Kishida, Sahar Derakhshan, Sifat Muin, Yousef Bozorgnia, Sean K. Ahdi, Jonathan P. Stewart, Robert B. Darragh, Walter J. Silva, and Esmael Farzanegan. December 2016.

PEER 2016/07 *Hybrid Simulation Theory for a Classical Nonlinear Dynamical System*. Paul L. Drazin and Sanjay Govindjee. September 2016.

PEER 2016/06 *California Earthquake Early Warning System Benefit Study*. Laurie A. Johnson, Sharyl Rabinovici, Grace S. Kang, and Stephen A. Mahin. July 2006.

PEER 2016/05 *Ground-Motion Prediction Equations for Arias Intensity Consistent with the NGA-West2 Ground-Motion Models.* Charlotte Abrahamson, Hao-Jun Michael Shi, and Brian Yang. July 2016.

PEER 2016/04 *The M_W 6.0 South Napa Earthquake of August 24, 2014: A Wake-Up Call for Renewed Investment in Seismic Resilience Across California.* Prepared for the California Seismic Safety Commission, Laurie A. Johnson and Stephen A. Mahin. May 2016.

PEER 2016/03 *Simulation Confidence in Tsunami-Driven Overland Flow.* Patrick Lynett. May 2016.

PEER 2016/02 *Semi-Automated Procedure for Windowing time Series and Computing Fourier Amplitude Spectra for the NGA-West2 Database*. Tadahiro Kishida, Olga-Joan Ktenidou, Robert B. Darragh, and Walter J. Silva. May 2016.

PEER 2016/01 *A Methodology for the Estimation of Kappa (κ) from Large Datasets: Example Application to Rock Sites in the NGA-East Database and Implications on Design Motions.* Olga-Joan Ktenidou, Norman A. Abrahamson, Robert B. Darragh, and Walter J. Silva. April 2016.

PEER 2015/13 *Self-Centering Precast Concrete Dual-Steel-Shell Columns for Accelerated Bridge Construction: Seismic Performance, Analysis, and Design*. Gabriele Guerrini, José I. Restrepo, Athanassios Vervelidis, and Milena Massari. December 2015.

PEER 2015/12 *Shear-Flexure Interaction Modeling for Reinforced Concrete Structural Walls and Columns under Reversed Cyclic Loading*. Kristijan Kolozvari, Kutay Orakcal, and John Wallace. December 2015.

PEER 2015/11 *Selection and Scaling of Ground Motions for Nonlinear Response History Analysis of Buildings in Performance-Based Earthquake Engineering*. N. Simon Kwong and Anil K. Chopra. December 2015.

PEER 2015/10 *Structural Behavior of Column-Bent Cap Beam-Box Girder Systems in Reinforced Concrete Bridges Subjected to Gravity and Seismic Loads. Part II: Hybrid Simulation and Post-Test Analysis*. Mohamed A. Moustafa and Khalid M. Mosalam. November 2015.

PEER 2015/09 *Structural Behavior of Column-Bent Cap Beam-Box Girder Systems in Reinforced Concrete Bridges Subjected to Gravity and Seismic Loads. Part I: Pre-Test Analysis and Quasi-Static Experiments*. Mohamed A. Moustafa and Khalid M. Mosalam. September 2015.

PEER 2015/08 *NGA-East: Adjustments to Median Ground-Motion Models for Center and Eastern North America*. August 2015.

PEER 2015/07 *NGA-East: Ground-Motion Standard-Deviation Models for Central and Eastern North America*. Linda Al Atik. June 2015.

PEER 2015/06 *Adjusting Ground-Motion Intensity Measures to a Reference Site for which V_{S30} = 3000 m/sec*. David M. Boore. May 2015.

PEER 2015/05 *Hybrid Simulation of Seismic Isolation Systems Applied to an APR-1400 Nuclear Power Plant.* Andreas H. Schellenberg, Alireza Sarebanha, Matthew J. Schoettler, Gilberto Mosqueda, Gianmario Benzoni, and Stephen A. Mahin. April 2015.

PEER 2015/04 *NGA-East: Median Ground-Motion Models for the Central and Eastern North America Region*. April 2015.

PEER 2015/03 *Single Series Solution for the Rectangular Fiber-Reinforced Elastomeric Isolator Compression Modulus*. James M. Kelly and Niel C. Van Engelen. March 2015.

PEER 2015/02 *A Full-Scale, Single-Column Bridge Bent Tested by Shake-Table Excitation.* Matthew J. Schoettler, José I. Restrepo, Gabriele Guerrini, David E. Duck, and Francesco Carrea. March 2015.

PEER 2015/01 *Concrete Column Blind Prediction Contest 2010: Outcomes and Observations.* Vesna Terzic, Matthew J. Schoettler, José I. Restrepo, and Stephen A Mahin. March 2015.

PEER 2014/20 *Stochastic Modeling and Simulation of Near-Fault Ground Motions for Performance-Based Earthquake Engineering*. Mayssa Dabaghi and Armen Der Kiureghian. December 2014.

PEER 2014/19 *Seismic Response of a Hybrid Fiber-Reinforced Concrete Bridge Column Detailed for Accelerated Bridge Construction*. Wilson Nguyen, William Trono, Marios Panagiotou, and Claudia P. Ostertag. December 2014.

PEER 2014/18 *Three-Dimensional Beam-Truss Model for Reinforced Concrete Walls and Slabs Subjected to Cyclic Static or Dynamic Loading*. Yuan Lu, Marios Panagiotou, and Ioannis Koutromanos. December 2014.

PEER 2014/17 *PEER NGA-East Database.* Christine A. Goulet, Tadahiro Kishida, Timothy D. Ancheta, Chris H. Cramer, Robert B. Darragh, Walter J. Silva, Youssef M.A. Hashash, Joseph Harmon, Jonathan P. Stewart, Katie E. Wooddell, and Robert R. Youngs. October 2014.

PEER 2014/16 *Guidelines for Performing Hazard-Consistent One-Dimensional Ground Response Analysis for Ground Motion Prediction*. Jonathan P. Stewart, Kioumars Afshari, and Youssef M.A. Hashash. October 2014.

PEER 2014/15 *NGA-East Regionalization Report: Comparison of Four Crustal Regions within Central and Eastern North America using Waveform Modeling and 5%-Damped Pseudo-Spectral Acceleration Response*. Jennifer Dreiling, Marius P. Isken, Walter D. Mooney, Martin C. Chapman, and Richard W. Godbee. October 2014.

PEER 2014/14 *Scaling Relations between Seismic Moment and Rupture Area of Earthquakes in Stable Continental Regions*. Paul Somerville. August 2014.

PEER 2014/13 *PEER Preliminary Notes and Observations on the August 24, 2014, South Napa Earthquake*. Grace S. Kang and Stephen A. Mahin, Editors. September 2014.

PEER 2014/12 *Reference-Rock Site Conditions for Central and Eastern North America: Part II – Attenuation (Kappa) Definition*. Kenneth W. Campbell, Youssef M.A. Hashash, Byungmin Kim, Albert R. Kottke, Ellen M. Rathje, Walter J. Silva, and Jonathan P. Stewart. August 2014.

PEER 2014/11 *Reference-Rock Site Conditions for Central and Eastern North America: Part I - Velocity Definition*. Youssef M.A. Hashash, Albert R. Kottke, Jonathan P. Stewart, Kenneth W. Campbell, Byungmin Kim, Ellen M. Rathje, Walter J. Silva, Sissy Nikolaou, and Cheryl Moss. August 2014.

PEER 2014/10 *Evaluation of Collapse and Non-Collapse of Parallel Bridges Affected by Liquefaction and Lateral Spreading*. Benjamin Turner, Scott J. Brandenberg, and Jonathan P. Stewart. August 2014.

PEER 2014/09 *PEER Arizona Strong-Motion Database and GMPEs Evaluation*. Tadahiro Kishida, Robert E. Kayen, Olga-Joan Ktenidou, Walter J. Silva, Robert B. Darragh, and Jennie Watson-Lamprey. June 2014.

PEER 2014/08 *Unbonded Pretensioned Bridge Columns with Rocking Detail*. Jeffrey A. Schaefer, Bryan Kennedy, Marc O. Eberhard, and John F. Stanton. June 2014.

PEER 2014/07 *Northridge 20 Symposium Summary Report: Impacts, Outcomes, and Next Steps*. May 2014.

PEER 2014/06 *Report of the Tenth Planning Meeting of NEES/E-Defense Collaborative Research on Earthquake Engineering*. December 2013.

PEER 2014/05 *Seismic Velocity Site Characterization of Thirty-One Chilean Seismometer Stations by Spectral Analysis of Surface Wave Dispersion*. Robert Kayen, Brad D. Carkin, Skye Corbet, Camilo Pinilla, Allan Ng, Edward Gorbis, and Christine Truong. April 2014.

PEER 2014/04 Effect of Vertical Acceleration on Shear Strength of Reinforced Concrete Columns. Hyerin Lee and Khalid M. Mosalam. April 2014.

PEER 2014/03 *Retest of Thirty-Year-Old Neoprene Isolation Bearings.* James M. Kelly and Niel C. Van Engelen. March 2014.

PEER 2014/02 *Theoretical Development of Hybrid Simulation Applied to Plate Structures.* Ahmed A. Bakhaty, Khalid M. Mosalam, and Sanjay Govindjee. January 2014.

PEER 2014/01 *Performance-Based Seismic Assessment of Skewed Bridges.* Peyman Kaviani, Farzin Zareian, and Ertugrul Taciroglu. January 2014.

PEER 2013/26 *Urban Earthquake Engineerin*g. Proceedings of the U.S.-Iran Seismic Workshop. December 2013.

PEER 2013/25 *Earthquake Engineering for Resilient Communities: 2013 PEER Internship Program Research Report Collection.* Heidi Tremayne (Editor), Stephen A. Mahin (Editor), Jorge Archbold Monterossa, Matt Brosman, Shelly Dean, Katherine deLaveaga, Curtis Fong, Donovan Holder, Rakeeb Khan, Elizabeth Jachens, David Lam, Daniela Martinez Lopez, Mara Minner, Geffen Oren, Julia Pavicic, Melissa Quinonez, Lorena Rodriguez, Sean Salazar, Kelli Slaven, Vivian Steyert, Jenny Taing, and Salvador Tena. December 2013.

PEER 2013/24 *NGA-West2 Ground Motion Prediction Equations for Vertical Ground Motions*. September 2013.

PEER 2013/23 *Coordinated Planning and Preparedness for Fire Following Major Earthquakes*. Charles Scawthorn. November 2013.

PEER 2013/22 *GEM-PEER Task 3 Project: Selection of a Global Set of Ground Motion Prediction Equations.* Jonathan P. Stewart, John Douglas, Mohammad B. Javanbarg, Carola Di Alessandro, Yousef Bozorgnia, Norman A. Abrahamson, David M. Boore, Kenneth W. Campbell, Elise Delavaud, Mustafa Erdik, and Peter J. Stafford. December 2013.

PEER 2013/21 *Seismic Design and Performance of Bridges with Columns on Rocking Foundations*. Grigorios Antonellis and Marios Panagiotou. September 2013.

PEER 2013/20 *Experimental and Analytical Studies on the Seismic Behavior of Conventional and Hybrid Braced Frames*. Jiun-Wei Lai and Stephen A. Mahin. September 2013.

PEER 2013/19 *Toward Resilient Communities: A Performance-Based Engineering Framework for Design and Evaluation of the Built Environment.* Michael William Mieler, Bozidar Stojadinovic, Robert J. Budnitz, Stephen A. Mahin, and Mary C. Comerio. September 2013.

PEER 2013/18 *Identification of Site Parameters that Improve Predictions of Site Amplification*. Ellen M. Rathje and Sara Navidi. July 2013.

PEER 2013/17 *Response Spectrum Analysis of Concrete Gravity Dams Including Dam-Water-Foundation Interaction*. Arnkjell Løkke and Anil K. Chopra. July 2013.

PEER 2013/16 *Effect of Hoop Reinforcement Spacing on the Cyclic Response of Large Reinforced Concrete Special Moment Frame Beams.* Marios Panagiotou, Tea Visnjic, Grigorios Antonellis, Panagiotis Galanis, and Jack P. Moehle. June 2013.

PEER 2013/15 *A Probabilistic Framework to Include the Effects of Near-Fault Directivity in Seismic Hazard Assessment.* Shrey Kumar Shahi, Jack W. Baker. October 2013.

PEER 2013/14 *Hanging-Wall Scaling using Finite-Fault Simulations.* Jennifer L. Donahue and Norman A. Abrahamson. September 2013.

PEER 2013/13 *Semi-Empirical Nonlinear Site Amplification and its Application in NEHRP Site Factors*. Jonathan P. Stewart and Emel Seyhan. November 2013.

PEER 2013/12 *Nonlinear Horizontal Site Response for the NGA-West2 Project.* Ronnie Kamai, Norman A. Abramson, Walter J. Silva. May 2013.

PEER 2013/11 *Epistemic Uncertainty for NGA-West2 Models.* Linda Al Atik and Robert R. Youngs. May 2013.

PEER 2013/10 *NGA-West 2 Models for Ground-Motion Directionality.* Shrey K. Shahi and Jack W. Baker. May 2013.

PEER 2013/09 *Final Report of the NGA-West2 Directivity Working Group.* Paul Spudich, Jeffrey R. Bayless, Jack W. Baker, Brian S.J. Chiou, Badie Rowshandel, Shrey Shahi, and Paul Somerville. May 2013.

PEER 2013/08 *NGA-West2 Model for Estimating Average Horizontal Values of Pseudo-Absolute Spectral Accelerations Generated by Crustal Earthquakes*. I. M. Idriss. May 2013.

PEER 2013/07 *Update of the Chiou and Youngs NGA Ground Motion Model for Average Horizontal Component of Peak Ground Motion and Response Spectra*. Brian Chiou and Robert Youngs. May 2013.

PEER 2013/06 *NGA-West2 Campbell-Bozorgnia Ground Motion Model for the Horizontal Components of PGA, PGV, and 5%-Damped Elastic Pseudo-Acceleration Response Spectra for Periods Ranging from 0.01 to 10 sec*. Kenneth W. Campbell and Yousef Bozorgnia. May 2013.

PEER 2013/05 *NGA-West 2 Equations for Predicting Response Spectral Accelerations for Shallow Crustal Earthquakes*. David M. Boore, Jonathan P. Stewart, Emel Seyhan, and Gail M. Atkinson. May 2013.

PEER 2013/04 *Update of the AS08 Ground-Motion Prediction Equations Based on the NGA-West2 Data Set*. Norman Abrahamson, Walter Silva, and Ronnie Kamai. May 2013.

PEER 2013/03 *PEER NGA-West2 Database*. Timothy D. Ancheta, Robert B. Darragh, Jonathan P. Stewart, Emel Seyhan, Walter J. Silva, Brian S.J. Chiou, Katie E. Wooddell, Robert W. Graves, Albert R. Kottke, David M. Boore, Tadahiro Kishida, and Jennifer L. Donahue. May 2013.

PEER 2013/02 *Hybrid Simulation of the Seismic Response of Squat Reinforced Concrete Shear Walls*. Catherine A. Whyte and Bozidar Stojadinovic. May 2013.

PEER 2013/01 *Housing Recovery in Chile: A Qualitative Mid-program Review*. Mary C. Comerio. February 2013.

PEER 2012/08 *Guidelines for Estimation of Shear Wave Velocity.* Bernard R. Wair, Jason T. DeJong, and Thomas Shantz. December 2012.

PEER 2012/07 *Earthquake Engineering for Resilient Communities: 2012 PEER Internship Program Research Report Collection.* Heidi Tremayne (Editor), Stephen A. Mahin (Editor), Collin Anderson, Dustin Cook, Michael Erceg, Carlos Esparza, Jose Jimenez, Dorian Krausz, Andrew Lo, Stephanie Lopez, Nicole McCurdy, Paul Shipman, Alexander Strum, Eduardo Vega. December 2012.

PEER 2012/06 *Fragilities for Precarious Rocks at Yucca Mountain.* Matthew D. Purvance, Rasool Anooshehpoor, and James N. Brune. December 2012.

PEER 2012/05 *Development of Simplified Analysis Procedure for Piles in Laterally Spreading Layered Soils.* Christopher R. McGann, Pedro Arduino, and Peter Mackenzie–Helnwein. December 2012.

PEER 2012/04 *Unbonded Pre-Tensioned Columns for Bridges in Seismic Regions.* Phillip M. Davis, Todd M. Janes, Marc O. Eberhard, and John F. Stanton. December 2012.

PEER 2012/03 *Experimental and Analytical Studies on Reinforced Concrete Buildings with Seismically Vulnerable Beam-Column Joints*. Sangjoon Park and Khalid M. Mosalam. October 2012.

PEER 2012/02 *Seismic Performance of Reinforced Concrete Bridges Allowed to Uplift during Multi-Directional Excitation*. Andres Oscar Espinoza and Stephen A. Mahin. July 2012.

PEER 2012/01 *Spectral Damping Scaling Factors for Shallow Crustal Earthquakes in Active Tectonic Regions.* Sanaz Rezaeian, Yousef Bozorgnia, I. M. Idriss, Kenneth Campbell, Norman Abrahamson, and Walter Silva. July 2012.

PEER 2011/10 *Earthquake Engineering for Resilient Communities: 2011 PEER Internship Program Research Report Collection*. Heidi Faison and Stephen A. Mahin, Editors. December 2011.

PEER 2011/09 *Calibration of Semi-Stochastic Procedure for Simulating High-Frequency Ground Motions*. Jonathan P. Stewart, Emel Seyhan, and Robert W. Graves. December 2011.

PEER 2011/08 *Water Supply in regard to Fire Following Earthquake*. Charles Scawthorn. November 2011.

PEER 2011/07 *Seismic Risk Management in Urban Areas*. Proceedings of a U.S.-Iran-Turkey Seismic Workshop. September 2011.

PEER 2011/06 *The Use of Base Isolation Systems to Achieve Complex Seismic Performance Objectives*. Troy A. Morgan and Stephen A. Mahin. July 2011.

PEER 2011/05 *Case Studies of the Seismic Performance of Tall Buildings Designed by Alternative Means.* Task 12 Report for the Tall Buildings Initiative. Jack Moehle, Yousef Bozorgnia, Nirmal Jayaram, Pierson Jones, Mohsen Rahnama, Nilesh Shome, Zeynep Tuna, John Wallace, Tony Yang, and Farzin Zareian. July 2011.

PEER 2011/04 *Recommended Design Practice for Pile Foundations in Laterally Spreading Ground.* Scott A. Ashford, Ross W. Boulanger, and Scott J. Brandenberg. June 2011.

PEER 2011/03 *New Ground Motion Selection Procedures and Selected Motions for the PEER Transportation Research Program*. Jack W. Baker, Ting Lin, Shrey K. Shahi, and Nirmal Jayaram. March 2011.

PEER 2011/02 *A Bayesian Network Methodology for Infrastructure Seismic Risk Assessment and Decision Support*. Michelle T. Bensi, Armen Der Kiureghian, and Daniel Straub. March 2011.

PEER 2011/01 *Demand Fragility Surfaces for Bridges in Liquefied and Laterally Spreading Ground.* Scott J. Brandenberg, Jian Zhang, Pirooz Kashighandi, Yili Huo, and Minxing Zhao. March 2011.

PEER 2010/05 *Guidelines for Performance-Based Seismic Design of Tall Buildings.* Developed by the Tall Buildings Initiative. November 2010.

PEER 2010/04 *Application Guide for the Design of Flexible and Rigid Bus Connections between Substation Equipment Subjected to Earthquakes.* Jean-Bernard Dastous and Armen Der Kiureghian. September 2010.

PEER 2010/03 *Shear Wave Velocity as a Statistical Function of Standard Penetration Test Resistance and Vertical Effective Stress at Caltrans Bridge Sites.* Scott J. Brandenberg, Naresh Bellana, and Thomas Shantz. June 2010.

PEER 2010/02 *Stochastic Modeling and Simulation of Ground Motions for Performance-Based Earthquake Engineering.* Sanaz Rezaeian and Armen Der Kiureghian. June 2010.

PEER 2010/01 *Structural Response and Cost Characterization of Bridge Construction Using Seismic Performance Enhancement Strategies.* Ady Aviram, Božidar Stojadinović, Gustavo J. Parra-Montesinos, and Kevin R. Mackie. March 2010.

PEER 2009/03 *The Integration of Experimental and Simulation Data in the Study of Reinforced Concrete Bridge Systems Including Soil-Foundation-Structure Interaction.* Matthew Dryden and Gregory L. Fenves. November 2009.

PEER 2009/02 *Improving Earthquake Mitigation through Innovations and Applications in Seismic Science, Engineering, Communication, and Response*. Proceedings of a U.S.-Iran Seismic Workshop. October 2009.

PEER 2009/01 *Evaluation of Ground Motion Selection and Modification Methods: Predicting Median Interstory Drift Response of Buildings*. Curt B. Haselton, Editor. June 2009.

PEER 2008/10 *Technical Manual for Strata.* Albert R. Kottke and Ellen M. Rathje. February 2009.

PEER 2008/09 *NGA Model for Average Horizontal Component of Peak Ground Motion and Response Spectra.* Brian S.-J. Chiou and Robert R. Youngs. November 2008.

PEER 2008/08 *Toward Earthquake-Resistant Design of Concentrically Braced Steel Structures*. Patxi Uriz and Stephen A. Mahin. November 2008.

PEER 2008/07 *Using OpenSees for Performance-Based Evaluation of Bridges on Liquefiable Soils*. Stephen L. Kramer, Pedro Arduino, and HyungSuk Shin. November 2008.

PEER 2008/06 *Shaking Table Tests and Numerical Investigation of Self-Centering Reinforced Concrete Bridge Columns*. Hyung IL Jeong, Junichi Sakai, and Stephen A. Mahin. September 2008.

PEER 2008/05 *Performance-Based Earthquake Engineering Design Evaluation Procedure for Bridge Foundations Undergoing Liquefaction-Induced Lateral Ground Displacement*. Christian A. Ledezma and Jonathan D. Bray. August 2008.

PEER 2008/04 *Benchmarking of Nonlinear Geotechnical Ground Response Analysis Procedures.* Jonathan P. Stewart, Annie On-Lei Kwok, Yousseff M. A. Hashash, Neven Matasovic, Robert Pyke, Zhiliang Wang, and Zhaohui Yang. August 2008.

PEER 2008/03 *Guidelines for Nonlinear Analysis of Bridge Structures in California.* Ady Aviram, Kevin R. Mackie, and Božidar Stojadinović. August 2008.

PEER 2008/02 *Treatment of Uncertainties in Seismic-Risk Analysis of Transportation Systems*. Evangelos Stergiou and Anne S. Kiremidjian. July 2008.

PEER 2008/01 *Seismic Performance Objectives for Tall Buildings.* William T. Holmes, Charles Kircher, William Petak, and Nabih Youssef. August 2008.

PEER 2007/12 *An Assessment to Benchmark the Seismic Performance of a Code-Conforming Reinforced Concrete Moment-Frame Building.* Curt Haselton, Christine A. Goulet, Judith Mitrani-Reiser, James L. Beck, Gregory G. Deierlein, Keith A. Porter, Jonathan P. Stewart, and Ertugrul Taciroglu. August 2008.

PEER 2007/11 *Bar Buckling in Reinforced Concrete Bridge Columns.* Wayne A. Brown, Dawn E. Lehman, and John F. Stanton. February 2008.

PEER 2007/10 *Computational Modeling of Progressive Collapse in Reinforced Concrete Frame Structures*. Mohamed M. Talaat and Khalid M. Mosalam. May 2008.

PEER 2007/09 *Integrated Probabilistic Performance-Based Evaluation of Benchmark Reinforced Concrete Bridges*. Kevin R. Mackie, John-Michael Wong, and Božidar Stojadinović. January 2008.

PEER 2007/08 *Assessing Seismic Collapse Safety of Modern Reinforced Concrete Moment-Frame Buildings*. Curt B. Haselton and Gregory G. Deierlein. February 2008.

PEER 2007/07 *Performance Modeling Strategies for Modern Reinforced Concrete Bridge Columns*. Michael P. Berry and Marc O. Eberhard. April 2008.

PEER 2007/06 *Development of Improved Procedures for Seismic Design of Buried and Partially Buried Structures*. Linda Al Atik and Nicholas Sitar. June 2007.

PEER 2007/05 *Uncertainty and Correlation in Seismic Risk Assessment of Transportation Systems*. Renee G. Lee and Anne S. Kiremidjian. July 2007.

PEER 2007/04 *Numerical Models for Analysis and Performance-Based Design of Shallow Foundations Subjected to Seismic Loading.* Sivapalan Gajan, Tara C. Hutchinson, Bruce L. Kutter, Prishati Raychowdhury, José A. Ugalde, and Jonathan P. Stewart. May 2008.

PEER 2007/03 *Beam-Column Element Model Calibrated for Predicting Flexural Response Leading to Global Collapse of RC Frame Buildings*. Curt B. Haselton, Abbie B. Liel, Sarah Taylor Lange, and Gregory G. Deierlein. May 2008.

PEER 2007/02 *Campbell-Bozorgnia NGA Ground Motion Relations for the Geometric Mean Horizontal Component of Peak and Spectral Ground Motion Parameters*. Kenneth W. Campbell and Yousef Bozorgnia. May 2007.

PEER 2007/01 *Boore-Atkinson NGA Ground Motion Relations for the Geometric Mean Horizontal Component of Peak and Spectral Ground Motion Parameters*. David M. Boore and Gail M. Atkinson. May 2007.

PEER 2006/12 Societal Implications of Performance-Based Earthquake Engineering. Peter J. May. May 2007.

PEER 2006/11 *Probabilistic Seismic Demand Analysis Using Advanced Ground Motion Intensity Measures, Attenuation Relationships, and Near-Fault Effects*. Polsak Tothong and C. Allin Cornell. March 2007.

PEER 2006/10 *Application of the PEER PBEE Methodology to the I-880 Viaduct*. Sashi Kunnath. February 2007.

PEER 2006/09 *Quantifying Economic Losses from Travel Forgone Following a Large Metropolitan Earthquake*. James Moore, Sungbin Cho, Yue Yue Fan, and Stuart Werner. November 2006.

PEER 2006/08 *Vector-Valued Ground Motion Intensity Measures for Probabilistic Seismic Demand Analysis*. Jack W. Baker and C. Allin Cornell. October 2006.

PEER 2006/07 *Analytical Modeling of Reinforced Concrete Walls for Predicting Flexural and Coupled–Shear-Flexural Responses*. Kutay Orakcal, Leonardo M. Massone, and John W. Wallace. October 2006.

PEER 2006/06 *Nonlinear Analysis of a Soil-Drilled Pier System under Static and Dynamic Axial Loading*. Gang Wang and Nicholas Sitar. November 2006.

PEER 2006/05 *Advanced Seismic Assessment Guidelines.* Paolo Bazzurro, C. Allin Cornell, Charles Menun, Maziar Motahari, and Nicolas Luco. September 2006.

PEER 2006/04 *Probabilistic Seismic Evaluation of Reinforced Concrete Structural Components and Systems*. Tae Hyung Lee and Khalid M. Mosalam. August 2006.

PEER 2006/03 *Performance of Lifelines Subjected to Lateral Spreading.* Scott A. Ashford and Teerawut Juirnarongrit. July 2006.

PEER 2006/02 *Pacific Earthquake Engineering Research Center Highway Demonstration Project.* Anne Kiremidjian, James Moore, Yue Yue Fan, Nesrin Basoz, Ozgur Yazali, and Meredith Williams. April 2006.

PEER 2006/01 *Bracing Berkeley. A Guide to Seismic Safety on the UC Berkeley Campus.* Mary C. Comerio, Stephen Tobriner, and Ariane Fehrenkamp. January 2006.

PEER 2005/16 *Seismic Response and Reliability of Electrical Substation Equipment and Systems.* Junho Song, Armen Der Kiureghian, and Jerome L. Sackman. April 2006.

PEER 2005/15 *CPT-Based Probabilistic Assessment of Seismic Soil Liquefaction Initiation.* R. E. S. Moss, R. B. Seed, R. E. Kayen, J. P. Stewart, and A. Der Kiureghian. April 2006.

PEER 2005/14 *Workshop on Modeling of Nonlinear Cyclic Load-Deformation Behavior of Shallow Foundations.* Bruce L. Kutter, Geoffrey Martin, Tara Hutchinson, Chad Harden, Sivapalan Gajan, and Justin Phalen. March 2006.

PEER 2005/13 *Stochastic Characterization and Decision Bases under Time-Dependent Aftershock Risk in Performance-Based Earthquake Engineering*. Gee Liek Yeo and C. Allin Cornell. July 2005.

PEER 2005/12 *PEER Testbed Study on a Laboratory Building: Exercising Seismic Performance Assessment.* Mary C. Comerio, Editor. November 2005.

PEER 2005/11 *Van Nuys Hotel Building Testbed Report: Exercising Seismic Performance Assessment.* Helmut Krawinkler, Editor. October 2005.

PEER 2005/10 *First NEES/E-Defense Workshop on Collapse Simulation of Reinforced Concrete Building Structures.* September 2005.

PEER 2005/09 *Test Applications of Advanced Seismic Assessment Guidelines.* Joe Maffei, Karl Telleen, Danya Mohr, William Holmes, and Yuki Nakayama. August 2006.

PEER 2005/08 *Damage Accumulation in Lightly Confined Reinforced Concrete Bridge Columns.* R. Tyler Ranf, Jared M. Nelson, Zach Price, Marc O. Eberhard, and John F. Stanton. April 2006.

PEER 2005/07 *Experimental and Analytical Studies on the Seismic Response of Freestanding and Anchored Laboratory Equipment.* Dimitrios Konstantinidis and Nicos Makris. January 2005.

PEER 2005/06 *Global Collapse of Frame Structures under Seismic Excitations*. Luis F. Ibarra and Helmut Krawinkler. September 2005.

PEER 2005//05 *Performance Characterization of Bench- and Shelf-Mounted Equipment.* Samit Ray Chaudhuri and Tara C. Hutchinson. May 2006.

PEER 2005/04 *Numerical Modeling of the Nonlinear Cyclic Response of Shallow Foundations.* Chad Harden, Tara Hutchinson, Geoffrey R. Martin, and Bruce L. Kutter. August 2005.

PEER 2005/03 *A Taxonomy of Building Components for Performance-Based Earthquake Engineering.* Keith A. Porter. September 2005.

PEER 2005/02 *Fragility Basis for California Highway Overpass Bridge Seismic Decision Making*. Kevin R. Mackie and Božidar Stojadinović. June 2005.

PEER 2005/01 *Empirical Characterization of Site Conditions on Strong Ground Motion.* Jonathan P. Stewart, Yoojoong Choi, and Robert W. Graves. June 2005.

PEER 2004/09 *Electrical Substation Equipment Interaction: Experimental Rigid Conductor Studies.* Christopher Stearns and André Filiatrault. February 2005.

PEER 2004/08 *Seismic Qualification and Fragility Testing of Line Break 550-kV Disconnect Switches.* Shakhzod M. Takhirov, Gregory L. Fenves, and Eric Fujisaki. January 2005.

PEER 2004/07 *Ground Motions for Earthquake Simulator Qualification of Electrical Substation Equipment.* Shakhzod M. Takhirov, Gregory L. Fenves, Eric Fujisaki, and Don Clyde. January 2005.

PEER 2004/06 *Performance-Based Regulation and Regulatory Regimes.* Peter J. May and Chris Koski. September 2004.

PEER 2004/05 *Performance-Based Seismic Design Concepts and Implementation: Proceedings of an International Workshop.* Peter Fajfar and Helmut Krawinkler, Editors. September 2004.

PEER 2004/04 *Seismic Performance of an Instrumented Tilt-up Wall Building.* James C. Anderson and Vitelmo V. Bertero. July 2004.

PEER 2004/03 *Evaluation and Application of Concrete Tilt-up Assessment Methodologies.* Timothy Graf and James O. Malley. October 2004.

PEER 2004/02 *Analytical Investigations of New Methods for Reducing Residual Displacements of Reinforced Concrete Bridge Columns.* Junichi Sakai and Stephen A. Mahin. August 2004.

PEER 2004/01 *Seismic Performance of Masonry Buildings and Design Implications.* Kerri Anne Taeko Tokoro, James C. Anderson, and Vitelmo V. Bertero. February 2004.

PEER 2003/18 *Performance Models for Flexural Damage in Reinforced Concrete Columns.* Michael Berry and Marc Eberhard. August 2003.

PEER 2003/17 *Predicting Earthquake Damage in Older Reinforced Concrete Beam-Column Joints.* Catherine Pagni and Laura Lowes. October 2004.

PEER 2003/16 *Seismic Demands for Performance-Based Design of Bridges*. Kevin Mackie and Božidar Stojadinović. August 2003.

PEER 2003/15 *Seismic Demands for Nondeteriorating Frame Structures and Their Dependence on Ground Motions.* Ricardo Antonio Medina and Helmut Krawinkler. May 2004.

PEER 2003/14 *Finite Element Reliability and Sensitivity Methods for Performance-Based Earthquake Engineering*. Terje Haukaas and Armen Der Kiureghian. April 2004.

PEER 2003/13 *Effects of Connection Hysteretic Degradation on the Seismic Behavior of Steel Moment-Resisting Frames.* Janise E. Rodgers and Stephen A. Mahin. March 2004.

PEER 2003/12 *Implementation Manual for the Seismic Protection of Laboratory Contents: Format and Case Studies*. William T. Holmes and Mary C. Comerio. October 2003.

PEER 2003/11 *Fifth U.S.-Japan Workshop on Performance-Based Earthquake Engineering Methodology for Reinforced Concrete Building Structures*. February 2004.

PEER 2003/10 *A Beam-Column Joint Model for Simulating the Earthquake Response of Reinforced Concrete Frames.* Laura N. Lowes, Nilanjan Mitra, and Arash Altoontash. February 2004.

PEER 2003/09 *Sequencing Repairs after an Earthquake: An Economic Approach.* Marco Casari and Simon J. Wilkie. April 2004.

PEER 2003/08 *A Technical Framework for Probability-Based Demand and Capacity Factor Design (DCFD) Seismic Formats*. Fatemeh Jalayer and C. Allin Cornell. November 2003.

PEER 2003/07 *Uncertainty Specification and Propagation for Loss Estimation Using FOSM Methods.* Jack W. Baker and C. Allin Cornell. September 2003.

PEER 2003/06 *Performance of Circular Reinforced Concrete Bridge Columns under Bidirectional Earthquake Loading*. Mahmoud M. Hachem, Stephen A. Mahin, and Jack P. Moehle. February 2003.

PEER 2003/05 *Response Assessment for Building-Specific Loss Estimation.* Eduardo Miranda and Shahram Taghavi. September 2003.

PEER 2003/04 *Experimental Assessment of Columns with Short Lap Splices Subjected to Cyclic Loads*. Murat Melek, John W. Wallace, and Joel Conte. April 2003.

PEER 2003/03 *Probabilistic Response Assessment for Building-Specific Loss Estimation*. Eduardo Miranda and Hesameddin Aslani. September 2003.

PEER 2003/02 *Software Framework for Collaborative Development of Nonlinear Dynamic Analysis Program*. Jun Peng and Kincho H. Law. September 2003.

PEER 2003/01 *Shake Table Tests and Analytical Studies on the Gravity Load Collapse of Reinforced Concrete Frames.* Kenneth John Elwood and Jack P. Moehle. November 2003.

PEER 2002/24 *Performance of Beam to Column Bridge Joints Subjected to a Large Velocity Pulse.* Natalie Gibson, André Filiatrault, and Scott A. Ashford. April 2002.

PEER 2002/23 *Effects of Large Velocity Pulses on Reinforced Concrete Bridge Columns.* Greg L. Orozco and Scott A. Ashford. April 2002.

PEER 2002/22 *Characterization of Large Velocity Pulses for Laboratory Testing.* Kenneth E. Cox and Scott A. Ashford. April 2002.

PEER 2002/21 *Fourth U.S.-Japan Workshop on Performance-Based Earthquake Engineering Methodology for Reinforced Concrete Building Structures*. December 2002.

PEER 2002/20 *Barriers to Adoption and Implementation of PBEE Innovations.* Peter J. May. August 2002.

PEER 2002/19 *Economic-Engineered Integrated Models for Earthquakes: Socioeconomic Impacts.* Peter Gordon, James E. Moore II, and Harry W. Richardson. July 2002.

PEER 2002/18 *Assessment of Reinforced Concrete Building Exterior Joints with Substandard Details.* Chris P. Pantelides, Jon Hansen, Justin Nadauld, and Lawrence D. Reaveley. May 2002.

PEER 2002/17 *Structural Characterization and Seismic Response Analysis of a Highway Overcrossing Equipped with Elastomeric Bearings and Fluid Dampers: A Case Study*. Nicos Makris and Jian Zhang. November 2002.

PEER 2002/16 *Estimation of Uncertainty in Geotechnical Properties for Performance-Based Earthquake Engineering*. Allen L. Jones, Steven L. Kramer, and Pedro Arduino. December 2002.

PEER 2002/15 *Seismic Behavior of Bridge Columns Subjected to Various Loading Patterns*. Asadollah Esmaeily-Gh. and Yan Xiao. December 2002.

PEER 2002/14 *Inelastic Seismic Response of Extended Pile Shaft Supported Bridge Structures.* T.C. Hutchinson, R.W. Boulanger, Y.H. Chai, and I.M. Idriss. December 2002.

PEER 2002/13 *Probabilistic Models and Fragility Estimates for Bridge Components and Systems.* Paolo Gardoni, Armen Der Kiureghian, and Khalid M. Mosalam. June 2002.

PEER 2002/12 *Effects of Fault Dip and Slip Rake on Near-Source Ground Motions: Why Chi-Chi Was a Relatively Mild M7.6 Earthquake*. Brad T. Aagaard, John F. Hall, and Thomas H. Heaton. December 2002.

PEER 2002/11 *Analytical and Experimental Study of Fiber-Reinforced Strip Isolators*. James M. Kelly and Shakhzod M. Takhirov. September 2002.

PEER 2002/10 *Centrifuge Modeling of Settlement and Lateral Spreading with Comparisons to Numerical Analyses***.** Sivapalan Gajan and Bruce L. Kutter. January 2003.

PEER 2002/09 *Documentation and Analysis of Field Case Histories of Seismic Compression during the 1994 Northridge, California, Earthquake*. Jonathan P. Stewart, Patrick M. Smith, Daniel H. Whang, and Jonathan D. Bray. October 2002.

PEER 2002/08 *Component Testing, Stability Analysis and Characterization of Buckling-Restrained Unbonded Braces™*. Cameron Black, Nicos Makris, and Ian Aiken. September 2002.

PEER 2002/07 *Seismic Performance of Pile-Wharf Connections.* Charles W. Roeder, Robert Graff, Jennifer Soderstrom, and Jun Han Yoo. December 2001.

PEER 2002/06 *The Use of Benefit-Cost Analysis for Evaluation of Performance-Based Earthquake Engineering Decisions*. Richard O. Zerbe and Anthony Falit-Baiamonte. September 2001.

PEER 2002/05 *Guidelines, Specifications, and Seismic Performance Characterization of Nonstructural Building Components and Equipment*. André Filiatrault, Constantin Christopoulos, and Christopher Stearns. September 2001.

PEER 2002/04 *Consortium of Organizations for Strong-Motion Observation Systems and the Pacific Earthquake Engineering Research Center Lifelines Program: Invited Workshop on Archiving and Web Dissemination of Geotechnical Data, 4–5 October 2001*. September 2002.

PEER 2002/03 *Investigation of Sensitivity of Building Loss Estimates to Major Uncertain Variables for the Van Nuys Testbed*. Keith A. Porter, James L. Beck, and Rustem V. Shaikhutdinov. August 2002.

PEER 2002/02 *The Third U.S.-Japan Workshop on Performance-Based Earthquake Engineering Methodology for Reinforced Concrete Building Structures*. July 2002.

PEER 2002/01 *Nonstructural Loss Estimation: The UC Berkeley Case Study.* Mary C. Comerio and John C. Stallmeyer. December 2001.

PEER 2001/16 *Statistics of SDF-System Estimate of Roof Displacement for Pushover Analysis of Buildings.* Anil K. Chopra, Rakesh K. Goel, and Chatpan Chintanapakdee. December 2001.

PEER 2001/15 *Damage to Bridges during the 2001 Nisqually Earthquake.* R. Tyler Ranf, Marc O. Eberhard, and Michael P. Berry. November 2001.

PEER 2001/14 *Rocking Response of Equipment Anchored to a Base Foundation.* Nicos Makris and Cameron J. Black. September 2001.

PEER 2001/13 *Modeling Soil Liquefaction Hazards for Performance-Based Earthquake Engineering*. Steven L. Kramer and Ahmed-W. Elgamal. February 2001.

PEER 2001/12 *Development of Geotechnical Capabilities in OpenSees*. Boris Jeremić. September 2001.

PEER 2001/11 *Analytical and Experimental Study of Fiber-Reinforced Elastomeric Isolators*. James M. Kelly and Shakhzod M. Takhirov. September 2001.

PEER 2001/10 *Amplification Factors for Spectral Acceleration in Active Regions.* Jonathan P. Stewart, Andrew H. Liu, Yoojoong Choi, and Mehmet B. Baturay. December 2001.

PEER 2001/09 *Ground Motion Evaluation Procedures for Performance-Based Design.* Jonathan P. Stewart, Shyh-Jeng Chiou, Jonathan D. Bray, Robert W. Graves, Paul G. Somerville, and Norman A. Abrahamson. September 2001.

PEER 2001/08 *Experimental and Computational Evaluation of Reinforced Concrete Bridge Beam-Column Connections for Seismic Performance*. Clay J. Naito, Jack P. Moehle, and Khalid M. Mosalam. November 2001.

PEER 2001/07 *The Rocking Spectrum and the Shortcomings of Design Guidelines.* Nicos Makris and Dimitrios Konstantinidis. August 2001.

PEER 2001/06 *Development of an Electrical Substation Equipment Performance Database for Evaluation of Equipment Fragilities*. Thalia Agnanos. April 1999.

PEER 2001/05 *Stiffness Analysis of Fiber-Reinforced Elastomeric Isolators.* Hsiang-Chuan Tsai and James M. Kelly. May 2001.

PEER 2001/04 *Organizational and Societal Considerations for Performance-Based Earthquake Engineering*. Peter J. May. April 2001.

PEER 2001/03 *A Modal Pushover Analysis Procedure to Estimate Seismic Demands for Buildings: Theory and Preliminary Evaluation*. Anil K. Chopra and Rakesh K. Goel. January 2001.

PEER 2001/02 *Seismic Response Analysis of Highway Overcrossings Including Soil-Structure Interaction*. Jian Zhang and Nicos Makris. March 2001.

PEER 2001/01 *Experimental Study of Large Seismic Steel Beam-to-Column Connections.* Egor P. Popov and Shakhzod M. Takhirov. November 2000.

PEER 2000/10 *The Second U.S.-Japan Workshop on Performance-Based Earthquake Engineering Methodology for Reinforced Concrete Building Structures*. March 2000.

PEER 2000/09 *Structural Engineering Reconnaissance of the August 17, 1999 Earthquake: Kocaeli (Izmit), Turkey*. Halil Sezen, Kenneth J. Elwood, Andrew S. Whittaker, Khalid Mosalam, John J. Wallace, and John F. Stanton. December 2000.

PEER 2000/08 *Behavior of Reinforced Concrete Bridge Columns Having Varying Aspect Ratios and Varying Lengths of Confinement*. Anthony J. Calderone, Dawn E. Lehman, and Jack P. Moehle. January 2001.

PEER 2000/07 *Cover-Plate and Flange-Plate Reinforced Steel Moment-Resisting Connections.* Taejin Kim, Andrew S. Whittaker, Amir S. Gilani, Vitelmo V. Bertero, and Shakhzod M. Takhirov. September 2000.

PEER 2000/06 *Seismic Evaluation and Analysis of 230-kV Disconnect Switches.* Amir S. J. Gilani, Andrew S. Whittaker, Gregory L. Fenves, Chun-Hao Chen, Henry Ho, and Eric Fujisaki. July 2000.

PEER 2000/05 *Performance-Based Evaluation of Exterior Reinforced Concrete Building Joints for Seismic Excitation*. Chandra Clyde, Chris P. Pantelides, and Lawrence D. Reaveley. July 2000.

PEER 2000/04 *An Evaluation of Seismic Energy Demand: An Attenuation Approach*. Chung-Che Chou and Chia-Ming Uang. July 1999.

PEER 2000/03 *Framing Earthquake Retrofitting Decisions: The Case of Hillside Homes in Los Angeles.* Detlof von Winterfeldt, Nels Roselund, and Alicia Kitsuse. March 2000.

PEER 2000/02 *U.S.-Japan Workshop on the Effects of Near-Field Earthquake Shaking*. Andrew Whittaker, Editor. July 2000.

PEER 2000/01 *Further Studies on Seismic Interaction in Interconnected Electrical Substation Equipment.* Armen Der Kiureghian, Kee-Jeung Hong, and Jerome L. Sackman. November 1999.

PEER 1999/14 *Seismic Evaluation and Retrofit of 230-kV Porcelain Transformer Bushings*. Amir S. Gilani, Andrew S. Whittaker, Gregory L. Fenves, and Eric Fujisaki. December 1999.

PEER 1999/13 *Building Vulnerability Studies: Modeling and Evaluation of Tilt-up and Steel Reinforced Concrete Buildings*. John W. Wallace, Jonathan P. Stewart, and Andrew S. Whittaker, Editors. December 1999.

PEER 1999/12 *Rehabilitation of Nonductile RC Frame Building Using Encasement Plates and Energy-Dissipating Devices*. Mehrdad Sasani, Vitelmo V. Bertero, James C. Anderson. December 1999.

PEER 1999/11 *Performance Evaluation Database for Concrete Bridge Components and Systems under Simulated Seismic Loads*. Yael D. Hose and Frieder Seible. November 1999.

PEER 1999/10 *U.S.-Japan Workshop on Performance-Based Earthquake Engineering Methodology for Reinforced Concrete Building Structures*. December 1999.

PEER 1999/09 *Performance Improvement of Long Period Building Structures Subjected to Severe Pulse-Type Ground Motions*. James C. Anderson, Vitelmo V. Bertero, and Raul Bertero. October 1999.

PEER 1999/08 *Envelopes for Seismic Response Vectors.* Charles Menun and Armen Der Kiureghian. July 1999.

PEER 1999/07 *Documentation of Strengths and Weaknesses of Current Computer Analysis Methods for Seismic Performance of Reinforced Concrete Members*. William F. Cofer. November 1999.

PEER 1999/06 *Rocking Response and Overturning of Anchored Equipment under Seismic Excitations*. Nicos Makris and Jian Zhang. November 1999.

PEER 1999/05 *Seismic Evaluation of 550 kV Porcelain Transformer Bushings.* Amir S. Gilani, Andrew S. Whittaker, Gregory L. Fenves, and Eric Fujisaki. October 1999.

PEER 1999/04 *Adoption and Enforcement of Earthquake Risk-Reduction Measures.* Peter J. May, Raymond J. Burby, T. Jens Feeley, and Robert Wood. August 1999.

PEER 1999/03 *Task 3 Characterization of Site Response General Site Categories*. Adrian Rodriguez-Marek, Jonathan D. Bray and Norman Abrahamson. February 1999.

PEER 1999/02 *Capacity-Demand-Diagram Methods for Estimating Seismic Deformation of Inelastic Structures: SDF Systems*. Anil K. Chopra and Rakesh Goel. April 1999.

PEER 1999/01 *Interaction in Interconnected Electrical Substation Equipment Subjected to Earthquake Ground Motions*. Armen Der Kiureghian, Jerome L. Sackman, and Kee-Jeung Hong. February 1999.

PEER 1998/08 *Behavior and Failure Analysis of a Multiple-Frame Highway Bridge in the 1994 Northridge Earthquake*. Gregory L. Fenves and Michael Ellery. December 1998.

PEER 1998/07 *Empirical Evaluation of Inertial Soil-Structure Interaction Effects.* Jonathan P. Stewart, Raymond B. Seed, and Gregory L. Fenves. November 1998.

PEER 1998/06 *Effect of Damping Mechanisms on the Response of Seismic Isolated Structures*. Nicos Makris and Shih-Po Chang. November 1998.

PEER 1998/05 *Rocking Response and Overturning of Equipment under Horizontal Pulse-Type Motions*. Nicos Makris and Yiannis Roussos. October 1998.

PEER 1998/04 *Pacific Earthquake Engineering Research Invitational Workshop Proceedings, May 14–15, 1998: Defining the Links between Planning, Policy Analysis, Economics and Earthquake Engineering*. Mary Comerio and Peter Gordon. September 1998.

PEER 1998/03 *Repair/Upgrade Procedures for Welded Beam to Column Connections*. James C. Anderson and Xiaojing Duan. May 1998.

PEER 1998/02 *Seismic Evaluation of 196 kV Porcelain Transformer Bushings.* Amir S. Gilani, Juan W. Chavez, Gregory L. Fenves, and Andrew S. Whittaker. May 1998.

PEER 1998/01 *Seismic Performance of Well-Confined Concrete Bridge Columns.* Dawn E. Lehman and Jack P. Moehle. December 2000.

ONLINE PEER REPORTS

The following PEER reports are available by Internet only at http://peer.berkeley.edu/publications/peer_reports_complete.html.

PEER 2012/103 *Performance-Based Seismic Demand Assessment of Concentrically Braced Steel Frame Buildings.* Chui-Hsin Chen and Stephen A. Mahin. December 2012.

PEER 2012/102 *Procedure to Restart an Interrupted Hybrid Simulation: Addendum to PEER Report 2010/103.* Vesna Terzic and Bozidar Stojadinovic. October 2012.

PEER 2012/101 *Mechanics of Fiber Reinforced Bearings.* James M. Kelly and Andrea Calabrese. February 2012.

PEER 2011/107 *Nonlinear Site Response and Seismic Compression at Vertical Array Strongly Shaken by 2007 Niigata-ken Chuetsu-oki Earthquake.* Eric Yee, Jonathan P. Stewart, and Kohji Tokimatsu. December 2011.

PEER 2011/106 *Self Compacting Hybrid Fiber Reinforced Concrete Composites for Bridge Columns.* Pardeep Kumar, Gabriel Jen, William Trono, Marios Panagiotou, and Claudia Ostertag. September 2011.

PEER 2011/105 *Stochastic Dynamic Analysis of Bridges Subjected to Spacially Varying Ground Motions.* Katerina Konakli and Armen Der Kiureghian. August 2011.

PEER 2011/104 *Design and Instrumentation of the 2010 E-Defense Four-Story Reinforced Concrete and Post-Tensioned Concrete Buildings.* Takuya Nagae, Kenichi Tahara, Taizo Matsumori, Hitoshi Shiohara, Toshimi Kabeyasawa, Susumu Kono, Minehiro Nishiyama (Japanese Research Team) and John Wallace, Wassim Ghannoum, Jack Moehle, Richard Sause, Wesley Keller, Zeynep Tuna (U.S. Research Team). June 2011.

PEER 2011/103 *In-Situ Monitoring of the Force Output of Fluid Dampers: Experimental Investigation.* Dimitrios Konstantinidis, James M. Kelly, and Nicos Makris. April 2011.

PEER 2011/102 *Ground-Motion Prediction Equations 1964–2010.* John Douglas. April 2011.

PEER 2011/101 *Report of the Eighth Planning Meeting of NEES/E-Defense Collaborative Research on Earthquake Engineering.* Convened by the Hyogo Earthquake Engineering Research Center (NIED), NEES Consortium, Inc. February 2011.

PEER 2010/111 *Modeling and Acceptance Criteria for Seismic Design and Analysis of Tall Buildings.* Task 7 Report for the Tall Buildings Initiative - Published jointly by the Applied Technology Council. October 2010.

PEER 2010/110 *Seismic Performance Assessment and Probabilistic Repair Cost Analysis of Precast Concrete Cladding Systems for Multistory Buildlings.* Jeffrey P. Hunt and Božidar Stojadinovic. November 2010.

PEER 2010/109 *Report of the Seventh Joint Planning Meeting of NEES/E-Defense Collaboration on Earthquake Engineering. Held at the E-Defense, Miki, and Shin-Kobe, Japan, September 18–19, 2009.* August 2010.

PEER 2010/108 *Probabilistic Tsunami Hazard in California.* Hong Kie Thio, Paul Somerville, and Jascha Polet, preparers. October 2010.

PEER 2010/107 *Performance and Reliability of Exposed Column Base Plate Connections for Steel Moment-Resisting Frames.* Ady Aviram, Božidar Stojadinovic, and Armen Der Kiureghian. August 2010.

PEER 2010/106 *Verification of Probabilistic Seismic Hazard Analysis Computer Programs.* Patricia Thomas, Ivan Wong, and Norman Abrahamson. May 2010.

PEER 2010/105 *Structural Engineering Reconnaissance of the April 6, 2009, Abruzzo, Italy, Earthquake, and Lessons Learned.* M. Selim Günay and Khalid M. Mosalam. April 2010.

PEER 2010/104 *Simulating the Inelastic Seismic Behavior of Steel Braced Frames, Including the Effects of Low-Cycle Fatigue.* Yuli Huang and Stephen A. Mahin. April 2010.

PEER 2010/103 *Post-Earthquake Traffic Capacity of Modern Bridges in California.* Vesna Terzic and Božidar Stojadinović. March 2010.

PEER 2010/102 *Analysis of Cumulative Absolute Velocity (CAV) and JMA Instrumental Seismic Intensity (I_{JMA}) Using the PEER–NGA Strong Motion Database.* Kenneth W. Campbell and Yousef Bozorgnia. February 2010.

PEER 2010/101 *Rocking Response of Bridges on Shallow Foundations.* Jose A. Ugalde, Bruce L. Kutter, and Boris Jeremic. April 2010.

PEER 2009/109 *Simulation and Performance-Based Earthquake Engineering Assessment of Self-Centering Post-Tensioned Concrete Bridge Systems.* Won K. Lee and Sarah L. Billington. December 2009.

PEER 2009/108 *PEER Lifelines Geotechnical Virtual Data Center.* J. Carl Stepp, Daniel J. Ponti, Loren L. Turner, Jennifer N. Swift, Sean Devlin, Yang Zhu, Jean Benoit, and John Bobbitt. September 2009.

PEER 2009/107 *Experimental and Computational Evaluation of Current and Innovative In-Span Hinge Details in Reinforced Concrete Box-Girder Bridges: Part 2: Post-Test Analysis and Design Recommendations.* Matias A. Hube and Khalid M. Mosalam. December 2009.

PEER 2009/106 *Shear Strength Models of Exterior Beam-Column Joints without Transverse Reinforcement.* Sangjoon Park and Khalid M. Mosalam. November 2009.

PEER 2009/105 *Reduced Uncertainty of Ground Motion Prediction Equations through Bayesian Variance Analysis.* Robb Eric S. Moss. November 2009.

PEER 2009/104 *Advanced Implementation of Hybrid Simulation.* Andreas H. Schellenberg, Stephen A. Mahin, Gregory L. Fenves. November 2009.

PEER 2009/103 *Performance Evaluation of Innovative Steel Braced Frames.* T. Y. Yang, Jack P. Moehle, and Božidar Stojadinovic. August 2009.

PEER 2009/102 *Reinvestigation of Liquefaction and Nonliquefaction Case Histories from the 1976 Tangshan Earthquake.* Robb Eric Moss, Robert E. Kayen, Liyuan Tong, Songyu Liu, Guojun Cai, and Jiaer Wu. August 2009.

PEER 2009/101 *Report of the First Joint Planning Meeting for the Second Phase of NEES/E-Defense Collaborative Research on Earthquake Engineering.* Stephen A. Mahin et al. July 2009.

PEER 2008/104 *Experimental and Analytical Study of the Seismic Performance of Retaining Structures.* Linda Al Atik and Nicholas Sitar. January 2009.

PEER 2008/103 *Experimental and Computational Evaluation of Current and Innovative In-Span Hinge Details in Reinforced Concrete Box-Girder Bridges. Part 1: Experimental Findings and Pre-Test Analysis.* Matias A. Hube and Khalid M. Mosalam. January 2009.

PEER 2008/102 *Modeling of Unreinforced Masonry Infill Walls Considering In-Plane and Out-of-Plane Interaction.* Stephen Kadysiewski and Khalid M. Mosalam. January 2009.

PEER 2008/101 *Seismic Performance Objectives for Tall Buildings.* William T. Holmes, Charles Kircher, William Petak, and Nabih Youssef. August 2008.

PEER 2007/101 *Generalized Hybrid Simulation Framework for Structural Systems Subjected to Seismic Loading*. Tarek Elkhoraibi and Khalid M. Mosalam. July 2007.

PEER 2007/100 *Seismic Evaluation of Reinforced Concrete Buildings Including Effects of Masonry Infill Walls*. Alidad Hashemi and Khalid M. Mosalam. July 2007.

The Pacific Earthquake Engineering Research Center (PEER) is a multi-institutional research and education center with headquarters at the University of California, Berkeley. Investigators from over 20 universities, several consulting companies, and researchers at various state and federal government agencies contribute to research programs focused on performance-based earthquake engineering.

These research programs aim to identify and reduce the risks from major earthquakes to life safety and to the economy by including research in a wide variety of disciplines including structural and geotechnical engineering, geology/seismology, lifelines, transportation, architecture, economics, risk management, and public policy.

PEER is supported by federal, state, local, and regional agencies, together with industry partners.

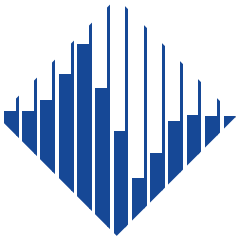

PEER Core Institutions:
University of California, Berkeley (Lead Institution)
California Institute of Technology
Oregon State University
Stanford University
University of California, Davis
University of California, Irvine
University of California, Los Angeles
University of California, San Diego
University of Southern California
University of Washington

PEER reports can be ordered at http://peer.berkeley.edu/publications/peer_reports.html or by contacting

Pacific Earthquake Engineering Research Center
University of California, Berkeley
325 Davis Hall, Mail Code 1792
Berkeley, CA 94720-1792
Tel: 510-642-3437
Fax: 510-642-1655
Email: clairejohnson@berkeley.edu

ISSN 1547-0587X